Université catholique de Louvain
Faculté d'Ingénierie Biologique, Agronomique et Environnementale
Earth and Life Institute

Overland flow connectivity
Theory and application at the interrill scale

Michaël Antoine

Septembre 2010

Thèse présentée en vue de l'obtention
du grade de Docteur en sciences agronomiques
et ingénierie biologique

Copromoteurs: Prof. Charles Bielders
Prof. Mathieu Javaux

Composition du jury:

Président:	Prof. Jacques Mahillon (UCL, Belgique)
Copromoteurs:	Prof. Charles Bielders (UCL, Belgique)
	Prof. Mathieu Javaux (UCL, Belgique)
Lecteurs:	Dr. Frédéric Darboux (INRA, France)
	Prof. Gerard Govers (KUL, Belgique)
	Prof. Emmanuel Hanert (UCL, Belgique)
	Prof. Victor Jetten (ITC, Pays-Bas)

Remerciements

L'ennui naquit un jour de l'uniformité (Antoine Houdar de la Motte). C'est bien l'éclectisme des approches et des techniques qui fut l'essence de ce travail original. Le réaliser fut tout sauf ennuyeux. Cela saute d'ailleurs aux yeux, à la lecture de mes notes de frais : piscine gonflable, tôle ondulée, poudre à mouler les dents, lait concentré, webcam pour enfant, tissu KW, chokotoff, paillasson, système d'arrosage des fleurs... Tout cela pour un usage scientifique, promis !

Je remercie avant tout les autorités de l'UCL et leur représentant direct au sein du laboratoire Marnik Vanclooster. Merci de m'avoir fait confiance pour les questions d'enseignement et de m'avoir offert la liberté de choisir, en toute indépendance, mon sujet de doctorat. Celui-ci ne s'inscrivait aucunement dans la continuité d'un projet antérieur. Il demanda dès lors une grande ouverture d'esprit de la part de mes promoteurs Charles Bielders et Mathieu Javaux et exigea de leur part la volonté de construire ensemble un nouveau domaine de recherche pour le laboratoire.

Charles et Mathieu, j'ai fort apprécié nos réunions de doctorat interminables où chaque idée était largement débattue. Vos relectures attentives de la thèse et des articles qui la composent m'ont beaucoup appris. Votre intérêt général pour mon travail constitua une formidable source de motivation. En terme marin, je dirais que votre entourage fut semblable à un vent portant, permettant une navigation rapide sous spi tout en préservant la maniabilité à la barre. Et à ce propos, merci de m'avoir permis de larguer les amarres un moment et d'avoir cru au retour d'Ulysse.

Je remercie les lecteurs de cette thèse, Frédéric Darboux, Gérard Govers, Emmanuel Hanert et Victor Jetten pour le temps qu'ils m'ont consacré, pour leurs remarques pertinentes et leurs encouragements. Je suis très honoré d'avoir pu vous transmettre de façon privilégiée les résultats de mes recherches.

Mention spéciale pour Frédéric qui prit part également à mon comité d'accompagnement. Merci de m'avoir ouvert les portes de ton laboratoire, d'avoir essuyé quelques averses (artificielles) avec moi et d'avoir partagé tes genouillères et ton goût pour la cuisine des terroirs. Tes travaux de recherches m'ont beaucoup inspiré ! J'espère d'ailleurs ne pas avoir copié inconsciemment...

J'ai eu l'honneur de partager certaines publications avec d'autres. Bartel Van Nieuwenhuyse, merci beaucoup de m'avoir associé à ton premier article. Je t'en souhaite beaucoup d'autres ! Claire Chalon, merci d'avoir réalisé ton mémoire dans le cadre de ma recherche. Ta contribution pour les essais de moulages constitua un énorme coup de pouce pour mon travail. Avec Mathieu, nous n'avons jamais eu l'objectif de te torturer; mais si nous l'avions eu, il aurait été largement atteint !

Le doctorat représente l'étape ultime du système d'éducation. Les prérequis sont donc indispensables. Je remercie en tout premier lieu mes parents et leur insupportable *c'est bien, mais je crois que tu es capable de mieux*. Merci de m'avoir épaulé depuis toujours. Merci pour l'intérêt porté à cette thèse, auquel j'associe également mes beaux-parents. Un merci particulier à Maman pour les relectures de l'anglais et à Anne pour la couture du simulateur de pluie. J'aimerais de plus remercier trois professeurs qui m'ont marqué au cours de mes études : Mr Camus (sixième primaire) pour l'esprit de groupe et l'esprit d'initiative, Mr Maingain (rhétorique) pour le goût de l'effort et de la communication et Mr Persoons (licence) pour le sens du terrain et pour avoir suscité ma vocation.

Le GERU est une grande famille ! Maintenant que j'ai deux enfants, je sais ce que ça représente. Même si a priori personne ne pleure et tout le monde est capable s'habiller tout seul comme un grand, il est vrai que, face à certaines questions administrativo-techniques, on se sent quelque fois tout petit. Merci à Maman Carine et Papa Guido pour leur soutien dans ces moments-là. Merci de rire de nos bêtises sans jamais nous gronder... Désolé pour le diesel à la place de l'essence, les oublis de TVA, les outils électroniques tombés dans l'eau, les lames de scie explosées, les notes de frais 6 mois plus tard, l'inondation du labo, le bleu partout... Merci aussi à mes frères et soeurs de misère, je me suis vraiment bien amusé ces 6 années avec vous. J'espère que nos vies professionnelles se recroiseront parfois et qu'on reparlera alors de ce bon vieux temps où l'on utilisait Matlab.

A sa manière, il contribua aussi à ma réflexion doctorale: Thomas et son franc-parler (*Tout ça ne me parait pas très clair !*). Mais surtout, il fut là aux moments clés de ces 6 dernières années. Merci pour ton amitié.

Je termine ces remerciements en m'adressant à la plus belle. Merci Tinou pour ton soutien indéfectible, malgré l'empiétement de ma thèse sur notre vie familiale. Ces six années, tu m'as offert la possibilité de me concentrer sur ma thèse sans me soucier de tous les impondérables familiaux. Souvent, lorsque j'étais tranquillement assis face à mon écran d'ordinateur, tu te transformais en super Nanny, en gestionnaire de chantier, en secrétaire de Monsieur Antoine, en capitaine, en taxiwomen. Je te décerne le grade de docteur en féedulogie, avec les félicitations du mari !

Contents

List of Figures

List of Tables

Chapter 1

Introduction

1.1 What is connectivity ? (state of the art)

The word 'connectivity' is used in a variety of disciplines, such as neurological sciences, mathematical graph theory, computer and communications technologies, meta-population biology, landscape ecology, hydrology and geomorphology. The connectivity concept has been developed to investigate the influence of the intrinsic organization of heterogeneities on the global behavior of the system that contains those heterogeneities. Heterogeneities, even when present in relatively small proportions, often have drastic impacts on the system behavior depending on their spatial distribution (Cappelaere *et al.*, 2000). Therefore they are an essential factor to take into account when modeling heterogeneous systems.

In the context of landscape ecology, the study of connectivity is an old concern. The original definition of landscape connectivity is *the degree to which the landscape facilitates or impedes movement between resource patches* (Taylor *et al.*, 1993). It combines the effect of the landscape structures as well as the species ability to move in this landscape and the associated risk (Tischendorf and Fahring, 2000). Hence landscape connectivity integrates two characteristics: the physical patterns in the landscape and the behavioral processes of the species in interaction with those patterns (Chetkiewicz *et al.*, 2006). Therefore landscape connectivity can be divided into two sub-concepts: the structural and the functional connectivity. Structural connectivity aims at describing the physical links among habitat patches and are measurable by spatial metrics whereas functional connectivity accounts for the flow of organisms through the landscape, which is species specific and may depend on broader-scale influences, such as the wind direction or the water currents (Taylor *et al.*, 2006).

In the context of subsurface hydrology, the study of connectivity has been specifically dedicated to the water fluxes per-se (to determine solute transport subsequently) in the vadose zone and in fractured media. Connectivity of the medium typically refers to the presence of continuous fast flow streamlines of water and/or solutes transport (Knudby and Carrera, 2006) or, on the contrary, to the presence of cut off structures that obstruct the flow (Cappelaere *et al.*, 2000; Hirsch and Schuette, 1999; Lehmann *et al.*, 2007). It is implicitly assumed to be a purely statistical concept (Deutsch, 1998; Vogel, 2000) associated with the geometry of the pore space (Knudby and Carrera, 2005) or the fractures (Xu *et al.*, 2006). This approach of the connectivity concept is mostly structural (in the sense defined in landscape ecology) as it is based on geometrical properties, although the extraction of the flow network out of the pore system is first of all based on a movement criterion (the local hydraulic conductivity needs to be high, or implicitly the pore radius needs to be large).

In the context of surface hydrology, it has been observed that some areas in a catchment could actively generate runoff locally without exporting it up to the outlet (Bronstert and Bardossy, 1999; Cammeraat, 2002; Cerdan *et al.*, 2004). This led Ambroise (2004) to distinguish between active versus contributing areas. Upstream generated runoff might re-infiltrate downstream or could be stored behind obstacles, on its way to the stream network, disconnecting part of the catchment in terms of surface flows. This explains why the spatio-temporal arrangement of source/sink areas, of the flow path networks, and the interactions between them form an important field of study (Cammeraat, 2002; Cerdan *et al.*, 2004) and has been increasingly referred to in surface hydrology (Bracken and Croke, 2007; Lexartza-Artza and Wainwright, 2009; Michaelides and Chappell, 2009; Ali and Roy, 2009).

Whatever the scale, the connection between zones that produce runoff and the outlet or zones that allow effective re-infiltration is governed by the intensity-duration-frequencies of rain (Puigdefabregas *et al.*, 1999; Lehmann *et al.*, 2007) and by physical and biological thresholds that have to be exceeded (Cammeraat, 2002). Infiltration is the primary factor that affects connectivity. It has been shown, at the scale of small catchments, that surface water connectivity increases with the mean soil water content (Western *et al.*, 2001), or when soil infiltration capacity decreases (Grayson *et al.*, 1997). Consequently, during short rainfall events, only few parts of the catchment are contributing actively to the runoff observed at the outlet. For longer duration of rain, more surface progressively connects to the outlet. In addition, the spatial structuration of soil water content provokes generally more runoff, both in terms of peak discharge and total volume (Bronstert and Bardossy, 1999). Surface storage is the second factor that affects surface water connectivity. Some natural factors tend to enhance surface storage by retaining or slowing down runoff (such as local depressions, ponds, hedges or vegetation bands). Others, such as surface sealing and erosion features, tend to reduce surface storage and increase connectivity. Anthropogenic factors can enhance the surface storage. For instance tillage increases the micro-topography and consequently the retention in local depressions (Takken *et al.*, 2001b,a). But more generally, man-made networks tend to decrease the buffer effect of the surface storage by concentrating and accelerating surface fluxes, e.g., roads (Carluer and De Marsily, 2004; Heathwaite *et al.*, 2005). Ditches can play both roles depending on the water table level (Carluer and De Marsily, 2004). A well connected catchment often implies a higher risk for infrastructures at the outlet, i.e., more flooding. It appears from the above that the connectivity concept may allow a better understanding of the runoff propagation, and hence the diffuse pollution and the erosion processes (Tyndale-Biscoe *et al.*, 1998). It may also be a key factor to bring our models and predictions a step forward (Western *et al.*, 2001; Grayson *et al.*, 2002; Mueller *et al.*, 2007).

Although being studied by many researchers, hydrological connectivity in the field of surface hydrology still misses of a widely accepted definition (Bracken and Croke, 2007; Ali and Roy, 2009) as its meaning varies from author to author, depending on the context and the sources of information that are used to characterize it. Because water flow is not easily observable by direct methods at every location in a landscape, hydrological connectivity has been studied through a variety of mostly indirect approaches, including the study of observable channel patterns (Cammeraat, 2002), terrain indices derived from surface topography (Guntner *et al.*, 2004; Heathwaite *et al.*, 2005), or potential water movement in the system combining topographical and land use information and modeling (Heathwaite *et al.*, 2005; Reaney *et al.*, 2007; Darboux *et al.*, 2002). If one refers to the functional and structural connectivity concepts used in ecology, then the connectivity derived from terrain information is of the 'structural' type whereas the connectivity derived from a combination of modeling and geographical information is of the 'functional' type. The study of observable patterns, such as vegetation patterns (Imeson and Prinsen, 2004), rill, gully and river networks (Favis-Mortlock, 1998), soil moisture patterns (Western *et al.*, 2001), may at first appear to be related to the structural connectivity concept, yet these footprints of water flow actually carry information regarding both the spatial continuity of the water (structural connectivity) as well as the amount of water and/or the discharge rate passing at different locations (functional connectivity). Hence, depending on the approach, hydrological connectivity studies highlight the structural connectivity, functional connectivity, or some partial combination of both concepts.

Clearly, functional connectivity must to some extent be dependent on structural connectivity, as pattern and process are expected to be linked (Gustafson, 1998), but the nature of this relationship is often complex. Processes acting on a landscape, over time, will lead to the development of patterns in a landscape. However, observed patterns may not be related to present-day processes but might have been created under past conditions (Cammeraat, 2002). Also, the emergence of topologies observed in nature may not exclusively be the outcome of growth mechanisms but may also arise from the interplay of dynamical mechanisms with an evolutionary selection process (Colizza *et al.*, 2004). For instance, river networks tend to evolve toward a dynamically reachable local optimum in terms of energy expenditure, so as to minimize all the energy losses occurring locally and globally in the system (Rodriguez-Iturbe *et al.*, 1992; Banavar *et al.*, 2000; Rinaldo *et al.*, 2004). Such optimal networks tend to develop dendritic patterns, especially if fast fluxes are present. Dendritic patterns optimize the length of networks that have to span an area, which increases the viability and the efficiency of such networks.

In order to promote progresses in the study of hydrological connectivity, it seems essential to settle on a common, precise definition. It is suggested here to make use of the connectivity concept employed in ecology as it has been applied successfully for a long time by a large scientific community, albeit in a different scientific domain. The conceptual definition of connectivity that will be used here is thus the *structural and/or functional continuity between elementary units or subsets of elementary units encompassed in a larger space. Structural* connectivity refers to continuum properties of state variables (such as altitude or soil surface properties) in space, whereas *functional* connectivity is process-based and reflects the capacity (or the rate of transfer) of water (and associated particles or molecules) to move in the system in response to a boundary stimulus. Let us note that Bracken and Croke (2007) speak of static and dynamic connectivity to distinguish between structural and functional connectivity. However, we prefer the term 'structural connectivity' over 'static connectivity', as structural connectivity is not necessarily a static property, i.e., surface topography can be temporally highly dynamic, especially at small scales. The term static may therefore be misleading.

It is apparent from the above definition that both structural and functional connectivity may be scale-dependent (Western *et al.*, 2001; Cerdan *et al.*, 2004). The longer is the path for runoff to flow from its origin to the outlet, the greater is the chance for runoff to encounter depressions or higher infiltration zones on its way and get disconnected from the outlet. The length of the path increases also the cumulative effect of friction, which increases the diffusion of the runoff propagation front. For those reasons, connectivity in general decreases with increasing scale. But this also depends on the position of the area compare to the position of the drainage network, as, when runoff reaches this network, the distance of connection increases significantly. At the same time, boundary effects in the observations can bias the decrease of connectivity with scale, as the artificial disconnecting action of the boundary effects decreases with scale too.

Structural and functional connectivity concepts may also depend on the history of flows through the system, as these flows are capable of modifying the surface topography and the network of other landscape elements that may affect surface flow (e.g., land use, vegetation).

As opposed to structural connectivity, functional connectivity will be directly dependent on the boundary conditions of the system. Indeed, the functional connectivity is revealed in the hydrological response of a surface to a stimulus applied at the boundary of the system. The promptness of the system to react to a modification of the boundary condition is a measure of functional connectivity (in the sense defined in landscape ecology, where the species are replaced by water molecules or solutes), such as an early arrival time in a breakthrough experiment for instance (Knudby and Carrera, 2006) or a high value of effective transmissivity in pumping test. Hence, whereas hydrological structural connectivity may be studied without specifying the boundary conditions, the characterization of functional connectivity cannot be dissociated from the boundary conditions. In addition, functional connectivity is dependent on initial conditions (e.g., spatial moisture patterns or partial filling of depressions before a rainfall). Let us note that the functional connectivity is also process-specific. For instance, connectivity is different for water flow and particle transfer (Darboux and Huang, 2005; Fryirs *et al.*, 2007), but artificial flow networks may act as conduits or short-circuits for the transport of contaminants, leading to by-pass some of the retardation mechanisms.

Structural connectivity between two points implies the presence of a continuous path of water at the soil surface. However, the presence of such a continuous path does not imply that water actually flows between those two points (think of two points in a pond at rest). To ensure motion, the presence of a gradient of energy (gravity, differences in hydraulic head) between those two points will ensure a functional connectivity. In most cases, downstream points are functionally connected to upstream points only, yet this needs some nuancing if backwater effects are considered. To summarize, functional connectivity between two points requires structural connectivity, whereas the existence of a structural connectivity link between two points does not automatically imply functional connectivity.

1.2 Why a study at the interrill scale ?

As far as runoff is concerned, connectivity has been studied mostly at the watershed scale, to study runoff stoppage provoked by local obstructing elements or high infiltration zones (Imeson and Prinsen, 2004; Croke *et al.*, 2005; Heathwaite *et al.*, 2005; Fryirs *et al.*, 2007; Bracken and Croke, 2007; Mayor *et al.*, 2008; Meerkerk *et al.*, 2009) or water table disruption due to hillslope-river transitions (Ocampo *et al.*, 2006; Stieglitz *et al.*, 2003; Lehmann *et al.*, 2007; Jencso *et al.*, 2009; Lane *et al.*, 2009; Hopp and McDonnell, 2009). Since connectivity can be treated explicitly at such scales by available physically-based hydrological models or by current data acquisition techniques, the connectivity concept has so far mainly been used as a means of understanding catchment responses rather than for prediction purposes. The greatest challenge, however, resides in the development of connectivity indices that can be used to refine current surface water flow modeling at the subgrid scale of distributed hydrological models. Indeed, although barely studied, connectivity considerations also apply in the interrill zones in-between surface channels (rills, gullies, ditches, etc..) where water flow is governed by the soil micro-topography and which typically corresponds to the subgrid scale of most spatially-distributed hydrological models. At these scales, the spatial heterogeneity is still important, both in terms of infiltration capacity of the soil (Fox *et al.*, 1998; Langhans *et al.*, 2010) and the water storage capacity at the soil surface (Darboux *et al.*, 2002). This results in a mosaic of source and sink entities in the interrill zone influencing the degree of connection between interrill zones and the rill network. As a matter of fact, one could argue that the greatest potential benefits of applying the connectivity concept lie at the subgrid scale of distributed hydrological models and not at the watershed scale. But connectivity cannot be treated explicitly without increasing input data / data collection requirements and computation times by several orders of magnitude. Subgrid connectivity functions may therefore provide a means of improving the response of distributed hydrological models without strongly increasing computation and input data requirements. Therefore in this study, we will focus our analysis on small bare plots that have similar dimension as the dimension of the numerical gridcell of spatially distributed hydrological hillslope models (i.e., $\sim m^2$).

At the interrill scale, the micro-topography controls, in interaction with the general slope, the initiation and the direction of overland flow. Depending on the spatial configuration of the soil micro-topography, the water at the soil surface may conceptually be distributed among two compartments (Fig. 1.1): the depression storage and the surface detention (Stammers and Ayers, 1957). The **depression storage** (also called surface retention or dead storage) is the amount of water stored in surface pits and depressions, when the water supply rate is larger than the soil infiltration capacity for those depressions. When a depression is fully filled with water, the water surplus overflows and fills downstream depressions or produces runoff. The water stored in the depressions will subsequently infiltrate or evaporate. At the scale of a rainfall event, depression storage leads to a significant decrease of runoff volume, as maximum depression storage is able to store, on agricultural fields, from 0.2 to 15 mm of water (Kamphorst *et al.*, 2000; Picouet *et al.*, 2009). This depends on the roughness of the soil surface, which generally increases the depression storage, and the slope, which decreases it. Therefore, depression storage is potentially an important factor in preventing runoff and erosion in agricultural fields (Kamphorst *et al.*, 2005). The **surface detention** corresponds to the water storage in excess of depression storage. It is due to the presence of flowing water and depends on the discharge itself. Surface detention depth will increase until discharge reaches equilibrium with the rate of supply to the surface runoff (Mwendera and Feyen, 1992). At the end of the runoff event, this amount of water will deplete as discharge decreases. The current subgrid modeling approaches in physically-based surface hydrology models rely on the definition, for each grid cell, of an effective maximum depression storage and an effective friction factor linked to the surface detention (Singh, 1995; Singh and Frevert, 2002; Smith *et al.*, 2007). In some hydrological models, the depression storage is mixed with the interception of the rainfall by the vegetation cover, to form an initial loss factor (Picouet *et al.*, 2009). In some others, the depression storage is simply neglected, as the error on the infiltration may be so large that taking into account an additional process such as the depression storage would not improve the model performance (Picouet *et al.*, 2009). However, as we work at the interrill scale, the depression storage is a significant characteristic that we have to consider in order to avoid large bias in the hydrographs.

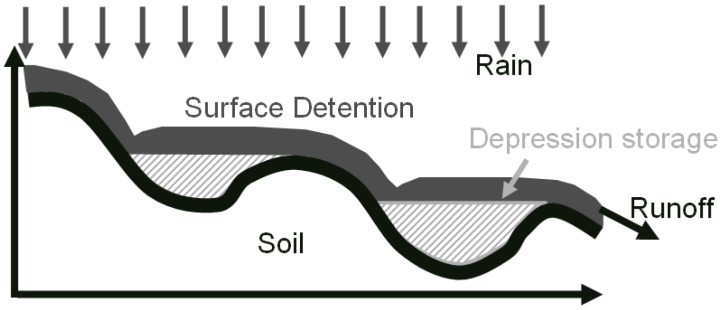

Figure 1.1: Distinction between depression storage and surface detention (without infiltration).

Surface detention and depression storage depend on micro-topography, which evolves over time (Chahinian *et al.*, 2006) through the combined action of rain (Guzha, 2004) and overland flow (interrill erosion). Erosion-deposition processes will modify the surface micro-topography, breaking down soil aggregates (Paz-Ferreiro *et al.*, 2008), filling depressions (Guzha, 2004), incising channels at the outlet of puddles (Darboux *et al.*, 2002) and favoring the development of preferential eroded pathways (Favis-Mortlock, 1998). Turbulences will allow the flow to modify the bed roughness especially if small hydraulic jumps occur (Tatard *et al.*, 2008), onsetting new rills that will subdivide previous interrill areas. With time, flow network structure evolves into a self-organized configuration where overall geometry of flow paths is similar to those developed in river networks (Helming *et al.*, 1998), unless anthropogenic actions such as tillage reset a new micro-topography, ready to be eroded.

Take note that oriented roughness features, such as furrows for instance, may increase or decrease surface storage (= depression storage + surface detention). It depends on discharge and the interaction between the main slope and the oriented roughness features. Regarding surface detention, if slope and oriented roughness features direct water in roughly the same direction, then oriented roughness features facilitate the drainage of surface water and decrease surface detention. On the contrary, if oriented roughness features and main slope show more divergent directions, flowpaths will be deviated from the main direction that would have been followed in absence of oriented roughness. This increases the length of the flowpath and, as a result, the size of surface detention. Regarding depression storage, it is expected that roughness of oriented roughness elements will in general be lower than that of the interrill random roughness because of the smoothing action of the flowing water (except in case of scouring). Hence, oriented roughness would decrease depression storage. However, in the extreme case of oriented roughness features being perpendicular to the main slope, they will form depressions to be filled by overland flow and will increase drastically the depression storage. Overall, down-slope oriented roughness is therefore expected to decrease surface storage, but this effect decreases as the orientation changes from down-slope to cross-slope. In the special case of oriented roughness following the contour lines, surface storage may actually increase compared to the situation without oriented roughness.

1.3 Objectives

The overall goal of this thesis is to investigate the influence of micro-topography on surface flow connectivity properties at the interrill scale. This thesis has 3 main objectives and several specific objectives.

Objective 1 is to measure the effect of micro-topography on overland flow at the interrill scale. The specific objectives are as follow:

- to study the specific effect of micro-topography on depression storage and surface detention, both under laboratory conditions and through numerical modeling ;
- to determine how temporal changes in micro-topography affect depression storage and surface detention ;

Objective 2 is to find runoff-relevant connectivity properties of a micro-topography at the interrill scale. The specific objectives are as follow:

- to test the relevance of existing and a new connectivity indicators ;
- to propose a conceptual framework for the connectivity properties of a micro-topography ;
- to study the temporal evolution of connectivity ;

Objective 3 is to introduce the micro-topographical connectivity properties at the subgrid (interrill) scale in distributed hydrological models, by defining corrective strategies to merge, at the grid scale, the subgrid surface detention and depression storage dynamics.

This work has mainly been carried out at the square meter scale for bare tilled loamy soil surfaces. The two hypotheses that underline this work are that the infiltration rate never exceeds rainfall intensity, such that there is always a zero or a net supply of water, and that this net supply is spatially uniform.

1.4 Outline of the thesis

In the first section, we try to assess the impact of micro-topographies observed at the interrill scale on depression storage and surface detention. Those two properties will partially disconnect or delay the runoff. In Chapter 2, we present a novel molding method which allows to study the impact of micro-topography on runoff without interference from infiltration. In Chapter 3, we use the molding method to study the rainfall-induced evolution of depression storage and surface detention for a freshly tilled bare loamy soil.

In a second section, we try to assess, in a numerical framework, the impact of the micro-topographical configuration on overland flow. In a primary step, we build a numerical overland flow model. Then this model is applied on virtual scenarios of contrasted micro-topographies (Chap. 4).

The third section will cover the characterization of connectivity properties of micro-topographies. In Chapter 5, several existing structural indicators are benchmarked based on the virtual scenarios of contrasted micro-topography. A new functional indicator is also proposed which provides a conceptual framework for studying the functional connectivity properties of micro-topography and which can be integrated in physically-based hydrological models. In Chapter 6, we look at the temporal evolution of connectivity caused by rainfall-induced changes in micro-topography for the freshly tilled bare loamy soil of Chapter 3.

Finally, we propose, in the fourth section (Chap. 7), a methodology to implement the interrill connectivity properties observed on the bare loamy soil into the framework of current distributed runoff models.

The list of the supporting publications is provided at the end of the manuscript.

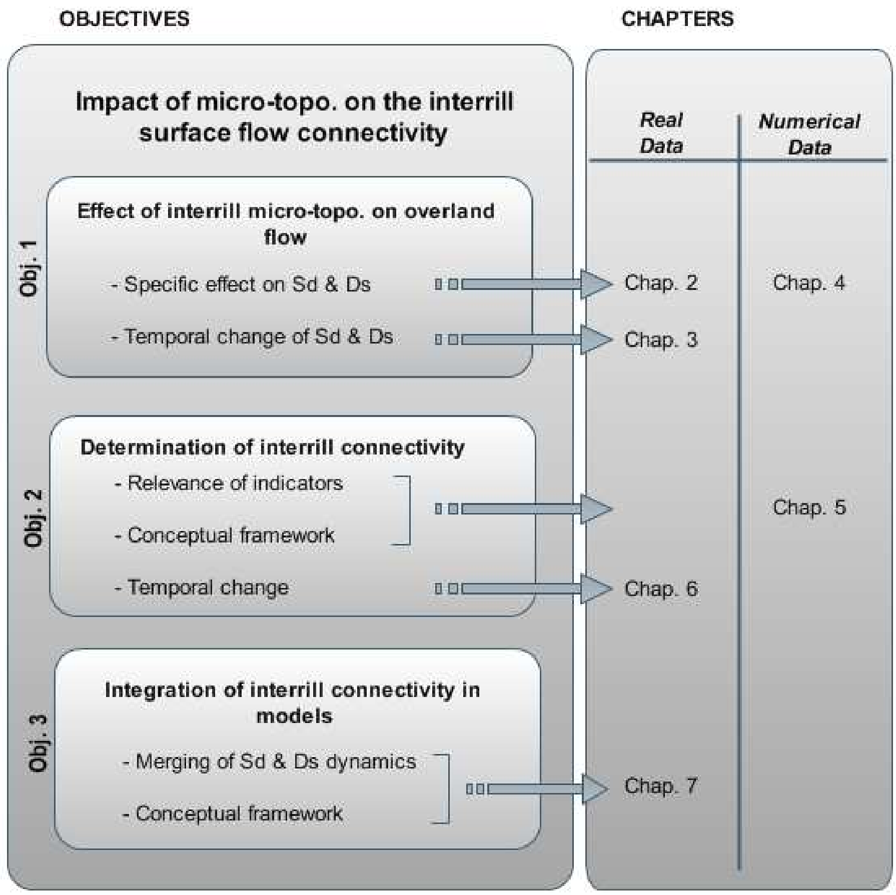

Figure 1.2: Outline of the thesis, showing the correspondence between the objectives and the chapters. We classified the chapters according if they were mainly based on real observations or simulated data.

Chapter 2

A cheap and fast method to mold the soil surface micro-topography[1]

2.1 Outline

In order to study the impact of the micro-topography on runoff without interference from infiltration, we developed a fast and cheap in-situ molding method (+/- 85 €/m^2) that combines alginate, plaster and lacquer. It allows to create stable and impermeable artificial micro-topographies that reproduce real fields situations and that can be submitted to various laboratory runoff simulations. Both the original soil and its artificial reproduction have been measured with a laser scanner in order to assess the quality of the molding method. This method is shown to be precise with a standard deviation of 0.55 millimeter in z, close to the 0.5 mm of spatial resolution in x, y and z for the laser scanner method.

2.2 Introduction

Given the difficulty to measure infiltration and its high variability even at the m^2 scale (Fox *et al.*, 1998), it is necessary to work with impermeable soil surfaces if one wants to measure directly the effect of the micro-topography on the runoff propagation.

[1]Adapted from: *Estimating changes in interrill surface detention and depression storage using a cheap and fast method to mold the soil surface micro-topography*, Antoine, M., Chalon, C., Darboux, F., Javaux, M. and Bielders, C., **Catena** (accepted with minor changes)

Two options are possible, either by impregnating the soil in-situ with a liquid that solidifies and waterproofs the soil surface, or by making an impermeable reproduction with molding methods. Langford and Turner (1972) chose the first option by spraying, over a finely-cultivated fallow, a thin skin of bituminous emulsion. Gayle and Skaggs (1978) also impregnated the soil surface but with a polyester resin. On their side, Takken and Govers (2000) sprayed a mixture of wood glue (PVA) and water to fix the soil surface, refilled cracks with a mixture of glue, water and soil and, finally, sprayed a waterproofer for tents on the whole surface. The second option, i.e. the molding method, has been used by Foster *et al.* (1984), Garcia-Sanchez (1997), Kamphorst and Duval (2001) and Roche *et al.* (2007). Foster *et al.* (1984) used plaster reinforced with straw to make the mold, and fiberglass and resin for the casting. Garcia-Sanchez (1997) also used some plaster for the mold, but an elastomer for the casting. However problems were encountered during the removal of the cast from the mold. Therefore, Kamphorst and Duval (2001) improved their technique by using an elastic silicone elastomer for the mold and a polyester resin for the casting. This method produced robust and impermeable copies of the micro-topography and details less than 0.1 mm width were correctly reproduced. The first drawback of the technique is the time required to mold the surface (24h), and the fact that the silicone partially infiltrates into the soil, which subsequently requires a manual removal of some silicone features corresponding to pore space rather than depressions. The second drawback is the price of materials used (± 600 €/m^2). This can limit to some extent the number of repetitions and the sampling frequency of the micro-topographies investigated during a study. This is not desirable, as the soil properties that govern the retention and detention of overland flow are variable in space, but also evolve in time (Chahinian *et al.*, 2006) with the history of flows through the system. Therefore, our objective is to demonstrate the potential of a new cheap molding technique to reproduce real waterproof micro-topographies.

2.3 Materials and Methods

2.3.1 Development of the molding method

As numerous molds will have to be created, we had to develop a new method to produce impermeable surfaces at a lower cost and in a less time-consuming manner than current molding methods of soil surface. The materials used for making the footprint of the soil (i.e., the mold) and, subsequently, for making the copy of the soil (i.e., the cast) need to have some specific properties:

- The material poured on the soil needs to be sufficiently fluid to tightly conform to the shape of the micro-topography, but it must not infiltrate too excessively in the soil.
- It must be possible to make the mold under a wide range of roughness and wetness conditions.
- The material used for making the copy needs to be waterproof and must not be degradable over time.
- The overhangs [2] need to be well represented in the copy. This implies that at least one of the two materials is flexible enough so that overhangs don't break during the removal of the casting from the mold.

Based on discussions with people using molding methods for particular applications (dentists, podiatric physicians, criminal squad and model makers), we identified several cheap materials and fast procedures either to fix and waterproof the soil surface or to mold it. To assess the feasibility of those procedures to mold soil surfaces under real field conditions, we first tested them in the laboratory on wet soil samples. For the waterproofing of the soil surface, the tested materials were: a water-repellent additive for concrete, a liquid latex, some color spray painting and an acrylic polyurethane lacquer. For the molding procedure, we tested the following materials for the mold: agar jelly, paraffin, plaster, alginate and cement for wet environment with a fast setting time. For the cast, we tested: cement, latex, alginate and plaster.

2.3.2 Validation of the molding method

In order to assess the quality (in terms of precision in the reproduction of the micro-topography) of the selected molding method, we measured the elevation of both the original micro-topographies and their reproductions with a laser scanner (Darboux and Huang, 2003). The micro-topographies considered in the validation procedure are: a 2-D profile of a flat PVC surface with three peaks, a 2-D profile of a patterned PVC surface and a 3-D surface of a real rough and wet soil sample (0.07 m^2). In addition, the original profiles of the two 2-D profiles were directly

[2] An overhang is produced where a border of a clod hangs over in the air, leaving space for the water to flow underneath while blurring that space to the detection tools placed above.

measured with an iron ruler and a caliper rule to show the noise linked to the laser measurement itself.

The laser scanner consists of two laser diodes that project vertically on the surface a narrow line of intense light. The distortion of this line by the micro-topography, when viewed from an oblique angle, is captured by a camera. Using a calibration procedure, the image of the distorted line is back-transformed to an elevation profile. To obtain the entire micro-topography, the line is scanned across the surface with an increment of 0.5 mm, which determines the spatial x-y resolution. The vertical resolution is also 0.5 mm which results from the distance between the mold and the camera as well as the laser beam thickness (Darboux and Huang, 2003). Shading effects can appear when the micro-topography itself hides some portions of the line, which will result in an incomplete digital elevation model. Therefore, two scans were made, with the camera on one or the other side of the line, so that the shadow effects do not always occur on the same side of the protruding objects. An image registration is then required to allow the merging of the information contained in the two incomplete digital elevation models. Common control points are identified on both digital elevation models in order to compute a first adjustment. This adjustment is then refined by an optimization algorithm that minimizes the discrepancies between the two digital elevation models. The procedure is schematized in Figure 2.1.

2.4 Results and Discussion

2.4.1 Development of the molding method

The different trials are listed and briefly discussed in Tables 2.1, 2.2 and 2.3. None of the products used for waterproofing the soil surface gave reliable results, due either to a bad waterproofing or to a modification of the micro-topography. We concluded that in situ waterproofing of soil was difficult and we focused our trials on molding methods. Regarding the mold, Alginate (alginate aroma fine® DF III normal), which is a polysaccharide extracted from brown algae and which constitutes the raw material for dental molding, gave the best results and was easily cleaned of loose soil. Regarding the cast, the best association with alginate was plaster (molda® III normal). The plaster cast was subsequently coated with a thin layer of lacquer (French Polish of Ciranova®) to render it impermeable and non-erodible, without altering the micro-topography.

The molding procedure is illustrated in Figure 2.2. The alginate powder is mixed with water (1 kg alginate powder/5 kg water) and

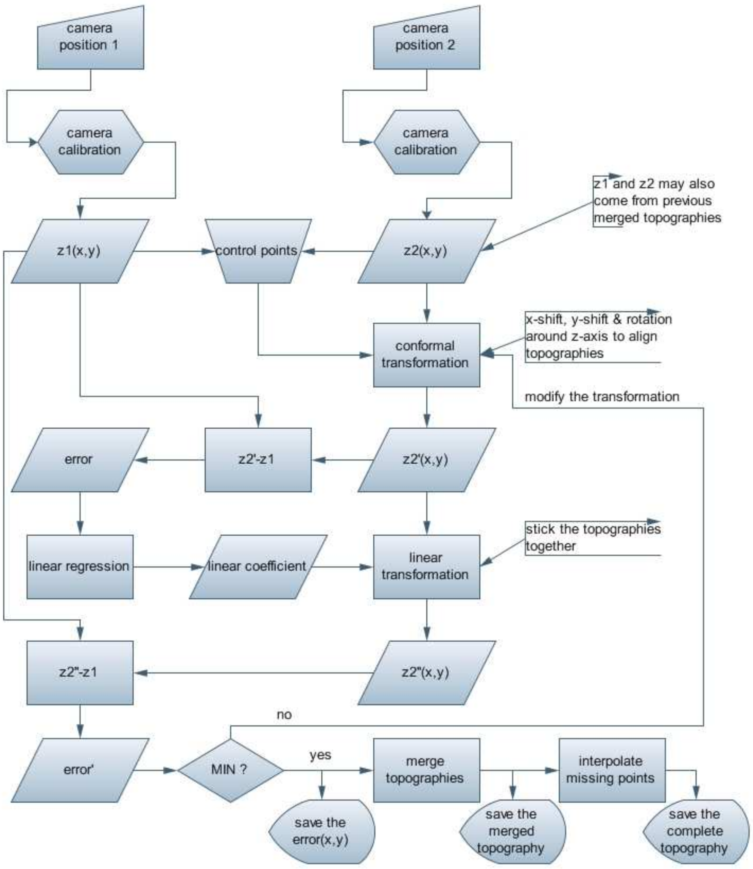

Figure 2.1: Flowchart to compute the micro-topography from the images provided by the laser scanner.

Table 2.1: Summary of the different materials used to produce an impermeable soil micro-topography: in-situ waterproofing.

Material	Main Application	Procedure	Results
Plastidich®	Water-repellent additive for concrete	Sprayed pure or mixed with 15 or 30% water	No waterproofing
Industrial silicon spray	Industrial lubrication	Spraying repeated 5 times	No waterproofing
Isolastic®	Liquid latex	Poured pure on the soil	The liquid infiltrates totally, no waterproofing
Color spray painting	Painting that covers well and prevents rust	Sprayed twice	Good waterproofing except on cracks; some accumulation in depressions is observed
Acrylic polyurethane lacquer	Protection of woods	Applied several times with a paintbrush	Modifies the topography because of brush contact with soil

Table 2.2: Summary of the different materials used to produce an impermeable soil micro-topography: molding, material for the mold.

Material	Main Application	Procedure	Results
Agar jelly	Culture medium in biology	0.5, 1, 3, and 5% concentration, poured during the cooling of the jelly	Good molding but cracks during drying
Cellophane	Food packaging	Laid on the soil and compressed by a liquid	Bad molding
Paraffin	Candles	Poured liquid on the soil	Brittles
Alginate	Dental mold-making and food industry	Mixed with water in a ratio 1 kg alginate/ 5 kg water	Good molding (perfect with wet soil), flexible and robust, shrinks as it dries
Plaster molda® III normal	Precision plaster for detail application	Mixed with water in a ratio 1.35 kg plaster/ 1 kg water	Good molding but cracks upon drying and is hardly cleaned of loose soil
Cement Lampocem®	Cement for wet environment with a fast setting time	Mixed with various quantities of water and sand	Tears and very hardly cleaned of loose soil

Table 2.3: Summary of the different materials used to produce an impermeable soil micro-topography: molding, material for the cast

Material	Results
Cement on alginate	Not compatible
Alginate on alginate	Ok, but bubble forming
Isolastic on alginate	Shrinking of the latex with time and UV-sensitive
Plaster on alginate	Ok, but requires to waterproof the plaster with a lacquer (French Polish of Ciranova®)

agitated during one minute, avoiding the formation of too many bubbles. Then it is poured onto the soil surface that was previously delimited by a frame. The alginate polymerizes in less than 2 minutes. After 10 minutes, the mold can be manipulated and removed from the soil surface. It is washed with water to get rid of the loose soil particles or aggregates that can stick to the alginate mold. Take note that the alginate mold shrinks when it dries and needs thus to be kept in a humid environment (e.g., by keeping it in a sealed plastic bag). The plaster is mixed with water (1.35 kg plaster/1 kg water) and agitated during one and a half minute. Then it is poured onto the alginate mold framed by the previous frame. A steel grid was submerged in the plaster to reinforce it. The plaster will begin to harden after 10 minutes. After 2 hours, the plaster is separated from the alginate. Six hours later, the lacquer is sprayed onto the plaster that has been cleaned of the last spots of alginate. The entire procedure takes about 8 hours and costs about 85 € per square meter (alginate: 14 €/kg x 4 kg/m^2, plaster: 0.4 €/kg x 30 kg/m^2; lacquer: 16 €/liter x 1 liter/m^2), which is much cheaper than traditional silicone molds.

The maximum amplitude of the roughness we ever investigated was 8 cm, but it is not a limit. To save alginate or to avoid too heavy molds difficult to manipulate without breaking them, it is not necessary to spread a uniform layer of alginate inside the frame and some additional alginate mixture can be added (before the mold is dry !) where the highest clods protrude through the alginate layer. However, the good reproduction of the top of the clods is not always necessary as, for surface

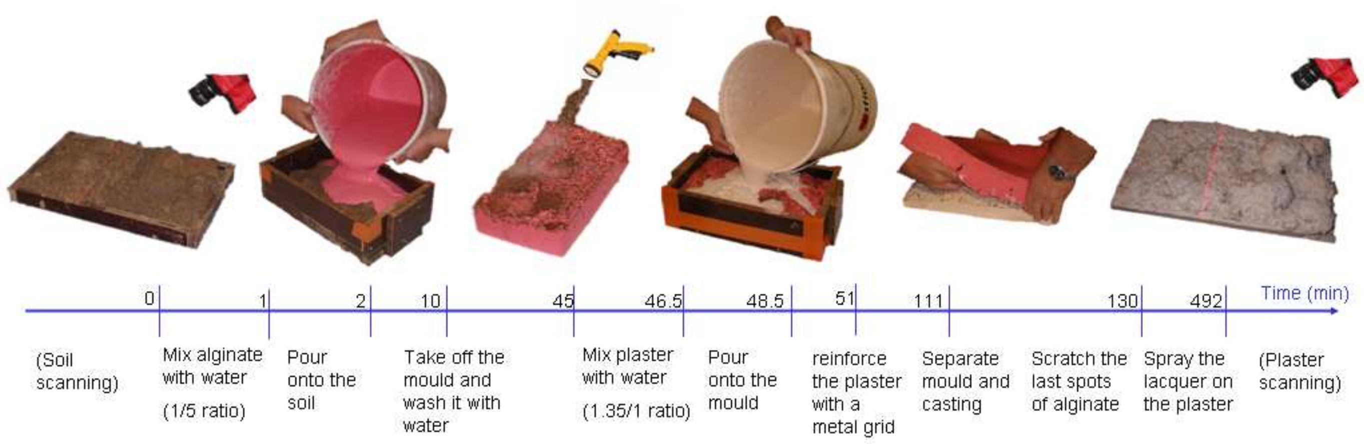

Figure 2.2: Procedure to cast the soil surface roughness.

detention and depression storage, it is mostly the depressions and the connecting paths that need to be well reproduced in the cast. If we deal with a non flat alginate layer, then an additional layer of plaster on top of the alginate layer needs to be done to avoid deformation of the alginate layer when turned over and used as a mold.

2.4.2 Validation of the molding method

Visual inspection of the 2-D profiles of the 2 PVC surfaces shows that horizontal lines stay mostly linear and the distances between maxima are preserved (Fig. 2.3). Some discrepancies are observed between the profiles, but those are mostly below the resolution of the laser scanner of 0.5 mm, which is linked to the distance between the cast and the camera of the scanner (Darboux and Huang, 2003). Furthermore, some details less than 0.5 mm wide were perfectly reproduced.

In a second step, we scanned a real rough and wet soil sample, as well as its plaster reproduction. The digital elevation models of the soil surface and its plaster cast are shown in Figure 2.4 (a) and (b). Missing data in the digital elevation models, due to uncompensated shading effects during the scanning process, are left white. Missing data are usually in the neighborhood of clods that produce shadow effects. Those missing values can be estimated by interpolation procedures but in order to analyze the discrepancy between the different micro-topographies, they are not considered. Figure 2.4 (c) shows the difference between the plaster micro-topography and the soil micro-topography. The largest positive errors (which correspond to a higher topographical level on the reproduction than on the soil) are located in the upper-left corner and in the center-right, whereas negative errors are located in the lower-left and upper-right corners. They may be due to a small deformation of the alginate mold or plaster cast. Those discrepancies remain mainly within the limits of the resolution of the laser: since we subtract two variables each having 0.5 mm uncertainty, the result has 0.7 mm uncertainty ($\sqrt{0.5^2 + 0.5^2}$). Figure 2.5 shows the distribution of the error which is almost symmetrical around the mean, indicating a good accuracy. The absence of bias is due, among other, to the registration procedure. The standard deviation is 0.55 mm, almost equivalent to the laser scanning resolution. Moreover, in their estimation of measurement precision, Darboux and Huang (2003, Fig. 7(b)) found a standard deviation of 0.39 mm when comparing two measurements of the same soil surface. The present standard deviation is only slightly larger while we are comparing a surface and its cast. To conclude, we can say that the proposed molding method allows to reproduce accurately the soil micro-

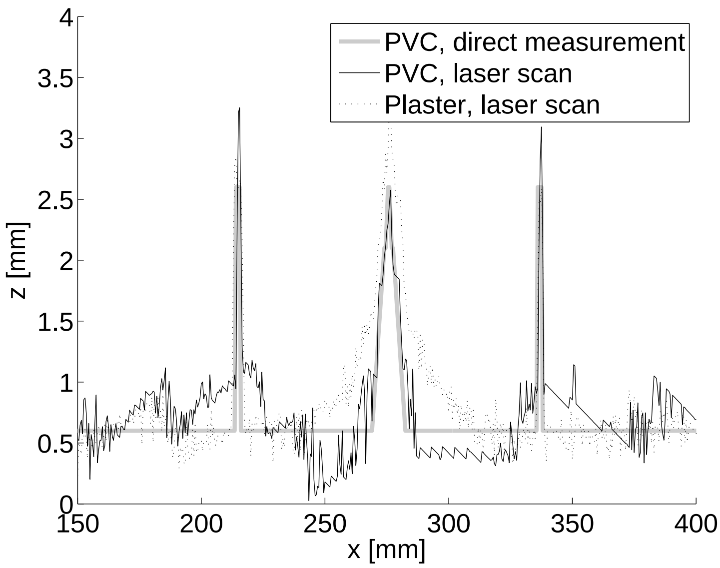

(a)

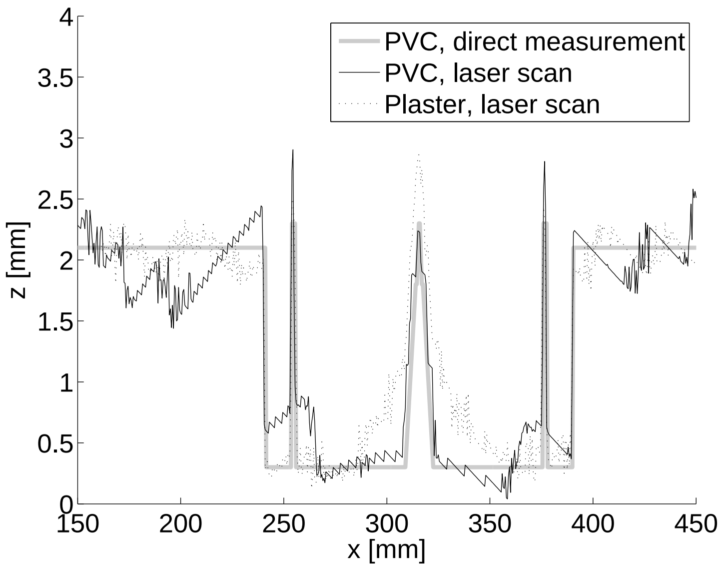

(b)

Figure 2.3: Comparison of 2-D profiles of a flat surface with 3 peaks (a) and a patterned PVC surface (b) with their plaster copies, measured manually and with the laser scanner.

topography with a precision of at least 1 mm, remembering that the largest errors may be due to a global deformation of the mold. However, since the observed precision is better than the resolution of the laser process, the reality of the systematic error due to the mold deformation may be questioned.

2.5 Conclusions

We developed a cheap and fast molding method based on alginate and plaster that is able to reproduce real soil surface micro-topography within at least 1 mm of precision, but we have to pay attention to a global deformation of the mold. The molds are impermeable, which allows to study, under laboratory conditions, the effect of the micro-topography on the runoff characteristics without interference from infiltration. Given the low cost, it becomes realistic to create a collection of micro-topographical reproductions, in order to study the combined actions of rain and agriculture practices on the micro-topographical properties. Moreover, molds can be made on vegetated fields, as long as stems are sufficiently rigid to remain in their position when pouring the alginate onto the soil and wide enough to be reproduced in the plaster cast (e.g., mature maize crop).

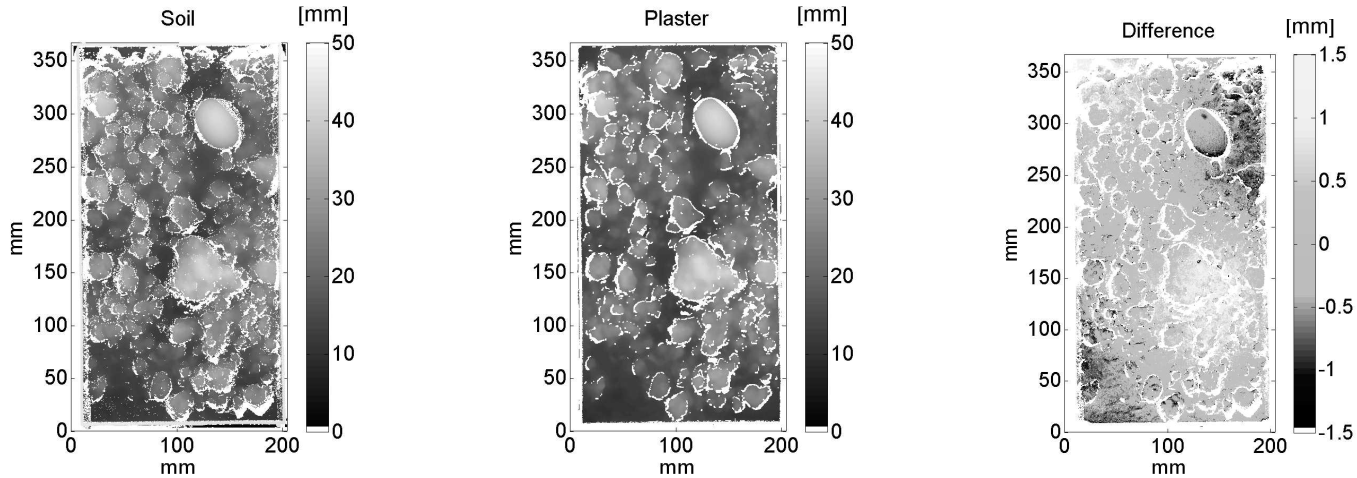

(a) (b) (c)

Figure 2.4: Digital elevation models of the soil (a), of the corresponding plaster reproduction (b), and the discrepancies between the two (c): $z_{Plaster} - z_{Soil}$. Missing data are left white.

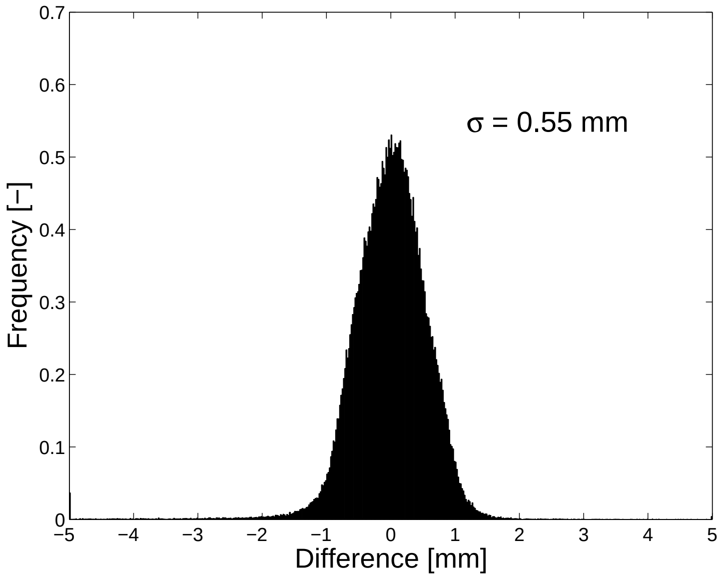

Figure 2.5: Distribution of the observed difference between the digital elevation models of the plaster reproduction and the original soil.

Chapter 3

Estimating changes in interrill surface detention and depression storage [1]

3.1 Outline

Surface detention and depression storage constitute the two conceptual water storage compartments at the soil surface and depend on the spatial configuration of the micro-topography. The molding method explained in Chapter 2 was applied to get ten footprints of the micro-topography of a tilled bare silt loam soil, at different levels of cumulative rainfall erosivity. We studied the evolution of depression storage and surface detention and related the measured hydraulic properties of the micro-topography to cumulative rainfall erosivity. If a clear link could be identified between rainfall erosivity and properties that determine depression storage and surface detention, then the R factor could help for the modeling of runoff from soil surfaces whose micro-topography evolves with the accumulation of rain events. We observed a general decrease of both forms of storage. In addition, we tested if the classical Darcy-Weisbach equations for an equivalent laminar sheet flow could provide similar detention values, in order to use our measurements as effective parameters for current hillslope models where the size of our molds corresponds then to the size of one single grid-cell. Based on that last analysis, we proposed a simple model to compute the surface

[1] Adapted from: *Estimating changes in interrill surface detention and depression storage using a cheap and fast method to mold the soil surface micro-topography*, Antoine, M., Chalon, C., Darboux, F., Javaux, M. and Bielders, C., **Catena** (accepted with minor change)

detention as a function of the discharge per unit width and cumulative rainfall erosivity value.

3.2 Introduction

Depending on the spatial configuration of the soil micro-topography, overland flow may conceptually be distributed among two compartments: depression storage and surface detention (Stammers and Ayers, 1957). Those two compartments are explicitly expressed, for a given area, in the storage equation (Stammers and Ayers, 1957):

$$\frac{\partial (D_s + S_d)}{\partial t} = -\frac{\partial q_0}{\partial x} + P - F \tag{3.1}$$

where D_s is the depression storage [mm], S_d is the surface detention [mm], t is the time [s], q_0 is the discharge per unit width [mm^2/s], x is the distance in the slope direction [mm], P is the rainfall rate [mm/s] and F is the infiltration rate [mm/s]. Evaporation is neglected in this equation. Therefore, it is only applicable during a rainfall event during which evaporation is assumed to be negligible. To close this equation, soil surface topography and roughness needs to be taken into account to allow the separation between surface storage and depression storage, and to compute the discharge per unit width.

On small experimental plots, P and q_0 are directly measurable, whereas F is often modeled or estimated from additional measurements. On the contrary, D_s and S_d are not easily measured due to the infiltration that occurs simultaneously. Therefore, D_s and S_d are usually evaluated indirectly.

D_s can be evaluated numerically with a filling algorithm (Planchon and Darboux, 2002) if a detailed survey of micro-topography has been made. Alternatively, attempts have been made to find simpler estimations of the maximum value of depression storage $D_{s\,\mathrm{max}}$ that are based on direct measurements of roughness indicators in the field. In a comparative study of different roughness indicators, Kamphorst *et al.* (2000) found that random roughness, combined with the mean slope of the plot, provided the best estimation of $D_{s\,\mathrm{max}}$ (with an error of 3 mm of water depth). Take note that random roughness is classically determined at the meter scale (Jester and Klik, 2005; Elbasit *et al.*, 2009), which is consistent with the spatial scale adopted in the present thesis.

S_d depends on the integration of the continuity equation for surface flow and will evolve locally toward a dynamic equilibrium between water reaching (by runon and precipitation) the specific location for which

S_d is computed and water leaving that location (by runoff and infiltration). If the micro-topography is known at high spatial resolution, S_d can be evaluated through detailed hydraulic modeling (Chap. 4). Interrill flows are usually modeled as uniform and broad sheet flows (Smith *et al.*, 2007), where the effect of the micro-topography is incorporated in a friction or resistance factor. The Darcy-Weisbach friction factor λ is often used to model resistance, and it can be converted to Chézy or Manning friction parameters (Smith *et al.*, 2007). λ has been linked, among others, to random roughness (Gilley and Finkner, 1991; Smart *et al.*, 2002), relative roughness parameterized with grain size distribution (Henderson, 1966) and inundation ratio (Lawrence, 1997). A commonly used alternative is to calibrate λ, based on the comparison of observed and modeled hydrographs (Esteves *et al.*, 2000; Tatard *et al.*, 2008).

However, all these indirect parameter evaluations may be erroneous due to spatial resolution limitations in the digital elevation models (Abedini *et al.*, 2006; Martin *et al.*, 2008), overhang problems (Kamphorst and Duval, 2001), or modeling simplifications and numerical approximations. When correlations with topographic indicators are used, the spatial configuration of roughness is often ignored despite being a strong determinant (Dunkerley, 2003). Therefore we used the molding method of Chapter 2 to measure $D_{s\,\max}$ and S_d directly.

An additional difficulty arises from the fact that surface properties that govern $D_{s\,\max}$ and S_d may rapidly evolve over time (Mwendera and Feyen, 1992; Chahinian *et al.*, 2006) with the history of rainfall and flows through the system. Erosion-deposition processes resulting from splash and surface flows will modify the surface micro-topography, breaking down soil aggregates (Paz-Ferreiro *et al.*, 2008), filling depressions (Guzha, 2004), incising channels at the outlet of puddles (Darboux *et al.*, 2002) and favoring the development of preferential eroded pathways (Favis-Mortlock, 1998). This is particularly true at the fine spatial scale on which we focus our thesis. Therefore the objective of this chapter is to directly determine $D_{s\,\max}$ and S_d for real field micro-topographies. We will provide bulk values of $D_{s\,\max}$ and S_d for the entire molds in order to provide effective values to current hillslope models where the single gridcells have a similar size as our entire molds. We will evaluate how the temporal dynamic of surface roughness affects these bulk properties and study the evolution of an effective friction factor corresponding to an equivalent laminar sheet flow at the scale of the hillslope single gridcell.

3.3 Materials and Methods

3.3.1 Study field and rainfall erosivity measurement

An experimental plot was selected in a cultivated field, from which all the soil samples used in this study were sampled. This experimental plot is situated in the loess belt of central Belgium (Long. 4^o38'41.631 E, Lat. 50^o40'4.622 N, elevation 136 m, 10% average slope), near the city of Louvain-la-Neuve. The soil is a silt loam (Haplic Luvisol; FAO *et al.* (1998)). At the begining of the experiment (11 March 2009), the soil of the field had been tilled and sown with spring wheat using the following seedbed preparation tools: field cultivator, moldboard plow, spring tine cultivator and combined drill with rotary harrow and cage roller. Ten meters downstream of the upper field border, an area of 3 x 10 m^2 (the long side of the rectangle is perpendicular to the mean slope) was kept bare, by spraying an herbicide on the young shoots of wheat. Nine molds (0.5-m wide and 1-m long in the slope direction) were taken at 4 different times during a three month period on different locations inside the bare area. We hypothesized that molds were representative of the micro-topographical configuration evolution for the all bare plot, allowing comparison of depression storage and surface detention values between molds whatever the location they were sampled on. However, we repeated the molding procedure two or three times the same day to verify this assumption.

Take note that there was a wheel track just 1 m upstream of the experimental plot, which isolated it from upstream runoff. The maximum length for runon to occur was thus 3 meters before it flows into the area covered by a mold. Therefore we wade the hypothesis that rainfall reshaped the surface much more than interrill erosion. Rainfall rate was measured with a tipping bucket rainfall gauge at 1-min. intervals with a 0.2-mm resolution. Those measurements were converted to rainfall erosivity computed on 10-min. intervals, based on the methodology of Verstraeten *et al.* (2006). Each of the nine molds were associated with a cumulative rainfall erosivity (R) expressed in $MJ.ha^{-1}.mm.h^{-1}$. Indeed, Alberts *et al.* (1995) reported that the evolution of surface properties such as random roughness could be related to cumulative input of energy by the rain, which is considered in erosion models such as WEPP (Flanagan and Nearing, 1995) or CREDHYS (Laloy and Bielders, 2008). If a clear link could be identified between rainfall erosivity and properties that determine depression storage and surface detention, then the R factor could help for the modeling of runoff from soil surfaces whose micro-topography evolves with the accumulation of rain events.

The following molds were taken: 2 molds on the 11th of March 2009, just after tillage (R=0), 2 molds on the 20th of April 2009 (R=45), 3 molds on the 18th of May 2009 (R=115) and 2 molds on the 29th of July 2009 (R=230), with the unit of R being $MJ.ha^{-1}.mm.h^{-1}$. An additional mold was sampled from another field. On this field, a seedbed has been prepared in March 2009 for sugarbeet but it was thereafter left bare and exposed to rainfall for more than 6 months. This corresponds to the period of the year when most of the intense thunderstorms occur. Based on visual inspection of the soil surface, we hypothesized that this last mold corresponded to the final stage of soil micro-topography evolution and subjectively associated it with a one year value of erosivity in Belgium (R=677, Verstraeten *et al.* (2001)).

Finally, The digital elevation models (DEM) of the casts were obtained by scanning the surface with a horizontal resolution of 0.5 mm using the method of Darboux and Huang (2003). To compute the random roughness (RR), we first removed the planar trend in the topographical data, to avoid interference with a general slope. Then we computed the standard deviation σ of the residuals. The residuals whose values were outside of the interval +/- 3 σ were considered as outliers and were not used further. We recomputed again σ (without the previous outliers), and looked for new outliers, in a repeated way until no outliers were found anymore. Finally the last computed standard deviation was considered as the random roughness RR value, similarly to the study of Kamphorst *et al.* (2000).

3.3.2 Surface detention and depression storage measurements

On the experimental plot, the different molds were taken parallel to the soil surface, and the slopes were measured. In the laboratory, the corresponding casts were first submerged for 12 hours in a water basin to avoid the absorption of water by the cast in case the waterproof coating was damaged, then tilted to the same slopes as in the field.

The casts were hydrologically isolated to avoid any escaping flows on the upper and the side boundaries. Water was supplied to the impermeable micro-topography in two ways: either through sprinkling[2] over

[2]The sprinkler system consists in a line of oscillating nozzles where the flow is periodically deflected from continuously flowing Veejet nozzles. The system is placed at 4 m height above the cast surface. The rainfall rate is modified by changing the pressure in the system or adjusting the time during which water is deflected. The simulator can produce rainfall rates between 5 to 100 mm/h Details about the sprinkler system are provided in Darboux

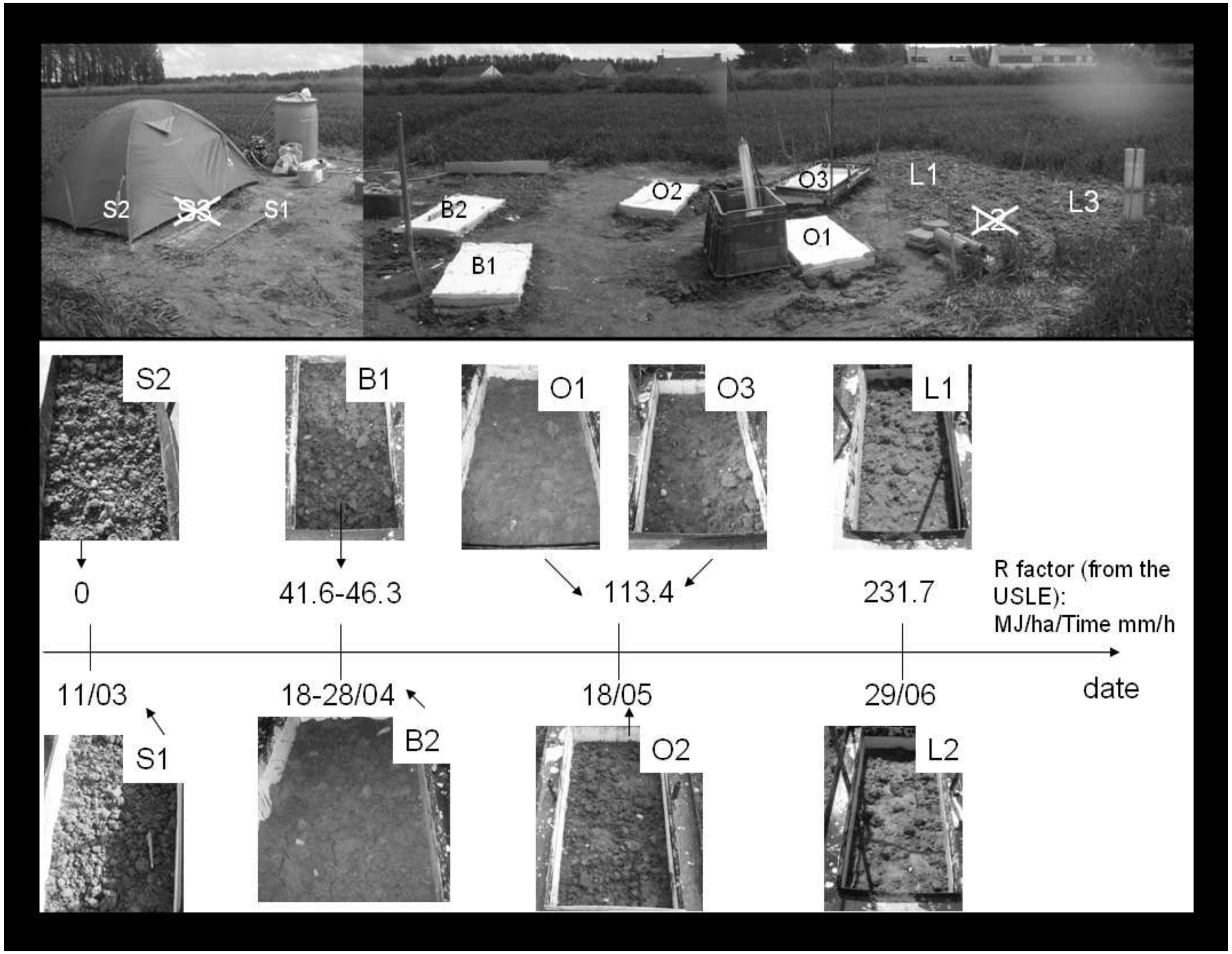

Figure 3.1: Localization of the molds on the experimental plot and their associated R values.

the entire surface (*rain*), or as runon[3] over the entire width of the upstream boundary (*runon*). Each of the 10 molds were subjected to 3 (or 4) constant rainfall rates, ranging between 5 mm/h to 60 mm/h (see Table 3.1). Runoff water was collected in a gutter at the downstream boundary of the cast. The runoff rate was determined by collecting the cumulative runoff during fixed time intervals (low supply rate: 120 s, medium supply rate: 30 s, high supply rate: 15 s) and weighing the collected water.

We calculated a mean effective height of water as well as a mean effective velocity in the direction of the main slope. In this approach, the whole cast is considered as an elementary surface representative of a single grid cell (1 meter long) in a hillslope model. We chose that option to provide modelers with representative effective values of surface detention and depression storage at the scale at which classical hillslope models perform. Langford and Turner (1972) had observed that, even at the bottom depression, water was flowing and therefore included the water depth in the depression storage to compute the outflows. As opposed to them, we chose to consider that the water in the depression storage did not contribute to the flow, to fit better classical models conceptualization. Therefore, the detention storage was the only active layer and the velocity was computed by dividing the runoff rate by the surface detention (expressed in water depth) and by the width of the mold. Doing so, we conformed to classical concepts of hillslope models that explicitly distinguish surface detention S_d from depression storage D_s (Singh, 1995; Singh and Frevert, 2002).

$D_{s\max}$ was directly measured by spraying a large amount of water onto the cast. We waited until no water flowed anymore at the downstream boundary and collected the water remaining on the cast, similarly to Mwendera and Feyen (1992). The volume of collected water was divided by the area of the cast projected on the horizontal plane to express the depression storage in water depth units. The full operation is repeated 3 times on each cast to be able to assess the variance, and the mean result was computed.

S_d was assessed through a runoff experiment on the cast with a constant water supply (rain or runon). We waited until the runoff rate reached the dynamic equilibrium, when surface detention and depres-

---

et al. (2002) or on the web: `http://www.orleans.inra.fr/orleans/les_unites/ur_science_du_sol/equipements/simulateur_de_pluie`

[3]The runon system consisted of a peristaltic pump connected to a plastic tube pierced every 2 cm with a needle for the medium and high supplies or to porous tube (Gardena® Soaker Hose) for the lowest supply. The tube was place along the upstream border of the cast.

sion storage do not increase anymore. We measured the steady state runoff rate (mean of 3 measurements) to determine the water supply upslope. After that, we stopped the water supply and started immediately to collect the runoff. Since no water was supplied anymore, the water flowing across the downstream boundary corresponds to the surface detention. The total volume of collected runoff was divided by the area of the cast projected on the horizontal plane to express the surface detention in water depth units.

3.4 Results and Discussion

3.4.1 Assessing depression storage evolution

Figure 3.2 (a) shows the evolution of the measured maximum depression storage as a function of the cumulative rainfall erosivity (**R**). Under the influence of successive rainfall events, the micro-topography becomes smoother, as a results of aggregate breakdown, erosion, deposition processes, and the formation of physical soil crust occurs. We observe a general decrease of the maximum depression storage as R increases, except for the transition between R=0 and R=45. Our explanation is that, on the R=0 molds, the soil aggregates produced by soil tillage had a small contact area with the soil at their bottom, leaving a lot of space for the water to flow under the clods. Such micro-topography does not form a well-defined soil surface but is rather a porous medium made of clods. The soil-air interface consists therefore in a transition zone. On the contrary, the aggregates on the R=45 molds are more subsided and really obstruct water. The values of the depression storage are of the same order of magnitude as the data collected on eight different soils, during 2 years in northwestern Europe (Kamphorst *et al.*, 2000). Gayle and Skaggs (1978) had observed a similar decrease of maximum depression storage after seedbed preparation on clay loam and sandy loam soils.

Figure 3.2 (b) shows the evolution of the Random Roughness (RR) as a function of the cumulative rainfall erosivity. Except for the R=677 mold that is clearly smoother than the others, the rest of the molds do not present a clear decreasing trend of RR as R increases. This means that RR is not sensitive to the small changes in micro-topography that diminish the depression storage, such as the little incisions at the outlet of puddles. In fact, RR is not sensitive to change in micro-topographies as it does not take the spatial configuration of roughness into account.

To compare the direct measurements of maximum depression storage with more classical indirect evaluations, we scanned all the micro-

Table 3.1: Main characteristics of the 10 waterproof micro-topographical fields. The different rainfall and runon rates are given as well as the related average surface detention depths at dynamic equilibrium. Surface detention and depression storage volumes have been divided by the horizontal projections of the casts areas, to be expressed in water depth units.

Cast Name	S1	S2	B1	B2	O1	O2	O3	L1	L3	C
Date	11/03	11/03	23/04	23/04	18/05	18/05	18/05	29/06	29/06	12/09
R [MJ/ha mm/h]	0	0	45	45	115	115	115	230	230	677
Length [cm]	97.9	94.4	87.8	96.6	95.2	96	94.7	96.4	97.7	92.9
Width [cm]	49	49.3	45	46.5	46	45.5	46	47	46	48
Slope [%]	4.8	4.45	7.06	9.11	7.35	10	7.6	5.19	7.57	4.52
Random Roughness [cm]	1.22	0.97	1.1	0.98	1.21	0.97	1.12	0.89	1.25	0.33
Depression Storage [mm]	1.04	0.99	1.5	1.04	0.8	0.45	1.19	0.58	0.67	0.25
Low Rain [mm/h]	11.4	10.8	10.9	10.4	6.3	9.9	5.1	10.6	10.1	10.2
Surface Detention [mm]	0.47	0.4	0.98	0.7	0.41	0.6	0.29	0.46	0.57	0.30
Med. Rain 1 [mm/h]	9.1	9.1						16.3	14.9	15.9
Surface Detention [mm]	0.63	0.44						0.54	0.67	0.34
Med. Rain 2 [mm/h]	16.7	20.2	27.7	27.8	25.7	25.1	17.6	24.7	16.4	24.6
Surface Detention [mm]	0.53	0.61	1.19	0.92	0.93	0.74	0.49	0.58	0.63	0.37
High Rain [mm/h]	52.1	53.3	62.5	63	57.5	59.5	40.6	62.3	46.3	61.8
Surface Detention [mm]	1.2	1.05	1.82	1.35	1.25	1.08	0.83	0.87	0.94	0.63
Low Runon [mm/h]	18.2	4.6	17.3	18.5	15.7	16.2	17.4	6.0	22.6	1.2
Surface Detention [mm]	0.65	0.20	1.22	1.06	0.70	0.48	0.80	0.22	0.75	0.21
Med. Runon [mm/h]	24.6	12.6	33.3	30.6	30.4	35.8	35.5	22.1	34.0	20.6
Surface Detention [mm]	0.82	0.37	1.31	1.18	0.74	0.70	0.99	0.38	0.86	0.38
High Runon [mm/h]	98.4	19.3	52.4	45.6	49.7	50.5	43.1	32.9	60.8	43.1
Surface Detention [mm]	1.80	0.39	1.51	1.39	1.05	0.80	1.09	0.46	1.09	0.59

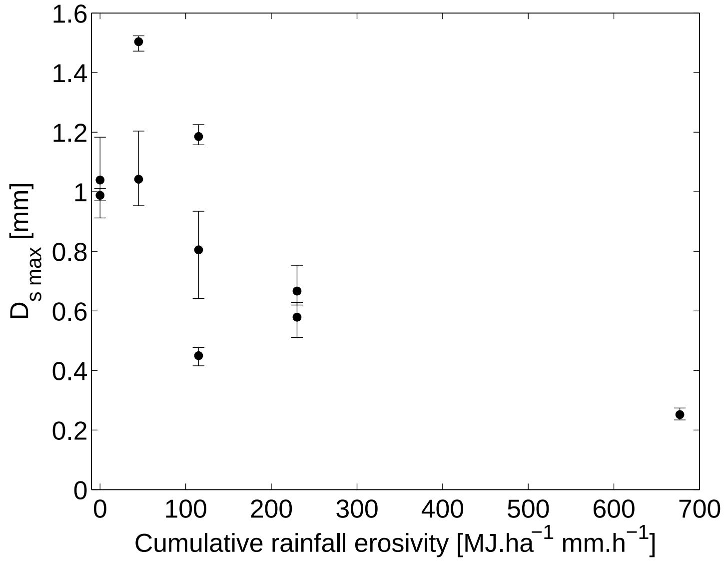

(a)

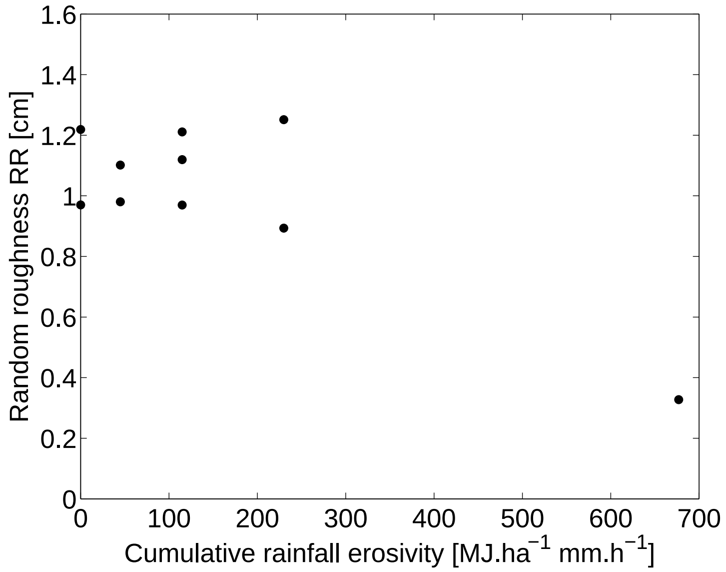

(b)

Figure 3.2: Evolution of the measured maximum depression storage (a) and random roughness (b) as a function of cumulative rainfall erosivity (error bars cover to the measurement ranges).

topographies and used a filling algorithm (described in Chap. 5) to evaluate the different maximum depression storages (Fig. 3.3a). We also computed the maximum depression storages using the regression proposed by Kamphorst (2000a) that is based on the slope and the random roughness (Fig. 3.3b). The filling algorithm methodology, in our case, overestimates the maximum depression storage. We attribute the discrepancies to the fact that the digital elevation models used by the filling algorithm represent the upper sides of the clods, which can hide some of the connectors at the bottom of clods that link hydraulically depressions together. For instance, we have observed, on several casts, clods with arch-like structures, which allow water to flow under what would be virtually an obstacle when represented in a digital elevation model. Another explanation could be linked to leakages in our casts, due to micro-fractures provoked during manipulation. The regression of Kamphorst (2000a), in our case, overestimates the maximum depression storages, but the results are still in the order of precision (3 mm) given by the authors. Kamphorst (2000a) also used a filling algorithm to estimate maximum depressions storages, which explains the overestimation.

3.4.2 Assessing surface detention evolution

The experimental results are presented in Figure 3.4 for the 2 methods of water supply : sprinkling over the entire surface, or runon over the entire width of the upstream boundary. To facilitate the comparison between the two cases, we express the water supply in the same units (i.e., a rain intensity, or an equivalent rain intensity). Therefore, for the runon case, the upstream water supply expressed by a volumetric rate [$m^3.s^{-1}$] has been divided by the surface [m^2] of the mold. It is as if all the rain that would have fallen on the mold had been concentrated at the upstream boundary. Take note that for rain fed experiments, overland flow occurs over the entire surface of the cast yet discharge gradually increases as water flows downstream, whereas for the runon experiments, overland flow occurs only along preferential paths but discharge is constant.

The R=45 molds generally show a larger detention storage value than the others, for an equivalent rain intensity. On the contrary, the R=677 mold has generally the lowest detention storage. One would expect that, with increasing R values, water moves with a higher velocity for a same discharge, decreasing the detention storage for an equivalent rain intensity. It is therefore surprising that the surface detention of the R=0 molds is not greater or similar to the surface detention of the R=45 molds. As discussed for the depression storage, this may be due to the fact that the micro-topography of the R=0 molds does not exhibit

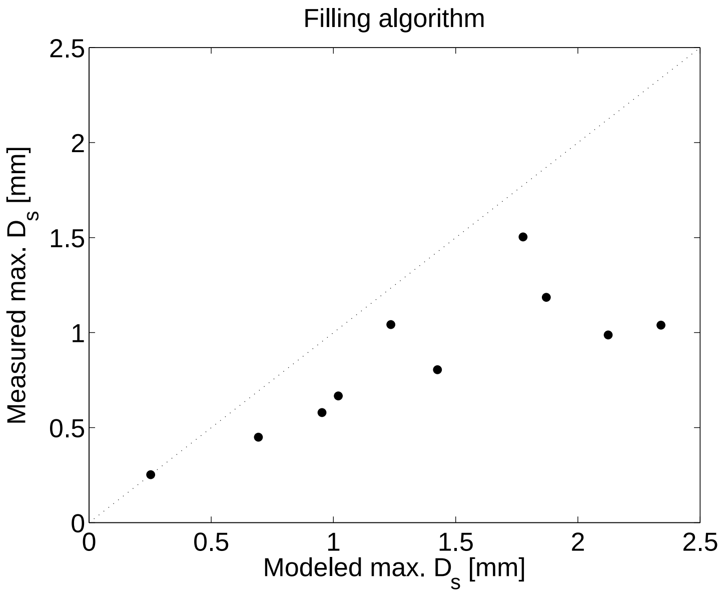

(a)

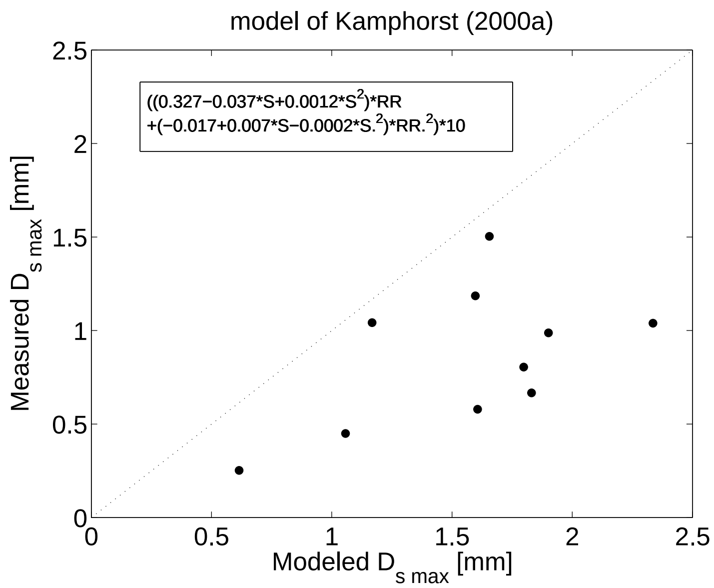

(b)

Figure 3.3: Indirect evaluations versus direct measurements of maximum depression storage [mm]: with a filling algorithm of the laser scanned topography (x-y spatial resolution: 2 mm) (a) or with the regression of Kamphorst (2000a), knowing the slope S [%] and the random roughness RR [cm].

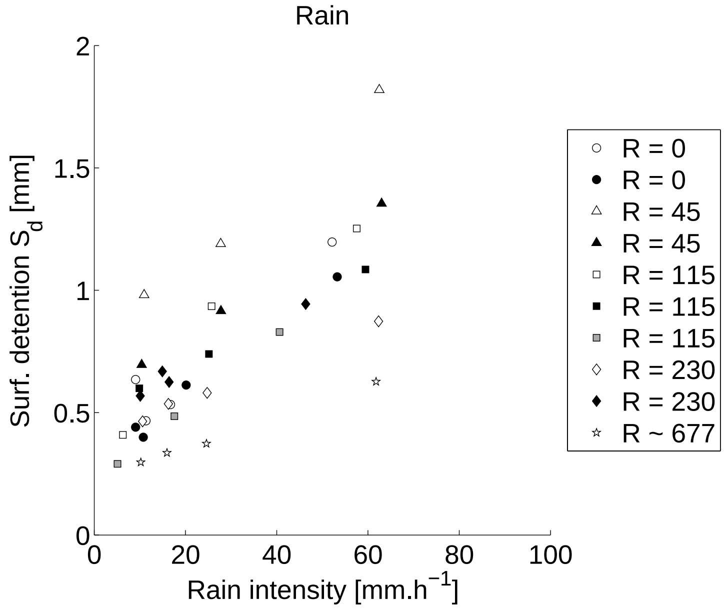

(a)

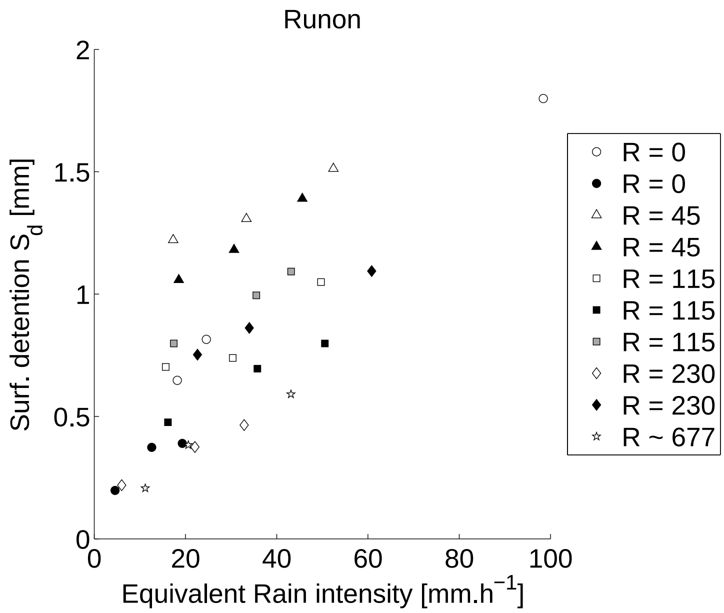

(b)

Figure 3.4: Surface detention as a function of the water supply rate: uniform rain (a) and runon (b). The runon flow rate was divided by the mold surface in order to be expressed in the same units as rainfall. Each symbol represents a different mold. The molds are named according to their cumulative rainfall erosivity value (R).

any spatial organization. Overland flow does not really concentrate into channels but rather moves in a sheet flow around the obstacles. Moreover the soil at that time was like a loose porous material with small and weak contacts between aggregates, and water could easily flow around and below them. Flow paths were thus fairly straight. On the contrary, the aggregates on the R=45 molds had subsided and forced the water to flow around them, rendering the flow paths more tortuous.

The experimental relationship between the surface detention and the mean velocity in the direction of the main slope is shown in Figure 3.5. For each mold taken separately, the velocities increase with the surface detention values, and the relationship shows a decreasing positive slope. The relationship is sharper for the R=677 mold. An explanation is that the real directions of the flow paths are mostly parallel to the main slope direction, so that the effective velocity tends toward to be the real velocity. On the other molds, the water follows more tortuous paths. The increase of the real velocity with the increase of water depth is thus mitigated, when projected along the main slope direction.

3.4.3 Parameterization of the surface detention by an effective friction factor

Surface detention is related to the discharge, but also to the slope. Due to experimental constraints, we could not ensure an identical slope for the different molds (4 to 10 %). Although the experimental plot presented a relatively homogeneous slope of 10%, we aligned our molds to the observed paths of water, which were not forcedly in the direction of the main slope. This effect of the slope explains partially the dispersion of the experimental data in the previous figures. To avoid this blurring effect, we can use the momentum equation that relates slope, surface detention, and friction forces to the discharge. In most hillslope models of runoff and erosion, such as KINEROS (Woolhiser *et al.*, 1990), WEPP (Flanagan and Nearing, 1995), LISEM (de Roo *et al.*, 1998), EUROSEM (Morgan *et al.*, 1994) or CREDHYS (Laloy and Bielders, 2008), micro-topography is implicitely considered through a friction factor. Based on the measured mean effective velocity, mean effective water depth and mean surface slope, we calculated the effective friction factors for our molds. The experimental points are summarized in a log-log Moody diagram (Figure 3.6). The Moody diagram expresses the Darcy-Weisbach friction factor λ [-] as a function of the Reynolds number $\mathrm{Re} = \frac{\bar{v}D}{\vartheta} = \frac{\bar{v}4R_h}{\vartheta}$, where $\bar{v}$ is the mean flow velocity along the global slope [m.s^{-1}], D is a characteristic length that is four times the hydraulic radius R_h [m] and ϑ is the kinematic viscosity [m^2.s^{-1}]. The

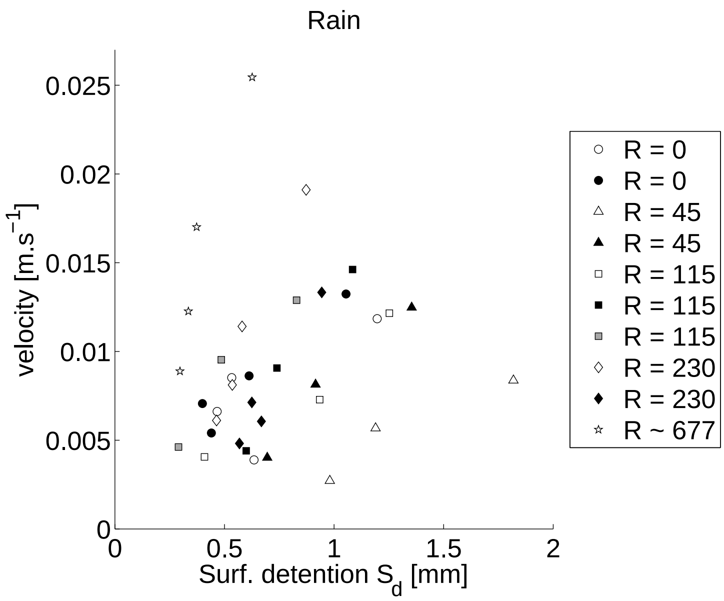

(a)

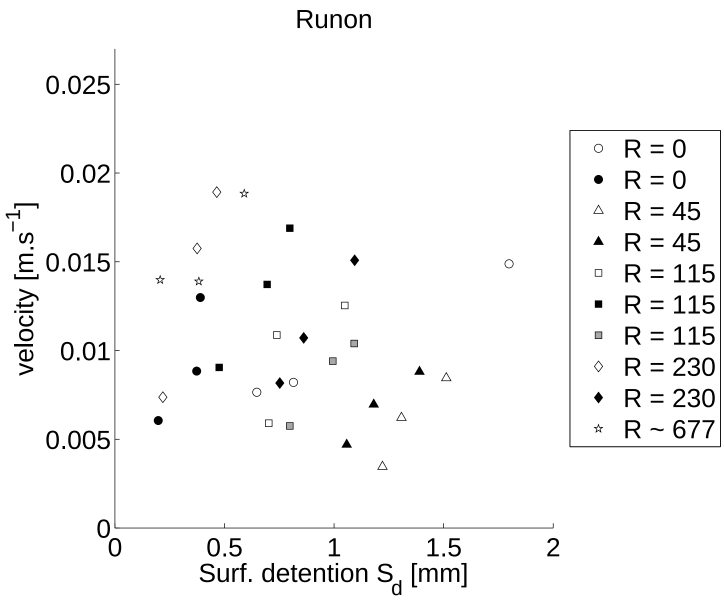

(b)

Figure 3.5: Effective velocity in the main slope direction as a function of the surface detention (or active layer depth): uniform rain (a) and runon (b). The runon flow rate has been divided by the mold surface in order to be expressed in the same units as rainfall. Each symbol represents a different mold. The molds are named according to their cumulative rainfall erosivity value.

hydraulic radius corresponds to the mean local water depth $\bar{h}$ [m], which is our surface detention value, when assuming an equivalent sheet flow on a planar surface. Take note that, in reality, the hydraulic radius of rough surfaces is actually less than the water depth, because the wetted perimeter is much larger than its projection on the horizontal plane. λ was determined by inverting the Darcy-Weisbach formulation and assuming a uniform flow (Chow *et al.*, 1988):

$$S_f = S_0 = \lambda \frac{1}{4R_h} \frac{\bar{v}^2}{2g} \tag{3.2}$$

where g is the gravitational acceleration [m.s^{-2}], S_0 is the mean global slope of the soil and S_f is the friction slope. The kinematic wave approximation was here considered as we wanted to represent the bulk runoff properties for the entire mold, as if there was a uniform sheet flow covering all the area of the mold, assuming this area would cover one single gridcell in current hillslope models.

All our experimental data are in the laminar domain (Re $\leq$ 2000), if the Reynolds number is computed as a bulk value. A bulk value was considered in order to parametrize an equivalent sheet flow for one elementary gridcell of the size of our mold. A mean velocity and a mean water depth on the entire cast were therefore considered for calculating the Reynolds number. In reality, flow filaments and backwater flows as described by Dunkerley (2003) coexist and turbulent flows occur locally next to laminar flows. For laminar flow, the friction factor is determined by (Chow *et al.*, 1988):

$$\lambda = \frac{C_L}{\mathrm{Re}} \tag{3.3}$$

where C_L is a constant that is equal to 96 for a smooth surface and is larger if the surface is rough (Dunkerley, 2001). Our micro-topographies are clearly rough, and the roughness is largely higher than the water depth itself, which forces the water to follow tortuous paths. The Darcy-Weisbach, Chézy and Manning equations are classically used in most of runoff and erosion models, although they originated from studies on one-dimensional pipe flow under very different conditions than those occurring with overland flow (Smith *et al.*, 2007). In particular, the hypothesis of micro-roughness, i.e., the water covers all the soil surface, is not met for interrill flow. Therefore, the classical approaches have been criticized and new explanatory factors such as the inundation ratio have been put forward (Lawrence, 1997, 2000; Takken and Govers, 2000; Roche *et al.*, 2007). However, in our experiments where water is supplied by the rain, the entire surface is subject to overland flow. We

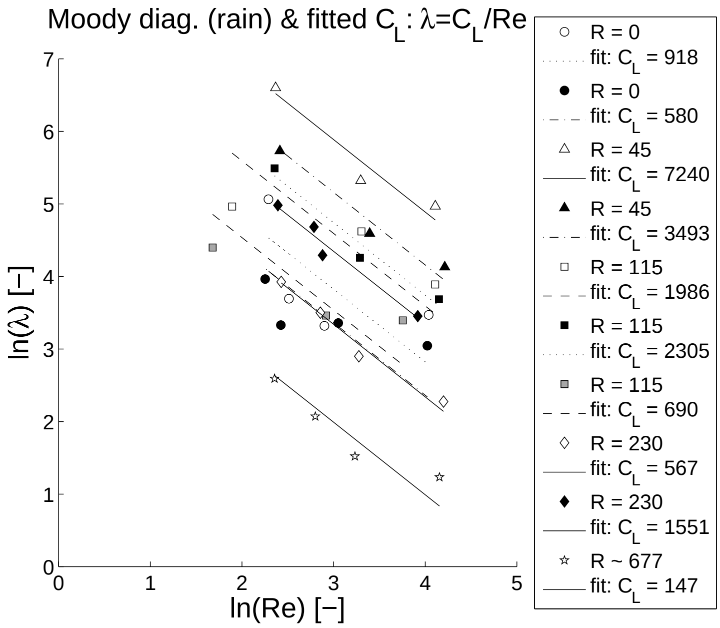

(a)

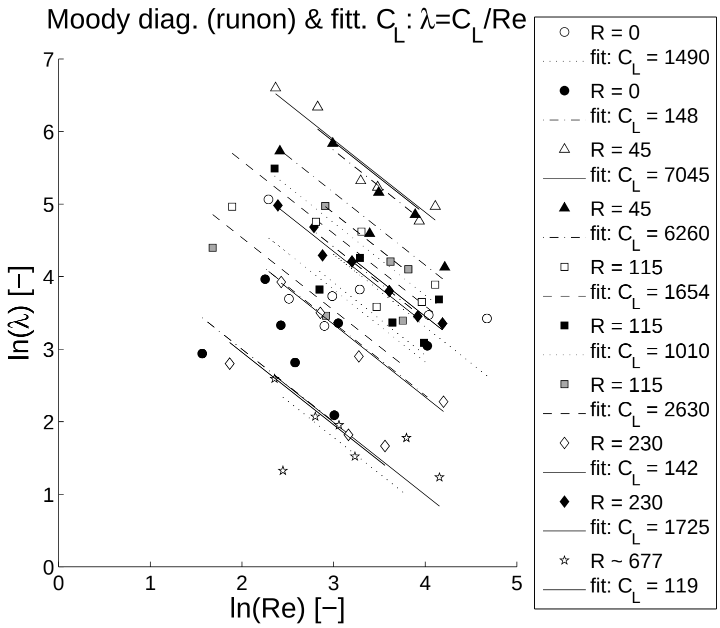

(b)

Figure 3.6: Log-log Moody diagrams with the experimental data and the fitted linear relations. Experimental points from a common mold are represented by a same symbol. The molds are name according to their cumulative rainfall erosivity value.

can therefore not compute any inundation ratio, except by defining arbitrarily a minimum level of water to distinguish between what is part of the runoff network and what is not. Moreover, most of the hillslope models still work with elementary homogeneous grid cells (Singh, 1995; Singh and Frevert, 2002). Consequently, it is still of interest to see if the simple classical equation 3.3 holds in our case. Therefore, we fitted the C_L factor by computing the following linear regression in the log- log-Moody diagram (Figure 3.6):

$$\ln(\lambda) = -\ln(\mathrm{Re}) + \ln(C_L) \tag{3.4}$$

The fact that we impose a -1 slope in the relationship $\ln(\lambda)$ versus $\ln(\mathrm{Re})$ does not allow to properly model some data, such as for the R=0 and R=677 molds with an upstream water supply. In reality, f-Re relation is not ubiquitous and may show positively and negatively sloping power-law relations as well as convex-upward relations. Frictional resistance of overland flow differs a lot from the functional dependence demonstrated in pipes and later applied in hydrological models (Smith *et al.*, 2007). Positive sloping f-Re relations occur in flows with emergent obstacles that protrude through the water layer. As discharge increases, the width of the bed in contact with water increases too, this results in an increasing obstruction to the flow (Dunkerley, 2003). Therefore, the hydraulic resistance evolves as part of the surface becomes progressively submerged (Takken and Govers, 2000). Moreover, when macroscale roughness elements are present, Lawrence (1997) proposed to reduce significantly the Reynolds number at which the roughness ratio becomes the dominant dimensionless group and where lambda value starts to be decoupled from the Re value.

Figure 3.7 shows the relationship between the fitted C_L factor and the R value. We note a general decrease of the C_L factor with R value, as the soil gets smoother, except at the beginning. As explained earlier about the R=0 molds, we found a large number of interstices at the bottom of the clods through which the water was flowing easily. These interstices will generally disappear after the first runoff when the clods will begin to subside and stick to the soil at their bottom. Therefore the initial state (R=0) will not be considered any further in this Chapter. In addition, a runoff field experiment with a 100 mm/h rain during 1 hour had not produced any significant runoff for a seedbed of R=0, making that state not relevant for runoff modeling.

Finally, excluding the data of the R=0 data, we fitted a simple model of the type (Fig. 3.7):

$$C_L = aR^b \tag{3.5}$$

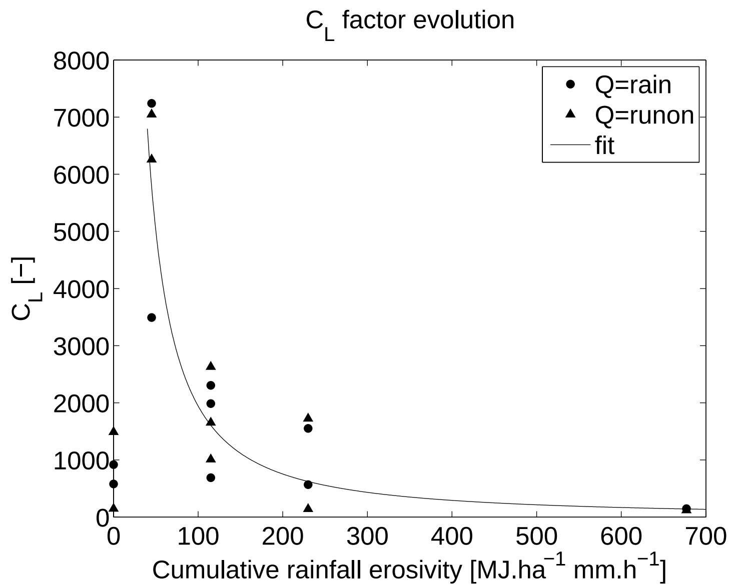

Figure 3.7: Evolution of the fitted C_L values with the accumulation of rainfall erosivity.

where a and b are shape factors. In our case, the best results where $a = 1.0455\text{x}10^6$ and $b = -1.37$. When we know λ, and assume a uniform flow, we can calculate the mean water depth equivalent to the surface detention, using the following equation (Chow *et al.*, 1988):

$$\bar{h} = \left(\frac{\lambda q_0^2}{8gS_0}\right)^{1/3} \tag{3.6}$$

where q_0 [$\text{m}^2.\text{s}^{-1}$] is the discharge per unit width and is equal to $\bar{v}\bar{h}$. q_0 can be found by dividing the runoff rate [$\text{m}^3.\text{s}^{-1}$] by the width of the mold [m]. Combining Equations 3.5 and 3.6 leads to:

$$\bar{h} = \left(\frac{aR^b\vartheta q_0}{32gS_0}\right)^{1/3} \tag{3.7}$$

This simple equation summarizes the effect of the rainfall erosivity R on the overland flow behavior. We applied this equation to model $\bar{h}$, and we modeled $\bar{v}$ by dividing q_0 by the modeled $\bar{h}$, for all our experimental points. Figure 3.8 shows the modeled values and the experimental measurements. The root mean square error (RMSE) are 0.2272 mm for $\bar{h}$ and 0.0037 m/s for $\bar{v}$. In comparison, if we had ignored the non-stationarity of the value of C_L with time and thus had considered a unique mean value for C_L ($\bar{C}_L$=2085) for all our field, the RMSE would have been 0.5896 mm for $\bar{h}$ and 0.0081 m/s for $\bar{v}$.

In the context of thin flows on rough surfaces, two other equations have been proposed to link the soil roughness to effective friction factors. Gilley and Finkner (1991) proposed the following equation:

$$\lambda = \frac{6.30\,(1000RR)^{1.75}}{Re^{2/3}} \tag{3.8}$$

where RR is the random roughness [m]. Smart *et al.* (2002) proposed the following equation:

$$\lambda = \frac{8RR}{\bar{h}} \tag{3.9}$$

where $\bar{h}$ is the mean effective water depth [m]. Introducing equation 3.8 in equation 3.6 gives:

$$\bar{h} = \left(\frac{0.3125\,(1000RR)^{1.75}\,\vartheta^{2/3} q_0^{4/3}}{gS_0} \right)^{1/3} \tag{3.10}$$

Introducing equation 3.9 in equation 3.6 gives:

$$\bar{h} = \left(\frac{RRq_0^2}{gS_0} \right)^{1/4} \tag{3.11}$$

We tested the latter two equations for all our experimental points and compared the modeled and measured surface detentions and mean velocities. RMSE is 0.2991 mm for $\bar{h}$ and 0.0048 m/s for $\bar{v}$ with the model of Gilley and Finkner (1991). With the model of Smart *et al.* (2002), RMSE is 0.4827 mm for $\bar{h}$ and 0.0071 m/s for $\bar{v}$.

The good agreement between observed surface detentions and modeled surface detentions, which were computed thanks to the simple equation 3.3 in association with an effective friction parameter λ, illustrates the fact that a simple model may provide a good approximation of a complex process.

3.5 Conclusions

Surface detention and the maximum depression storage were shown to generally decrease with the cumulative rainfall erosivity, as demonstrated previously under laboratory condition by Mwendera and Feyen (1992). But those decreases were not reflected systematically in the random roughness (RR) evolution, meaning that the spatial configuration

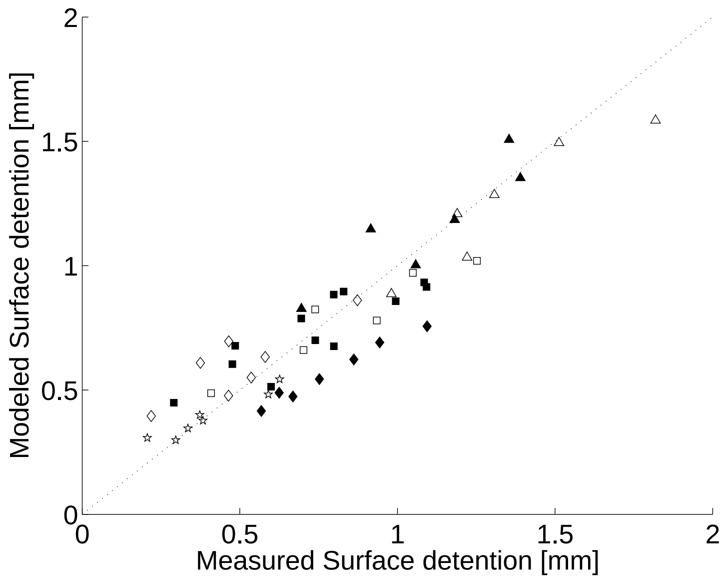

(a)

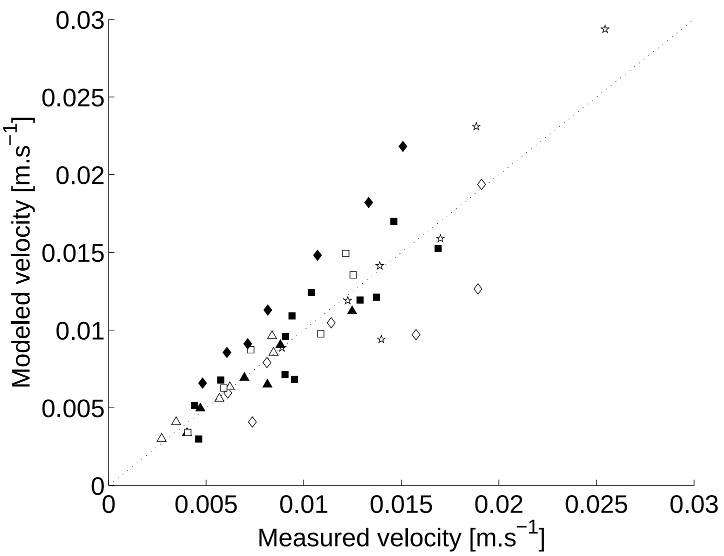

(b)

Figure 3.8: Comparison of the observed and modeled (Eq. 3.7) surface detention (a) and derived mean velocity (b) in the global slope direction.

of micro-topography may be an important property to take into consideration on top of random roughness and slope, as already discussed by Kamphorst *et al.* (2000) for the maximum depression storage, and Takken and Govers (2000) and Dunkerley (2003) for the surface detention. Indeed, some channels may appear with time and favor the runoff propagation without modifying significantly the distribution of heights. Therefore we will investigate numerically the specific impact of spatial configuration in Chapter 4.

The experimental measurements of surface detention were useful to validate the modeling of the effective friction factor and the resulting effective velocities at the meter scale. We proposed a simple model to determine, for the laminar domain, the evolution of the friction factor with the rain erosivity.

The high level of runoff discharge studied here is artificial as it would rarely occur under natural circumstances in the presence of infiltration, especially before the surface starts to be sealed. We performed runoff experiments in situ on the real soil surfaces that were subsequently molded and, under an artificial rainfall intensity of 100 mm/h during 1h, we indeed never observed a runoff coefficient larger than 0.12. Therefore, rainfall intensity of 12 mm/h should be a limit to reproduce realistic runoff on our waterproof surfaces as if it was a rainfall intensity of 100 mm/h in field condition. Although, the effective friction constants we found are theoretically (if we assume that equation 3.3 is correct) independent of runoff intensity which influences rather the Reynolds number.

Chapter 4

Impact of the micro-topographical configuration on overland flow, a numerical experiment [1]

4.1 Outline

The goal of this chapter is to demonstrate that the spatial configuration of micro-topography impacts on the hydrograph, even when macroscopic properties such as slope, random roughness and spatial covariance are kept constant. It is difficult to find real micro-topographies that present at the same time similar macroscopic properties and sufficiently contrasted patterns. Therefore, we generated numerical micro-topographies meeting those requirements, based on the method of Zinn and Harvey (2003). An overland flow model is designed to simulated the propagation of water on those numerical micro-topographies. The model is based on the diffusive wave simplification of the Saint-Venant Equations, and is validated by comparing simulations and observations of overland flow on rugged planes and on one waterproof micro-topography. Based on numerical runoff experiments, it was found that the spatial configura-

[1]Adapted from: *What indicators can capture runoff-relevant connectivity properties of the micro-topography at the plot scale ?*, Antoine, M., Javaux, M. and Bielders, C., **Adv. Water Res.** 32(8):1297:1310, **2009**.

tion of micro-topography played a major role on the depression storage as well as, to a smaller extend, on the surface detention.

4.2 Introduction

Water flowing on a rough micro-topography can be captured in the depression storage or delayed by the surface detention in relation with the friction effect of the roughness. In addition to the amplitude of the roughness, the spatial configuration of obstructing elements in the way of the flow impacts a lot on the overland flow propagation. This chapter will focus on the specific effect of particular micro-topographical configurations on the hydrograph, through numerical runoff experiments on contrasted numerical micro-topographies.

4.3 Materials and Methods

4.3.1 Contrasted numerical fields of micro-topography

We used the method of Zinn and Harvey (2003) to generate the numerical fields of micro-topography. This method allows to generate fields that have contrasted structural connectivity properties (in our case the way depressions connect or not to each other) while presenting, for the pixels heights, identical probability density functions (therefore identical random roughness) as well as near-identical isotropic spatial covariance functions. The three types of numerical fields are (see Fig. 4.10): (1) a field with connected patterns of depressions, (2) a standard Gaussian field and (3) a field with connected patterns of crests that isolate the depressions from each others. For the sake of clarity, we will speak about the River micro-topography for the first field, the Random micro-topography for the second and the Crater micro-topography for the third one.

The method proposed by Zinn and Harvey (2003) is based on the following probabilistic property. Given a continuous random variable Y characterized by any kind of cumulative density function $F_y(y)$ ($Y \sim F_y$) and another random variable X uniformly distributed between 0 and 1 ($X \sim Un(0,1)$), it can be shown that $Y = F_y^{-1}(X)$ (Bogaert, 2005). This method is used to generate series that follow any kind of distribution $F_y(y)$ starting with series of uniformly distributed variables. Conversely, given a continuous random variable Z characterized by any kind of cumulative density function $F_z(z)$, the random variable X uniformly distributed between 0 and 1 can be generated by applying

$X = F_z(Z)$. Combining the two approaches, we can then generate Y based on Z by transforming successively Z into X and X into Y. Thus $Y = F_y^{-1}(F_z(Z))$.

To generate their fields, Zinn and Harvey (2003) propose a four-step procedure that starts with the generation of a Gaussian field Y, using a sequential (unconditional) simulation method. It is illustrated in Figure 4.1. Since the link between their method and the concept we explained in the previous paragraph is not described in their article, we provide some more details.

$$Y \sim N\left(\mu, \sigma^2\right) \tag{4.1a}$$
$$\Rightarrow F_Y(y) = \frac{1}{2}\left(1 + erf\left(\frac{y-\mu}{\sigma\sqrt{2}}\right)\right) \tag{4.1b}$$
$$\Rightarrow F_Y^{-1}(y) = erf^{-1}(2y-1)\,\sigma\sqrt{2} + \mu \tag{4.1c}$$

where N is the Normal distribution with mean μ and variance σ^2.

Extreme values in the field tend to cluster in isolated blobs while values close to the mean tend to form channels that span the entire field. The second step is to generate a new field Z by taking the absolute value of the centered Gaussian field Y. The lowest values become the highest and values originally close to the mean become the lowest.

$$Z = |Y - \mu| \tag{4.2a}$$
$$\Rightarrow F_Z(z) = P(Z \leq z) \tag{4.2b}$$
$$\Rightarrow F_Z(z) = P(|Y-\mu| \leq z) = P(-z \leq Y - \mu \leq z) \tag{4.2c}$$
$$\Rightarrow F_Z(z) = P(Y-\mu \leq z) - P(Y-\mu \leq -z) \tag{4.2d}$$
$$\Rightarrow F_Z(z) = P(Y-\mu \leq z) - (1 - P(Y-\mu \leq z)) \tag{4.2e}$$
$$\Rightarrow F_Z(z) = 2P(Y-\mu \leq z) - 1 = 2F_{Y-\mu}(z) - 1 \tag{4.2f}$$
$$\Rightarrow F_Z(z) = 2\frac{1}{2}\left(1 + erf\left(\frac{z-0}{\sigma\sqrt{2}}\right)\right) - 1 \tag{4.2g}$$
$$\Rightarrow F_Z(z) = erf\left(\frac{z}{\sigma\sqrt{2}}\right) \tag{4.2h}$$

In a third step, the histogram of the values is then converted back to a univariate Gaussian distribution by mapping the Cumulative Density Function (CDF) value at each point to a standard normal CDF. This transformation is the application of the probabilistic property explained above.

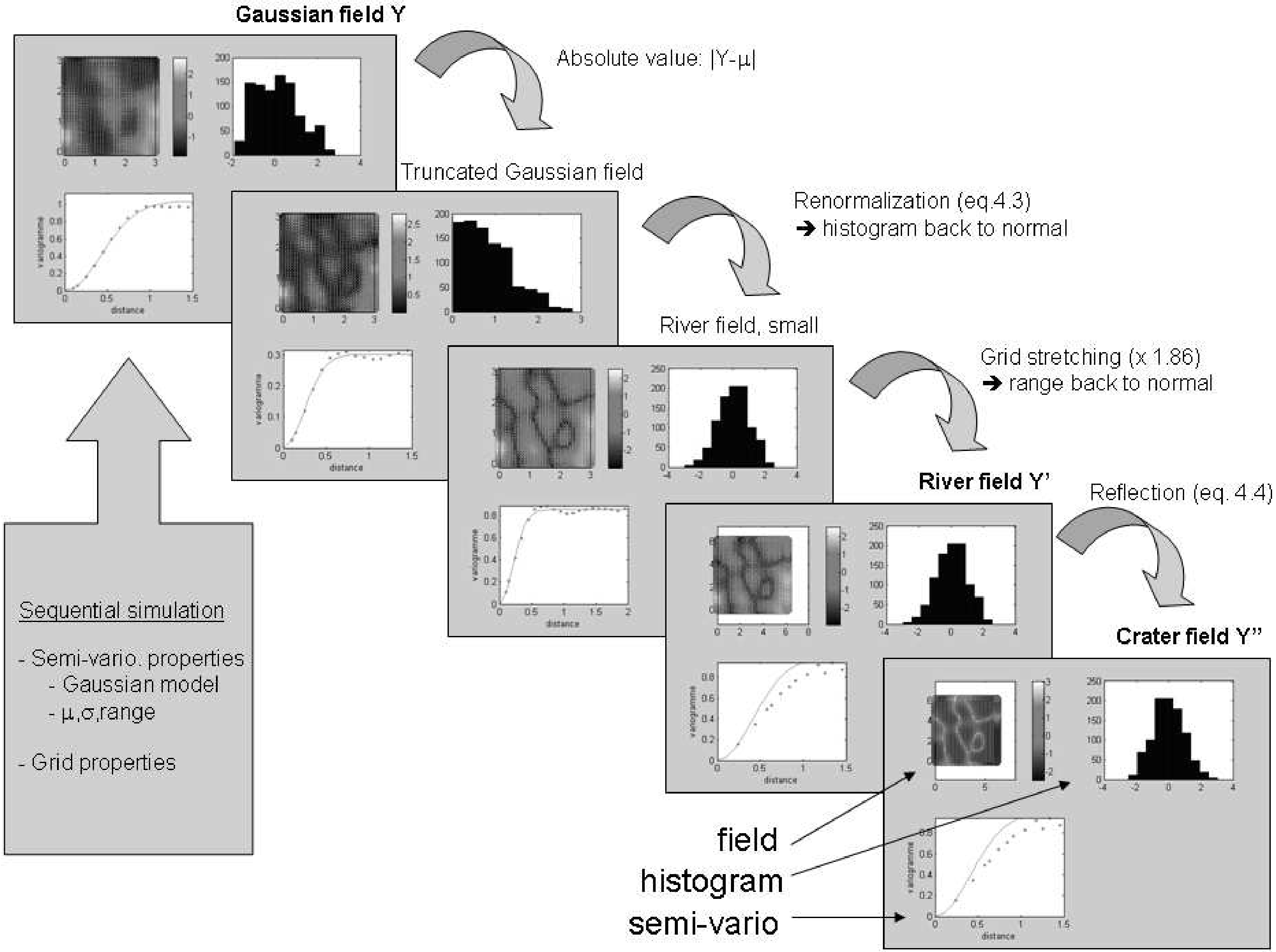

Figure 4.1: Method of Zinn and Harvey (2003) to generate fields that have contrasted structural connectivity properties.

$$Y' = F_Y^{-1}\left(F_Z\left(Z\right)\right) = erf^{-1}\left(2erf\left(\frac{|Y-\mu|}{\sigma\sqrt{2}}\right)-1\right)\sigma\sqrt{2}+\mu \quad (4.3)$$

Y' are the transformed values and Y are the original values. This method will produce a field Y' where the lowest values will be connected. This is used to generate the River micro-topography. In order to generate the Crater micro-topography, with the highest values connected, the values of the previous field Y' are reflected around the mean to create the new field Y''. This operation preserves the mean and the standard deviation.

$$Y'' = 2E[Y'] - Y' \quad (4.4)$$

Zinn and Harvey (2003) demonstrated that spatial correlations are almost preserved if a scale factor of 1.86 is taken into account.

We will generate ten replicates of the River- , Crater- and Random-type numerical micro-topographies, considering, for the distribution of heights, $\mu = 0$ and σ^2= 100 mm^2, and, for the spatial covariance, a sill of 100 mm^2 and a range of 100 mm. The fields considered for the runoff experiments will have a size of 1 m^2 and will be discretized in 1-cm^2 cells. A general 1 percent slope was finally added to the micro-topographical fields. Take note that such a method to generated micro-topography cannot take into account any oriented anthropogenic roughness such as ridges and furrows.

4.3.2 Runoff model

Overland flow can be described by the depth-averaged unsteady flow equations commonly referred to as the shallow water equations or Saint-Venant equations (de Saint-Venant, 1871; Esteves *et al.*, 2000). These equations are highly nonlinear and therefore no analytical solution exists (Kazezyilmaz-Alhan and Medina, 2007). If computed in 1-D along the x-axis, the equation of momentum is expressed by:

$$\frac{1}{g}\frac{\partial \bar{v}_x}{\partial t} + \frac{\bar{v}_x}{g}\frac{\partial \bar{v}_x}{\partial x} + \frac{\partial h}{\partial x} + \frac{\partial z}{\partial x} + \frac{\partial h_r}{\partial x} = 0 \quad (4.5a)$$

$$\frac{\partial h}{\partial t} + \frac{\partial \bar{v}_x \bar{h}_x}{\partial x} + \frac{\partial \bar{v}_y \bar{h}_y}{\partial y} = \phi \quad (4.5b)$$

where g is the gravity acceleration [m s^{-2}], $\bar{v}_x$ the depth-averaged velocity [m s^{-1}], h the water layer thickness [m], z the soil level [m] and $\frac{\partial h_r}{\partial x}$ the friction slope [-]. In the equation of continuity, ϕ is a sink/source term that is equal to the rainfall rate minus the infiltration rate [m/s]. In the following, since only impervious surface are considered, $\phi \geq 0$. We have always considered a positive source term, either by neglecting infiltration or considering a net effective rainfall supply (rain-infiltration).

Due to the complexity of the soil surface micro-topographies which gives rise to high spatial gradients in depth and velocity, the application of the full equation to our complex micro-topographies resulted in numerical problems, such as high frequency spurious oscillations caused near steep gradients (Bhallamudi and Chaudhry, 1992). The problem does not stem from the full overland flow equation, but rather from its numerical resolution. To overcome this problem, a strategy is to decrease the equation complexity by using the diffusive wave form of the Saint-Venant equation which is expressed by:

$$\frac{\partial h}{\partial x} + \frac{\partial z}{\partial x} + \frac{\partial h_r}{\partial x} = 0 \tag{4.6a}$$

$$\frac{\partial h}{\partial t} + \frac{\partial \bar{v}_x \bar{h}_x}{\partial x} + \frac{\partial \bar{v}_y \bar{h}_y}{\partial y} = \phi \tag{4.6b}$$

In this simplified equation, both the local acceleration term ($\frac{1}{g}\frac{\partial \bar{v}_x}{\partial t}$) and the convective term ($\frac{\bar{v}_x}{g}\frac{\partial \bar{v}_x}{\partial x}$) are neglected. Such simplification is acceptable if the flow resistance is dominant and the acceleration and inertial terms are small (Chanson, 2006). The following adimensional analysis supports this hypothesis. If we put forward characteristic values from equation 4.5, it can be rewritten as:

$$\frac{1}{g}\frac{V}{T}\frac{\partial V^*}{\partial T^*} + \frac{V}{g}\frac{V}{X}\frac{\partial V^*}{\partial X^*} + \frac{H}{X}\frac{\partial H^*}{\partial X^*} + \frac{Z}{X}\frac{\partial Z^*}{\partial X^*} + \frac{Hr}{X}\frac{\partial Hr^*}{\partial X^*} \tag{4.7a}$$

$$10^{-5} \qquad 10^{-1} \qquad 1 \qquad 1 \qquad 1 \tag{4.7b}$$

With g the gravity acceleration (9.81 m/s^2), V a characteristic velocity (10^{-1} m/s) and its dimensionless value dV* (= 1), T a characteristic time (10^3 s) and its dimensionless value dT* (= 1), X a characteristic length (10^{-2} m) and its dimensionless value dX* (= 10), H a characteristic water depth (10^{-2} m) and its dimensionless value dH* (= 1), Z a characteristic bed level (10^{-2} m) and its dimensionless value dZ* (= 1) and Hr a characteristic friction depth (10^{-2} m) and its dimensionless value dHr* (= 1). It is clear that the last three terms of the equation dominate the first two, which support the use of the diffusive wave simplification. In Equation 4.6, backwater effects are only reflected in the pressure term ($\frac{\partial h}{\partial x}$) and no hydraulic jump can be modeled. This equation is normally used for steady-state non-uniform flow regime. However, unsteady flow is preserved through the continuity equation (Kazezyilmaz-Alhan and Medina, 2007). Time is discretized in time steps in which the steady state is thus assumed. We used the Darcy-Weisbach formula for the friction head.

$$\frac{\partial h_r}{\partial x} = \lambda \frac{1}{4R_h} \frac{\bar{v}_x^2}{2g} \tag{4.8}$$

where λ [-] is the Darcy-Weisbach friction factor and R_h $[m]$ is the hydraulic radius that is equal to $\bar{h}$ the mean local water depth on the small interval ∂x. By combining equations (4.6) and (4.8) we can find a relation between the velocity and the gradient of absolute water level.

$$\bar{v}_x = \sqrt{-\frac{8g\bar{h}}{\lambda} \frac{\partial (h+z)}{\partial x}} \tag{4.9}$$

For turbulent flow, the Reynolds number $\mathrm{Re} = \frac{\bar{v}D}{\vartheta} = \frac{\bar{v}4R_h}{\vartheta} \cong \frac{\bar{v}4\bar{h}}{\vartheta} \geq 2000$, where D is the characteristic length [m] and the denominator ϑ is the kinematic viscosity [m^2 s^{-1}]. Contrarily to the previous chapter, the Reynolds number is here computed with the local water depth and for each node. Consequently, the lambda value will be specific for each node. In the present case, the friction factor was determined by Henderson (1966):

$$\frac{1}{\sqrt{\lambda}} = -2\log_{10}\left(\frac{\varepsilon}{3} + \frac{2.5}{\mathrm{Re}\sqrt{\lambda}}\right) \tag{4.10}$$

with ε the relative roughness [-]:

$$\varepsilon = \frac{k_s}{4\bar{h}} \tag{4.11}$$

where k_s [m] is the diameter of soil particles that produce the surface roughness. The form of these experimental equations are originally due to numerous experiments performed, between 1932 and 1935, by Nikuradse (1933) for turbulent flows in pipes uniformly coated with sand grains of uniform size and, between 1937 and 1939, by Colebrook and White (Colebrook and White, 1937; Colebrook, February 1939) for transition flows in commercial circular pipes. The coefficients of the original equation were slightly modified to match open channel observations, based on a large review process (Journal of the Hydraulic Division, 89-2, March-April 1963, Friction factors in open channels) sponsored by the American society of Civil Engineers. Equations 4.9 and 4.10 are solved iteratively, in a double iteration process for Re and λ.

For laminar flow (Re $\leq$ 2000), the friction factor was determined by (Chow *et al.*, 1988):

$$\lambda = \frac{C_L}{\mathrm{Re}} \tag{4.12}$$

where C_L is a constant that is equal to 96 for a smooth surface and is larger if the surface is rough. Introducing Equation 4.12 into Equation 4.9 and expressing the Reynolds number explicitely, the velocity for laminar flow is :

$$\bar{v}_x = \sqrt{-\frac{8g\bar{h}4\bar{v}_x\bar{h}}{C_L\vartheta}\frac{\partial\,(h+z)}{\partial x}} \tag{4.13}$$

We can simplify this equation and evacuate v_x from the right-hand side of the equation:

$$\bar{v}_x = -\frac{32g\bar{h}^2}{C_L\vartheta}\frac{\partial\,(h+z)}{\partial x} \tag{4.14}$$

Note that the temperature dependence of ϑ was assessed with the Sutherland's Law of viscosity for liquids.

For a particular location (or node), the Reynolds number of the preceding time step is used to guess the type of flow at the present time, in order to choose between laminar or turbulent velocity equations. After computation of the velocity, the Reynolds number is updated. If it appears that the type of flow was not guessed correctly, we update the velocity using the other velocity equation. In case this updated velocity would again change the type of flow, then the mean velocity between the laminar and the turbulent equations is considered.

The algorithm is implemented in space using a de-centered (staggered) regular grid (Figure 4.2), similarly to Zech *et al.* (1983) except for the soil level. For every time step, velocities are computed independently in the x-direction and y-direction based on Equations 4.9 or 4.14.

Water is allowed to flow out of the field only at its downstream boundary. At the outflow boundary, the velocity is computed with equations 4.9 or 4.14, but assuming $\frac{\partial(h+z)}{\partial y} = \frac{h}{\Delta y}$, which means that the velocity of the boundary flows are proportional to the water depth h. On the other boundaries, the velocity is null. The upstream boundary condition can also be defined by a specified inflow rate $\bar{v}_y\bar{h}_y$, in order to simulate runon.

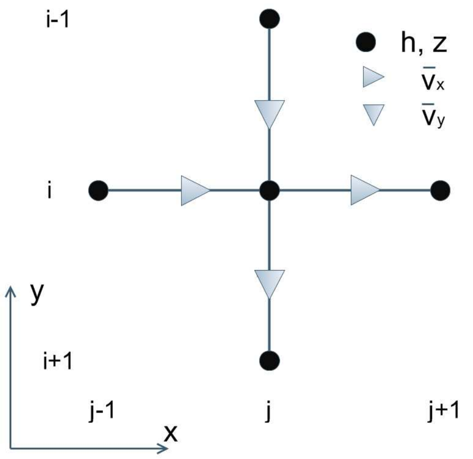

Figure 4.2: Two-dimensional fixed grid with the asymmetric velocity computation scheme.

Equation 4.6b is solved by an explicit difference scheme, taking only into account the previous time step (Euler):

$$\begin{aligned} h_{i,j}^{t+1} = & h_{i,j}^{t} - \frac{\Delta t}{\Delta x}\left(\bar{v}_{x(i,j+1/2)}^{t}\bar{h}_{x(i,j+1/2)}^{t} - \bar{v}_{x(i,j-1/2)}^{t}\bar{h}_{x(i,j-1/2)}^{t}\right) \\ & - \frac{\Delta t}{\Delta y}\left(\bar{v}_{y(i+1/2,j)}^{t}\bar{h}_{y(i+1/2,j)}^{t} - \bar{v}_{y(i-1/2,j)}^{t}\bar{h}_{y(i-1/2,j)}^{t}\right) + \phi \end{aligned} \tag{4.15}$$

where $h_{i,j+1/2} = \frac{h_{i,j}+h_{i,j+1}}{2}$.

We also implemented an explicit scheme that took into account the three previous time steps (Adams-Bashforth scheme AB3). This algorithm did not lead to a significant improvement of the simulation (Fig. 4.3) while increasing the computation time. Therefore, the Adams-Bashforth scheme is not used any further in this thesis.

To insure stability of an explicit computation scheme, water particles can not progress further than a single grid cell during a time step (Esteves *et al.*, 2000). Therefore we used a classical Courant-Friedrichs-Lewy (**CFL**) condition (Courant *et al.*, 1928) to determine the time step Δt:

$$\Delta t = \min_{\forall i,j} \frac{CN}{\frac{|v_{x(i,j)}|}{\Delta x} + \frac{|v_{y(i,j)}|}{\Delta y} + \sqrt{\frac{gh_{i,j}}{\Delta x^2} + \frac{gh_{i,j}}{\Delta y^2}}} \tag{4.16}$$

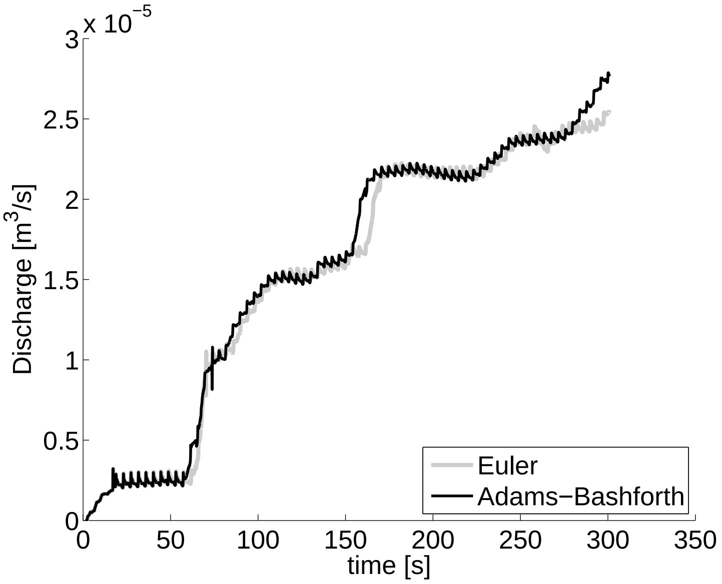

Figure 4.3: Impact of the choice of integration scheme on the hydrograph for a Random micro-topography.

where CN is a constant that needs to be inferior to 1 to insure mathematical convergence, and even less to ensure numerical stability (we fixed arbitrarily CN to 0.05).

Although not physical, negative water depths may appear during computations on particular nodes, where divergence of flow is high during rainfall or where the water layer is emptying after rainfall. It is known that the presence of dry zones is a crucial numerical problem to be solved (Vincent *et al.*, 2001), especially in the context of soil erosion by runoff modeling (Heng *et al.*, 2009). The strategy proposed by Esteves *et al.* (2000) has been implemented. It consists in setting a negative water depth back to zero and to retrieve the corresponding amount of water from the four direct neighbors, proportionally to their respective water depths, in order to preserve the mass balance of water. Yet, water from four direct neighbors might not be sufficient, leading to error in the mass balance when canceling anyway the negative values. Therefore, we have extended the strategy of Esteves *et al.* (2000) to a larger neighborhood by allowing a negative water depth on a particular node to be filled in by water retrieved from the four direct neighbors first (n=1), and if it is not sufficient, from neighbors of neighbors (n=2), and so on. The source code of the model is provided in the Annexe D.

4.3.3 Model validation

As recommended by Beven (2001), we first tested the impact of changing the spatial resolution on velocity and water depth, for a steady-state flow supplied by rain or runon on a regular 1-D slope. We considered spatial resolutions ranging from 0.1 to 5 cm. In a second step, we confronted the numerical solutions to the observations of experimental 1-D steady-state overland flows on two rough planes, one covered by an abrasive paper P40 (ks = 0.41 mm) and one covered by sifted gravels (ks = 1.5 mm) glued on the plane (Fig. 4.4). In the experimental flumes, both the slope (3%, 5-8%,14%) and the inflow rate (low-high runon) were adjustable. Only runon was considered for the overland flow experiments on rough planes. The sides of the flume were transparent, which allowed us to measure water depth with a caliper rule on the side, without perturbing the flow. The velocity was assessed by timing floating expanded polystyrene beads traveling over a known distance.

We also compared a modeled hydrograph for one particular waterproof micro-topography (B1) presented in Chapter 3 (and in the annex A) with the observed hydrograph when the micro-topography was submitted to an experimental rainfall experiment (see Chap. 7, medium rain). The digital elevation model of the micro-topography had a 8-mm spatial resolution to reduce the computation time without distorting too much the original soil micro-topography.

4.3.4 Application of the runoff model on complex micro-topographies

The numerical micro-topographies (River, Random and Crater) are considered impervious. Those micro-topographies, initially water-free, were submitted to a uniform and net supply of water of 100 mm/h. A high rain intensity was considered for computation time reasons. This high intensity must last 5-10 minutes in order to ensure that the discharge at the outlet reaches steady-state.

4.4 Results and Discussion

4.4.1 Quality assessment of the runoff model

Negative water depths

Hydrographs computed for a constant rain falling during 17 seconds on a 1-m^2 Random micro-topography and the associated error in the mass

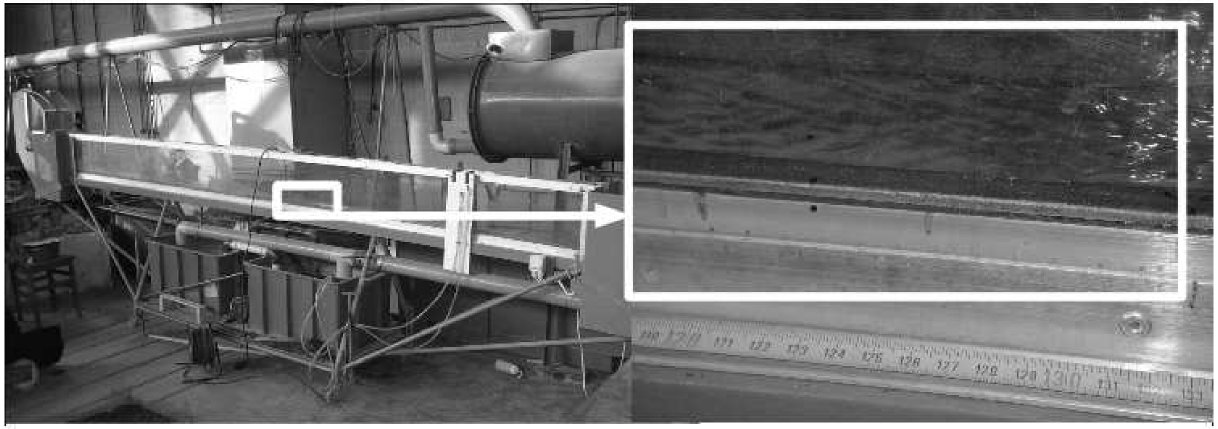

Figure 4.4: Experimental transparent flume to measure overland flow on rough planes.

balance are shown in Figure 4.5 for the different strategies that were implemented to correct negative water depths.

If we artificially cancel negative water depths without compensating it by an equivalent retrieval of water elsewhere, we would maintain an unphysical discharge and increase the mass balance error. Clearly, if the recession limb of the hydrograph needs to be modeled, the production of numerous negative water depths during the drainage process would require water retrieval from a large neighborhood. Once a central node and its four direct neighboring nodes are all dry, a negative depth can not be generated anymore on the central cell, as water velocity will be null (as all the mean water depths $\bar{h}$ around the central node equal 0). Let us note that the neighboring nodes from which water is retrieved should theoretically be nodes belonging to the same streamline. However, this was not considered, for computation time reasons, and water was retrieved from nodes physically not connected to the node where a negative water depth is being compensated.

Effect of the grid size

Besides the problem of loosing topographical information as the spatial resolution gets coarser, the size of the grid may also alter the numerical computation. Therefore we tested the effect of the spatial resolution on the mean water depth and mean flow velocity for a simulated steady-state sheet flow on a regular plane. It is shown in Figure 4.6, for a runon or a rainfall supply of water. We observe a small increase of water depth as the resolution gets coarser. Velocity follows the inverse trend, which results from a compensation effect to maintain discharge. For the rainfall supply, the confidence intervals (calculated as ± 1.96 the standard deviation and shown by vertical lines) are large as water discharge varies along the slope. For a runon supply, the confidence intervals increase as grid gets coarser due to the increasing effect of numerical oscillations.

The variation of mean velocity and water depth as a function of grid resolution is smaller than any of the confidence intervals. We can thus reasonably state that the grid resolution has no significant impact on the simulation, although it increases the uncertainty. A coarser grid allows to save time in the computation as the time steps are determined by the CFL condition proportionally to the spatial resolution, and also because less nodes are necessary to cover the same distance. We chose to work with a 1 cm resolution as a balance between computation time and uncertainty.

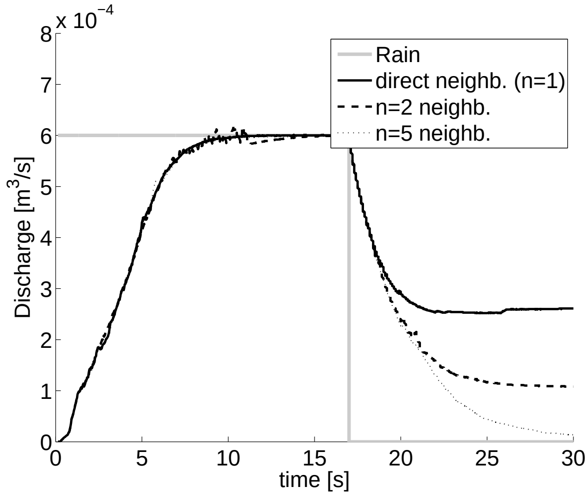

(a)

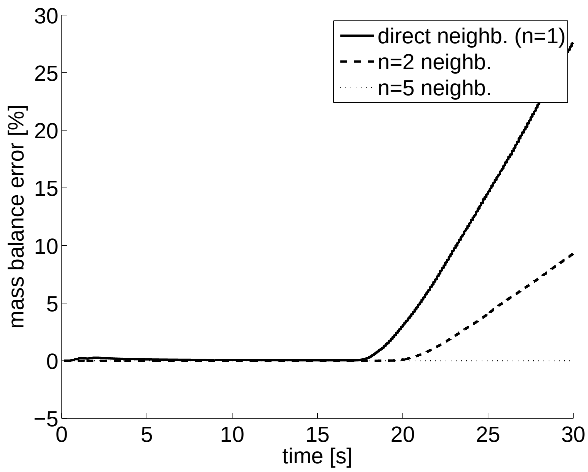

(b)

Figure 4.5: Impact of the strategy to avoid negative water depths on the simulated hydrographs (a) and on the resulting mass balance errors (b). n=1: 4 cells, n=2: 12 cells, n=5: 60 cells.

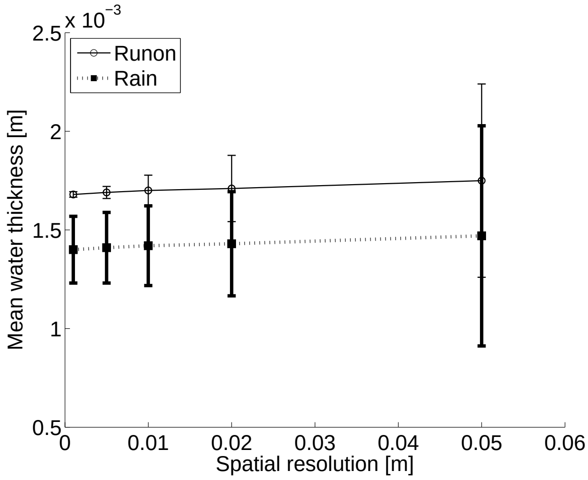

(a)

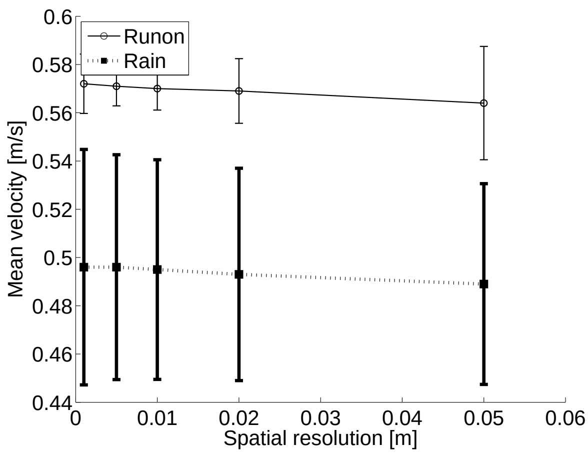

(b)

Figure 4.6: Effect of the spatial resolution on the mean water depth (a) and mean flow velocity (b), for an overland flow fed by a runon or a rainfall supply of water, on a regular slope (the associated confidence intervals are represented by vertical lines)

Model validation: experimental overland flows on rough planes VS numerical simulations

The main characteristics of the flume experiment on rough planes are provided in Table 4.1. Measurements of depth and velocity were repeated 3 times in order to get an estimation of the confidence intervals (calculated as ± 1.96 the standard deviation). Figure 4.7 shows the comparison between the measurements and the simulations. The RMSE is 0.10 m/s for the velocity, 0.85 mm for the water depth and 2.55 s for the time of propagation of the wave at the front of the flow when starting the experiment on a dry bed, which all correspond to about 10% of the range of explored values.

Another factor that may explain the discrepancies between observed and simulated velocities is the transition from laminar to turbulent flows. Figure 4.8 shows that transition for different levels of roughness and slope. We see that an inconsistent oscillation occurs passing from laminar to turbulent flow when the water depth is about the same as the medium grain size (ks). In order to render the transition between the laminar and the turbulent flow continuous, it might be interesting to increase the friction constant C_L in equation 4.12 when the medium size of grains increases too. This has not been investigated, although it might explain the quasi systematic underestimation of the propagation time for the gravel surface.

From all those validation steps, we can conclude that the major drawback of the model is the use of the diffusive wave equation instead of the full Saint-Venant equation. This is also illustrated for an overland flow on a corrugated surface in the Annexe B. For complex micro-topographies, hydraulic jumps may become important factors for assessing correctly the water depth, and we need to keep in mind that our model underestimates the surface detention. Promising work (Razafison *et al.*, not communicated; Delestre, 2010) from the METHODE project[2] suggests that the use of the full Saint-Venant equation on complex micro-topographies might be possible. Although, the basic hypothesis of the shallow water equations may not be verified : water height is not small compared to pixel width. In such case, we might even better use Navier-Stokes equations.

[2] `http://methode.netcipia.net/`

Table 4.1: Main characteristics of the overland flow experiments on rough planes.

mean grain diameter [mm]	Slope [%]	q_0 [cm^2 s^{-1}]	velocity [m s^{-1}]	water depth [mm]	propagation time [s]
0.41 ± 0.05	2.98	2.40 ± 0.50	0.25 ± 0.08	1.68 ± 0.63	25.6
	2.98	34.2 ± 0.28	0.61 ± 0.12	5.62 ± 0.58	10.8
	4.80	5.30 ± 0.50	Not measured	1.69 ± 0.55	20.5
	4.80	34.6 ± 0.80	Not measured	4.98 ± 0.63	9.9
	13.86	5.70 ± 0.48	0.60 ± 0.13	1.41 ± 0.55	12.4
	13.86	33.7 ± 0.35	0.97 ± 0.04	2.79 ± 0.42	8.6
1.5 ± 0.5	2.86	20.1 ± 0.44	0.41 ± 0.04	6.27 ± 1.44	15.8
	2.86	34.7 ± 0.81	0.52 ± 0.02	8.49 ± 1.79	12.1
	8.08	9.50 ± 2.00	0.42 ± 0.02	3.59 ± 0.76	Exp. problem
	8.08	33.9 ± 1.34	0.67 ± 0.04	5.79 ± 1.00	10.2
	14.56	6.90 ± 0.11	0.31 ± 0.18	2.38 ± 0.99	Exp. problem
	14.56	34.5 ± 0.3	0.83 ± 0.04	5.38 ± 0.73	10.8

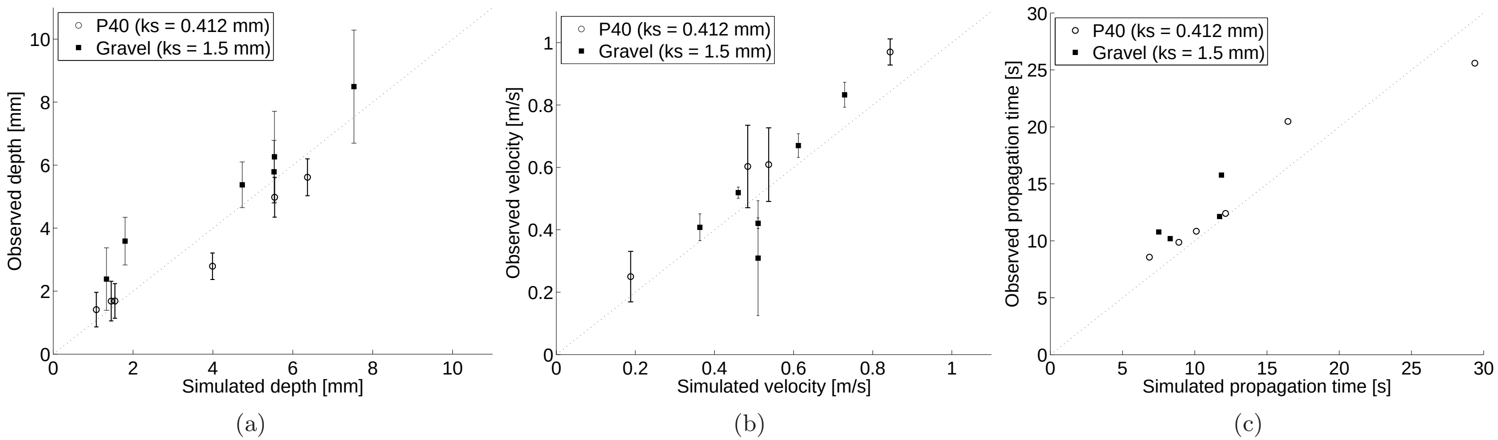

Figure 4.7: Comparison between simulations and observations of overland flow properties, for rough planes. The error bars account for ± 1.96 the standard deviation, and the dashed line corresponds to the 1:1 line.

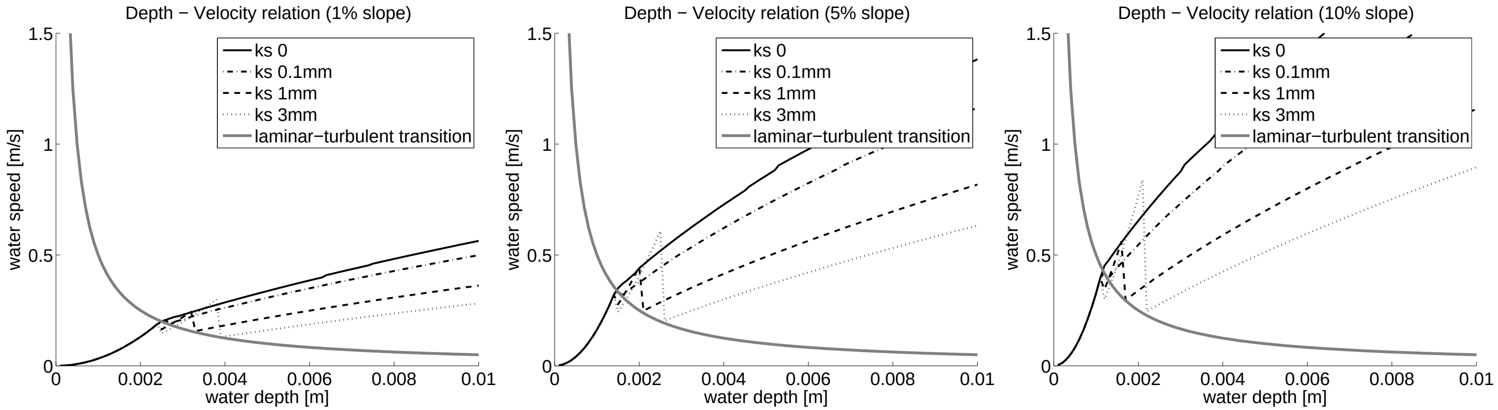

(a) (b) (c)

Figure 4.8: Relation between the depth and the velocity computed in both laminar (left bottom corner of each graph) and turbulent domains, for 3 different slopes and 4 different medium sizes of grains (ks).

Model validation: experimental overland flow on a waterproof micro-topography VS numerical simulation

Figure 4.9 shows the comparison of an observed hydrograph with the simplified hydrograph computed with the filling algorithm and the 2-D Diffusive Wave (2-D DW) solutions of the Saint-Venant equations computed for two levels of medium grain size ks or imposing a large value of lambda and C_L. We clearly see that the surface detention is largely underestimated as the 2-D DW hydrographs do not detach sufficiently from the simplified hydrograph where surface detention is null. The effect of changing the medium grain size ks did not modify a lot the hydrographs. We tried to compensate this effect by increasing the value for the friction constant and imposing a large value for lambda, but without success. This indicates that the key factor explaining friction is not being dealt correctly for such rough surface. Our physical model only considers friction with the particles of soil (= grain resistance), while, for rough surface, energy dissipation due to the shape of the macro-roughness that protrudes through the water layer (= form resistance) is big. Moreover, the use of the diffusive wave simplification of the Saint-Venant equations leads to the absence of representation of small scale hydraulic jumps provoked by inertial change. Yet, backwater effects are significant contributors for the surface detention. We must therefore pay attention that the use of the diffusive wave simplification leads to a significant underestimation of the surface detention for runoff on surfaces with macro-roughness. The use of an hydraulic model based on the full Saint-Venant equations should be clearly preferred.

4.4.2 Contrasted numerical fields of micro-topography

An example of each of the three micro-topography types is given in Figures 4.10 and 4.11. The fields presented here a size of 2×2 meters. Let us note that Crater and River surfaces are the exact inverse of one another. The connected patterns of depressions (River) or crest (Crater) are clearly identifiable. With an increasing slope, River micro-topographies become more realistic as the drainage network become more dendritic. Although, discussion on the effect of the slope is not included in the chapter. We assume that slope affects the flow pathways so that connections in the direction of the main slope will be favored as slope increases. Some connections may disappear while new ones may be created. The depression storage decreases with increasing slopes (Kamphorst *et al.*, 2000; Reaney *et al.*, 2007).

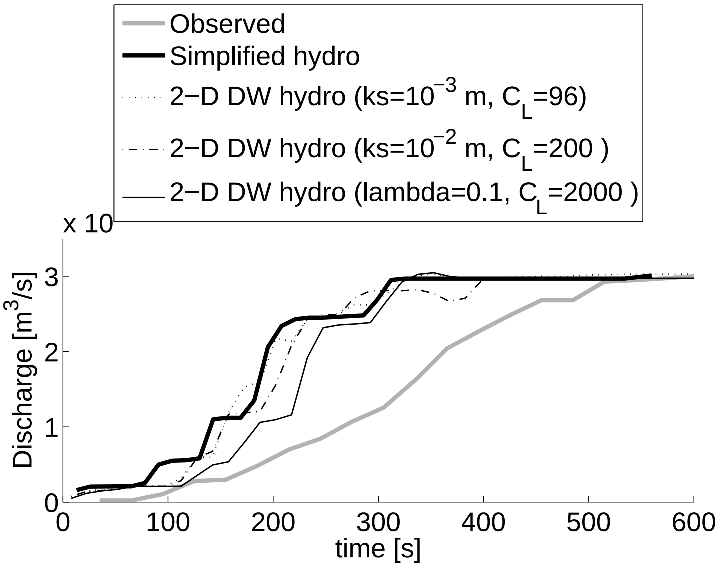

Figure 4.9: Comparison of an observed hydrograph with the simplified hydrograph computed with the filling algorithm and the 2-D Diffusive Wave (2-D DW) solutions of the Saint-Venant equations computed for two levels of medium grain size ks.

4.4.3 Effect of the spatial arrangement of micro-topography on the hydrograph

To reduce the computation time, the numerical runoff experiments were conducted on only a quarter of each field (1 m^2). If distinct hydraulic behaviors already emerge at that scale among the 3 micro-topographical types, this distinction will be enhanced as we consider larger fields due to the decreasing impact of border effects.

The River fields are the first to reach the steady state runoff rate (Fig. 4.12) that is theoretically equal to the rainfall intensity (since no infiltration is considered). It is followed by the Random and then by the Crater cases. Although there is some variability among the replicates, there is a clear effect of the micro-topography type. The more the depressions are isolated from each other, the longer it takes for the runoff rate to tend toward the rainfall intensity. The main factor is the effect of micro-topography on both the depression storage and surface detention (Tab. 4.2) that need to be fully filled before reaching steady state. The depression storage seems to be the major factor that discriminates among the different micro-topographies, although we must

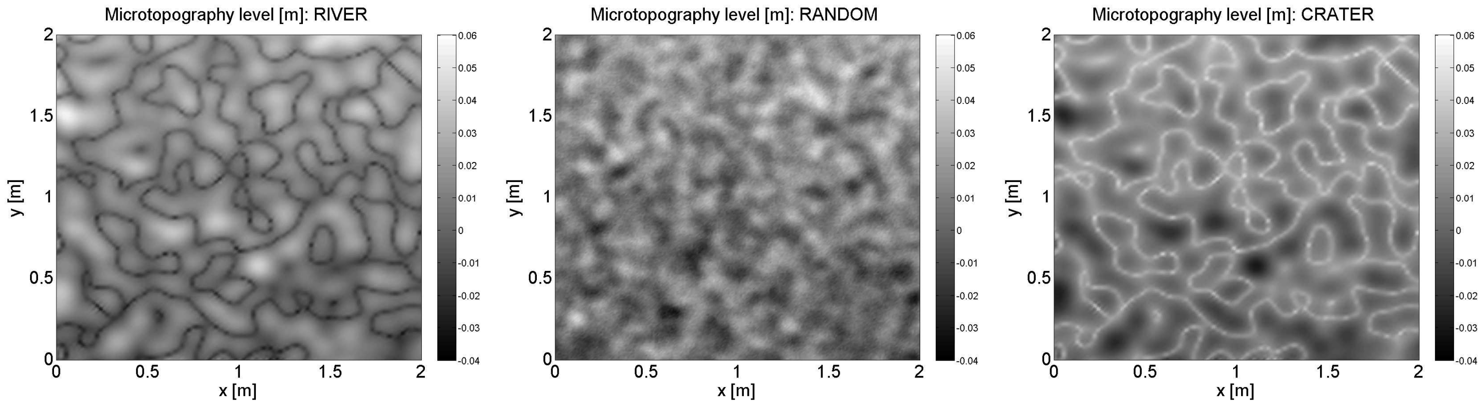

(a) (b) (c)

Figure 4.10: River (a), Random (b) and Crater (c) micro-topographies (the color of the pixels corresponds to the surface height). The mean altitude decreases from the top to the bottom of the images with a 1 percent slope (Grid cells: 1 cm x 1 cm).

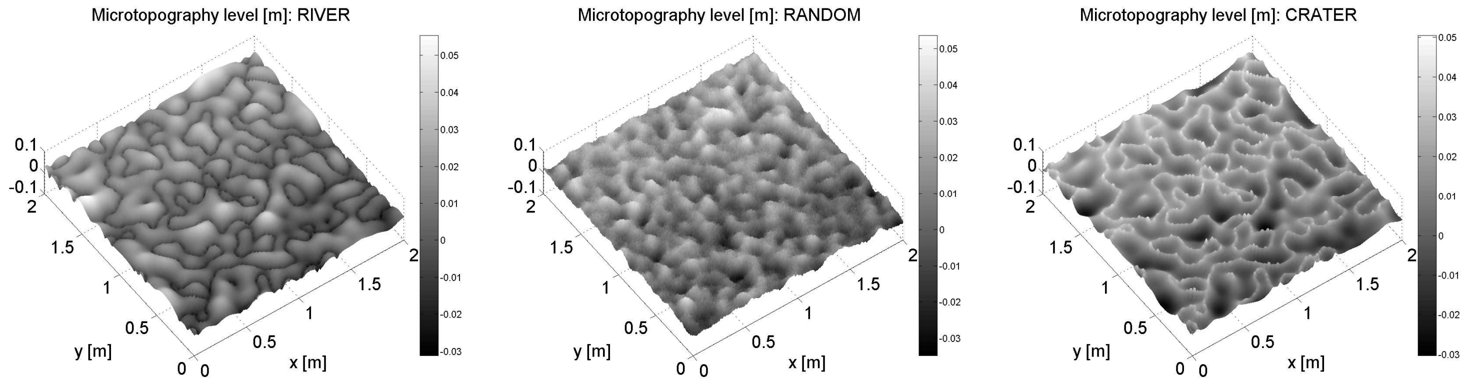

(a) (b) (c)

Figure 4.11: 3D view of the River (a), Random (b) and Crater (c) micro-topographies (the color of the pixels corresponds to the surface height). The mean altitude decreases from the top to the bottom of the images with a 1 percent slope (Grid cells: 1 cm x 1 cm).

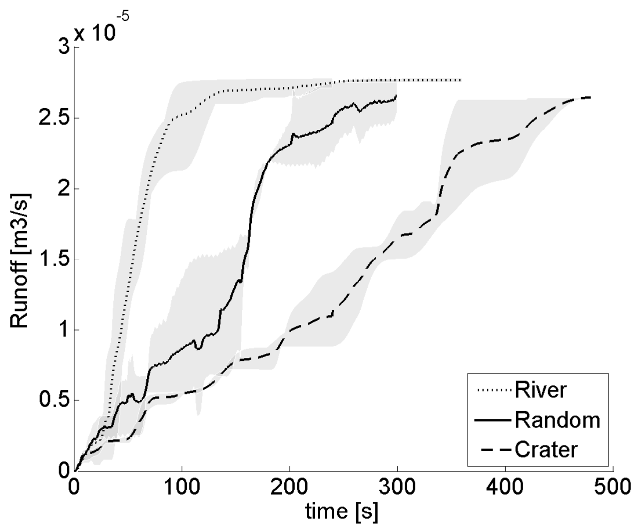

Figure 4.12: Impact of the micro-topography type on the hydrograph, for a constant rainfall intensity of 100 mm/h. The mean runoff values (number of replicates = 10) are given for each micro-topography type as well as the envelop delimited by the 1st and 9th deciles.

be aware that the hydraulic model underestimates the surface detention due to the diffusive wave simplification.

4.4.4 Representativity of the numerical micro-topographies

The numerical micro-topographies used in this chapter are fictive. Real micro-topographies will behave intermediately between River and Crater cases if we assume that, on a same field, some of the depressions will always be well connected while others will remain mostly isolated. Even if the numerical micro-topographies do not fully mimic reality, they are

Table 4.2: Depression storage and surface detention in function of the micro-topographical type.

Type	Depression storage [mm]	Surface detention [mm]
Crater	5.30 ± 2.85	1.07 ± 0.41
Random	2.91 ± 1.14	0.84 ± 0.36
River	1.14 ± 0.56	0.51 ± 0.23

parametrized by realistic values for the sill (100 mm^2) and the range (100 mm) of their semivariograms (see Figure 5.6). Similar values have been observed on experimental plots (Darboux *et al.*, 2002) and real fields (Vidal Vazquez *et al.*, 2005).

It is tempting to link the artificial micro-topographies in some way to the temporal evolution of real states of the soil surface. For instance, just after tillage, depressions are mainly isolated from each other and form Crater-type topographies (Moreno *et al.*, 2008; Carvajal *et al.*, 2006). Due to the shaping action of the overland flow itself that incises the borders of the crests where water overflows (Darboux *et al.*, 2002), the soil surface evolves to create a connected micro-topography (Favis-Mortlock, 1998), such as eroded soil after heavy rain periods, forming River-type topographies (Gomez and Nearing, 2005).

4.5 Conclusions

A methodology was presented to build synthetic fields of micro-topography presenting similar statistics in terms of mean, standard deviation and semivariogram, but very contrasted in terms of depressions connectivity. Oriented roughness was not considered as we focus our study at the interrill scale.

We developed also an hydraulic model based on the diffusive wave simplification of the Saint-Venant equations. This model works consistently in 2-D and reproduces well overland flow on rough planes. Although, it has the drawback to be based on the diffusive wave simplification. This implies to neglect the hydraulic jumps that occurs at our scale, which leads to an underestimation of the surface detention.

The model was applied to 10 replicates of contrasted numerical micro-topographies. It was found that, independently of the random roughness value that was equivalent (RR = 10 mm) on all our micro-topographies, the spatial organization of the micro-topography affected the surface detention in a ratio of 1 to 2, and the depression storage in a ratio of 1 to more than 4, under a constant and uniform net rainfall supply. Connectivity properties of micro-topography play thus an important role on the runoff triggering and on the shape of the hydrograph, which can not be captured by conventional macroscopic surface micro-topography indicators such as the random roughness or semivariogram parameters. There is therefore a need for additional indicators which better characterize the hydraulic response of interrill plots.

Chapter 5

What indicators can capture runoff-relevant connectivity properties of the micro-topography ?[1]

5.1 Outline

We evaluate different quantitative indicators of hydrological connectivity, using the concepts of structural and functional connectivity. The indicators were tested on contrasted numerical fields of micro-topography that present distinct hydrological responses, as demonstrated in Chapter 4.

The investigated structural connectivity indicators, mostly used so far in porous or fractured media, were the semivariogram, the bivariate entropy integral scale, the n-point rectilinear connectivity integral scale, the connectivity function integral scale, the percolation threshold and the Euler number. The first three indicators were not able to discriminate between the three extreme types of micro-topographical fields whereas the last three indicators were successful. However, relating the latter three indicators to the hydrological response of a topographical field appears uncertain. We therefore proposed a functional connectivity indicator by adapting the 'volume to breakthrough' concept: the degree of surface connection as a function of the depression storage filling. This indicator was capable of discriminating between the micro-topographical

[1]Adapted from: *What indicators can capture runoff-relevant connectivity properties of the micro-topography at the plot scale ?*, Antoine, M., Javaux, M. and Bielders, C., **Adv. Water Res.** 32(8):1297:1310, **2009**.

types. It could be used to conceptualize the process of depression filling and therefore may become an effective characteristic of an elementary representative area in large scale hydrological model.

5.2 Introduction

Although connectivity is acknowledged as a key factor of catchment hydrological behavior, it still misses reference evaluation methodologies. For Gustafson (1998), semivariograms are useful in a primary step to determine the appropriate scale at which patterns must be investigated. Nevertheless Western *et al.* (1998) state that semivariograms are better at describing continuity than connectivity. Indeed, in their study, connected and random patterns of soil water content were not distinguished by traditional geostatistics. This is due to the conventional assumption in geostatistics that relations between points depend only on their Euclidean distance, even though it is most of all the presence of connecting paths that determines the connectivity (Western *et al.*, 1998). In a similar context, Knudby and Carrera (2005) found that 2-point statistics, including the semivariogram and the bivariate entropy, were inadequate to account for the structural connectivity impact on water and solute transport. On the other hand, multiple-point statistics, such as the connectivity function of Allard and HERESIM-Group (1993), performed better (Knudby and Carrera, 2005). With this function, Western *et al.* (2001) could also discriminate between spatial patterns exhibiting contrasted structural connectivity characteristics, and relate it to different hydrological behaviors. Topological properties of the structures, such as the Euler number, may be used to quantify the connectivity properties, and may constrain the construction of realistic numerical fields (Vogel and Roth, 2001). When cut off structures (terraces and dams for Bellin *et al.* (2009), vegetation bands for Imeson and Prinsen (2004)) or impermeable interfaces (Mathias *et al.*, 2005) obstruct the flows, the ratio between the actual connections (limited by the obstructing elements) and the potential connections (if the obstructing elements where missing) is a straightforward measurement of structural connectivity. In subsurface hydrology, Scheibe (1993) proposed that breakthrough curves may provide functional indicators of connectivity, as the way high or low conductivity regions are patterned are reflected in the arithmetic mean velocity and the early and late arrival times. Indeed, the functional connectivity indicators that were based on the information provided by the breakthrough curve performed best for Knudby and Carrera (2005). In a global context, Bracken and Croke (2007) put the *volume to break-*

through forward as an unifying concept in quantifying the functional connectivity at a range of spatial scale.

Because it is independent of boundary conditions, the characterization of structural connectivity appears more straightforward than functional connectivity. Yet it is functional connectivity that best reflects the hydrological behavior of a given surface. Clearly, functional connectivity must to some extent be dependent on structural connectivity, as pattern and process are often assumed to be linked (Gustafson, 1998), but the nature of this relationship is complex. It is therefore of interest to investigate whether structural connectivity indicators can be used to assess the functional connectivity for specific boundary conditions. Therefore, the general objective of this chapter is to test and compare different quantitative indicators of both structural and functional connectivity and to evaluate their robustness in relation to particular hydrological behavior. Our specific objectives are (1) to assess the discriminating capacity of previously defined indicators of structural connectivity with regard to distinct hydrological behaviors and (2) to derive a simple functional connectivity indicator for surface hydrology.

5.3 Materials and Methods

5.3.1 Structural connectivity indicators derived from point to point analysis

The structural connectivity indicators are applied on the topographical fields in the absence of any trend (the macroscopic slope is subtracted), so it is only the effect of the local micro-topography that is taken into account.

Methods applicable to continuous fields

Semivariogram

The semivariogram γ describes the degree of spatial dependence of a random field $Z(\mathbf{x})$, with $\mathbf{x}$ a position vector in the spatial domain D. For a distance vector $\mathbf{d}$:

$$\gamma\left(\mathbf{d}\right) = \frac{1}{2} Var\left[Z(\mathbf{x}) - Z(\mathbf{x}+\mathbf{d})\right] \forall \mathbf{x} \in D \tag{5.1}$$

It has been used in the context of connectivity by, among others, Western *et al.* (2001).

Entropy

Entropy is a measure of disorder, whereas connectivity may imply order. Therefore, entropy of a connected field may be smaller than for an unconnected field (Knudby and Carrera, 2005). If $f_d(\zeta,\zeta')$ is the stationary bivariate probability density function (PDF) of the random variables $\zeta = Z(\mathbf{x})$ and $\zeta' = Z(\mathbf{x}+\mathbf{d})$, separated by a distance vector $\mathbf{d}$, then the entropy $H_f(\mathbf{d})$ of the distribution $f_d(\zeta,\zeta')$ is defined by:

$$H_f\left(\mathbf{d}\right) = -\int_{-\infty}^{\infty}\int_{-\infty}^{\infty}\left(\ln f_d\left(\zeta,\zeta'\right)\right) f_d\left(\zeta,\zeta'\right)\partial\zeta\partial\zeta' \tag{5.2}$$

Since the functions $\ln f_d\left(\zeta,\zeta'\right)$ and $f_d(\zeta,\zeta')$ increase together, paired combinations with low probabilities will increase the entropy value (Journel and Deutsch, 1993). This occurs when the number of distinct combinations of pairs increases. Thus the higher the disorder, the higher the entropy (this will be the case for instance if couple combinations follow a uniform bivariate distribution). A discrete approximation to this distribution can be computed by distributing the value of each random variable among K categories (intervals of values) and by computing the following equation (Journel and Deutsch, 1993):

$$H_f\left(\mathbf{d}\right) = -\sum_{k=1}^{K}\sum_{k'=1}^{K}\left(\ln p_{k,k'}\left(\mathbf{d}\right)\right) p_{k,k'}\left(\mathbf{d}\right) \tag{5.3a}$$

$$p_{k,k'}\left(\mathbf{d}\right) = \text{Prob}\left\{Z(\mathbf{x}) \in \text{category k}, Z(\mathbf{x}+\mathbf{d}) \in \text{category k'}\right\} \tag{5.3b}$$

The relative bivariate entropy $H_r(\mathbf{d})$ is defined by:

$$H_r\left(\mathbf{d}\right) = \frac{H_f\left(\mathbf{d}\right) - H_f\left(0\right)}{H_f\left(0\right)} \tag{5.4a}$$

$$H_f\left(0\right) = -\sum_{k=1}^{K}\left(\ln p_k\right) p_k \tag{5.4b}$$

$H_r(\mathbf{d})$ varies between 0 and 1. $H_r = 1$ means a maximum entropy and corresponds to the case of two independent variables.

Methods applicable to binary fields

BINARIZATION BY THRESHOLD

Methods described hereafter require binary fields (fields of 0 and 1). Given a field Z composed of multiple pixels, it can be divided into two subsets of pixels S and S^C labeled 0 and 1, so that $Z = S \bigcup S^C$ (Z is thus completely defined by a binary field). Depending on the subset of interest, S or S^C is used to compute the connectivity indicators. The rules used for dividing the field into two depend on the context. A common way is to attribute a pixel $\mathbf{x}$ to S or S^C depending on whether its value $Z(\mathbf{x})$ is above or below a threshold value z (Neuweiler and Cirpka, 2005; Samouelian *et al.*, 2007; Knudby and Carrera, 2005; Western *et al.*, 2001). We will consider that the threshold value z accounts for the mean absolute water level. Every pixel whose height is under that level is submerged by water and thus is considered as being part of the runoff pathways and receives a value of 1.

$$I_{th}(\mathbf{x}; z) = \begin{cases} 1 \text{ if } Z(\mathbf{x}) \leq z \\ 0 \text{ else} \end{cases} \tag{5.5}$$

This procedure presents some limitations as we will explain in the next paragraph. However, it is the only one that generates comprehensive binary fields for the Euler number (This parameter is explained later). Therefore, this binarization process I_{th} will be used to compute the Euler number as a function of z. The field of interest is in that case the subset of pixels whose elevation is below the threshold value z ($I_{th} = 1$, equ. 5.5).

BINARIZATION BY WATERSHED PROCEDURE

Because the level of a pixel can be above a certain threshold yet its water may (in some cases) or may not (in other cases) flow up to the outlet, we tested another binarization procedure than the common threshold-based one. It is based on the delineation of the area hydrologically connected to the downstream boundary of the field (i.e., a watershed delineation for which the outlet is made of all the pixels at the downstream boundary). We raise step by step a mean horizontal level of water z $[m]$ that submerges gradually the micro-topography. For each step, the topography is modified by considering, at every point, the maximum altitude between the original soil surface height and the absolute submerging level z. This incrementally updated topography is considered for the watershed delineation corresponding to the submerging level z. The binarization procedure attributes to every pixel a value of 1 or 0 depending on whether it is part or not of the updated watershed corresponding to the z value. As surface depressions are progressively submerged by the fictive water level z, more and more surface becomes part of the watershed related to the downstream boundary.

$$I_{ws}(\mathbf{x}; z) = \begin{cases} 1 \text{ if } \max(Z(\mathbf{x}), z) \in \text{ watershed of the downstr. bound.} \\ 0 \text{ else} \end{cases} \tag{5.6}$$

n-Point rectilinear connectivity integral scale

n-Point rectilinear connectivity is the probability that pixels at n locations located along a linear path are all in the field of interest and given a height threshold z, the n-point connectivity $K(\mathbf{u}; n; z)$ is:

$$K(\mathbf{u}; n; z) = \text{Prob}\left\{I_{ws}(\mathbf{x}; z) = 1, I_{ws}(\mathbf{x}+\mathbf{u}; z) = 1, ..., I_{ws}(\mathbf{x}+n\mathbf{u}; z) = 1\right\} \tag{5.7a}$$

$$= E\left[I_{ws}(\mathbf{x}; z) I_{ws}(\mathbf{x}+\mathbf{u}; z) ... I_{ws}(\mathbf{x}+n\mathbf{u}; z)\right] \tag{5.7b}$$

$$= E\left\{\prod_{j=1}^{n} I_{ws}\left[\mathbf{x}+(j-1)\mathbf{u}; z\right]\right\} \tag{5.7c}$$

where $\mathbf{x}$, $\mathbf{x}+\mathbf{u}$, $\mathbf{x}+2\mathbf{u}$, ... $\mathbf{x}+n\mathbf{u}$ are the locations at which the binary indicator variable I_{ws} is evaluated. $K(\mathbf{u}; n; z)$ gives the probability of observing a continuous string of n points in the field of interest. We can then compute the n-point rectilinear connectivity integral scale which corresponds to the mean length L_K [m] of the continuous string:

$$L_K = pixel\_length \int_0^{n\_\max} \mathrm{K}\left(\mathbf{u}; \mathrm{n}; \mathrm{z}\right) \partial n \tag{5.8}$$

where *n_max* is the maximum number of pixels in the field along the direction considered. This indicator measures only straight rectilinear connectivity; any undulation would break that connectivity and reduce L_K (Krishnan and Journel, 2003). We computed this indicator starting the string at the outlet side of the field and following the original mean slope direction (that had been previously subtracted). This means that the linear features taken into account are parallel to the macroscopic slope and are connected at one end to the downstream boundary.

Connectivity function integral scale

The connectivity function defined by Allard and HERESIM-Group (1993) has been used among others by Western *et al.* (2001), Pardo-Iguzquiza and Dowd (2003), Knudby and Carrera (2005) and Xu *et al.* (2006). Given a point located at $\mathbf{x}$, and another point located at $\mathbf{x}+\mathbf{d}$ separated from the first by a direct distance $\mathbf{d}$ and belonging to the same subset ($I_{ws} = 1$ in our case), those points are said to be connected ($\mathbf{x} \Leftrightarrow \mathbf{x}+\mathbf{d}$) if they can be joined by a path whose points are in their subset. The connectivity function $\tau(\mathbf{d}, z)$ expresses the probability that two points of the subset of interest separated by a direct distance $\mathbf{d}$ are linked by pixels of their subset:

$$\tau(\mathbf{d}, z) = P(\mathbf{x} \Leftrightarrow \mathbf{x} + \mathbf{d}, I_{ws}(\mathbf{x} + \mathbf{d}; z) = 1 | I_{ws}(\mathbf{x}; z) = 1) \tag{5.9}$$

$\tau(\mathbf{d}, z)$ is the same as $K(\mathbf{u}; n = \mathbf{d}/pixels_{size}; z)$ if computed in one single direction. The connectivity function integral scale L_τ $[m]$ represents the average distance over which pixels are connected and can be computed by:

$$L_\tau(z) = \int_0^\infty \tau(\mathbf{d}, z)\, \partial \mathbf{d} \tag{5.10}$$

Percolation

Percolation theory considers that a medium is connected if a continuous path exists between opposite boundaries. The percolation threshold is the threshold value for the binarization procedure that generates a cluster in the subset of interest that spans the entire domain and connects boundaries in case the domain is finite. If the domain is infinite, in some specific cases (for instance when the field is discretized on a square grid and when the values are set at random in the field), a theoretical value for the percolation threshold exists (Hunt, 2005; Lehmann *et al.*, 2007). If the domain is finite, border effects occur and the percolation threshold is expressed by a probability. In our case, the field of interest is determined by watershed delineation. Values of the pixels are not set at random and therefore the value of the threshold is not in accordance with classical percolation theory. Consequently, our percolation function provides only the observed probabilities that the watershed connected to the downstream boundary of the field reaches at least one pixel of the upstream boundary.

Euler number

The Euler number χ (or Euler characteristics, Euler-Poincaré characteristics) is defined for 2-D binary shapes as (equ. 5.11) the number of isolated objects N (close convex) minus the number of holes G (closed concave). G is equivalent to the number of redundant connections (a redundant connection can be cut without creating an additional isolated component). According to Euler's formula, χ can be calculated by the number of nodes minus the number of bonds. In case the structure is partitioned into convex volume elements each defined by a number of vertices, edges and faces, the Euler number may be calculated for 2D grids by $\#vertices - \#edges + \#faces$. The Euler characteristics reported to the volume of investigation is called the volumetric Euler characteristic, and was used previously to characterize the connectivity of pore space and cracks (Vogel, 2000; Vogel and Roth, 2001):

$$\chi(z) = N\left(I_{th}(z) = 1\right) - G\left(I_{th}(z) = 1\right) \tag{5.11}$$

5.3.2 Functional connectivity indicator: simplified hydrograph and Relative Surface Connection (RSC) function

When the soil infiltration rate is lower than the rainfall intensity, water starts to accumulate at the surface. Puddles progressively overflow and water either accumulates in adjacent depressions, or flows to the downstream boundary, initiating runoff (Darboux *et al.*, 2002). As the ponded water layer thickness increases, a larger part of the plot that produces local runoff connects to the downstream boundary and consequently the global runoff coefficient of the field increases. To account for the effect of the micro-topography on the initiation of runoff, a cellular automaton model was used. It is a simple filling algorithm where the velocity of the water is considered infinite. Given a rainfall intensity I [m s^{-1}], for a field of surface S [m^2] during a specific time interval Δt [s], a small volume of water $\Delta V = SI\Delta t$ [m^3] is uniformly distributed on the surface of the plot. The water volume by pixel $\Delta V_{i,j}$ is equal to $\Delta V/\#pixels$. Each $\Delta V_{i,j}$ moves immediately to the lowest point it can reach following the steepest absolute water level gradient (soil level + water thickness) computed in a 8-neighbor scheme. $\Delta V_{i,j}$ is eventually added to previous accumulated water in the depression and increases the water thickness at that point. If the depression overflows, the excess water flows further. When the lowest point reached by the water is situated at the downstream boundary, the water is taken out of the field and is summed up in the simplified hydrograph. After all the $\Delta V_{i,j}$ have been redistributed, the time is increased by Δt. This method is similar to the one of Darboux *et al.* (2002) except that these authors randomly distribute the water. The computation principle is illustrated in Figure (5.4).

The method produces simplified hydrographs as it does not take explicitly into account the transfer time of water inside the field, i.e. the water velocity is infinite. As a result, the surface detention is null. In summary, these simplified hydrographs result from a simple filling algorithm that is fast to compute and they only show the effect of the water storage in the depressions (depression storage) on runoff triggering, under the hypothesis that depression storage is empty at the beginning of the experiment. The source code of the filling algorithm is provided in the Annexe D.

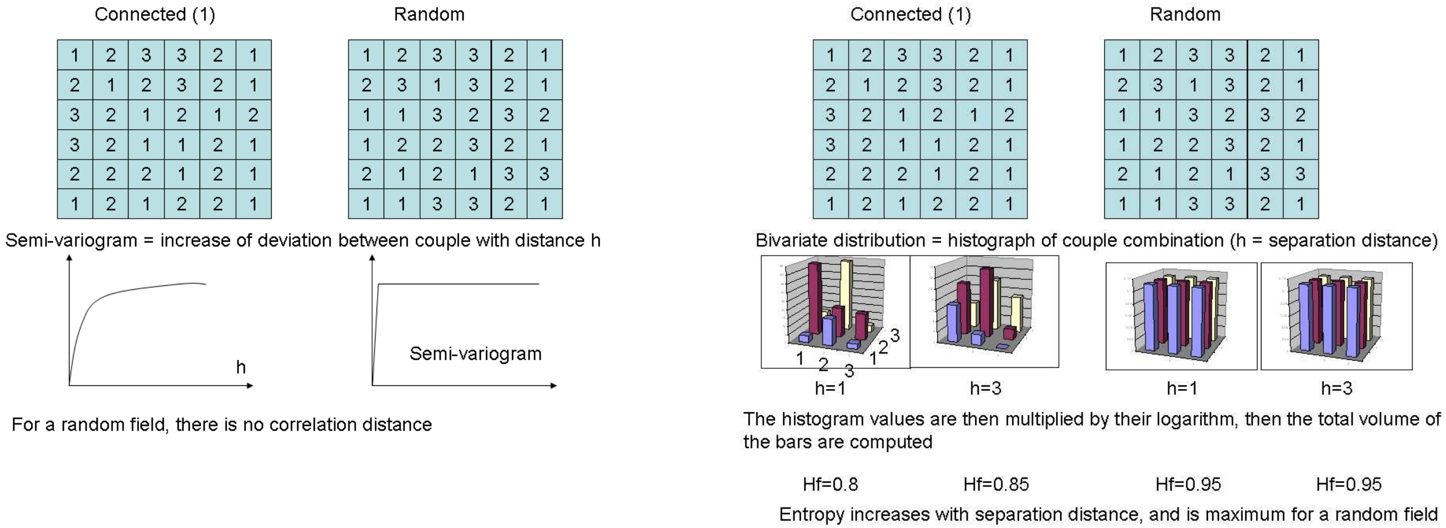

(a) (b)

Figure 5.1: Example of structural connectivity indicator computation.

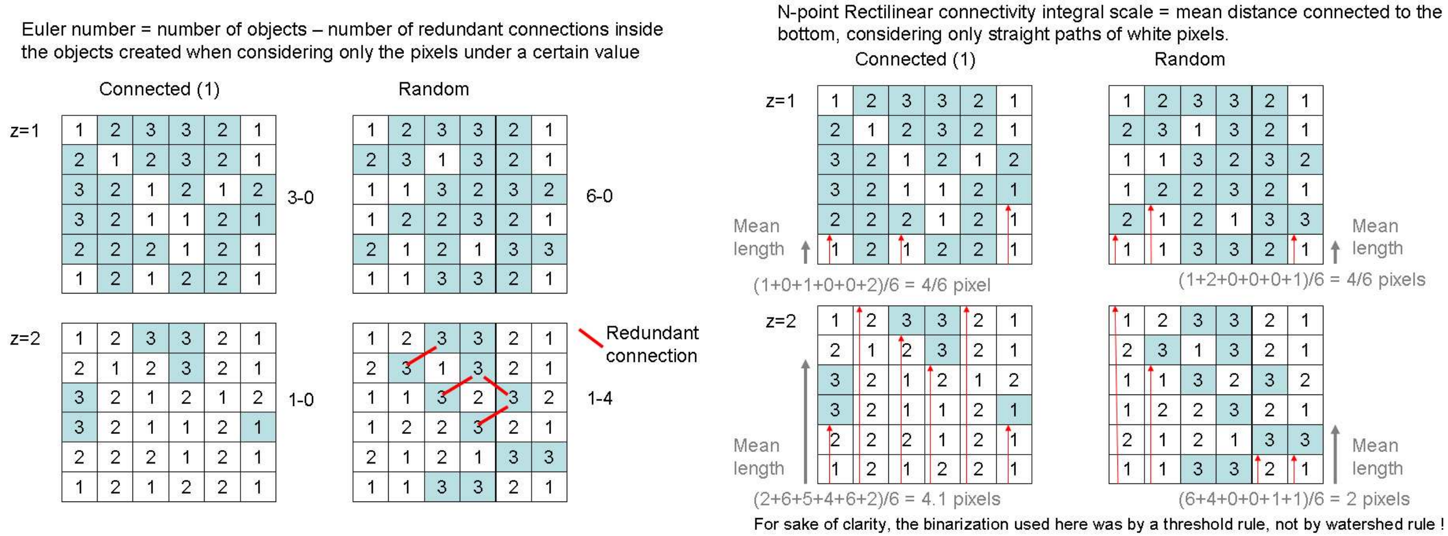

(a) (b)

Figure 5.2: Example of structural connectivity indicator computation.

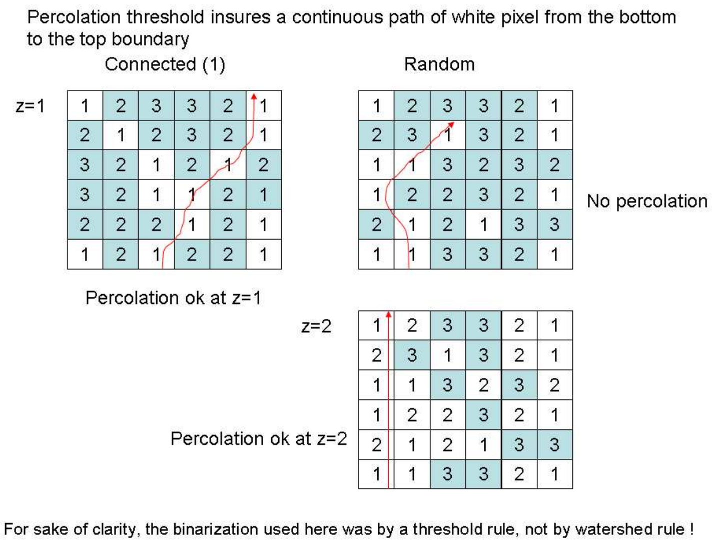

(a)

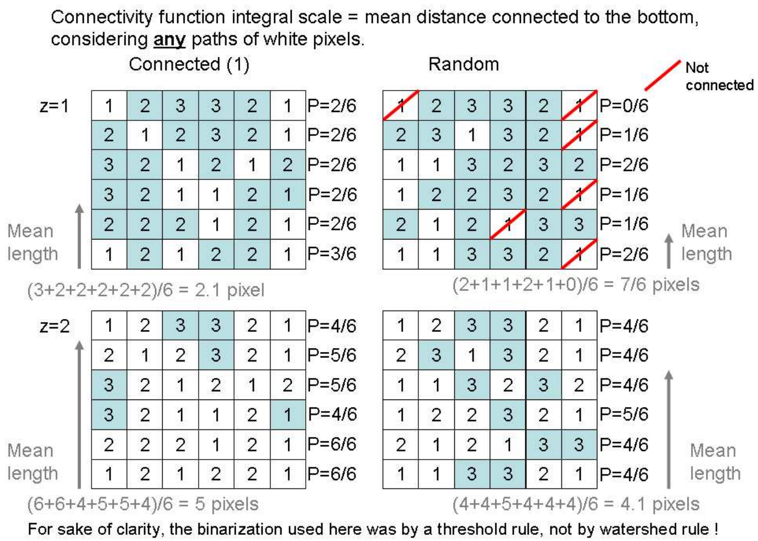

(b)

Figure 5.3: Example of structural connectivity indicator computation.

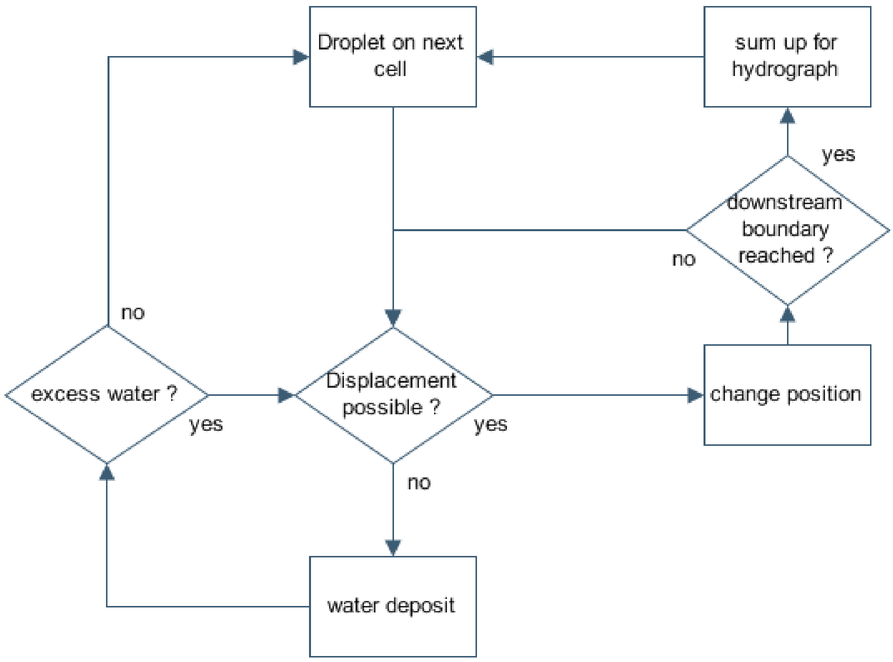

Figure 5.4: Flowchart of the filling algorithm to compute the simplified hydrograph.

These simplified hydrographs can be scaled when we express the runoff coefficient C (instantaneous outflow / instantaneous inflow) as a function of the cumulative inflow [m^3]. Since no infiltration and transfer time were considered in the model, and since the rain is uniform, C is equivalent to the ratio of area connected to the downstream boundary to the total surface of the topographical field [m^2/m^2]. The runoff coefficient C will vary between 0 and 1 when the full surface will be connected to the outflow boundary. The area under the curve C as a function of the cumulative inflow is equal to the total volume of runoff [m^3] (Fig. 5.5a). The area between 1 and the curve C as a function of the cumulative inflow corresponds to the actual depression storage [m^3]. We can thus express the ratio of surface connected to total surface as a function of the water stored in the depressions of the field (Fig. 5.5b). We will call this indicator the RSC function. It describes the dynamical effect of the depression storage and it may serve as an indicator for surface functional connectivity.

Table 5.1 shows the comparison between the physical overland flow model presented in Chapter 4 and the filling algorithm explained here. The physical overland flow model can determine the effect of the micro-topography on the surface detention, which depends on the runoff velocity (and thus on the rainfall intensity). It implies the use of a CFL condition that imposes small time steps for our scale of investigation. The requirement of small time steps on top of the iterative computation of the friction factor causes long computation time. In the context of establishing a fast and robust method to determine an indicator of functional connectivity, this long computation time would be a severe constraint. As the filling algorithm is more than 1000 times faster than the runoff model, due to the simplification of the runoff routing, it will be used to produce the functional connectivity indicator.

5.3.3 Case study: numerical fields

Some of the potential indicators of connectivity described in the previous sections require a complete knowledge of the micro-topography. Therefore our study is based on numerical experiments, which meet more easily this requirement. To evaluate the potential of the different indicators, we investigated their discriminative capacity on the extreme micro-topographies described in Chapter 4. Every type of micro-topography (River, Random and Crater) have been replicated 10 times to have an idea of the dispersion of the indicators inside of a micro-topographical type.

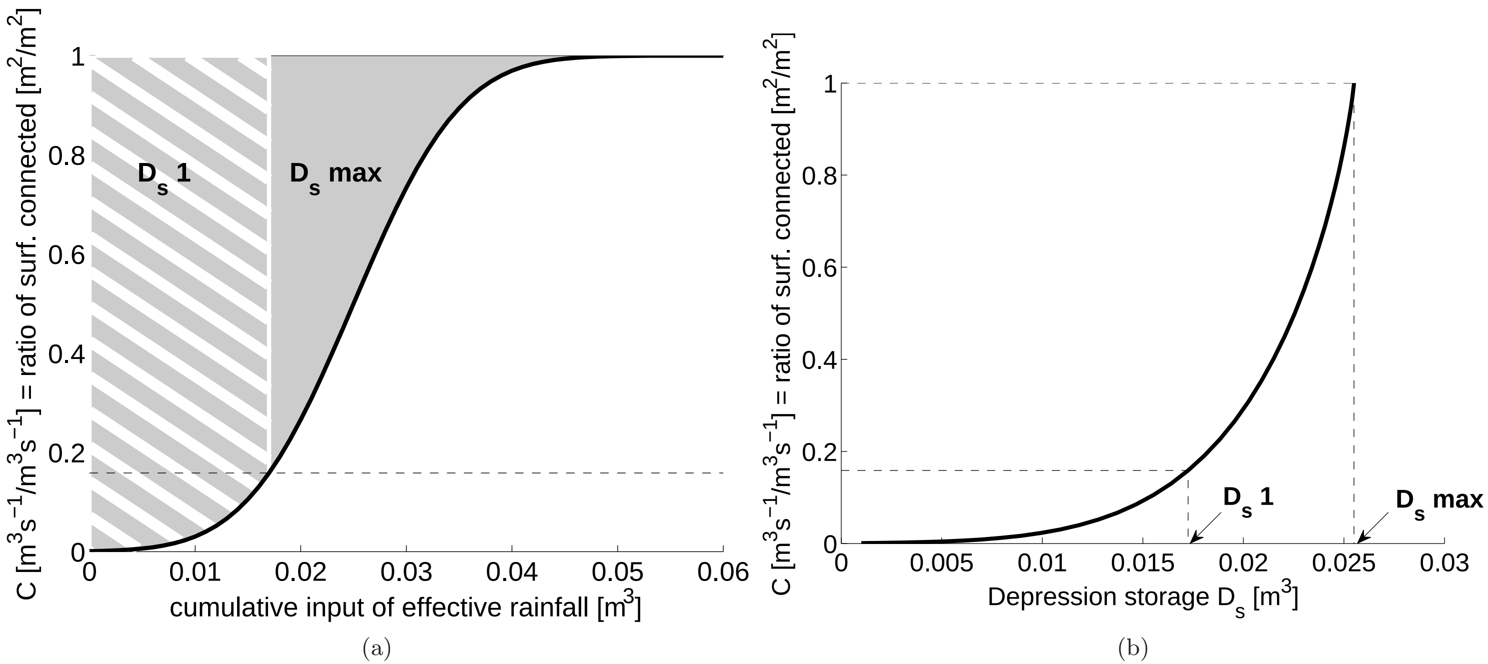

Figure 5.5: Simplified hydrograph (a) and the derived Relative Surface Connection (RSC) function (b).

Table 5.1: Comparison of the physical overland flow model (Chap. 4) and the filling algorithm.

Physical Runoff Model	Filling Algorithm
Input	**Input**
Topography $z(x, y)$	Topography $z(x, y)$
Rainfall intensity ϕ	
Roughness parameters k_s, C_L	
Kinematic viscosity of the water ϑ	
Output	**Output**
Runoff coefficient $C(t)$	Simplified runoff coefficient C(cumulated inflow)
Water depth field $h(x, y, t)$	Water depth field $h(x, y,$cumulated inflow)
Velocity fields $\bar{v}_x(x, y, t)$, $\bar{v}_y(x, y, t)$	
Processes	**Processes**
Flow following the slope of water	Flow following the slope of water
Multiple flow, de-centered (staggered) 4-neighbor scheme	Simple flow, 8-neighbor scheme
Velocity based on Darcy-Weisbach formula	Infinite velocity, water reaches directly the lowest point it can get to
Surface detention and depression storage	Depression storage
Time steps	**Time steps**
depending on CFL condition ($\bar{\Delta t} \approx 0.001$ s)	Fixed ($\Delta t = 1$ s)
Time of computation	**Time of computation**
computation time / simulation time = 300	computation time / simulation time = 0.3

5.4 Results

5.4.1 Robustness of the structural connectivity indicators

The robustness of the structural connectivity indicators was tested by computing these indicators for ten realizations of each of the three types of micro-topography and assessing the variability within and in-between the 3 types of micro-topography. We consider as relevant the connectivity indicators that are able to discriminate among the three micro-topography types.

The computations of the semivariograms, the bivariate entropy and the n-point rectilinear connectivity do not require a full knowledge of the micro-topography. Since they are statistical properties, semivariogram and entropy may be established on only a reduced sample of the micro-topography, as long as the resolution is sufficiently smaller than the correlation length and the domain investigated at least twice as large as this length. The n-point rectilinear connectivity only requires knowledge of a 1-D micro-topographical profile in the mean slope direction. For practical assessment in the field, this can easily be achieved with a classical roughness meter (Guillobez and Arnaud, 1998). Therefore, these three indicators present some practical advantages. However, as we see in Figure 5.6, the three methods do not sufficiently discriminate between the three micro-topography types. These indicators are therefore not considered as relevant structural connectivity indicators.

The other structural connectivity indicators (connectivity function, Euler number and percolation probability) require the full knowledge of the micro-topography (which in practice requires more sophisticated tools such as laser technique), because their computation takes into account all the possible connections in 2-D. Figure 5.7 presents these structural connectivity indicators. For all three indicators, the River scenarios tend to increase more rapidly as the threshold level z is increased, followed by the intermediate cases (Random) and finally by the Crater micro-topographies. The visual inspection of these three last indicators shows their discriminative capacity.

5.4.2 Robustness of the functional connectivity indicator

Figure 5.8 (a) shows the results for the simplified hydrographs. There is a clear distinction between micro-topography types. For the Crater micro-topography, a larger input of water is necessary before outflow equals inflow. Since no infiltration was taken into account, the water added to the system that did not produce runoff was stored in local depressions and represents the actual depression storage. After a suf-

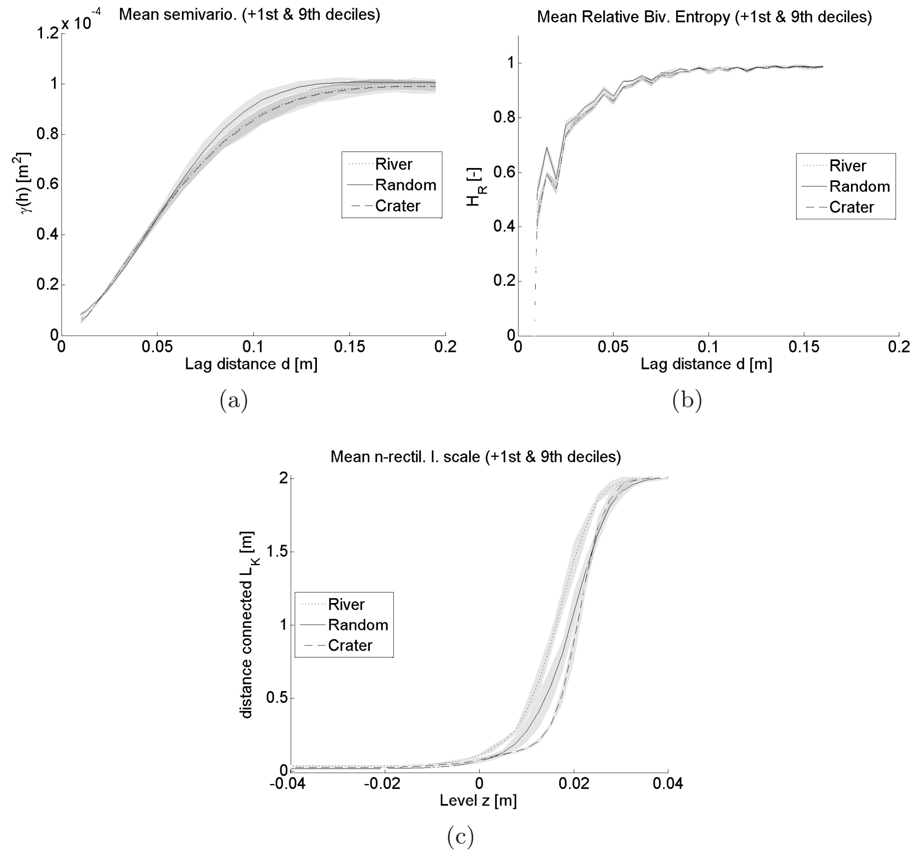

Figure 5.6: Semivariograms (a), relative bivariate entropy (b) and n-point rectilinear connectivity integral scale (c) calculated for ten realizations of each of the Crater, Random and River-type micro-topographies. The mean values are given for each micro-topography type as well as the envelop limited by the 1st and 9th deciles.

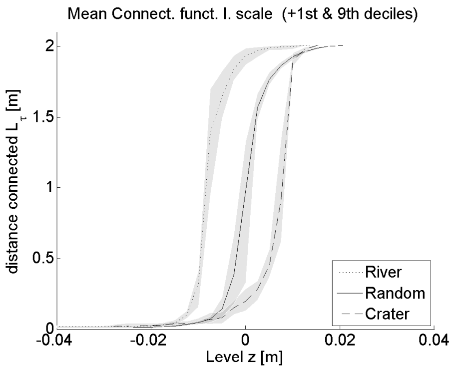

(a)

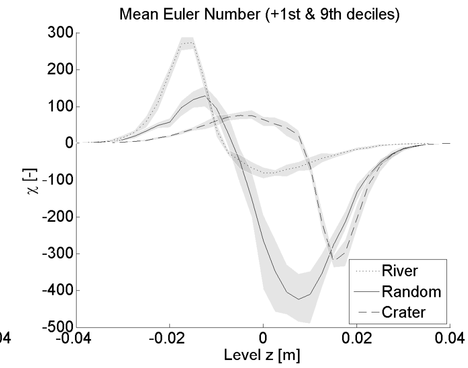

(b)

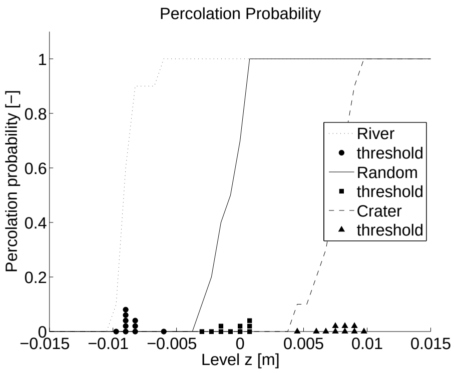

(c)

Figure 5.7: Connectivity function integral scale (a), Euler number (b) and Percolation thresholds (c) with the derived Percolation probability curve, calculated for 10 realizations of each of the 3 micro-topographical types: River, Random and Crater. The mean values are given for each micro-topography type as well as the envelop limited by the 1st and 9th deciles.

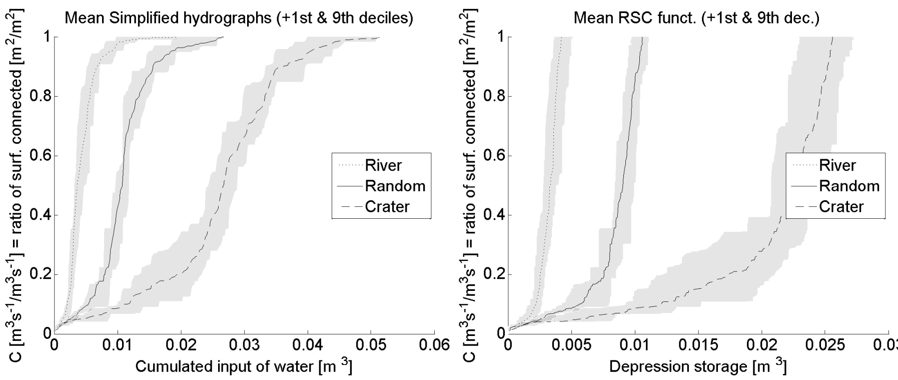

(a) (b)

Figure 5.8: Simplified hydrographs (a) and derived relative surface connection functions (b). The mean values (number of replicates = 10) are given for each micro-topography type as well as the envelop limited by the 1st and 9th deciles.

ficient cumulative input of water, this area does not increase anymore. At that stage, all the potential depression storage has been fully filled and corresponds to the maximal depression storage. It can be regarded as the volume to full breakthrough.

Based on the scaled hydrographs, we can derive the relative surface connection function. This is shown in Figure 5.8 (b). It clearly shows that maximal depression storage is higher for the Crater micro-topography than for the River micro-topography, in ratio more than 4 to 1. Secondly, we clearly see that depression storage does not have to be entirely filled before significant runoff is produced. As already shown by Moore and Larson (1979), storage and runoff amounts increase continuously as water accumulates in micro-depressions, but the percentage of area contributing to runoff increases by steps. However, a widely-used simplification made in hydrological modeling is that no runoff can occur before the maximum depression storage is reached (Singh, 1995; Singh and Frevert, 2002), and so there is no contributing area until depression storage is fully field.

5.5 Discussion

Table 5.2 summarizes the indicators for structural and functional connectivity investigated in this study.

Table 5.2: Summary of the structural and functional connectivity indicators investigated in this Chapter.

Connectivity Indicator	Connectivity Type	Information Requirement	Binarization Procedure	Discriminant ?
(1) Semivariogram	structural	sampling points	none	no
(2) Relative Bivariate Entropy	structural	sampling points	none	no
(3) n-Point Rectilinear Connectivity	structural	transect information	by watershed rules	no
(4) Connectivity Function Integral Scale	structural	full knowledge	by watershed rules	yes
(5) Euler Number	structural	full knowledge	threshold based	yes
(6) Percolation Thresholds	structural	full knowledge	by watershed rules	yes
(7) Relative Surface Connection Function	functional	full knowledge	none	yes

5.5.1 Robustness of the structural connectivity indicators: success and failures

Semivariograms were not able to distinguish the different micro-topography types because the scenarios were built with a method that was specifically conceived to preserve the semivariogram shape. All fields have a similar distribution thanks to the back-transformation given in equation 4.3 of Chapter 4. Despite the fact that this transformation is non-linear, Zinn and Harvey (2003) showed that the covariance between points separated by a lag distance was little affected if a scale factor was considered to preserve the integral scale of the correlation coefficient. The semivariograms are rectilinear in that they do not take into account the curvilinearity of the structures (Krishnan and Journel, 2003) and so they are not appropriate to capture connectivity. This confirms the results of Western *et al.* (2001) and Grayson *et al.* (2002).

Relative bivariate entropy depends directly on the bivariate PDF. For two random variables $\zeta \sim N(\mu, \sigma)$ and $\zeta' \sim N(\mu', \sigma')$ both normally distributed, their bivariate PDF is expressed by:

$$f_h\left(\zeta, \zeta'\right) = \frac{1}{2\pi\sigma\sigma'\sqrt{1-\rho^2}} \exp\left[-\frac{1}{2\left(1-\rho^2\right)}\left(\left(\frac{\zeta-\mu}{\sigma}\right)^2 - \frac{2\rho\left(\zeta-\mu\right)\left(\zeta'-\mu'\right)}{\sigma\sigma'} + \left(\frac{\zeta'-\mu'}{\sigma'}\right)^2\right)\right] \tag{5.12}$$

where μ and μ' are the means, σ and σ' are the standard deviations and ρ is the correlation coefficient defined by:

$$\rho_{\zeta\zeta'} = \frac{Cov\left[\zeta, \zeta'\right]}{\sqrt{Var\left[\zeta\right] Var\left[\zeta'\right]}} \tag{5.13}$$

By keeping μ, μ', σ, σ' and ρ constant between the different scenarios, we leave the bivariate PDF unchanged. If ζ represents the variable values at the locations $\mathbf{x}$ and ζ' at the location $\mathbf{x}+\mathbf{d}$, because of the stationarity of order 1 and 2 of the Gaussian fields, we know that $\mu = \mu'$, $\sigma = \sigma'$. Moreover, thanks to the renormalization procedure (Equation 4.3), μ and σ keep the same values whatever the fields. $\rho_{\zeta\zeta'}$ can be directly determined from the semivariograms, since by stationarity of order 2:

$$\gamma\left(\mathbf{d}\right) = \sigma^2 - Cov\left[\mathbf{x}, \mathbf{x}+\mathbf{d}\right] \tag{5.14}$$

If the semivariograms $\gamma\left(\mathbf{d}\right)$ are similar, for a fixed lag distance $\mathbf{d}$, the covariance and thus the correlation coefficient will also be similar. All factors of the bivariate PDF are kept constant whatever the scenarios and leave the entropy unchanged. Therefore, entropy, like the semivariograms, can not distinguish between the three micro-topography types.

N-direct connectivity does not take into account the curvilinearity of the structures (Krishnan and Journel, 2003). Any obstacle in the way of the flow would be considered as a definitive stop, although in reality water could flow around that obstacle. Some linear connected features in the axis of the mean slope are still captured. This explains why the indicator could slightly discriminate between the three topographic types (curves are juxtaposed next to each other in function of the type). However, as there is some overlap between curves of different micro-topographical types, this indicator was considered insufficiently robust.

The connectivity function integral scale represents an equivalent mean distance from the outlet up to which the surface is connected. Its value is between 0 up to the maximal distance of the field (in our case 2 meters). This function, which is the equivalent of the n-direct connectivity function but takes into account the possibility of the runoff to flow in 2 dimensions around the obstacles, improves a lot the discrimination between the three micro-topography types. The main assumption, due to the choice of binarization process, is that the water in all the depressions is at the same absolute level, which is not valid in practice since depressions have different storage volumes and drainage areas. Moreover, the outlet is considered as a depression that fills in. The result is an over-estimation of the mean water level in the system to ensure the full connection of the surface. Nevertheless this gives us already a rough estimation of the relation between the depression storage and the surface connectivity if we transform the level into a depression storage.

$$D_s = S \int_{-\infty}^{z} P\left(Z \leq z\right) \partial z \qquad (5.15)$$

where D_s is the depression storage [m^3] and S is the surface of the field [m^2].

Take note that since all three micro-topography types have the same distribution, $P\left(Z \leq z\right)$ will be equivalent for them whatever z. So the relation between the surface storage and the z-level will be the same for the different cases.

Percolation probability is a cumulative density function (CDF) and requires all the 10 scenarios to calculate it. All the threshold values (presented as geometric symbols in Figure 5.7 (bottom left) are well grouped as a function of the micro-topography types. Hence, this indicator is capable of discriminating the topography type. It is a measure of the continuity between the upstream and downstream ends of the topographical fields, yet it provides no information on how the continuity of the water field evolves as the water level is raised. This type of indicator is therefore of no use to characterize the within-field connectivity, but it may be of use to characterize the connectivity between adjacent fields. Indeed, water produced upstream on a slope will only join the downstream drainage network if all the patches that it needs to cross are all at least at the percolation threshold. Hence those values could be useful for subsequent upscaling of the runoff process, but this falls beyond the scope of this thesis. The percolation thresholds reported here are not in adequacy with standard percolation theory, since in our case pixels are in the field of interest according to watershed rules and not according to a certain level of probability of occurrence equally distributed over the entire field, as in percolation theory.

Euler number χ presents some discriminative properties. The curves for all the fields present a similar shape that is due to a same behavior: as the threshold level z is increased, more and more pixels are in the field of interest due to the binarization procedure. Those pixels are, in the beginning, often isolated from each others (N increases) and we find few connections (G is comparatively low). This increases the Euler number ($\chi = N - G$). After a certain threshold level (z_a), the previously isolated patches tend to connect to each other progressively. The Euler number begins to decrease as the number of multiple connections (G) increases between the patches. Rising again the threshold level z, particular patches begin to merge (N decreases), which erases their previous multiple interconnections (G decreases faster than N). This increases again the Euler number. We see that z_a is lower for the River micro-topography for which depressions quickly connect to each other as opposed to the Crater micro-topography. We also see that z_a is not so different between River and Random micro-topographies. But the χ-value reached by the former one is lower than for the latter. This means that the Random cases are more chaotic as the number of interconnections explodes (but thus are less strong) whereas the River cases keep relatively few but stable connections. As we see, the change in Euler number with increasing water level contains information on the dynamics of pond formation.

5.5.2 Robustness of the functional connectivity indicator: success and development

Simplified hydrographs and especially the derived relative surface connection functions were clearly able to discriminate the three micro-topography types. River structures improve the evacuation of the water and reduce the depression storage, whereas Crater structures favor the storage of water in depressions. Simplified hydrographs are shifted to the right as maximum depression storage increases.

A theoretical framework is proposed (see Figure 5.9) to correlate the local depression storage distribution to the simplified hydrographs and to the relative surface connection. The four conceptual multiple-compartment topographies have the same maximum depression storage but the intrinsic distribution of the depression storage differs. The first case (a) is an on/off type of surface. All the local depressions of the field have equivalent storage capacity (i.e., the ratio between particular depressions volumes and their respective contributing areas are constant). Thus the actual depression storage will have to reach the maximum depression storage value before runoff occurs. As outlined before, it is a widely-used simplification made in hydrological modeling. The second case (b) is a surface whose local storage values are distributed uniformly. A droplet of rain therefore has the same probability of filling a small depression, than a medium or a large one. It will produce a linear simplified hydrograph. For the third case (c), local storage values follow a Gaussian distribution. The simplified hydrograph has a sigmoid form. The last case (d) accounts for a surface whose relative surface connection function evolves linearly with the filling of the depression storage. It corresponds to the case $k = \frac{1}{D_{s\,\max}}$ for the Linsley *et al.* (1949) equation of the depression storage filling:

$$D_s = D_{s\,\max}\left(1 - \exp\left(-kQ_{inC}\right)\right) \tag{5.16}$$

where D_s is the surface storage value [m^3], $D_{s\,\max}$ is the maximal surface storage [m^3], k is a constant [m^{-3}] and Q_{inC} is the cumulated input of effective rain [m^3].

We established the mathematical expressions for the simplified hydrographs and the relative surface connection functions (Tables 5.3 and 5.4). Those simple models are parametrized by few parameters (1 or 2): the maximal depression storage only (a, b, d) or the maximal depression storage and a shape factor (c). A combination of the (a) case with the three others (b, c, d) is easily implemented by subtracting an initial value to the cumulative rainfall and to the actual depression storage (e.g., LISEM v 1.63 and earlier is a combination of (a) and (d) [2]). In terms of functional connectivity, the quicker the curve of surface connection rises, the more reactive the surface is to rain input. The (d) case reacts like that. An extreme case would be the existence of one deep

[2]`http://www.itc.nl/lisem/index.html`

depression that would account for most of the total depression storage, but that would only be fed by a small part of the total surface. In that case, even if the actual depression storage would be low, most of the surface would be well connected and would participate to the export of runoff. Connectivity thus increases passing from the (a) to (c), (b) and (d) conceptual fields (except for relative storage close to 1.).

We can now chose either to work with the true simplified hydrographs and derived relative surface connection functions or to parameterize them with one (or a combination) of the simplified models (a, b, c, d). This last option may be useful for later upscaling procedure or for regular implementation in actual hydrological models (see Chap. 7). Our observations were best fitted with the gaussian model (c). Results are shown in Figure 5.10. The factor μ_{BC} (from Tables 5.3 and 5.4) is almost equivalent to the maximum depression storage and we have imposed this value. The factor σ is a formal factor that accounts for the spread of the simplified hydrographs. The lower its value the sharper the hydrograph. When σ tends to zero, then case (c) tends to case (a) with a step hydrograph. On the contrary, the larger the sigma, the higher the potential connectivity is. We compare the dispersion of the fitted parameters in Figure (5.11). The μ and σ factors are distinct between the micro-topography types, but the coefficient of variations are alike for all the micro-topographies meaning that the distribution of local depression storage compartments are comparatively similar. This means that if the pixel height values of a River-type micro-topographical field were all multiplied by a unique scaling factor, the new field may produce a similar hydrograph as the one for a Crater-type field. This may come from the method used to build the different micro-topographical fields.

5.5.3 The scale problem

The spatial resolution of the digital elevation model for the micro-topography is crucial for the computation of its connectivity properties. The key elements are the small channels that link the depressions together. Those can be missed if the spatial resolution is too low. As stated by Western *et al.* (2001), the apparent presence of near connectedness is scale dependent. The evaluation of the retention capacity of the depressions is also dependent on the resolution. Real concavities or convexities between the points of measurement can be missed by the interpolation methods, resulting in an underestimation or an overestimation of the depression volume, respectively. In summary, the resolution plays an important role both in terms of identification of connections and evaluation of depression storage

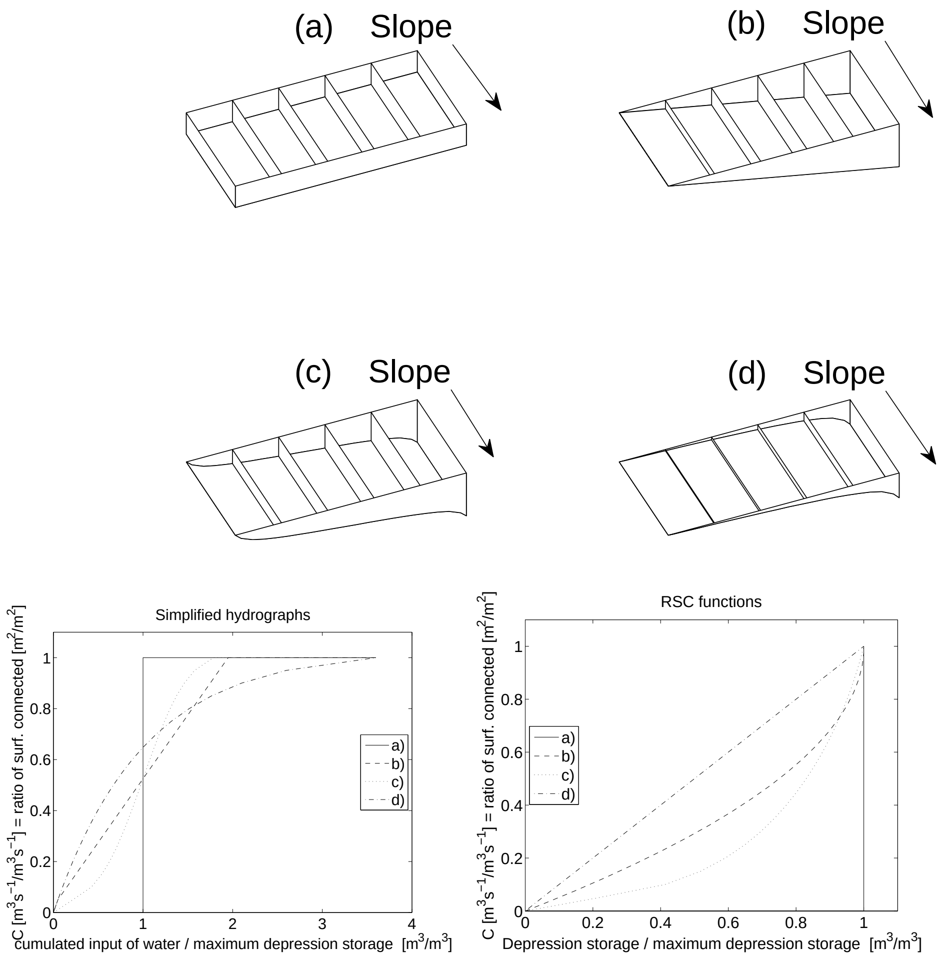

Figure 5.9: Conceptual multiple-compartment topographies, their simplified hydrographs and their derived relative surface connection (RSC) functions. The local storage depths are distributed according to: a) a single value, b) a uniform distribution, c) a Gaussian distribution, and d) a particular distribution so that the relative surface connection function is linear.

Table 5.3: Mathematical expressions of the simplified hydrographs presented in Figure (5.9) for the different conceptual multiple-compartment topographies.

Depression Storage Distribution	Simplified Hydrograph $C = \frac{Q_{out}}{Q_{in}} = \mathrm{f}\left(Q_{inC}\right)$
(a) Single value	$\mathrm{f}\left(Q_{inC}; D_{s\,\max}\right) = \begin{cases} 0 & \text{if } Q_{inC} < D_{s\,\max} \\ 1 & \text{else} \end{cases}$
(b) Uniform	$\mathrm{f}\left(Q_{inC}; D_{s\,\max}\right) = \begin{cases} \frac{Q_{inC}}{2D_{s\,\max}} & \text{if } Q_{inC} < 2D_{s\,\max} \\ 1 & \text{else} \end{cases}$
(c) Gaussian	$\mathrm{f}\left(Q_{inC}; \mu \approx D_{s\,\max}, \sigma\right) = \frac{1}{2}\left(1 + \mathrm{erf}\left(\frac{Q_{inC} - \mu}{\sigma\sqrt{2}}\right)\right)$
(d) Specific so that $C \propto D_s$	$\mathrm{f}\left(Q_{inC}; D_{s\,\max}\right) = -\exp\left(-\frac{Q_{inC}}{D_{s\,\max}}\right) + 1$

with Q_{out} the runoff [m^3/s], Q_{in} the input of rain [m^3/s], Q_{inC} the cumulated input of rain [m^3], D_s the actual depression storage [m^3], $D_{s\,\max}$ the maximal depression storage [m^3], μ a factor approximatively equal to $D_{s\,\max}$ [m^3] and σ a factor of dispersion [m^3].

Table 5.4: Mathematical expressions of the relative surface connection functions presented in Figure (5.9) for the different conceptual multiple-compartment topographies.

Depression Storage Distribution	Relative Surface Connection Function $C = \frac{S_{connected}}{S_{tot}} = \mathrm{g}\left(D_s\right)$
(a) Single value	$\mathrm{g}\left(D_s; D_{s\,\max}\right) = \begin{cases} 0 & \text{if } D_s < D_{s\,\max} \\ 1 & \text{if } D_s = D_{s\,\max} \end{cases}$
(b) Uniform	$\mathrm{g}\left(D_s; D_{s\,\max}\right) = 1 - \sqrt{1 - \frac{D_s}{D_{s\,\max}}}$
(c) Gaussian	$\mathrm{g}\left(D_s; \mu \approx D_{s\,\max}, \sigma\right) = \frac{1}{2}\left(1 + \mathrm{erf}\left(\frac{Q_{inC}(D_s) - \mu}{\sigma\sqrt{2}}\right)\right)$ where $D_s(Q_{inC}) = \mathrm{h}\left(Q_{inC}; \alpha = \frac{1}{\sigma\sqrt{2}}, \beta = \frac{-\mu}{\sigma\sqrt{2}} \approx \frac{-D_{s\,\max}}{\sigma\sqrt{2}}\right)$ $= \frac{1}{2}\left(Q_{inC} + \mu - \frac{\beta \mathrm{erf}(\delta)}{\alpha} - Q_{inC}\mathrm{erf}\left(\delta\right) - \frac{\exp\left(-(\delta)^2\right)}{\alpha\sqrt{\pi}}\right)$ with $\delta = \beta + \alpha Q_{inC}$
(d) Specific so that $C \propto D_s$	$\mathrm{g}\left(D_s; D_{s\,\max}\right) = \frac{D_s}{D_{s\,\max}}$

$S_{connected}$ the surface connected to the downstream boundary [m^2], S_{tot} the total surface [m^2], D_s the actual depression storage [m^3], $D_{s\,\max}$ the maximal depression storage [m^3], μ a factor approximatively equal to $D_{s\,\max}$ [m^3], σ a factor of dispersion [m^3] and Q_{inC} the cumulated input of rain [m^3].

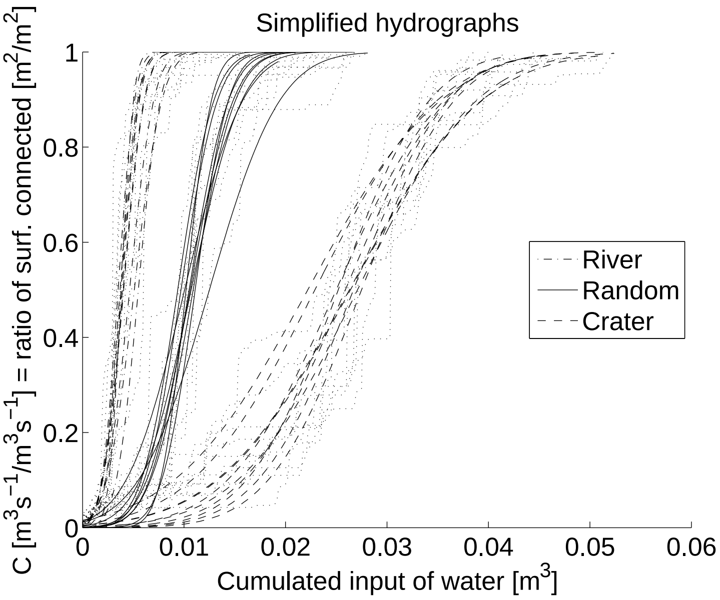

(a)

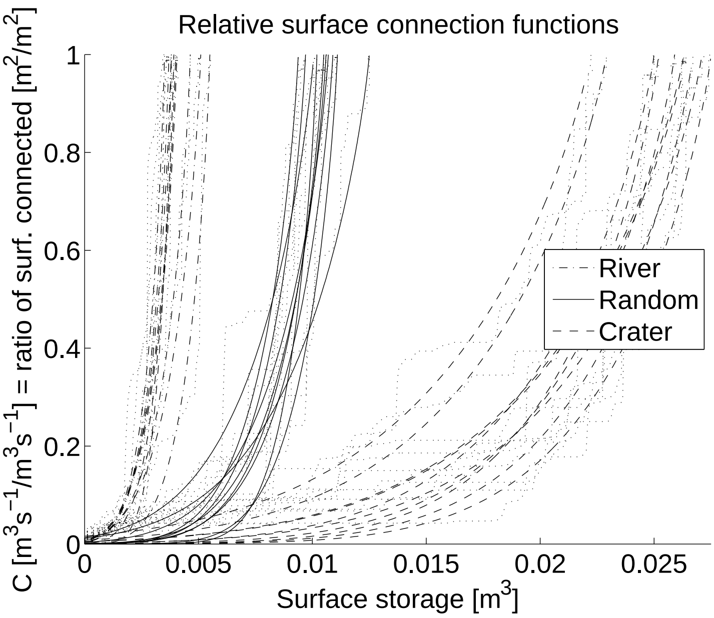

(b)

Figure 5.10: Fitted simplified hydrographs (left) and derived fitted relative surface connection functions (right). Gaussian model (c) was used for the fitting. The gray dotted lines are the fitted curves.

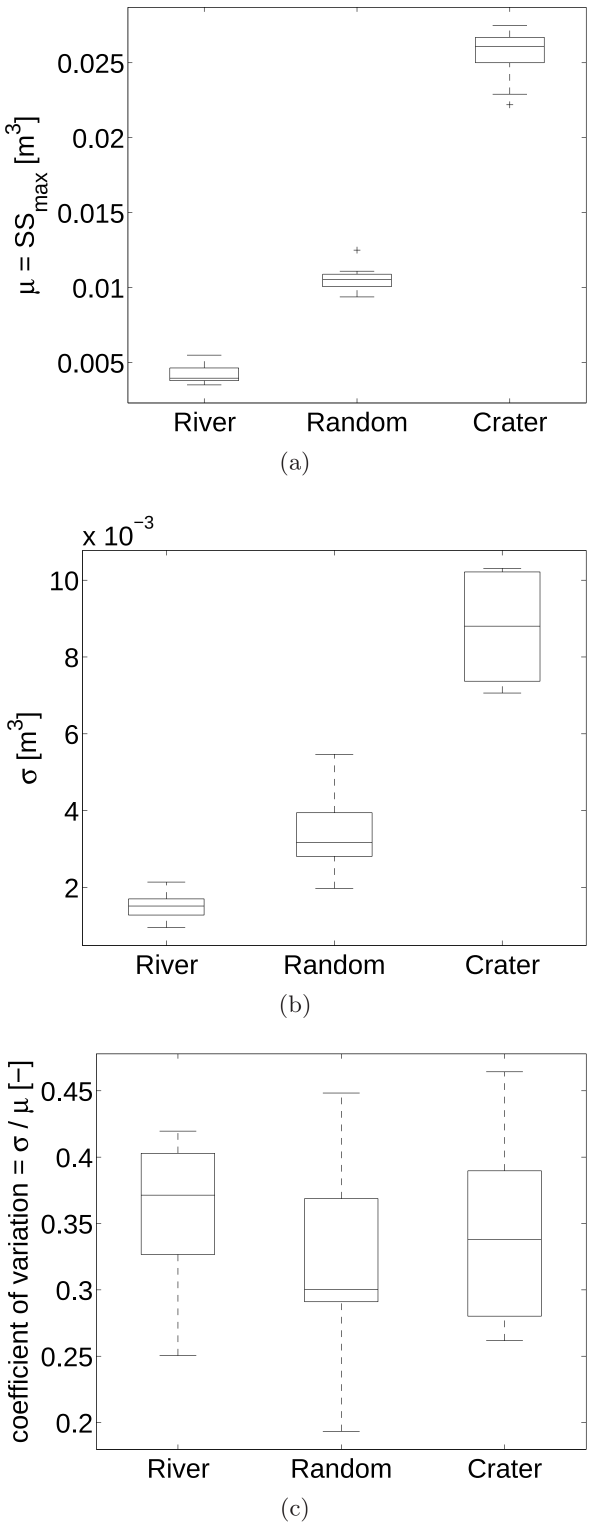

Figure 5.11: Box plots of the fitted μ or maximum surface storage (a), the fitted σ (b) and the coefficients of variation (c) for the 3 contrasted micro-topographies. Gaussian model (c) was used for the fitting.

Carvajal *et al.* (2006) and Martin *et al.* (2008) both observed a decrease of maximal depression storage when pixel size increased (from a mm to a 2 cm scale resolution for the first study, and from the centimeter to a half meter scale for the second). On the contrary, Abedini *et al.* (2006) observed an increase occasionally followed by a decrease of the ponds volume when pixel size increased from 5 mm to 3 cm. Kamphorst *et al.* (2000) did not observe a significant change in maximum depression storage when passing from a mm to a 2 cm scale resolution. The effect of the resolution is thus not obvious and the strategy is to adapt the resolution in function of the correlation lengths of the field and the size of the connectors.

As long as the field is sufficiently larger than the correlation length, Semivariogram and Bivariate Entropy are not dependent on the scale if stationarity of order 1 and 2 can be assumed (which is true at least for Gaussian fields). Similarly, the Euler Number for a random binary field is independent of the scale. This would also be the case for the percolation threshold if the binary field was random. But the fact that we consider a watershed rule in this particular binarization process does not fulfill that condition anymore. In addition, boundary effects affect more the results when the size of the field decreases, which increases the uncertainty on the percolation threshold value. Finally, the N-point rectilinear connectivity integral scale and the connectivity function integral scale both provide results in length unit and inform on the mean distance over which pixels are connected. Therefore, those functions include already the scale in their results.

5.6 Conclusions

- The semivariogram, the bivariate entropy and the n-point rectilinear connectivity are structural connectivity indicators that were not able to discriminate clearly among the contrasted micro-topographies. Therefore we think that those methods must not be used to study the structural connectivity of natural micro-topographies unless they are improved to integrate spatial patterns.

- The connectivity function integral scale, the percolation probability and the Euler number are structural connectivity indicators that had a discriminative capacity. Whereas the connectivity function integral scale and Euler number provide information regarding the development of connectivity within micro-topographical fields, the percolation threshold appears more suitable to characterize connectivity between adjacent fields. In any case, despite their discriminating power, relating the latter three structural connectivity indicators to the hydrological response of a topographical surface will prove to be a challenging task.

- We proposed a functional connectivity indicator, namely the relative surface connection function, that is the ratio of surface connected as a function of the actual depression storage. It was computed using a fast and simple filling algorithm that produces simplified hydrographs based only on the depression storage dynamics. The simulation in Chapter 4 had indeed shown that the depression storage was the major factor of discrepancies between our contrasted scenarios. This indicator was discriminant and could be used to conceptualize the process of depression filling. Once computed for a small surface, this function could become a descriptive function of the subgrid dynamics to be integrated in hillslope or watershed models for which the surface considered for the computation of the connectivity indicator corresponds to a single grid cell. We recommend this indicator as it requires the same information than the discriminant structural indicators, it is almost as fast to compute, but it contains information more directly linkable to runoff dynamics.

- At this stage, the proposed functional connectivity indicator does not take into account the upper boundary conditions, i.e., the effect of rainfall intensity, nor the surface detention dynamics. This effect should be integrated in an effective way to correct the present functional connectivity indicator (see Chap. 7). Finally, the successful indicators are now to be applied on real field data, which will be done in Chapter 6.

Chapter 6

Connectivity evolution[1]

s

6.1 Outline

We evaluated the ability of different connectivity indicators to capture temporal change in soil micro-topographical properties. Our study was based on 9 scanned reproductions of soil surface micro-topographies which had been subjected to different amounts of cumulative rainfall erosivity. Among the different connectivity indicators, only the RSC function was able to detect an evolution in micro-topographical properties. The RSC function provides the ratio of area that is contributive as a function of depression storage filling. One major parameter of the RSC function is the maximum depression storage. A methodology was therefore proposed to build numerical micro-topographies, taking into account the depression storage evolution on top of the slope, the random roughness and the spatial correlation. It allowed to produce numerical micro-topographies showing realistic RSC functions, which could be useful for later stochastic modeling. With that method, the user choose a gap factor Δ that modifies the spatial configuration of micro-topography, which affects the maximum depression storage value.

6.2 Introduction

It has been demonstrated, based on a numerical study in Chapter 4, that micro-topographies presenting near-identical macroscopic proper-

[1]Adapted from: *Connectivity evolution of microtopography: measurement for a bare loamy plot and reproduction in a numerical field generator*, Advances in Water Resources, article to be submitted

ties (such as slope, random roughness and semivariogram) may show very contrasted hydrological behaviors, which we attributed to differences in connectivity properties not captured by classical macroscopic properties.

In Chapter 5, it was demonstrated that only 3 indicators of connectivity taken in the literature allow to discriminate between contrasted micro-topographies. Those are indicators of structural connectivity, and are difficult to integrate into current hydrological models. An other indicator of connectivity, functional this time, was therefore proposed and appeared relevant.

Under the combined action of rain and runoff, we know that the surface of cultivated plot evolves (Chap. 3). Depression storage and the effective friction factor decrease as a function of cumulative rainfall erosivity. Random roughness is relatively less sensitive, at least in the early times (Fig. 3.2). We can think that this evolution impacts also on the spatial distribution of surface fluxes, and thus on connectivity.

Therefore, the first objective is to assess if the evolution of the soil micro-topography leads to an evolution of functional connectivity. The second objective is to assess if this evolution leads to an evolution of structural connectivity.

The numerical micro-topographies we used in Chapter 4 accounted for 2 extreme types of scenarios (River and Crater) we associated arbitrarily to the initial and final states of micro-topography of a tilled soil exposed to rain. But we should be able to produce intermediary scenarios if we want to better fit reality and to reflect the connectivity evolution of the soil micro-topography between the Crater and the River states. Therefore our last objective is to present a methodology to generate numerical micro-topographies conditioned by the functional connectivity, in addition to classical macroscopic properties, which are the slope, the random roughness and the semivariogram.

6.3 Materials and Methods

6.3.1 Connectivity indicators evolution

The digital elevation models (DEM) of the 9[2] casts described in Chapter 3 were used for calculating the RSC functional connectivity indicator

[2]The 10th cast (R≈677) was not considered in this chapter as it corresponds to another plot submitted to another tillage work. Therefore the patterns of micro-topography found on the 10th cast are not the evolution of the patterns of micro-topography observed on the main experimental plot where the 9 first molds were sampled.

and the following 3 structural connectivity indicators: connectivity function integral scale, Euler number and Percolation thresholds. These indicators were described in Chapter 5 and were found capable of discriminating between contrasted numerically-generated micro-topographies. The 9 molds cover a range of surface roughnesses, starting from a tilled soil and ending with a severely eroded surface corresponding to 230 $MJ.ha^{-1}.mm.h^{-1}$ of cumulative rainfall kinetic energy (R). The molds represented 0.5 m^2 of soil micro-topography and were sampled at 4 different levels of R: 0 (2 repetitions), 45 (2 repetitions), 115 (3 repetitions) and 230 (2 repetitions). Their digital elevation models are shown in Appendix A.

6.3.2 Numerical micro-topography generator

Contrasted numerical fields of micro-topography can be generated based on the method proposed successively by Vogel (2002) and by Zinn and Harvey (2003). This method, explained in detail in Chapter 4, enabled to generate 3 types of micro-topographical fields that present contrasted structural and functional connectivity properties while showing identical random roughness values as well as near-identical isotropic spatial covariances. The three types of numerical fields are: (1) a field with connected patterns of depressions (River), (2) a standard multi-Gaussian field (Random) and (3) a field with connected patterns of crests that isolate from each others the depressions (Crater).

Just after tillage, depressions are mainly isolated from each other and form Crater-type topographies (Moreno *et al.*, 2008; Carvajal *et al.*, 2006). After some time, rainfall and overland flow will reshape the micro-topography, flattening clods, filling depressions and digging small channels at the soil surface (Favis-Mortlock, 1998; Darboux *et al.*, 2002; Gomez and Nearing, 2005), which may alter the flow paths and decrease the maximum depression storage value. Real micro-topographies may therefore present intermediate situations between Crater and River micro-topographies. Hence, we propose a modification of the original method of Zinn and Harvey (2003) to generate intermediate scenarios between Crater and River micro-topographies.

The original method is based on the following characteristic of continuous fields: pixels whose value corresponds to the mean of the entire field form together a connected network that spans the whole field. On the contrary, if we consider pixels with the same value but not equal to the mean of the field, those pixels will form a set of smaller closed networks. As we consider pixels with values further from the mean,

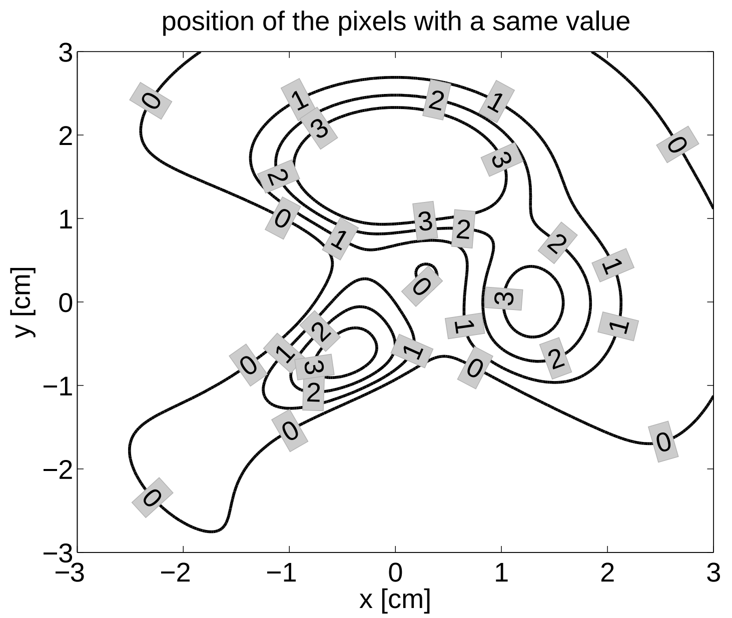

Figure 6.1: Position of the pixels from a Gaussian field ($\mu = 0$) with a same value, which form together contour lines. The values of the contour lines [mm] are shown on the lines.

the resulting networks will become smaller and more isolated. This is illustrated in Figure 6.1.

The methods of Zinn and Harvey (2003) considered that the pixels with an initial value equal to the mean (forming thus a connected network) would become the pixels with the lowest values. This was done by taking the absolute value of a Gaussian fields Y centered on 0.

$$Z = |Y - \mu| \tag{6.1}$$

In our case, we will not consider the field centered on 0 anymore, and introduce a gap factor Δ [m] inside the absolute value operator:

$$Z = |Y - \mu + \Delta| \tag{6.2}$$

As Δ increases, the pixels that are going to receive the lower values are initially further and further from the mean value of the field and thus are less and less connected. If Δ is such that no negative value is generated inside the absolute operator, then the new field Z will be exactly the same as the initial field Y, but displaced vertically by the value of Δ. By varying the value of Δ, intermediate topographies in terms of depressions connections can be generated (or crest connections, if the final field is flipped horizontally, as expressed in Eq. 4.4).

As was done by Zinn and Harvey (2003), Z must be mapped back to a desired distribution. If the initial and the desired final fields both present a Normal distribution of heights, the transformation is:

$$\begin{aligned} Y' =& \mu' + \sigma'\sqrt{2} \\ & \mathrm{erf}^{-1}\left(2\left[\frac{1}{2}\mathrm{erf}\left(\frac{|Y-\mu+\Delta|+\Delta}{\sigma\sqrt{2}}\right)+\frac{1}{2}\mathrm{erf}\left(\frac{|Y-\mu+\Delta|-\Delta}{\sigma\sqrt{2}}\right)\right]-1\right) \end{aligned} \tag{6.3}$$

where $Y \sim N\left(\mu, \sigma^2\right)$ and $Y' \sim N\left(\mu', \sigma'^2\right)$.

Based on 10 repetitions of Y ($\mu = \mu' = 0$ and $\sigma^2 = \sigma'^2$=100 mm^2), we generated 10x10 scenarios of micro-topography considering 10 Δ values, which will be scaled by the standard deviation of the field σ computed in absence of the slope ($\frac{\Delta}{\sigma}$: 0, 0.25, 0.5, 0.75, 1, 1.25, 1.5, 2, 2.5 and 3). For each of the 100 scenarios, we considered a 4-m^2 field discretized into square centimeter pixels and characterized by a semivariogram with a 100 mm^2 sill and a 100 mm range. Finally, a global slope (1, 4, 7 or 10 %) was surimposed to the micro-topographical fields, leading to 10x10x4 scenarios in total. In Figure 6.2, we show the impact of $\frac{\Delta}{\sigma}$ on a virtual micro-topographical field (with a global slope of 1%, which was not considered when computing σ). The lower Δ is, the closer the micro-topography is to the initial River or Crater scenarios. When $\frac{\Delta}{\sigma}$ is larger than 2.5, the generated field remains "Random".

The successive use of the absolute operator (Eq. 6.2) and the mapping operation (Eq. 6.3) constitutes a nonlinear transformation of the original Gaussian field that decreases the correlation length without affecting too much the shape of the semivariogram. Zinn and Harvey (2003) demonstrated that, for $\Delta = 0$, the separation distance between pixels should be increased by the scale factor of 1.86, in order to preserve the initial range. When $\Delta \neq 0$, it is not obvious to find analytically a value for the scale factor. Therefore we will perform a numerical study to determine the value of the scale factor as a function of Δ, in order to be able to produce micro-topographies where the range is preserved.

Finally, we will look at the impact of Δ on the maximum depression storage value ($D_{s\,\max}$). We know from other studies (Kamphorst and Duval, 2001) that the slope of the field impacts $D_{s\,\max}$. Therefore we will also include the impact of the slope in the analysis. We will express $D_{s\,\max}$ in water depth units so that it is independent to the size of the area taken into account and thus independent to the range too. Moreover, we will scale Δ and $D_{s\,\max}$ depth by the standard deviation of

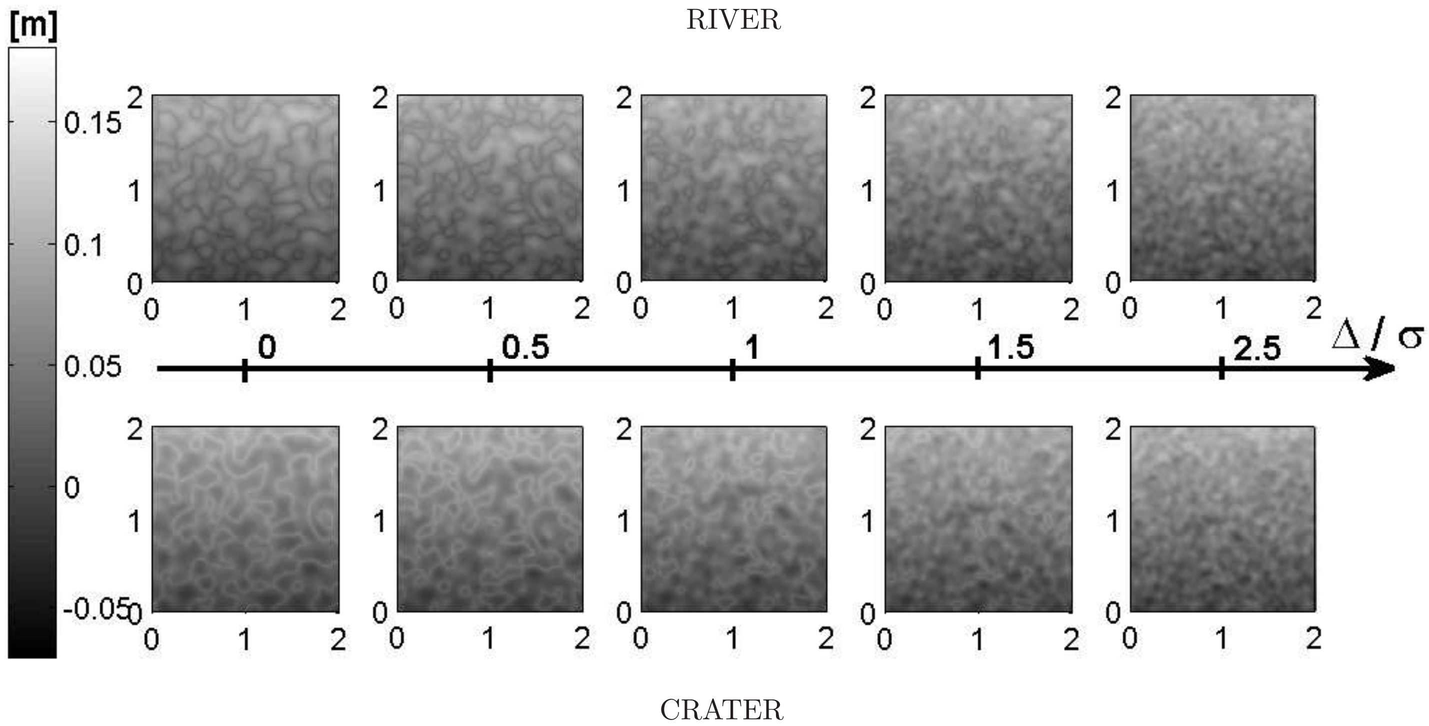

Figure 6.2: Evolution of 2x2 m^2 micro-topographies (1 % slope) as the factor Δ (scaled by the standard deviation of height σ) increases. River cases are considered above the arrow, and Crater cases beneath.

height σ to work in a complete dimensionless framework, transposable for any value of random roughness. Based on 10 replicates of micro-topography for each slope and each Δ value, we computed the mean $\frac{D_{s\max}}{\sigma}$ ratios [m/m] as well as the envelop curve limited by the 1st and 9th deciles.

6.4 Results and Discussion

6.4.1 Connectivity indicators evolution

As the cumulative rainfall erosivity R increases, the RSC functions tend to become steeper (Fig. 6.3a). This is due to the large variation in maximum depression storage between the different micro-topographies as shown in Chapter 3. Nevertheless, the variability of observed $D_{s\max}$ depths among micro-topographies with similar R-value results in an imperfect ranking of the different curves according to R. This can come from the natural variability of $D_{s\max}$ in space, but also from the limited size of our molds, which increases boundary effect. Larger samples would therefore provide $D_{s\max}$ values more representative for such a study. But this would be difficult to make in practice, unless to recompose one area with different neighboring molds.

When scaled by their respective maximum depression storage values (Fig. 6.3b), the scaled RSC functions for various R-values overlap. For instance, R=230 curves tend to encompass all the other curves beneath a 0.4 ratio of depression filling, while R=0 and R=115 curves tend to encompass the other curves, after a 0.55 ratio of depression filling. From a conceptual point of view, it means that the dynamics of depression connections is preserved but happens between depressions whose volume would be reduced, by deposition for instance. The maximum depression storage value is therefore the only identifiable factor that governs the RSC function evolution. Consequently, the evolution of the maximum depression storage with R represents, for our soil, a good proxy of functional connectivity evolution.

Figure 6.4 shows the structural connectivity indicators for the different molds. For the connectivity function integral scale (Fig. 6.4a), there is major overlapping between the different curves. The R=230 as well as the R=0 curves tend to encompass all the other curves, up to a threshold level z of 0.015. One R=45 curve and one R=230 curve deviate from the general trend above a threshold level z of 0.025. Clearly, the different curves can not be discriminated according to the R-value. This means also that the connectivity function integral scale seems not sensitive to

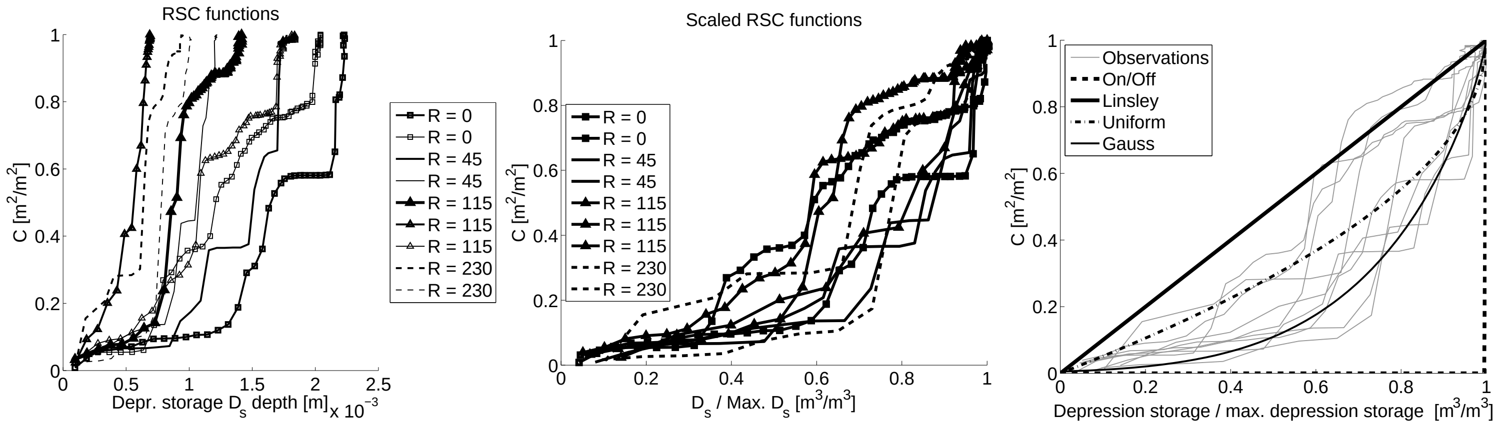

(a) (b) (c)

Figure 6.3: Observed RSC functions of the 9 micro-topographies (a), the same RSC functions but scaled by the maximum depression storage (b) and RSC functions for the 4 conceptual multiple compartment topographies explained in Chapter 5 (c).

the value of $D_{s\,\max}$ and that their is no evolution of the paths followed by water as R increases.

The Euler numbers (Fig. 6.4b) don't show clear distinct trends as a function of R either. This indicator is very sensitive to the noise in digital elevation models as small scale heterogeneities impact directly on the number of isolated objects and connections for some binarization thresholds. This explains the high Euler numbers for the R-0 curve at a z-level of -0.01, as its corresponding DEM was noisy, in addition to be irregular due to the tillage. Similarly to the connectivity function integral scale, the Euler numbers don't seem to be sensitive to the value of $D_{s\,\max}$ and the flow paths present similar configurations.

The percolation thresholds (Fig. 6.4c) don't show a clear decrease with R, except for R=230 micro-topographies. The limited size of our fields may lead to large boundary effects (no flow on the border sides), limiting percolation.

Even though it was shown in Chapter 5 that semivariograms are not valuable indicators of connectivity, we still show them in Figure 6.4d, as they are often the main characteristic used to describe a micro-topography, next to fractal properties (Paz-Ferreiro *et al.*, 2008). The effect of the soil evolution with R is not reflected clearly in the semi-variograms, as opposed to the observations of Darboux *et al.* (2002). But these authors had sampled micro-topography always at the same place and for rainfall experiments under controlled conditions, contrary to us. Moreover the evolution they noticed was small and only concerned the sill values. Moreover, there is variability among replicates larger than among semivariograms for different R-values. Some R=0 and R=45 curves overlap, and we note a lower sill for one R=115 curve only. The small connectors that develop with time on a soil surface are, in a way, invisible to the semivariogram, which is more sensitive to a general decrease of random roughness. As was shown in Chapter 4, random roughness (which should be similar to the sill of the semivariogram) is not a good explanatory factor of surface connectivity.

To summarize, we see that most of the previously identified runoff-relevant connectivity indicators were not able to capture the evolution of micro-topography with rainfall erosivity, except the RSC function.

6.4.2 Conceptual representation of the RSC function

As there is no clear evolution with R in the shape of the scaled RSC functions, we can define a common general shape based on the multiple-compartment concept (Chap. 5). Figure 6.3c shows the RSC functions for the 4 conceptual multiple-compartment topographies (On/Off, Lins-

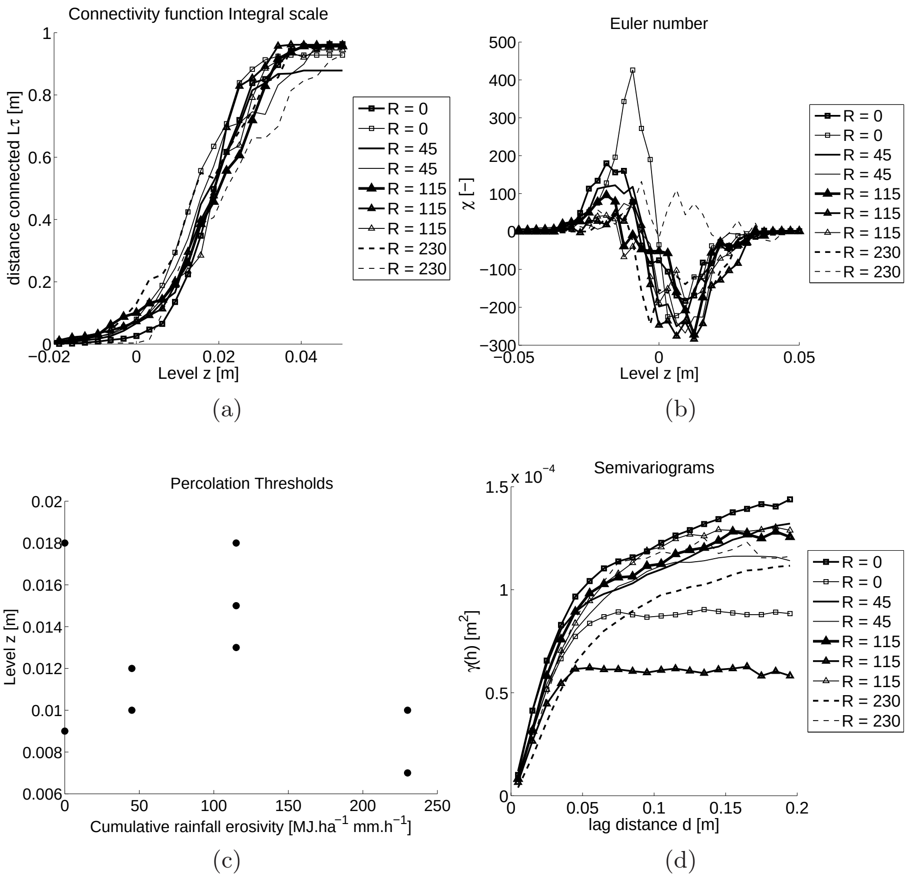

Figure 6.4: Structural connectivity indicators evolution

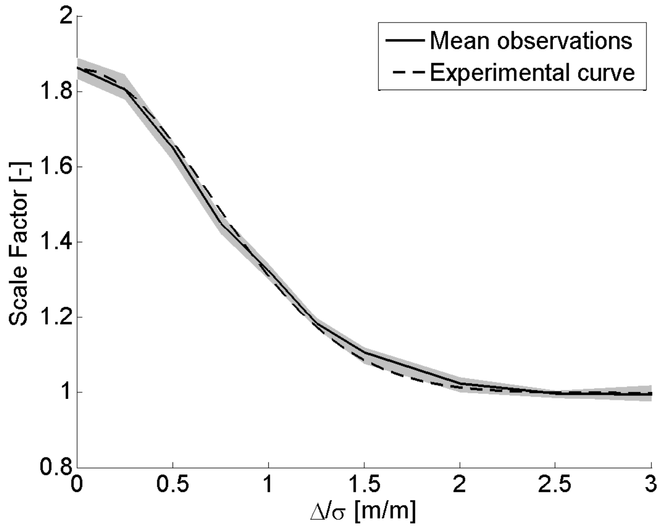

Figure 6.5: Impact of the gap factor Δ on the scale factor that will allow to correct the grid size in order to maintain the desired range in the semivariogram.

ley, Gaussian and Uniform) in front of the observations. It appears clearly that the On/Off classical assumption significantly underestimates the ratio of surface connected when the actual depression storage has not yet reached its maximum value. On the opposite, the Linsley assumption tends to overestimate that ratio. Uniform and Gaussian conceptual multiple compartment topographies better fit the observations. Note that the Gaussian shape factor was calibrated as 0.4 times the maximum depression storage value. Our micro-topographies could therefore be associated to a Gaussian or Uniform multiple-compartment topography whose global maximum depression storage value evolves with R.

6.4.3 Generation of micro-topographical scenarios conditioned by the RSC function evolution

In a first time, we performed a numerical study to determine the value of the scale factor. For each of the 100 generated micro-topographies, the scale factor is calibrated in order that the semivariogram fits the semivariogram for the initial Gaussian field Y. Figure 6.5 shows the mean value of the scale factor as well as the envelop limited by the 1st and 9th deciles.

The scale factor ranges from 1 to 1.86 as Δ decreases. We propose an experimental curve to represent it:

$$\text{Scale Factor} = 1 + 0.86 \exp\left(-\frac{(\Delta/\sigma)^2}{2\psi^2}\right) \tag{6.4}$$

where ψ is a shape factor evaluated experimentally at 0.6989. This curve is represented in Figure 6.5. We are now able to produce intermediate scenarios between Crater-Random-River micro-topographies, which all show similar spatial covariance when taking into account the scale factor expressed by Eq. 6.5.

We can look at the impact of Δ on the RSC function. The main characteristic of the RSC function is the maximum depression storage value ($D_{s\,\max}$). The impact of Δ on $D_{s\,\max}$ is shown in Figure 6.6 a (River cases) and b (Crater cases). If Δ increases, $D_{s\,\max}$ increases in case of River-type, or decreases in case of Crater-type micro-topographies. In every case, when the slope increases, $D_{s\,\max}$ decreases. We interpolated these results for any slope value. It is shown in Figure 6.7 a (River cases) and b (Crater cases). This shows that $D_{s\,\max}$ is directly proportional to the random roughness (σ) but, for a same level of random roughness, it may also vary up to a factor 5, if the slope is null, and up to a factor 3, if the slope is 10 %, when the spatial configuration changes from Crater to River with $\Delta = 0$. The slope indeed favors the connectivity and, as it increases, covers progressively the specific effect of the spatial configuration. When Δ increases, the difference between River and Crater scenarios decreases, as the micro-topographies tend to be more and more as the Random case.

Figure 6.7 allows us to choose the gap factor Δ in order to produce a numerical micro-topography constrained by the maximum depression storage value, if we know the slope, the random roughness (σ), the maximum depression storage and the correlation length, which will be preserved thanks to the shape factor found in Equation 6.4.

Finally, we investigate the effect of Δ on the shape of the RSC function. When scaled by $D_{s\,\max}$, the RSC functions are similar whatever Δ, as shown in Figure 6.8. If associated with a Gaussian multiple-compartment topography, the best Gaussian shape factor to consider is 0.39 times the maximum depression storage value. It is almost equivalent to the value of 0.4 that was found for our real data, which means that the numerical micro-topographies and the real observations show similar depression storage dynamics. However, the evolution of a numerical field of micro-topography with Δ will not correspond to a physical erosion-deposition process: indeed, the position of depressions and the

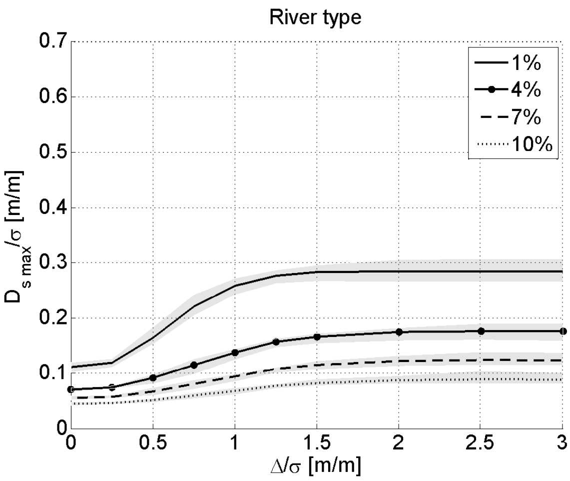

(a)

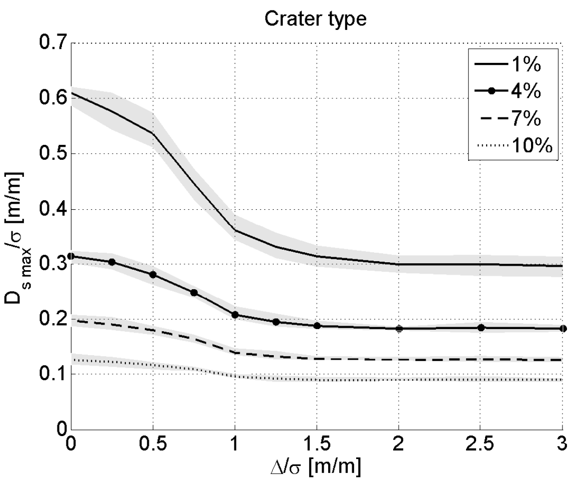

(b)

Figure 6.6: Impact of the gap factor Δ and the slope on the maximum depression storage $D_{s\,\max}$ (expressed in water depth), considering a River-type (a) or a Crater-type (b) micro-topography.

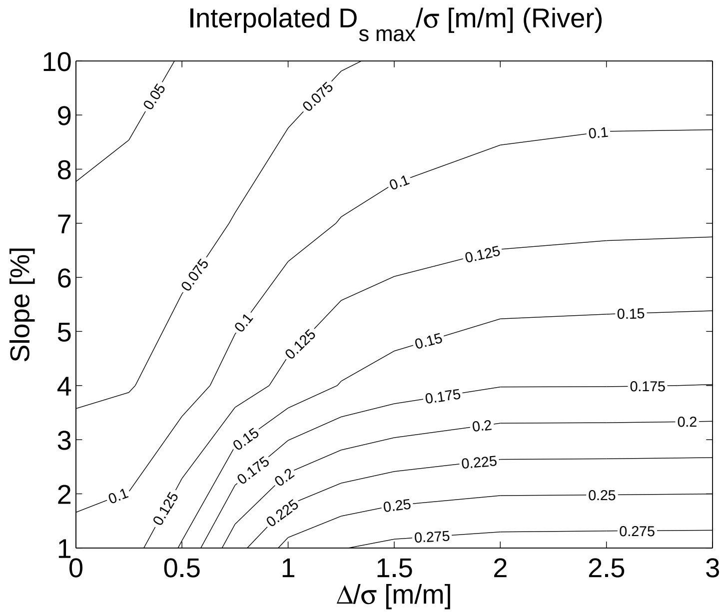

(a)

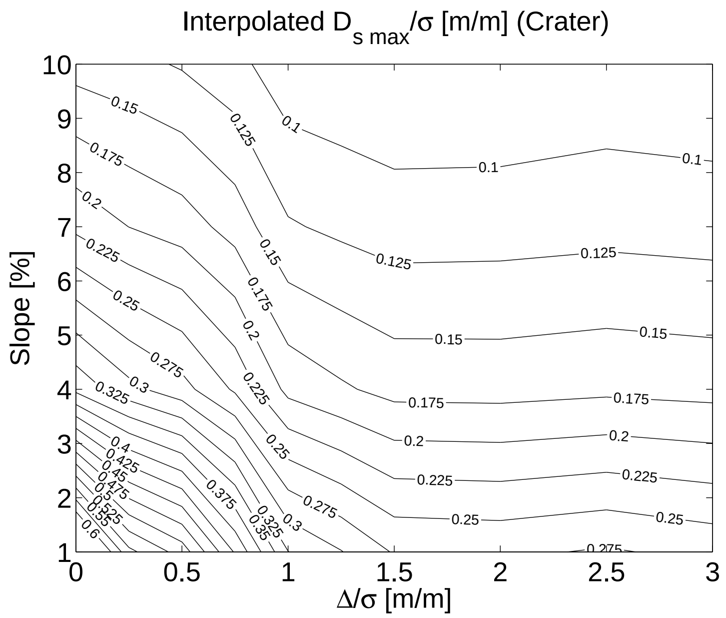

(b)

Figure 6.7: Impact of the gap factor Δ on the mean maximum depression storage (expressed in water depth and scaled by the standard deviation σ of micro-topographical height), interpolated against slope. Results are shown for River-type (a) or Crater-type (b) micro-topographies.

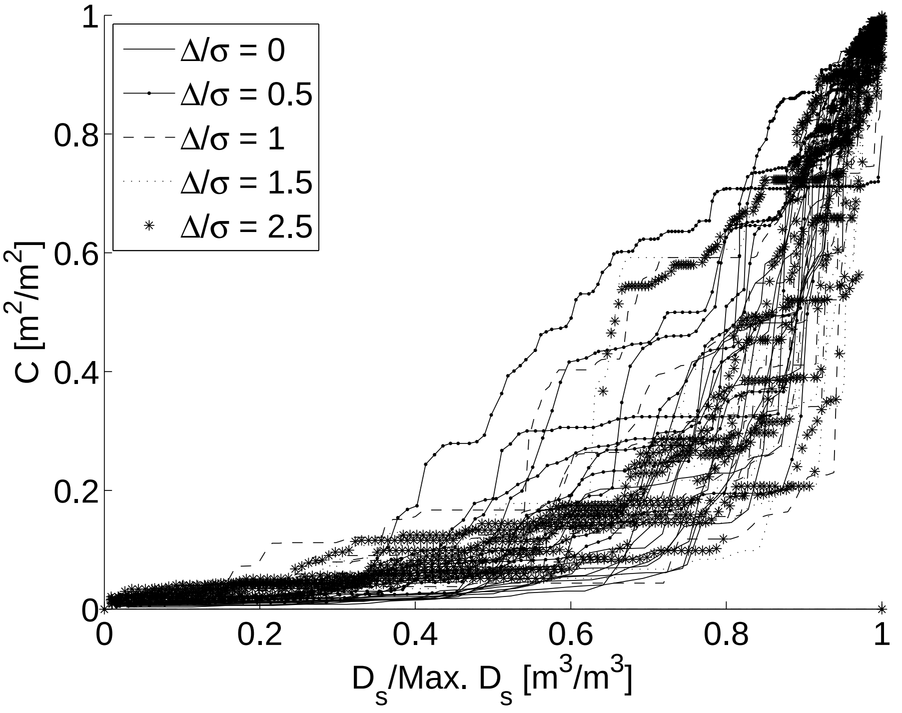

Figure 6.8: Impact of Δ on the scaled RSC functions

scale of the field will change when modifying Δ. The change in depression positions will of course also appear when considering DEM for casts whose molds were taken on different places, as we did in this study.

6.5 Conclusions

We have analyzed how the functional and structural connectivity properties of micro-topography evolved with the accumulation of rainfall erosivity. The structural connectivity indicators which were the connectivity function integral scale, the Euler numbers and the percolation thresholds could not detect any evolution clearly.

In contrary, the functional connectivity indicator, which was the RSC function, evolved with R. The range of the RSC function, which corresponds to $D_{s\,\max}$, decreased with R. But the shape of the RSC function when scaled by $D_{s\,\max}$ did not evolve. This allows us to describe all the various RSC functions by one single model such as the Gaussian multiple-compartment topography, parameterized by $D_{s\,\max}$ that evolves as a function of R.

As the only evolution to consider was thus $D_{s\,\max}$, we developed a method to generate artificial micro-topographies that are thus conditioned by $D_{s\,\max}$, on top of the macroscopic properties, which are the semivariogram characteristics (sill or random roughness and range), the random roughness and the slope. Those micro-topographies can be used for stochastic studies of runoff evolution with R.

The numerical study was performed under the hypothesis of Gaussian fields. Yet, other types of fields can be generated, which could affect the RSC function shape.

Chapter 7

Integrating subgrid connectivity properties of the micro-topography in distributed models [1]

7.1 Outline

In Chapter 5, we demonstrated the ability of the so-called Relative Surface Connection (RSC) function to capture, at the subgrid scale, the evolution of the contributing area as a function of the depression storage filling. However, this function neglects the effect of surface detention, which is proportional to the runoff rate and which must be taken into account if one wants to predict correctly the discharge dynamics. Therefore we tested two corrective procedures in association with the RSC function to integrate, at the grid scale, the effects of both depression storage and surface detention dynamics. The weighted-source corrective procedure consists in weighting the effective supply of water between depression storage and runoff using the RSC function. The weighted-surface corrective procedure consists in splitting a single grid into parallel independent strips that activate at various times and then participate to the global runoff production. Those methods allowed to mimic in a simple way and at the grid scale numerical and experimental hydrographs for complex subgrid micro-topographies.

[1] Adapted from: *Integrating subgrid connectivity properties of the micro-topography in distributed models*, Antoine, M., Javaux, M. and Bielders, C., **J. Hydrol.** (under review).

The weighted-source and especially the weighted-surface corrective procedures improved the hydrograph prediction compared to the classical approach where runoff only starts when depression storage capacity is full. An alternative to the Linsley *et al.* (1949) equation for the depression storage filling is proposed which allows a better description of surface runoff before maximal depression storage was reached.

7.2 Introduction

The spatial configuration of micro-topography affects the runoff connectivity at the interrill scale and, therefore, the shape of the hydrograph. Introducing connectivity information related to the micro-topographical configuration at the interrill scale might improve the prediction of runoff dynamics. In Chapter 5, we proposed the so-called Relative Surface Connection (RSC) function. This function expresses the proportion of an area that is connected to its downstream border as a function of the actual depression storage value of that area. The RSC function and related simplified hydrograph are three orders of magnitude faster to compute (Table 5.1 in Chap. 5) than solving the 2-D hydrograph based on the resolution of Saint-Venant equations, with the diffusive wave simplification (2-D DW). Moreover, as long as the micro-topography does not evolve, the simplified hydrograph remains valid. On the contrary, even if the micro-topography does not evolve, the 2-D DW hydrograph requires a new simulation for every change in effective rainfall rate. It is thus interesting, in terms of computation effort, to exploit the information given by the simplified hydrograph to assess the 2-D DW hydrograph behavior.

The drawback of the RSC function is that it does not take into account the boundary condition (rainfall-infiltration) but only depends on the micro-topography. Consequently, the RSC function does not take into account the surface detention. It only provides information on the depression storage dynamics during a rainfall event and the evolving proportion of the area that contributes to the runoff at the outlet. However, evidence from measurements (Chap. 3) showed that surface detention may represent a storage of water as large as the maximum depression storage itself, especially during intense rainfall events. Hence, a corrective procedure for the RSC function must be implemented to correctly predict runoff triggering.

Our study aims at predicting the hydrograph at the interrill scale, starting with information provided by the RSC function and correcting that information in order to take into account the boundary conditions (here the effective rainfall intensity). As in all of this thesis, the two hypotheses that underline this work are that the infiltration rate never exceeds rainfall intensity, such that there is always a zero or a net supply of water, and that this net supply is spatially uniform.

7.3 Materials and Methods

7.3.1 Hydrograph prediction from the RSC function

We propose two different approaches to take surface detention into account: a weighted-source or a weighted-surface corrective procedure. In both procedures, our topographical field is assumed to have a uniform 1-D slope on which the overland flow will run as a sheet flow. The amount of water forming the sheet constitutes the surface detention. The resolution of the 1-D Saint-Venant equation in the slope direction is therefore necessary to model that sheet flow. Again, we will use our hydraulic model based on the diffusive wave simplification, using effective parameters for the friction characterization.

Weighted-source corrective procedure

During the resolution of the 1-D Saint-Venant equation, the water level is adjusted in time by the equation of continuity:

$$\frac{\partial h}{\partial t} + \frac{\partial vh}{\partial x} = \phi \tag{7.1}$$

where h is the water depth [m] (in the surface detention only), t is the time [s], v is the mean water velocity [m s^{-1}] in the x-direction (x oriented in the main slope direction) and ϕ is a source term that is equal to the rainfall rate minus the infiltration rate [m s^{-1}] (hereafter called effective rainfall rate).

The weighted-source corrective procedure is easy to implement in distributed models. It consists in adjusting the runoff production of the field by weighting the source term ϕ with the RSC function $C\left(D_s\right)$, where D_s is the actual depression storage [m^3]. Equation 7.1 then becomes:

$$\frac{\partial h}{\partial t} + \frac{\partial vh}{\partial x} = C\left(D_s\right)\phi \tag{7.2}$$

The fraction of the source term that does not participate to the runoff serves to fill the actual depression storage:

$$\frac{\partial D_s}{\partial t} = (1 - C(D_s))\, S\phi \tag{7.3}$$

where S is the surface area of the field [m^2].

As an example, if the depression storage value D_s is such that the RSC function predicts $C = 60\%$ of the surface to be connected to the downstream boundary, the weighted-source procedure will consider that 100 % of the surface is connected but that only 60% of the effective rainfall ϕ will contribute to the overland flow. The other 40% is used for filling the depression storage D_s.

Weighted-surface corrective procedure

The second procedure, illustrated in Figure 7.1, considers that the micro-topographical field can be divided into parallel independent strips, with the same slope. Every strip is associated with an increment dC_i of the simplified hydrograph. The width of a particular strip i is given by:

$$dW_i = dC_i \cdot W \tag{7.4}$$

where W is the grid scale pixel width [m] and dW is the strip width [m]. Each time a rainfall increment provokes an increase dC_i of C, an additional strip is activated. Runoff starts on that strip and contributes to the total discharge R [m^3 s^{-1}].

At all times, the surface of the pixel connected to the outflow boundary corresponds to the sum of the activated strip areas. Take note that surface detention varies between strips, as newly activated strips might not yet have reached the dynamical equilibrium between inflow and outflow.

For a constant effective rainfall rate, each strip reaches its equilibrium flow rate (governed by 1-D Saint-Venant equations) in the same way, whatever the activation time. The only difference between strips is the delay with which each strip is activated. Therefore the temporal evolution of the discharge per unit width $q_0(t)$ [m^2 s^{-1}] at the downstream end of a strip, from activation to steady state, constitutes a kind of transfer function that distributes in time the contribution of a newly activated strip. By convolving this transfer function $q_0(t)$ with $dC(t)$ (the temporal increment of $C(t)$ for a temporal resolution of 1 second) multiplied by the pixel width W[m], we can reconstruct, with very limited computation effort, the total discharge $R(t)$ at the downstream end of the pixel [m^3 s^{-1}]. $R(t)$ incorporates both depression storage and surface detention dynamics inside the pixel. This can be mathematically expressed by:

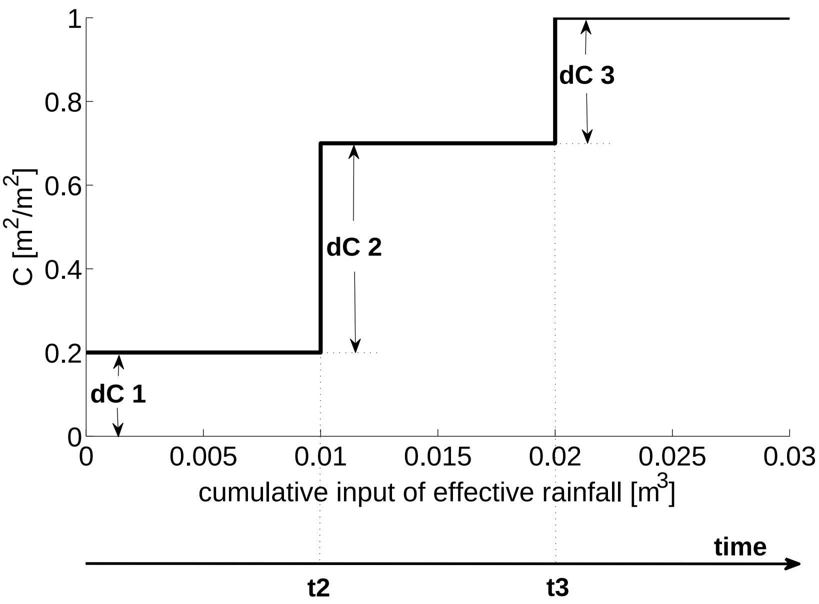

(a)

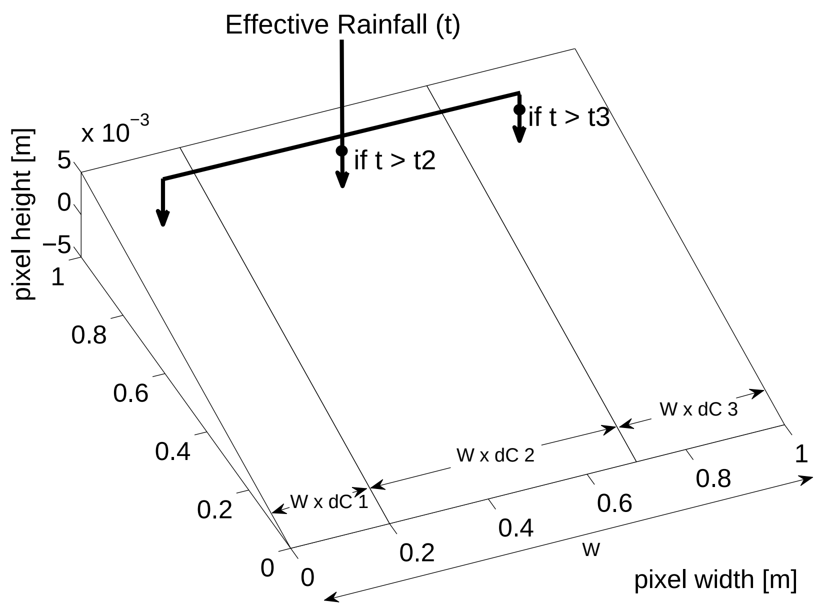

(b)

Figure 7.1: Principle of the weighted-surface corrective procedure where a single large pixel (b) is divided into parallel independent strips having the same 1-D slope. The width of each strip is proportional to the increment of relative surface connection (a) with which it is associated multiplied by the pixel width. Each strip gets progressively subjected to the effective rainfall as the cumulative effective rainfall increases and depression storage of the single large pixel fills.

$$R(t) = \sum_{\tau=0}^{\tau_{end}} W \mathrm{dC}(t-\tau)\, \mathrm{q}_0(\tau) \tag{7.5}$$

For a variable effective rainfall rate, the 1-D Saint-Venant equation must be solved independently for each strip. When a strip is activated, its source term ϕ is switched on. Finally, all the different runoff contributions from the different activated strips are summed up to determine the total discharge of the pixel.

7.3.2 Case studies

Runoff modeling on synthetic fields

We will use one repetition of the two contrasted numerical micro-topographical fields present in Chapter 4: the Crater and the River type. The maximum depression storage changes by a factor of 5 between the two fields (Table 4.2).

The 1-m^2 fields were discretized into square centimeter cells and a global 1 percent slope was added. The related hydrographs were computed by resolving the 2-D Saint-Venant equations on the numerical fields (diffusive wave simplification), with the runoff model described in Chapter 4.

Simulated rainfall-runoff experiments on waterproof molded surfaces

We used the 9 casts presented in Chapter 3 which cover a range of roughness states. The 10th cast (R=677) was not used as the runoff it produced was not sampled with sufficient temporal resolution, in relation with its small depression storage. The digital elevation models of the casts were obtained by scanning the surface with a horizontal resolution of 0.5 mm using the method of Darboux and Huang (2003).

In the laboratory, the casts were tilted to the same slopes as in the field and hydrologically isolated on the upstream and lateral borders using a plastic frame. A rainfall simulator (Chap. 3) was used to apply water at different rainfall rates, until steady state. Each of the nine molds were subjected to three constant rainfall rates, ranging between 5 mm/h to 60 mm/h, resulting in 27 different experimental hydrographs. Runoff water was collected in a gutter at the downstream boundary. The discharge was determined by collecting the runoff during fixed time intervals (low rainfall rate: 120 s, medium rainfall rate: 30 s, high rainfall rate: 15 s) and weighing the runoff samples.

Given that the casts are waterproof, surface detention could be determined by measuring the cumulative volume of runoff after the rainfall had ceased. Maximum depression storage was measured by collecting the water in the depressions with a sponge after runoff had completely stopped. Both volumes were divided by the horizontal projection of the cast surface and expressed in water thickness units.

7.3.3 Methodology

Through numerical runoff simulation experiments on the 2 synthetic fields, we first benchmark the classical On/Off approach, the weighted-source and the weighted-surface corrective procedures with the 2-D DW hydrograph taken as reference.

In a second step, we validate the best corrective procedure identified in the previous step, by comparing the hydrographs generated by the selected corrective procedure with experimental hydrographs from the laboratory rainfall-runoff experiments on the waterproof molded surfaces. The goodness of fit between the experimental and the modeled hydrographs are evaluated using two indicators: the error variance σ_ε^2 and the Nash and Sutcliffe (1970) coefficient E:

$$\sigma_\varepsilon^2 = \frac{1}{NT} \sum_{t=1}^{NT} \left(Q_t - \hat{Q}_t \left\{ \underline{\Theta}, \underline{Y} \right\} \right)^2 \tag{7.6a}$$

$$E = 1 - \frac{\sigma_\varepsilon^2}{\sigma_0^2} \tag{7.6b}$$

were Q_t is the observed discharge, $\hat{Q}_t \left\{ \underline{\Theta}, \underline{Y} \right\}$ is the simulated discharge given parameters $\underline{\Theta}$ and input data $\underline{Y}$, NT is the number of time steps, σ_0^2 is the variance of the observations.

The physical model we use is based on the diffusive wave equation and underestimates significantly the surface detention for rough surfaces. For rough surfaces, energy dissipation due to the shape of the macro-roughness that protrudes through the water layer (= form resistance) is much larger than energy dissipation due to the friction with the particles of soil (= grain resistance). Our physical model only considers grain resistance. Moreover, the use of the diffusive wave simplification of the Saint-Venant equations does not allow dealing with backwater effects that are significant contributors for the surface detention. Nevertheless, we still consider that using our physical model in this chapter gives valuable insights as: 1) the physical model was shown to perform very well for sheet flow (fig 4.6), which is at the base of both weighing methods and 2) the underestimation of the backwater detention capacities and form resistance effect was compensated for by choosing large friction factors that were calibrated for equivalent sheet flows in term of surface detention (fig 3.8). Yet, we still recommend to perform again this experiment with a full 2D Saint-Venant model able to work at our scale, to validate or reject our exploratory results.

7.4 Results and Discussion

7.4.1 Hydrograph prediction for the synthetic fields

Figure 7.2 shows the modeled hydrographs for the synthetic River (left) and Crater (right) fields, for constant (up) or variable (down) effective rainfall rates. The 2-D DW hydrograph is used as reference. The On/Off hydrograph assumes that the maximum depression storage needs to be reached before runoff can occur (On/Off method), which is a classical approach in rainfall-runoff models (Singh, 1995; Singh and Frevert, 2002). When the maximum depression storage is small compared to the surface detention (as for the River topography), using the classical On/Off approach does not lead to large errors. However, when maximum depression storage is large compared to surface detention (i.e., Crater case), the classical On/Off method does not result in realistic hydrographs. In Figure 7.2 (b) we clearly see that the 2-D DW hydrograph reacts quickly after the beginning of the effective rainfall, and rises up stepwise as soon as a new area connects to the downstream boundary, as can be seen from a comparison with the simplified hydrograph. However, there is not always a perfect match between those two hydrographs due to neighbor-connection schemes that differ between the filling algorithm of the simplified hydrograph (single-flow 8-neighbor scheme) and the hydraulic model (multiple-flow de-centered 4-neighbor scheme). Compared to all the others, the simplified hydrograph generally reacts in advance in terms of runoff production as the damping effect of surface detention is not taken into account.

For both topographies, the weighted-source hydrograph is delayed at the beginning of the runoff simulation, and therefore initially underestimates the 2-D DW hydrograph. This is due to the friction effect that strongly slows down the flow in thin water layers. Thin water layers are favored by the weighted-source procedure at the beginning. Later, the weighted-source hydrograph overestimates the 2-D DW hydrograph, due to compensation effects. Indeed, since the sum of maximum depression storage and surface detention at dynamical equilibrium is the same for all hydrographs (except the simplified one), an underestimation of the

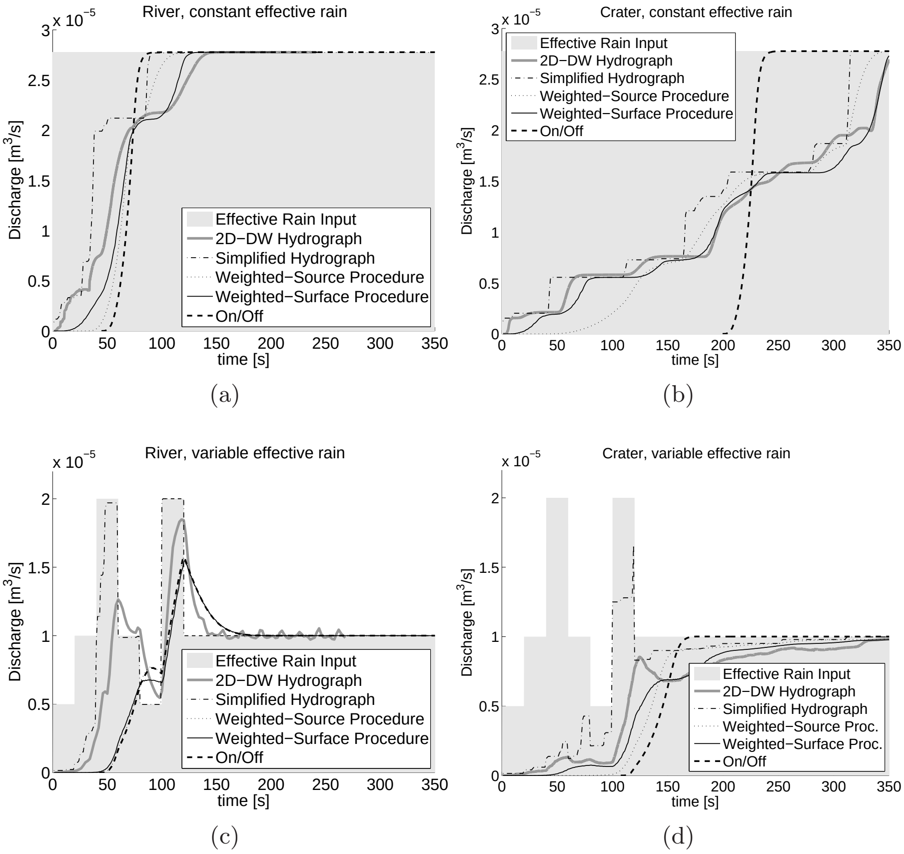

Figure 7.2: Comparisons of the 2-D DW hydrographs based on the 2-D Saint-Venant equations with the simplified hydrographs (where the abscissa is converted into time units, knowing the effective water supply rate), the hydrographs based on the weighted-source and weighted-surface corrective procedures, and the solution of the 1-D Saint-Venant equations assuming depression storage needs to be entirely filled before runoff can occur (On/Off). a & b: constant rainfall, c & d: variable intensity rainfall.

2-D DW hydrograph at the beginning must lead to an overestimation at the end to ensure mass conservation.

The weighted-surface hydrograph matches the best the 2-D DW hydrograph. We clearly see the runoff triggering controlled by the increase of surface connected to the downstream end, as is visible from a comparison with the simplified hydrograph. Every time the simplified hydrograph reaches a new step, the increase of connected surface ratio activates the transfer function and leads to the characteristic rising of the weighted-surface hydrograph. Take note that the area between the 2-D DW and the simplified hydrographs as well as the area between the weighted-surface and simplified hydrographs correspond to the surface detention in both cases.

For a transient rainfall (Figure 7.2, c & d), the relationships between the different hydrographs are less straightforward, but in general the On/Off method underestimates the early rising. With a variable effective rainfall rate, it is mainly the dynamical damping of runoff triggering by the surface detention that controls the shape of the 2-D DW hydrograph. Therefore, the simplified hydrograph, which does not consider surface detention, is not able to correctly characterize the 2-D DW hydrograph. Here, the weighted-surface is also the best approximation of the 2-D DW hydrograph.

7.4.2 Hydrograph prediction for the artificial rainfall experiments on waterproof molded surfaces

In the previous numerical experiment, it was found that the weighted-surface corrective procedure with the RSC function best approximated the 2-D DW hydrograph. Therefore only this procedure will be used in this section. The main characteristics of the molded surface are provided in Table 7.1, as well as the friction constants used for modeling the transfer function by means of the 1-D Saint-Venant equation, which were optimized in Chapter 3.

The RSC functions for the different molded surfaces were computed based on their digital elevation models. We also computed equivalent RSC functions for the 4 conceptual multiple-compartment topographies (On/Off, Linsley, Gauss and Uniform), based on the measured $D_{s\,\max}$ values and a Gaussian factor of 0.4 $D_{s\,\max}$ (Chap. 6).

Figure 7.3 shows one example of an experimental hydrograph for one specific uniform rainfall rate on one specific waterproof micro-topography (the others can be found in the Annexe C). Modeling that hydrograph using the 2-D Saint-Venant equation at a 2-mm spatial resolution would take us about 100 days of computation. We could lower that compu-

Table 7.1: Main characteristics of the 9 waterproof micro-topographical fields. The different rainfall rates are given as well as the related average surface detention depths at dynamic equilibrium. The optimized friction constants are given to relate the surface detention to the effective laminar discharge, where λ is the Darcy-Weisbach friction factor and Re is the Reynolds number. Surface detention and depression storage volumes have been divided by the horizontal projections of the cast areas, to be expressed in water depth units.

Cast Number	1	2	3	4	5	6	7	8	9
Length [cm]	97.9	94.4	87.8	96.6	95.2	96	94.7	96.4	97.7
Width [cm]	49	49.3	45	46.5	46	45.5	46	47	46
Slope [%]	4.8	4.45	7.06	9.11	7.35	10	7.6	5.19	7.57
Random Roughness [cm]	1.22	0.97	1.1	0.98	1.21	0.97	1.12	0.89	1.25
Depression Storage [mm]	1.04	0.99	1.5	1.04	0.8	0.45	1.19	0.58	0.67
Low Rain [mm/h]	11.4	10.8	10.9	10.4	6.3	9.9	5.1	10.6	10.1
Surface Detention [mm]	0.47	0.4	0.98	0.7	0.41	0.6	0.29	0.46	0.57
Med. Rain [mm/h]	16.7	20.2	27.7	27.8	25.7	25.1	17.6	24.7	16.4
Surface Detention [mm]	0.53	0.61	1.19	0.92	0.93	0.74	0.49	0.58	0.63
High Rain [mm/h]	52.1	53.3	62.5	63	57.5	59.5	40.6	62.3	46.3
Surface Detention [mm]	1.2	1.05	1.82	1.35	1.25	1.08	0.83	0.87	0.94
Friction Constant $C_n = \lambda \mathrm{Re}$	918	580	7240	3493	1986	2305	690	567	1551

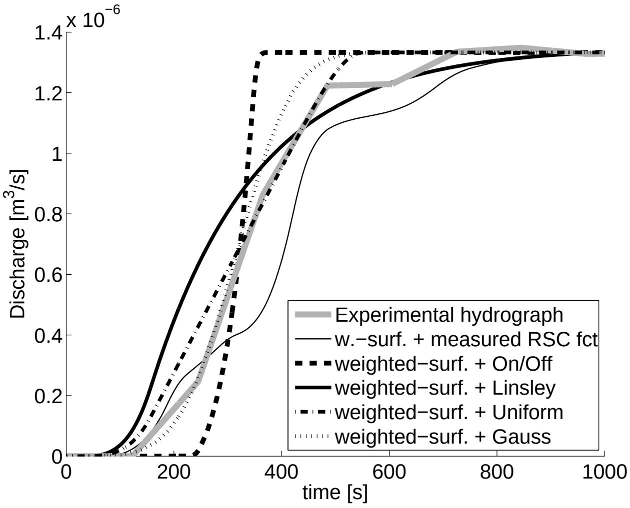

Figure 7.3: Example of one experimental hydrograph and the hydrographs based on the weighted-surface procedure using the observed RSC function or the 4 conceptual models. Because the effective rainfall rate is constant, the procedure is a simple convolution of a transfer function.

tation time by considering larger grid cells, but some of the channels that link depressions together would be omitted, leading to a significant overestimation of maximum depression storage capacity.

The convolved (= weighted-surface with constant effective rainfall rate) simplified hydrograph associated with the measured RSC function reproduces some features of the experimental hydrograph, especially around 450 seconds and 650 seconds. Discrepancies may be due to bad representation of some micro-topographical features in the digital elevation model. Although the scanning methodology allows a spatial resolution of 0.5 mm, there are always areas in the shadow of protruding objects where elevation data is missing. This missing data is then completed by means of an interpolation procedure (here, inverse distance weighting method with a power parameter of 2). Shadow effects usually occur at the edge of protruding objects, at the bottom of which some connecting hydraulic links were found (e.g., water flowing underneath clod overhangs). The fact that some of the connections are missed in the digital elevation model leads to an increase in maximum depression storage, as also observed for similar resolutions by Abedini *et al.* (2006). Consequently, the simplified hydrograph is shifted to the right.

As already said in the previous numerical experiments, the On/Off hydrograph underestimates the initiation of runoff, and later overestimates it. Note that the rising part of the On/Off hydrograph has the same shape as the transfer function used by the weighted-surface procedure. The Linsley hydrograph rises up early as a result of a larger surface connection ratio at the beginning of the depression storage filling. It therefore overestimates the reaction time of the micro-topographical field to a rainfall stimulus. Gaussian and Uniform hydrographs better represent the experimental hydrograph, which could already be expected based on Figure 6.3 in Chapter 6.

We computed the error variance σ_ε^2 and the Nash and Sutcliffe coefficient E for the 3 x 9 scenarios of constant rainfall rates and waterproof micro-topographies (Figure 7.4). The On/Off approach clearly leads to the worst predictions (higher σ_ε^2 quartiles and lower E quartiles). Depending on the aim of our simulations (good predictions on average, avoidance of extreme bad predictions), we can choose between the other approaches. The knowledge of the real RSC function seems in general to be the most reliable approach (low and little dispersed σ_ε^2 and lowest median E). But obtaining that real RSC function requires a good scanning methodology that is able to detect all the small hydraulic connectors in a soil surface micro-topography. From a practical point of view, it is easier to just find one parameter, i.e., the maximum depression storage value, either by direct measurement with the molding technique or calibrated against runoff and infiltration observations. The Gaussian framework is attractive in the sense that the simplified hydrograph is differentiable, although there is no analytical expression for its RSC function (only its inverse is described through nested error functions, Chap. 5). Therefore the Uniform model seems to be the easiest conceptual model to deal with and it performs globally well.

Note that the weighted-surface procedure is much faster with constant effective rainfall rate, as it only requires a convolution between the temporal incrementation of connected surface ratio with the transfer function describing the change in discharge per unit width through time, which is common to every strip. Therefore it might be useful, for computational reasons, to consider only a mean rainfall rate to determine a unique transfer function to be scaled by rainfall rate and convolved later. For transient effective rainfall condition, the gain in precision achieved by taking into account surface connectivity is partly lost by considering a single scaled transfer function for all strips.

Finally, after the end of the rainfall, runoff will continue to occur until the surface detention has either infiltrated or sewed away. On waterproof surfaces, the recession limb (not shown) of the hydrograph could be

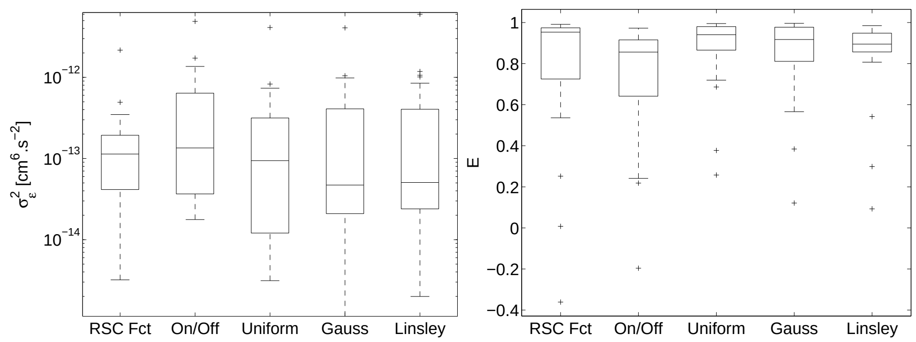

(a) (b)

Figure 7.4: Goodness of fit evaluation between observed and hydrographs simulated using the actual RSC function or different conceptual RSC functions (On/Off, Linsley, Uniform and Gauss): boxplots of the error variance σ_ε^2 (a) and Nash and Sutcliffe (1970) coefficient E (b).

modeled by an exponential decay function, but under field conditions at the interrill scale, we have always observed a quasi-instantaneous stop of the runoff after the rainfall ended.

7.4.3 Main findings

Tables 7.2 and 7.3 summarize the main findings from, respectively, the numerical experiments and the laboratory experiments to predict the hydrograph behavior. It was found that the weighted-source procedure associated with the Uniform multiple compartment topography model provided a useful methodology to integrate both sub-grid depression storage and surface detention dynamics at the grid-scale through two effective parameters: the maximum depression storage value and an effective friction coefficient.

Therefore we can schematize the hydrological behavior of a particular micro-topography by a conceptual pierced multiple compartment topography, shown in Figure 7.5, where the lower part accounts for the depression storage that partially blocks the flow, and the upper part accounts for the delaying (in relation with the friction factor, or size of the holes in the scheme) of the runoff flowing through the surface detention, both parts affecting the hydrological connectivity.

In our case the Uniform model allowed the best simulation. For such a conceptual topography, the actual depression storage D_s is modeled by: $D_s = Q_{inC}\left(1 - {Q_{inC}}/{4D_{s\,\max}}\right)$, for $Q_{inC} \leq 2D_{s\,\max}$, where D_s is the

Table 7.2: Summary of the numerical experiments to predict the hydrograph for synthetic fields.

Methods	Efficiency	Comments
On/Off	-	- Bad predictions when $D_{s\,\max}$ is important
Simplified hydrograph	+/-	+ Straightforward method - Over-estimation of the 2-D DW hydrograph
Weighted-source	+	+ Easy to implement in present distributed models + Allows an improvement compared to On/Off
Weighted-surface	++	+ Best approximation of the 2-D DW hydrograph - 1-D Saint Venant equation must be solved for each strip in case of transient rainfall

Table 7.3: Summary of the laboratory experiments to predict the hydrograph for waterproof molded surfaces, based on the weighted-surface procedure.

RSC function	Efficiency	Comments	
On/Off	-	-	Bad predictions, lowest E coefficients
Linsley	+/-	+	Method based on a classical equation
		-	Median E lower than in the next methods
Gaussian	+	+	Lowest median σ_{ε}^2
		-	No direct analytical expression for the RSC function
Uniform	++	+	Good prediction in general, high quartiles of E
		+	Method based on a simple equation
Measured	++	+	Best median E
		-	Sensitive to the scanning performance

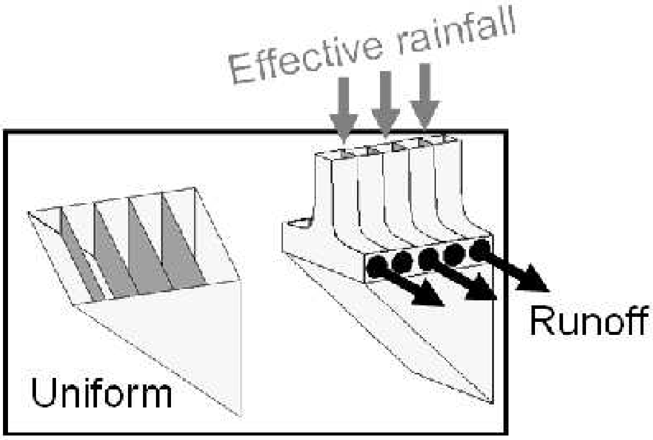

Figure 7.5: Full conceptual multiple compartment topography, reacting similarly than a real micro-topography.

actual depression storage value [m^3], $D_{s\,\max}$ is the maximum depression storage [m^3] and Q_{inC} is the cumulative input of effective rainfall [m^3]. This equation is an alternative we propose to the classical Linsley *et al.* (1949) equation (Eq. 5.16).

7.5 Conclusions

Although the surface micro-topography and its related flow connectivity have strong influence on the resulting hydrograph, the high computational requirements do not permit to solve the full 2-D Saint-Venant equations inside every grid-cell of distributed hydrological models. Hence, simplified methods that still use some of the micro-topographical information need to be explored. The method we propose is based on the relative surface connection function, which is a functional connectivity property of the micro-topography. However, that indicator is solely based on the dynamics of depression storage connection. In reality, surface detention must also be taken into account as it delays the runoff, thereby storing an increasing amount of water at the soil surface as the discharge increases. For high rainfall rates, surface detention can be larger than the maximum depression storage.

We considered two different corrective procedures, called *weighted-source* and *weighted-surface*, to merge both depression storage and surface detention dynamics. It was found that the weighted-source corrective procedure showed substantial improvement in discharge modeling compared to a classical On/Off procedure where runoff starts only when the maximum depression storage is reached. This method is easily implemented in current hydrological models.

The best approximations of 2-D DW hydrographs were, however, obtained using the weighted-surface corrective procedure. This method was tested in a second experiment and compared with measured hydrographs resulting from artificial rainfall on waterproof realistic microtopographies. From that experiment, it was shown that the weighted-surface corrective procedure associated with real measured RSC functions from scanned digital elevation models generally provides the best approximations of the experimental hydrographs. If the digital elevation models are not available for computing the real RSC functions, we recommend to use the Uniform conceptual multiple-compartment framework instead of the present day On/Off procedure or the Linsley approach. Yet, this might also depend on the soil and tillage systems as well as crop cover. Other soil surfaces should thus be investigated.

All these developments were performed under the assumption that the rainfall rate equals or exceeds the infiltration rate. In case infiltration is larger than rainfall, the relative surface connection function presents a clear hysteresis, as already discussed by Darboux *et al.* (2002b), if the depression storage is not set back to 0 between two rainfall events.

Chapter 8

Conclusions and perspectives

8.1 Conclusions

To correctly understand and predict the hydrological response of a catchment to a rainfall event, it is necessary to take into account the spatial distribution of soil properties. The concept of hydrological connectivity has been used to capture the specific effect of spatial configuration of soil properties on water fluxes. Connectivity can be subdivided into structural or functional connectivity. Structural connectivity describes the continuity of state variables that form identifiable patterns, whereas functional connectivity describes the facility with which water flows, in interaction with the patterns, in response to a boundary stimulus. Up to now, hydrological connectivity has mainly been studied at the scale of small catchments, in order to explain their particular hydrological behaviors rather than to improve the prediction of water fluxes. This is due to the lack of quantitative connectivity indicators that can effectively be integrated into hydrological models. In this thesis, we hypothesized that quantitative expressions of hydrological connectivity may be found that can help to improve the prediction of runoff propagation. Furthermore, the gain in hydrological prediction improvement is believed to be highest if the connectivity concept is applied at the subgrid scale of current hydrological models, which corresponds to the interrill scale. Therefore, we focused our study at the interrill scale and we analyzed how runoff propagates before it flows into the rill network, which has to be modeled separately.

To achieve this objective, it was necessary to study runoff without interference from infiltration. For this purpose a molding method was developed which relies on molding materials much cheaper than those currently proposed in the literature. The method is also fast, works on wet soil and is capable of reproducing complex surfaces with a 1-mm precision.

At the interrill scale, water flows from one depression to another and provokes their successive overflows. One part of the water at the soil surface is stored in the volume of depressions, forming the depression storage, and the other part is temporarily held in a water layer in excess of depression storage, which forms the surface detention.

Depression storage and surface detention act as two storages that buffer runoff propagation at the interrill scale. Their buffering capacities decrease with time when both the maximum depression storage value and the effective friction factor decrease through the action of erosion-deposition processes that favor the circulation of water at the soil surface. However, this trend is not systematically reflected in the random roughness evolution, which is unfortunately the main soil characteristic presently taken into account in hydrological models to assess surface detention and depression storage. Random roughness is related to depression storage, but, for a same value of random roughness, maximum depression storage may vary up to a ratio of 1 to 5 in numerical scenarios (1 to 3 in our field observations). Surface detention may also vary in a ratio of 1 to more than 2, while keeping the random roughness constant. Therefore it is better not to use the random roughness as an indirect measure of depression storage and surface detention but instead to use the molding technique we proposed to measure directly depression storage and to derive a friction constant to model surface detention.

The reason why random roughness does not provide robust predictions of depression storage is that it does not consider the spatial configuration of micro-topography. If we want to consider explicitly the spatial configuration of micro-topography, we need a holistic knowledge of the micro-topography to take into account all the possible connecting paths runoff can follow. Sparse sampled points or transect information are definitively not sufficient. Knowing the full micro-topography, we can characterize the spatial configuration through relevant structural connectivity indicators, such as the connectivity function integral scale, the Euler number or the percolation threshold. However, the relevance of these indicators was not confirmed when they were applied onto real micro-topographies, as opposed to the Relative Surface Connection (RSC) function, which is a functional connectivity property we developed and proposed in this thesis. Although some of the existing connectivity indicators allowed to partially discriminate among contrasted micro-topographies, rare appeared readily usable for integration into hydrological models. On the contrary, the RSC function is better able to discriminate among different micro-topographies. Furthermore, it requires the same information as the structural indicators, it is almost as fast to compute and it is more closely related to the process of interest. The RSC function can be approximated by conceptual multiple-compartment topographies, which may prove useful if detailed micro-topographical information is not available.

The RSC function expresses the ratio of a specific area that contributes to runoff discharge as a function of the depression storage filling. The RSC function is computed without considering any surface detention, even though surface detention might hold temporarily a significant amount of water at the soil surface. Therefore we have proposed a methodology for calculating pixel-scale hydrographs by combining the RSC function together with a corrective procedure to reproduce correctly the combined action of depression storage and surface detention on runoff propagation. The first procedure (weighted-source) consisted to split the rainfall supply into two, one part filling the depression storage and one part participating to the runoff propagation, in accordance with the ratio of connected surface provided by the RSC function. Although this first procedure improved already the hydrograph prediction compared to the classical approach where runoff is only allowed to flow once depression storage is fully filled, the second procedure outperformed it. This second procedure (weighted-surface) consisted in dividing the pixel width into independent strips that all accounted for an increase in the RSC function. Each strip was activated once the increase of the RSC function it represented occurred. When available, the use of the observed RSC function in the second procedure provided good results. In the absence of real RSC measurements, Gaussian and Uniform multiple-compartment topographies could replace them, with only one parameter to determine or calibrate: the maximum depression storage.

Subgrid characteristics of micro-topography, evolve over time. Our observations have shown a relatively constant shape of RSC function over time. Only the range of the function differed significantly among the micro-topographies, which is a reflection of the change in maximum depression storage. The measured RSC functions were encompassed between the RSC functions for the Gaussian and the Uniform multiple-compartment topographies. Those multiple-compartment topographies form a convenient modeling framework as there is only one parameter to consider: the maximum depression storage value. This parameter may evolve in time to take into account the evolution of micro-topography due to the action of erosion-deposition processes. Therefore, in present distributed models, we can use the RSC function of an equivalent Uniform or Gaussian multiple-compartment topography whose maximum depression storage value evolves in time with the cumulative rainfall erosivity and combine it, using the weighed-surface procedure, to the surface detention dynamics computed with an effective friction factor that also evolves in time with the cumulative rainfall erosivity.

In contrary, if we want to integrate at the subgrid scale the evolving effect of micro-topographical configuration on overland flow propagation, our methodology allows to generate scenarios of micro-topographies that are conditioned by the slope, the correlation length, the random roughness and the maximum depression storage value, taking into account that some of those properties will evolves with time, with the accumulation of rainfall erosivity.

Surprisingly, the evolution of the depression storage and the effective friction factor was not reflected in an evolution of the connectivity function integral scale, the Euler numbers and the shape of the scaled RSC function. It is as if the spatial configuration of flow paths did not evolve as a function of R, but that the surface flows connected, through more and more conductive paths, depressions with smaller and smaller retention capacities. This could be linked to a mechanism of erosion-deposition where depressions are progressively filled by deposition and where the small scale passes are progressively lowered and widened by erosion. This will need further investigation.

To summarize, this thesis has thus grounded practicals tools and numerical techniques to study the micro-topographical configuration and its impact on overland flow connectivity at the interrill scale.

8.2 Limitations and perspectives

Although very promising, several issues remain to be solved before the proposed connectivity indicator can be used effectively in distributed hydrological models. Indeed, the RSC function requires detailed micro-topography information, which is not easily obtained. We developed a methodology for characterizing the RSC function at the square meter scale based on micro-topographical measurements on molded surfaces, but this is not easily extended to larger scales for practical reasons. It is as yet unknown how the RSC function is affected by scale and whether its determination on 1 m^2 surface elements can be extrapolated to larger scales (10-100 m^2). A digital elevation model of an experimental plot with a spatial resolution of 1.5 mm millimeter was used to illustrate the effect of the scale on the RSC function. We computed the RSC function for a square area of 1.5 x 1.5 m, then for only the upper left quarter of

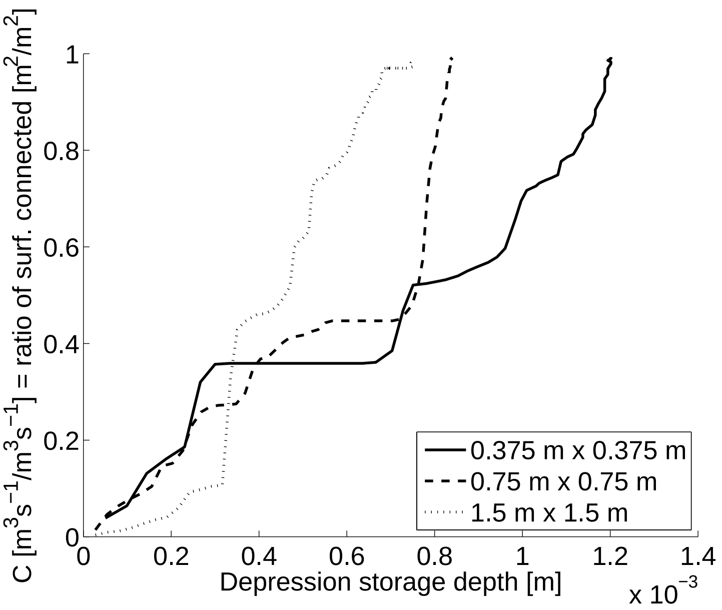

Figure 8.1: Scale effect on the RSC function, showed for nested areas of 3 different sizes.

it (0.75 x 0.75 m) and finally for the upper left quarter of the previous upper left quarter (1/16 of the initial surface, 0.375 x 0.375 m). The resulting RSC functions are shown in Figure 8.1. We see that there is a scale dependence, as the maximum depression storage depth tends to decrease with scale. This decrease is either due to the decrease of boundary effects that form a virtual barrier around the area considered, or is due to a natural change in the roughness or the connectivity of the surface with the slope distance. The effect of the spatial resolution of the elevation data on the RSC function will have to be investigated too.

Furthermore, it is necessary to determine the time rate of change of the RSC function as a function of initial soil roughness, soil characteristics, surface slope and boundary conditions. This would require the monitoring of the temporal dynamics of the RSC function for 1 m^2 plots for different initial soil roughnesses, slopes and soil types, with our molding method and a laser scanning or based on databases of digital elevation models.

To estimate the RSC function, the knowledge of the maximum depression storage seems essential. Yet, we have seen in Fig 3.3 that the estimation of the maximum depression storage based on the knowledge of the slope and RR may suffer of a significant overestimation, as the

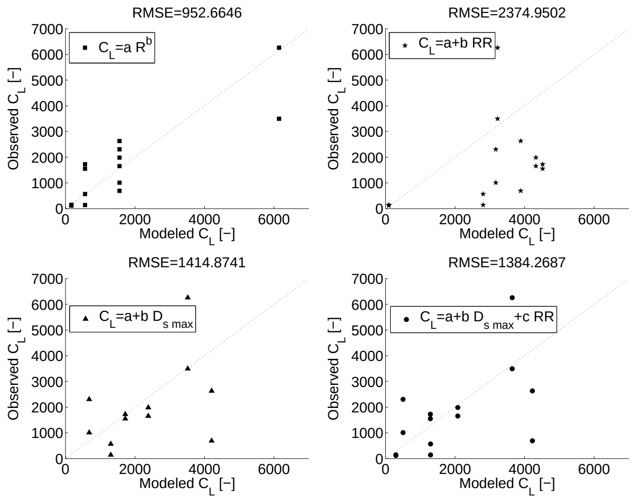

Figure 8.2: Estimations of the friction constant C_L [-] based on the cumulative rainfall erosivity value R [MJ.ha^{-1}.mm.h^{-1}], the random roughness RR [m] and the maximum depression storage value $D_{s\,\max}$ [m]. a, b and c are fitting constants.

appearance of small connectors at the soil surface can decrease the maximum depression storage significantly without affecting too much neither the random roughness value nor the slope. The scanning of the soil surface, or better its molding, may provide a more reliable approach to measure the maximum depression storage. The knowledge of the maximum depression storage value may also serve to assess the friction constant. Indeed we have seen that both terms evolved with R, among others because the erosion of the small passes between depressions affects both terms. The estimation of the friction constants C_L is illustrated in Figure 8.2. As we see, our best predictions of C_L were found using the rainfall erosivity value R. When using the RR value, the estimation is bad, while using the maximum depression storage value provides yet much better results. When combining RR with the maximum depression storage, the results are only slightly improved.

In addition, a methodology must be developed to integrate in practice the proposed connectivity function in a distributed hydrological model, for instance by simulating conjointly two systems: the interrill area and the rill network. This would require numerical simulation of water flow on large (10-1000 m^2) and smaller (e.g.,1 m^2) grid elements by means of a rainfall-runoff distributed hydrological model which solves the Saint-Venant equation, if possible not simplified, as well as comparison with measured hydrographs from an equipped hillslope. Various ways of combining subgrid hydrographs will have to be tested against modeled hydrographs based on available soil micro-topographical scans and field measured hydrographs from a hillslope. Our indice could also be computed in presence of oriented roughness features, whose effect was up to now neglected. But oriented roughness features may show a characteristic length much larger than the one of soil roughness provoked by clods distribution. Therefore we will have to pay extra attention to boundary effects, to avoid the overestimation of depression storage in oriented roughness features. We must thus compute our indice for areas sufficiently large to be representative of the real effect of oriented roughness features on depression storage. At the same time, we must consider the fact that oriented roughness may deviate the main flow direction and therefore may displace the reference point for which the connectivity must be assessed.

Finally, there is the problem of infiltration. As explicitly mentioned in its definition, functional connectivity depends on boundary conditions and hence on infiltration. Although, the two hypotheses that underlined this work were that the infiltration rate never exceeded rainfall intensity, such that there was always a zero or a net supply of water, and that this net supply is spatially uniform. This ensures that runoff is produced uniformly over the area and that the water depth in depressions never decreases. For the RSC function computation, a uniform infiltration could be taken into account without problem but its rate must be less or equal to the rainfall rate. The cumulated input of water considered for the computation of the simplified hydrograph and the RSC function will hence concern the effective rainfall supply, which is the rainfall supply minus the infiltration. Take note that permanent or non permanent supply will produce the same simplified hydrograph and RSC function as those are not dependent on the discharge rate but rather on its cumulative value.

If infiltration was not uniform but lower than the rainfall supply, the shape of the RSC function would then depend on initial and boundary conditions. Depressions would show various infiltration capacities. If a uniform water supply to overland flow was still conceptually considered to compute the RSC function, it will be as if the individual contributive areas for each depressions were proportionally increased or decreased in relation with the proportional decrease or increase of infiltration capacity.

If infiltration was uniform but larger than the rainfall supply, the water depth in depression would decrease. This will lead to hysteretic effects as the emptying of depressions will not occur in the inverse sequence of their filling. If infiltration was in addition not uniform, the system could not be characterized with a simple equation, but will require detail modeling, eventually with a full conceptual multiple compartment topography such as in Figure 7.5, which will be leaking this time.

The fact that we did not consider infiltration was chosen to simplify the problem. In practice, infiltration is highly variable in space, even at short distance. As an example, due to surface sealing, the infiltration is highly reduced in the depressions compared to infiltration at the clods surface. Differences in hydraulic head between depressions and clods may partly compensate for these differences. Therefore, the variability of infiltration should in theory be taken into account. But including spatially non uniform infiltration would first require measurement techniques that are able to capture this variability. Up to now, direct measurement tools applicable under field conditions investigated surfaces much larger than individual clods surface, which inevitably smooths out variability.

Appendices

Appendix A

Digital elevation models

In this section, we show the different digital elevation models (DEM) of the ten waterproof casts. The DEM are grouped by cumulative rainfall erosivity value (R) to which they correspond: R = 0 (2 repetitions), R = 45 (2 repetitions), R = 115 (3 repetitions), R = 230 (2 repetitions) and R $\approx$ 677 (1 repetition).

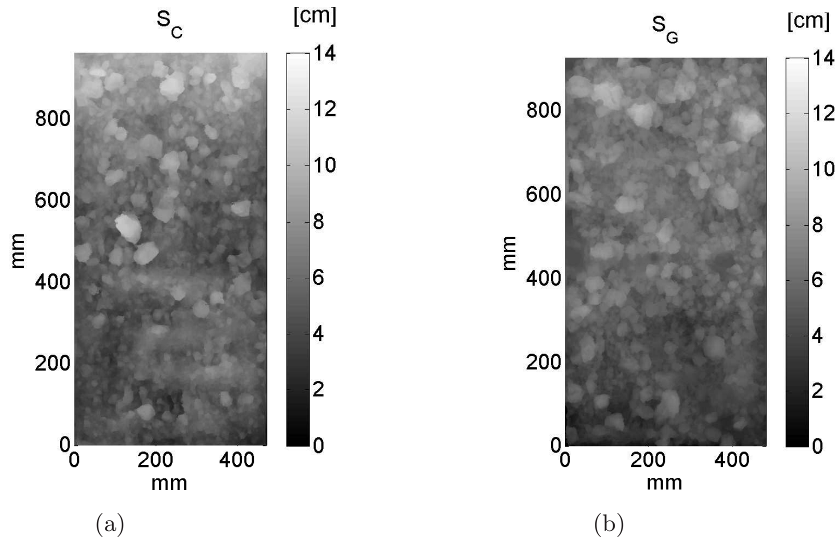

Figure A.1: Digital elevation models of the casts, just after tillage (R=0). $S_C = S1$, $S_G = S2$.

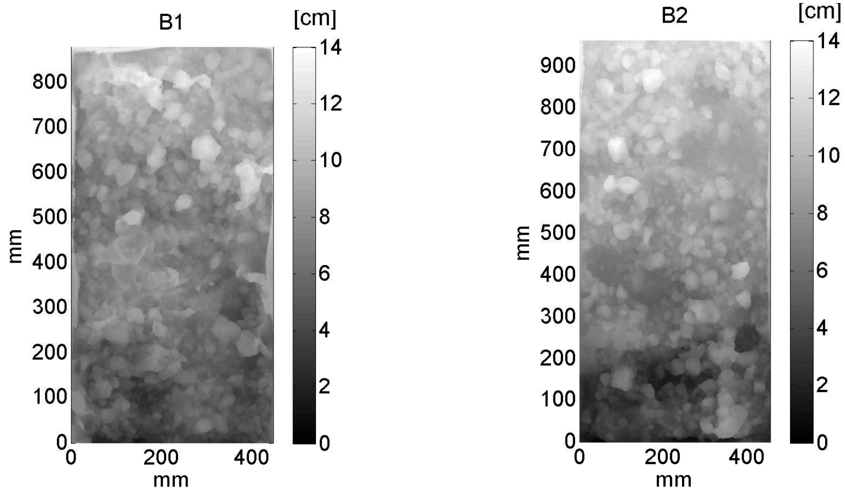

(a) (b)

Figure A.2: Digital elevation models of the casts, after a first period of rain (R=45)

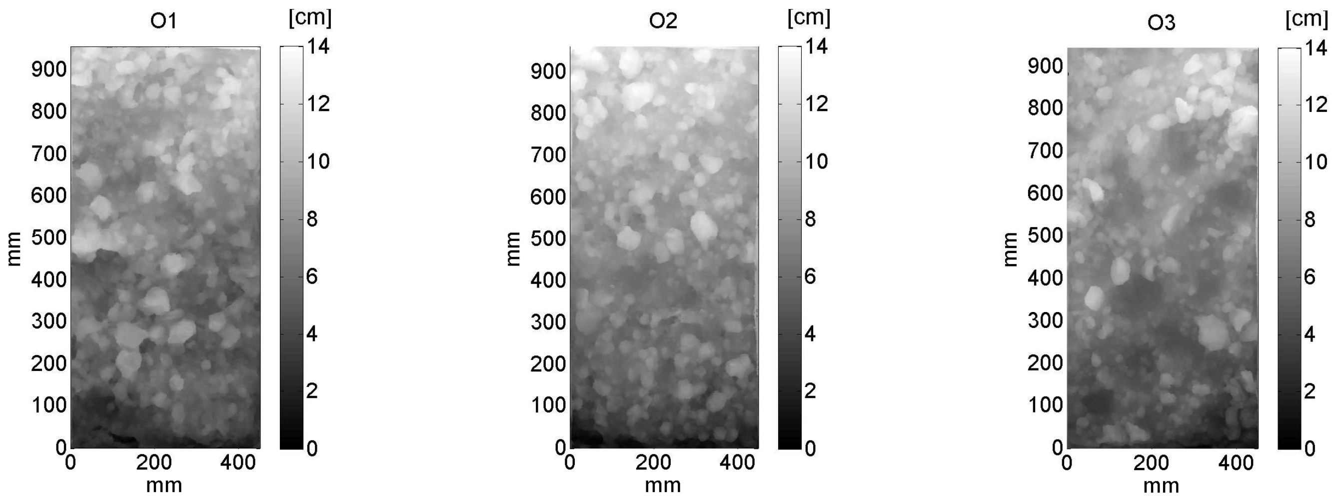

(a) (b) (c)

Figure A.3: Digital elevation models of the casts, after a second period of rain (R=115)

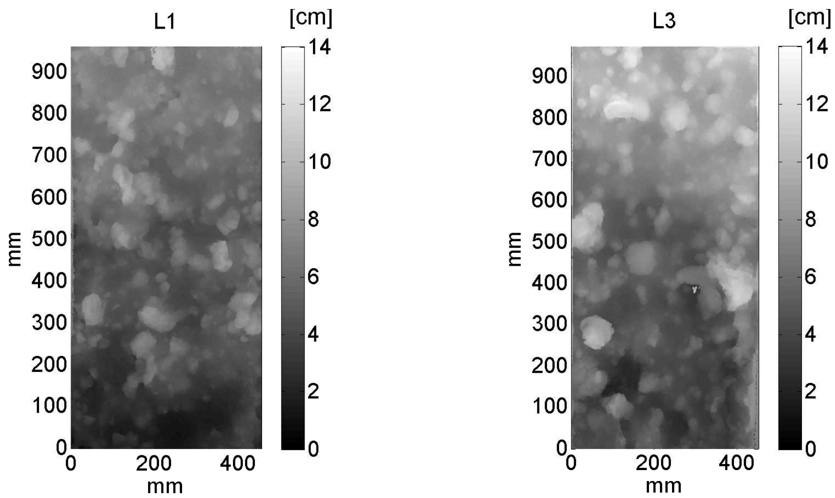

(a) (b)

Figure A.4: Digital elevation models of the casts, after a last period of rain (R=230)

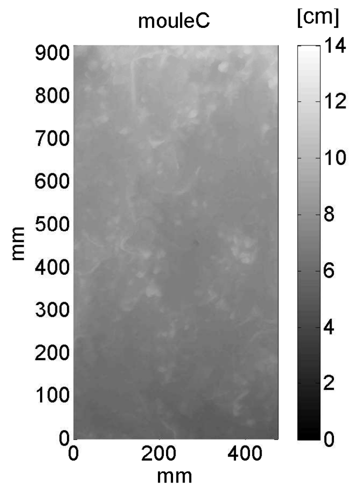

Figure A.5: Digital elevation model of the cast, taken on another plot, after 5 months of rain (R≈677)

Appendix B

Experimental overland flow on a corrugated surface

For the validation of the overland flow model (Chap. 4), we confronted the numerical solutions to the observations of experimental 1-D steady-state overland flows on a corrugated PVC surface (flow is perpendicular to the furrows), with an amplitude of 8 mm and a wave length of 32 mm. In the experimental flumes, the slope was adjustable as well as the runon intensity (Fig. B.1). Water depth was estimated by diving plastic sheets previously coated with a soluble dye (Potassium permanganate). Were the water was flowing, the dye was washed off the plastic sheets, allowing to clearly identify the water level on the plastic sheets. The mean water level was then computed. The velocity could no be assessed by floating polystyrene beads as they blocked on the crests of the corrugated PVC surface. Therefore the mean velocity was assessed by timing the center of a plume created with a droplet of dye (Brilliant Blue).

The main characteristics of the overland flow experiments on a corrugated PVC surface are provided in Table B.1. The experiment was repeated 6 times, considering 3 slopes ($\approx 2\%$, $\approx 5-8\%$ and $\approx 11\%$) and 2 types inflow rates (low and high runon). Measurements of velocity were repeated 3 times in order to get an estimation of the confidence intervals (calculated as ± 1.96 the standard deviation). The standard deviation of the water depth was directly derived from the variation of the observed water levels along the flow. Figure B.2 shows the comparison between the numerical simulations and the observations. The RMSE is 0.09 m/s for the velocity, 3.55 mm for the water depth and 2.37 s for the propagation time. Compared to the results for the flow on rough planes, water depth error is much larger. This is mainly due to the diffusive wave simplification that neglects the convective term ($\frac{\bar{v}_x}{g}\frac{\partial \bar{v}_x}{\partial x}$). In the

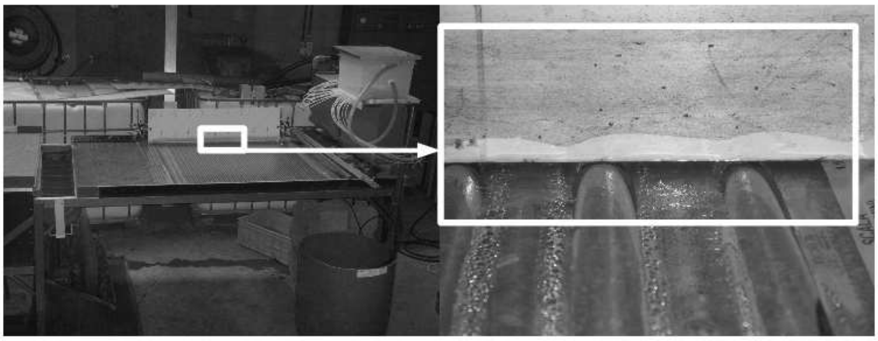

Figure B.1: Experimental flume to measure overland flow on a corrugated surface (left) and dye-coated plastic sheet used for measuring water thickness (right).

Table B.1: Main characteristics of the overland flow experiments on a corrugated PVC surface.

mean grain diameter [mm]	Slope [%]	q_0 [cm^2 s^{-1}]	velocity [m s^{-1}]	water depth [mm]	propagation time [s]
≈ 0	1.77	0.85 ± 0.05	0.06 ± 0.02	0.72 ± 0.72	-
≈ 0	2.58	7.29 ± 0.69	0.18 ± 0.05	4.41 ± 3.08	11.7
≈ 0	7.59	3.76 ± 0.69	0.11 ± 0.04	2.24 ± 1.66	13.8
≈ 0	4.77	7.28 ± 0.48	0.13 ± 0.02	3.48 ± 1.68	11.1
≈ 0	11.05	3.47 ± 0.51	0.10 ± 0.01	3.48 ± 2.60	13.1
≈ 0	10.82	9.64 ± 0.25	0.17 ± 0.03	7.54 ± 5.02	9.2

model, water can only flow in the direction of an absolute decreasing water level. The small hydraulic jumps are therefore not represented by the model although those are recognised as an important source of surface detention (Dunkerley, 2003). This is a major drawback of the model, which leads to an underestimation of the water depth, as shown in Figure B.3. This underestimation of surface detention migth possibly be compensated for by considering larger friction factors.

The discrepancies between the observed and simulated velocities may partially be explained by the fact that the velocity field was very heterogeneous, mainly due to velocity profiles not uniform at all, especially in depressions. Therefore assessing the mean velocity of the plume of dye was really difficult as some of the dye was blocked in quasi-immobile

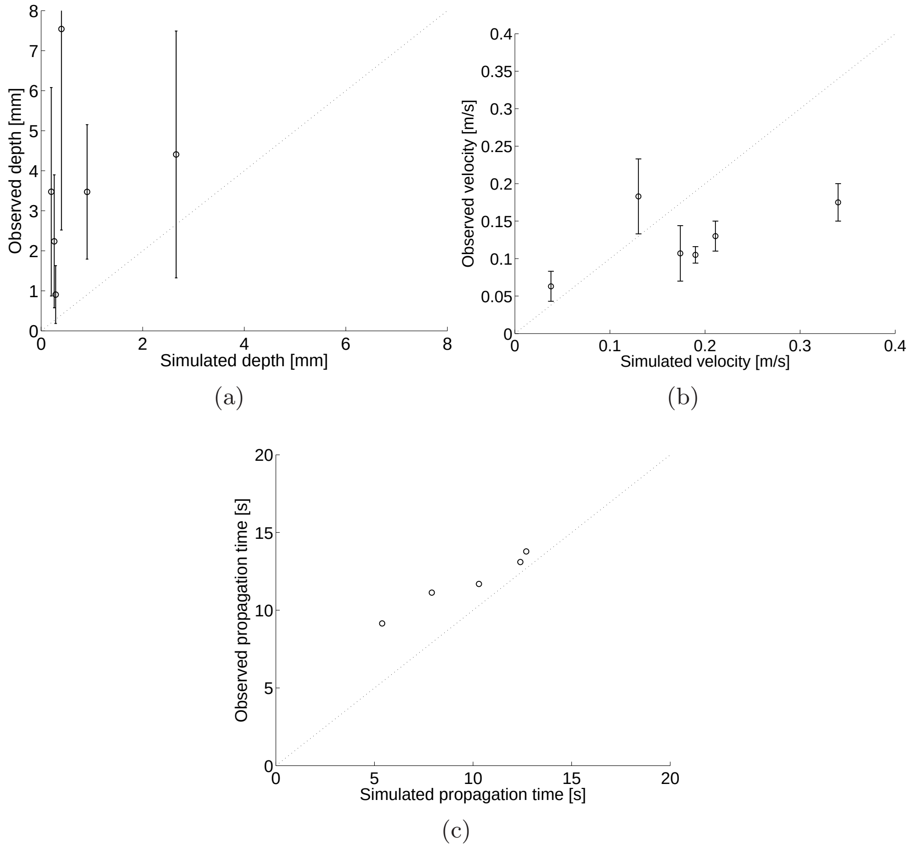

Figure B.2: Comparison between simulations and observations of overland flow properties, for a corrugated surface.

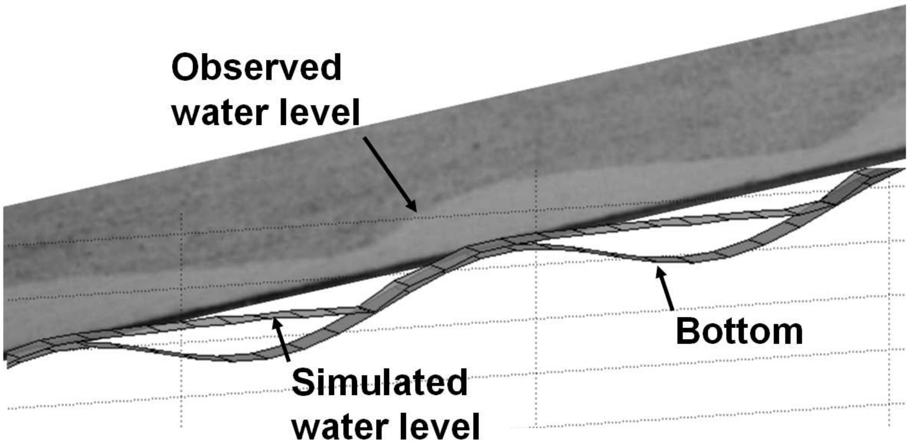

Figure B.3: Discrepancies between the modeled water level and the observation for an overland flow on a corrugated surface: underestimation of the surface detention provoked by hydraulic jumps

water at the bottom of depressions. Finally, the underestimation of the propagation time for the model is probably due to an underestimation of the surface detention, as, for the smaller runon rates that provoked the longest propagation times and the smaller surface detentions compared to depression storage, observations and simulations fitted more closely.

Appendix C

Measured and modeled hydrographs

In this section, we show the different modeled and measured hydrographs for the rainfall simulation on the waterproof casts. The hydrographs are grouped by cast.

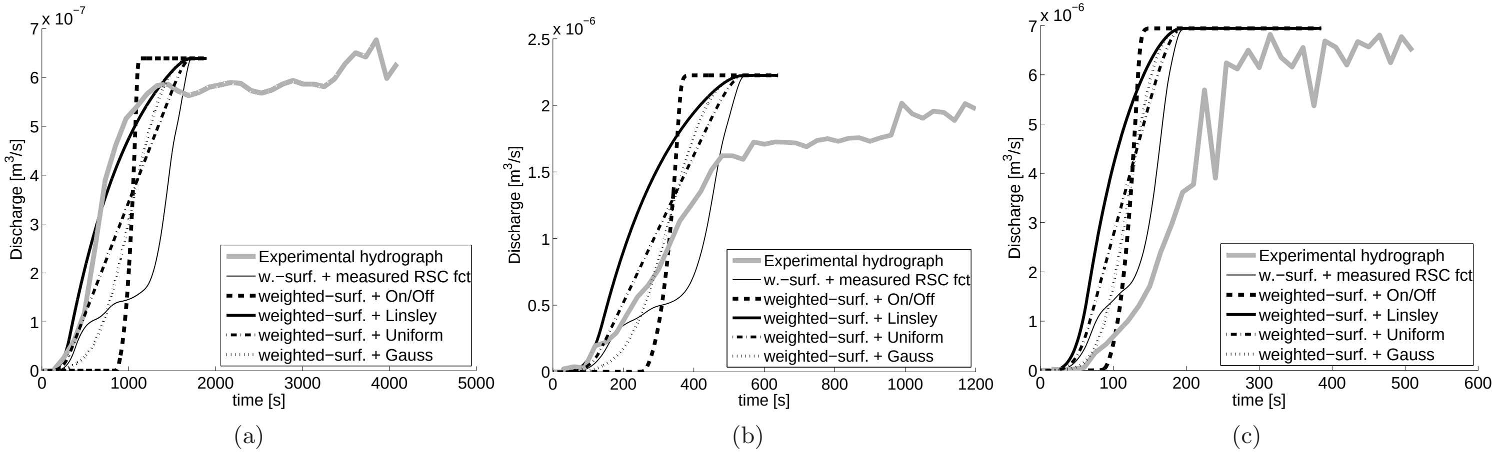

Figure C.1: Hydrographs for the cast 1 (S1), with a low (a), a medium (b) or a high (c) rainfall supply.

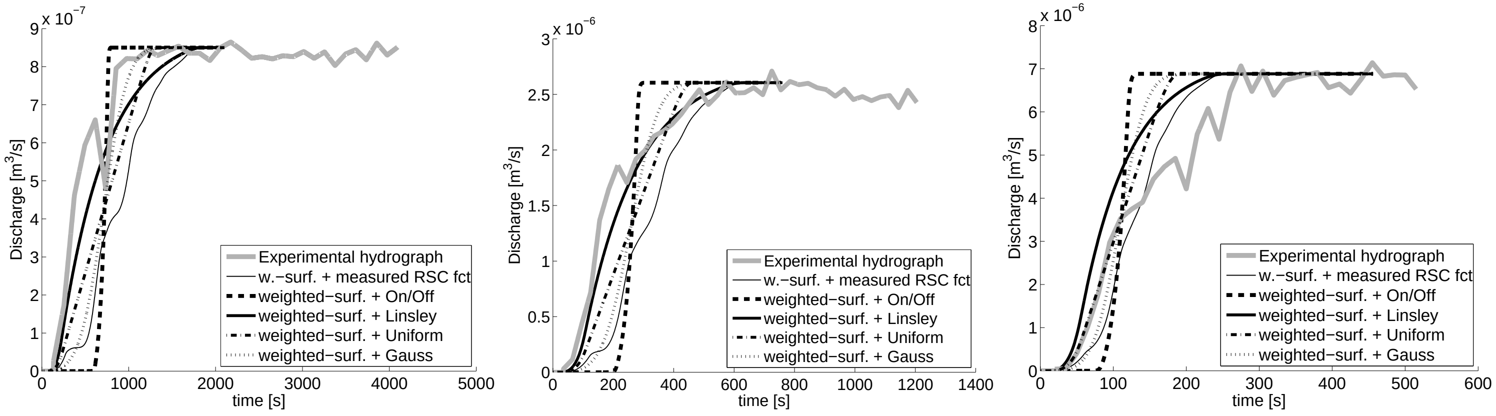

(a) (b) (c)

Figure C.2: Hydrographs for the cast2 (S2), with a low (a), a medium (b) or a high (c) rainfall supply.

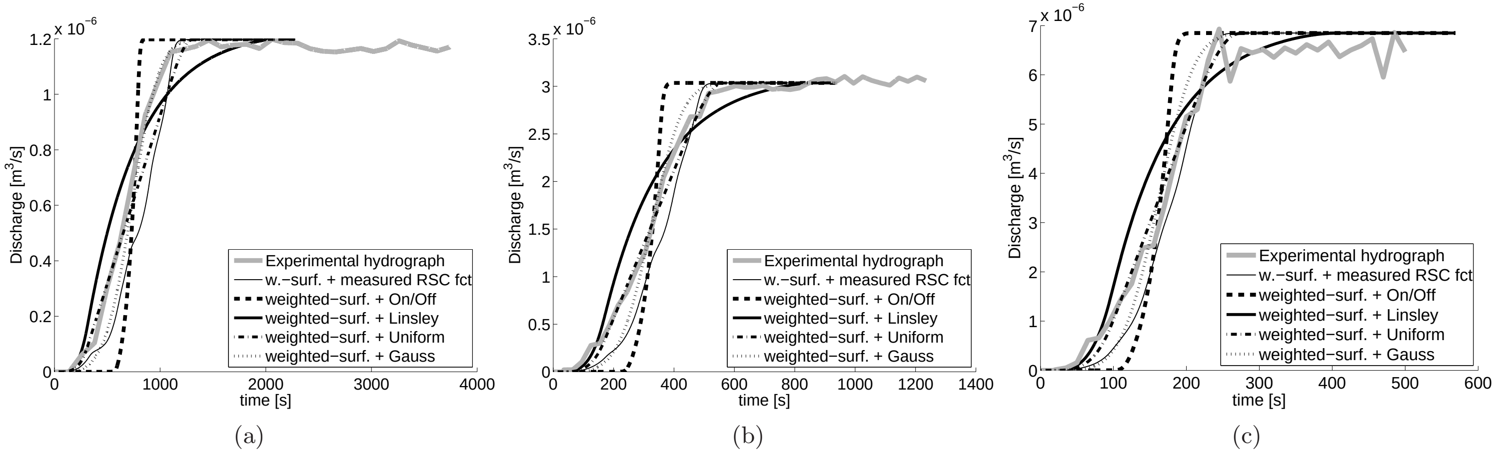

Figure C.3: Hydrographs for the cast 3 (B1), with a low (a), a medium (b) or a high (c) rainfall supply.

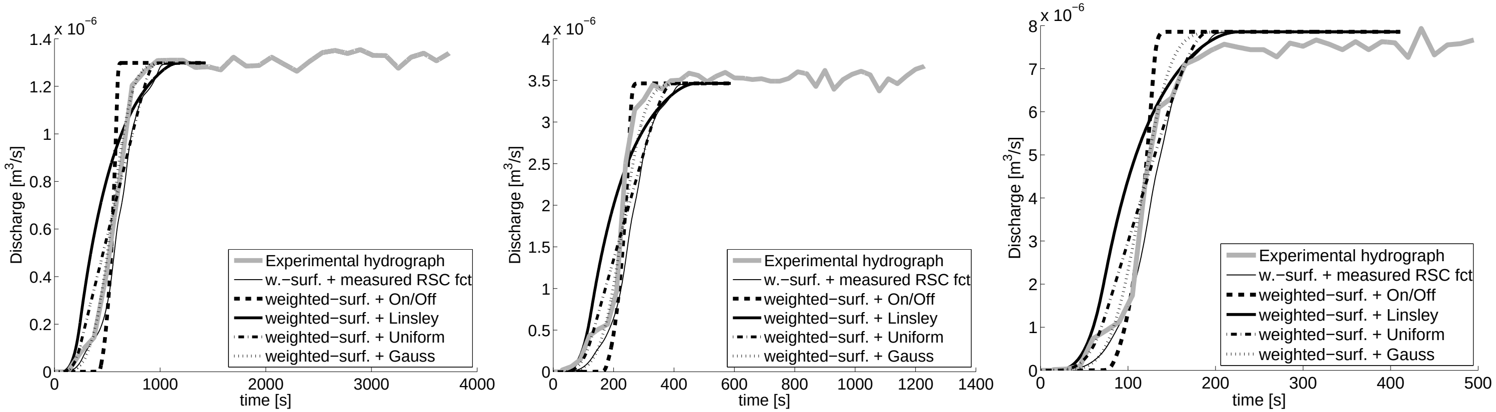

(a) (b) (c)

Figure C.4: Hydrographs for the cast 4 (B2), with a low (a), a medium (b) or a high (c) rainfall supply.

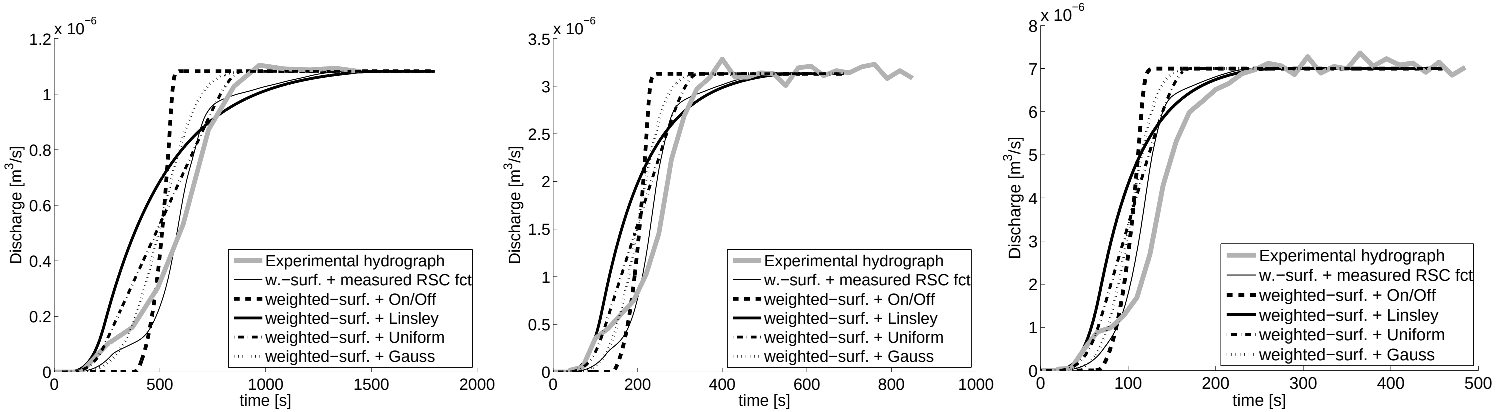

(a) (b) (c)

Figure C.5: Hydrographs for the cast 5 (O1), with a low (a), a medium (b) or a high (c) rainfall supply.

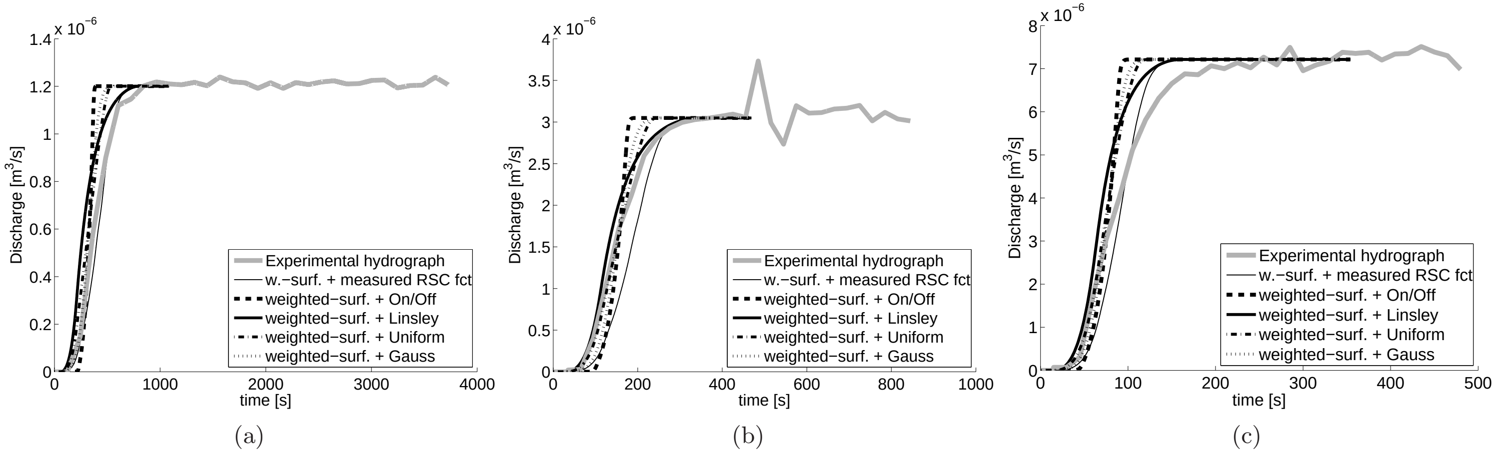

Figure C.6: Hydrographs for the cast 6 (O2), with a low (a), a medium (b) or a high (c) rainfall supply.

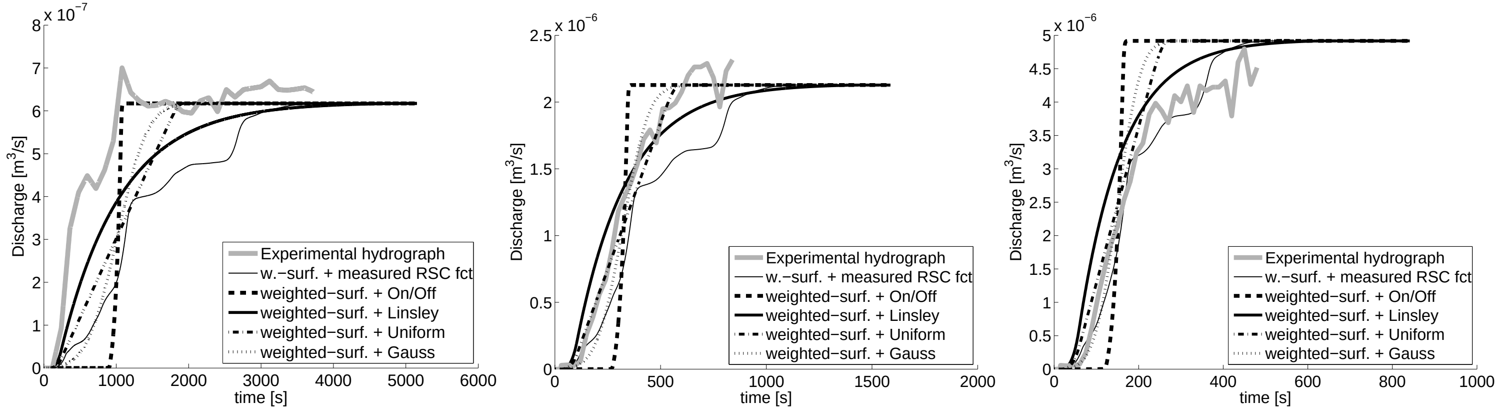

(a) (b) (c)

Figure C.7: Hydrographs for the cast 7 (O3), with a low (a), a medium (b) or a high (c) rainfall supply.

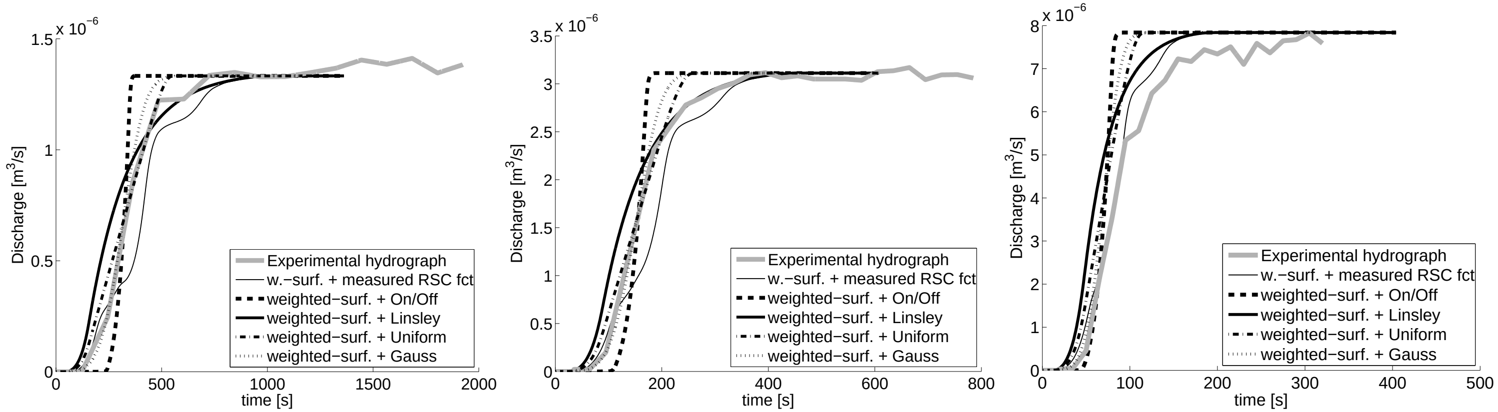

(a) (b) (c)

Figure C.8: Hydrographs for the cast 8 (L1), with a low (a), a medium (b) or a high (c) rainfall supply.

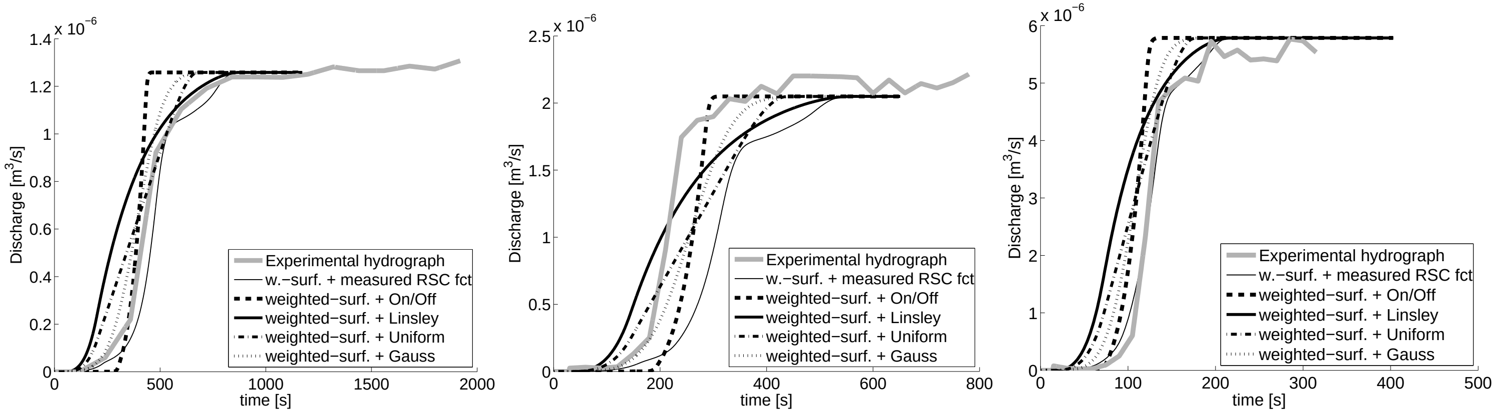

(a) (b) (c)

Figure C.9: Hydrographs for the cast 9 (L3), with a low (a), a medium (b) or a high (c) rainfall supply.

Appendix D

Source code

We provide here the source code, in FORTRAN 90 language, of the physical overland flow model (DIRECT FLOW), which use a function to compute the water velocity (WATERSPEED), and the filling algorithm (COND WALKER).

D.1 DIRECT FLOW script

```
!
!  PROGRAM:
! DIRECT_FLOW      - Entry point of console application.
!

!*****************************************************
!
!  Main: DIRECT_FLOW
!
! M. Antoine (19/04/07)
! Modèle de ruisselement, basé sur un bilan de force à
! l’équilibre au sein du pas de temps: pas de variation
! de quantité de mouvement dans l’espace pris en compte.
!
!*****************************************************

! shéma spatial:
! dem (nx,ny) est chargé dans z, en préservant une bande
! de 0 tout autour :
! -----
```

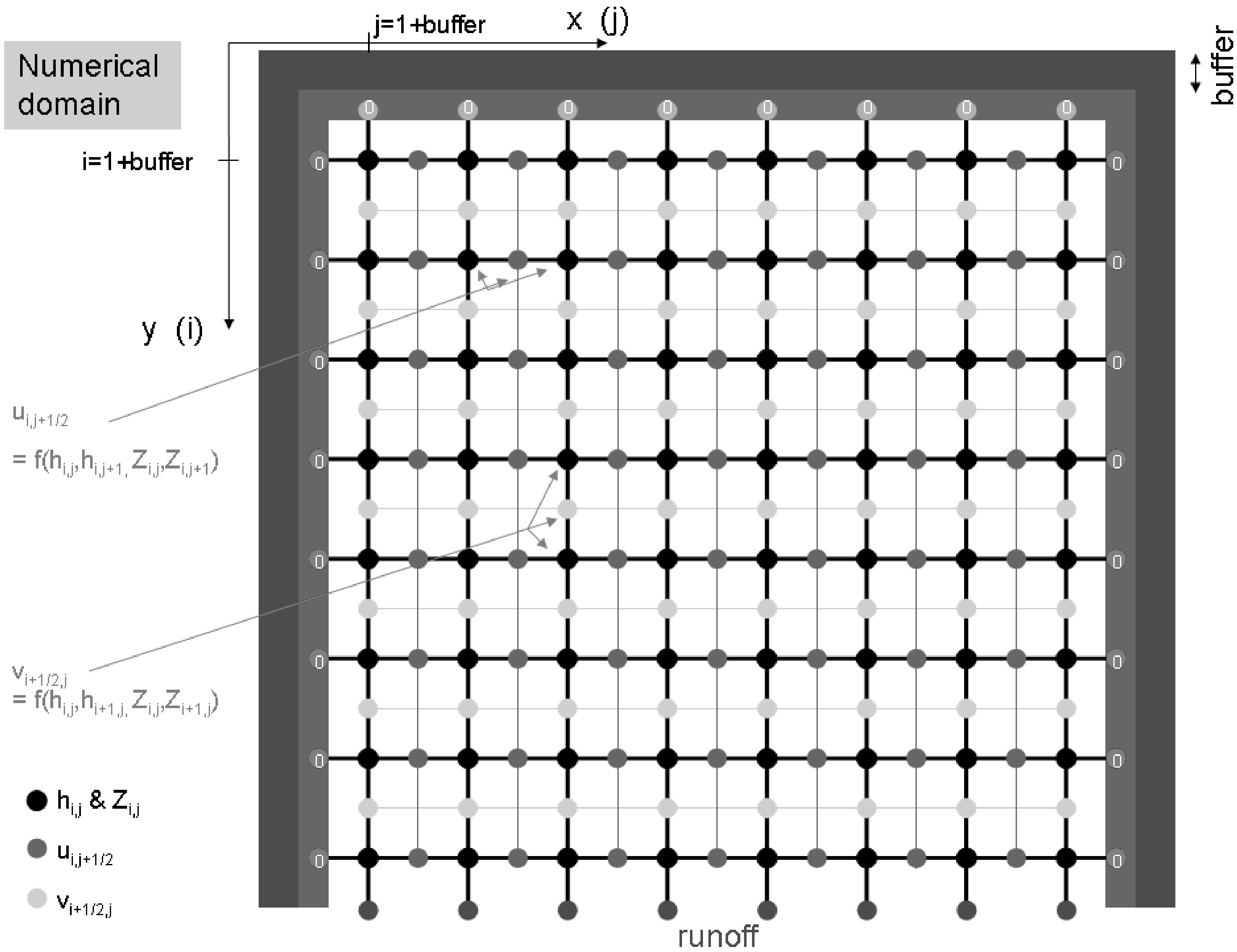

Figure D.1: DIRECT FLOW numerical domain.

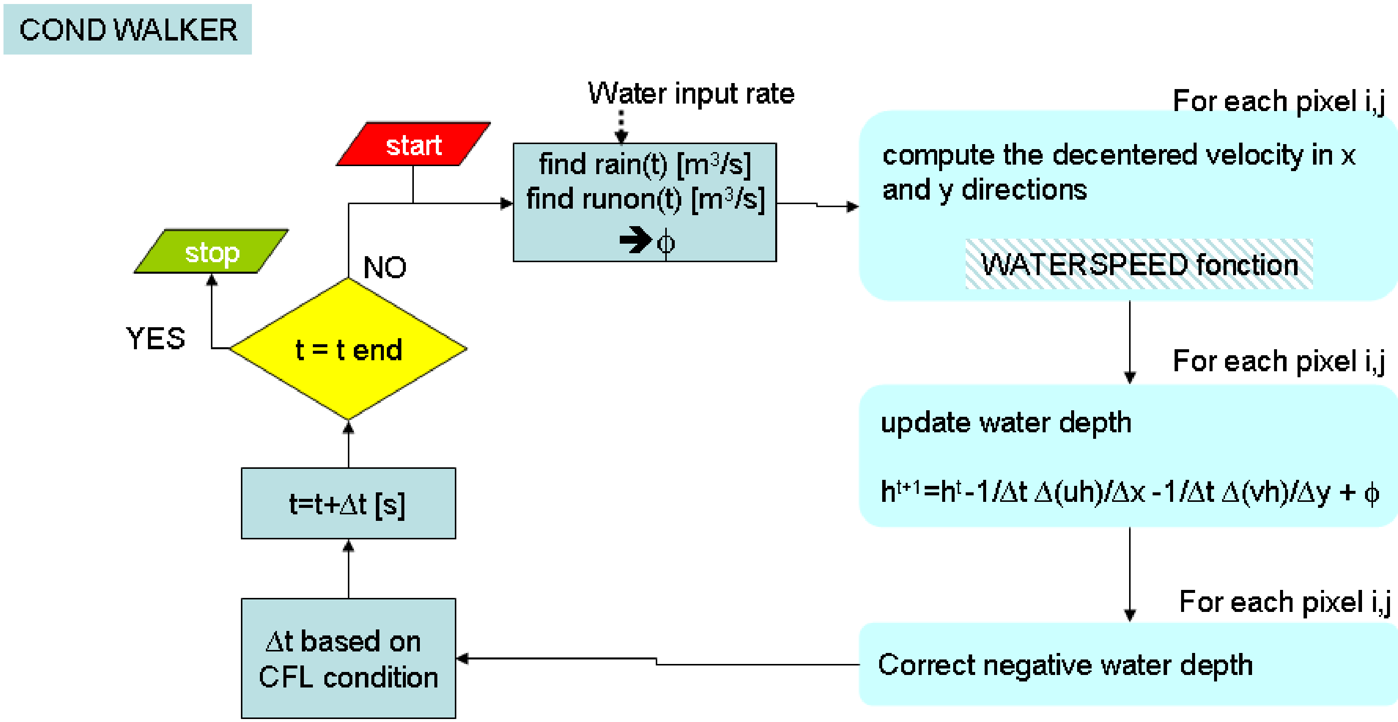

Figure D.2: DIRECT FLOW functioning scheme.

```
! |   |
! -----
!
! zone de calcul
! .....
! .   .
! .....
!
! o: h_t, h_tp1, z, u, v (nx+2*bufferStrip,ny+2*bufferStrip)
! x: h_x, u_dc (nx+2*bufferStrip-1,ny+2*bufferStrip)
! *: h_y, v_dc (nx+2*bufferStrip,ny+2*bufferStrip-1)
!
! bufferStrip =2
! <----------->
!
! o=0 x=0 o=0 x=0 o=0 x=0 o=0 x=0 o=0 x=0 o=0 x=0 o=0 x=0 o=0
!
! *=0     *=0     *=0     *=0     *=0     *=0     *=0     *=0
!
! o=0 x=0 o=0 x=0 o=0 x=0 o=0 x=0 o=0 x=0 o=0 x=0 o=0 x=0 o=0
!
! *=0     *=0     *=0     *=0     *=0     *=0     *=0     *=0
!                 .........................
! o=0 x=0 o=0 x=0 .o--x---o---x---o---x---o.  x=0 o=0 x=0 o=0
!                 .|                      |.
! *=0     *=0     .*      *       *       *.      *=0     *=0
!                 .|                      |.
! o=0 x=0 o=0 x=0 .o  x   o   x   o   x   o.  x=0 o=0 x=0 o=0
!                 .|                      |.
! *=0     *=0     .*      *       *       *.      *=0     *=0
!                 .|                      |.
! o=0 x=0 o=0 x=0 .o  x   o   x   o   x   o.  x=0 o=0 x=0 o=0
!                 .|                      |.
! *=0     *=0     .*      *       *       *.      *=0     *=0
!                 .|                      |.
! o=0 x=0 o=0 x=0 .o--x---o---x---o---x---o.  x=0 o=0 x=0 o=0
!                 .                        .
! *=0     *=0     .*      *       *       *.      *=0     *=0
!                 .........................
! o=0 x=0 o=0 x=0 o=0 x=0 o=0 x=0 o=0 x=0 o=0 x=0 o=0 x=0 o=0
!
! *=0     *=0     *=0     *=0     *=0     *=0     *=0     *=0
```

```
!
! o=0 x=0 o=0 x=0 o=0 x=0 o=0 x=0 o=0 x=0 o=0 x=0 o=0 x=0 o=0


!*******************************************************
! les conditions limites sont donc:
!   - une vitesse nulle sur les bords latéraux et sur le
! bord amont
!   - une vitesse calculée par WATERSPEED en considérant
!     une hauteur d'eau nulle à j+1 et un un altitude
! similaire à j et j+1

program DIRECT_FLOW

!USE AVDef
!USE DFLIB
   !****************************************************
! DECLARATION VARIABLES
implicit none
!coordonnées topographiqes
real, allocatable, dimension (:,:) :: dem, z
real dx,dy
!hauteurs d'eau [m] NB:a(m,n) = m columns and n lines
real, allocatable, dimension (:,:) :: h_t, h_tp1, h_x, h_y, hmean
!vitesses [m/s], en x (u) et en y (v)
real,allocatable,dimension (:,:) :: u,umean,u_dc,Qx_dcmean,u_dc_last
real,allocatable,dimension (:,:) :: v,vmean,v_dc,Qy_dcmean,v_dc_last
!débit aval [m3/s]
real, allocatable, dimension (:,:) :: Q_dev
!données temporelles et constantes de stabilité
real(8) t, dt, t_debut, t_fin, dt_ini, dt_max, dt_min
real Cn
!hydrogram (G étant la moyennisation de l'hydrogramme
!pour countMax itération)
real, allocatable, dimension (:,:) :: hydrogramG
!données d'apport d'eau (pluie et débit amont) et infiltraion
real, allocatable, dimension (:,:) :: Rain, Q_up, Connectivity
real Infi
!bilan de masse et masse en défaut [m3]
real BILAN, DEFAUT
!cumul des déversement aval, de la pluie et des apports amonts
real Q_dev_cum, Q_R_I_cum, Q_up_cum
```

```
!paramètre de détermination de l'apport à prendre en compte
real lastData, lastData2, R, Q
!paramètre de la procédure de comblement des hauteurs d'eau négatives
real h_neg, h_sum
!valeur pour calcul des moyennes sur countMax itérations
real tmean, dtmean, Q_devT_mean, RT_mean, RT_QT_mean, Rmean
! fonction de calcul de la vitesse par Darcy Weisbach
real WATERSPEED
real t_print
! prise en compte de la connectivité dans plan linéaire
integer ConnectOK
real SurfStorage, Conn ! true/false, m3, -
! methode d'integration lineaire multistep d'Adams-Bashforth
integer AdamsOK
integer AdamsCount
real, allocatable, dimension (:,:) ::rh_0,rh_1,rh_2
real, allocatable, dimension (:,:) ::Q_dev_0,Q_dev_1,Q_dev_2
!compteurs divers
integer nx, ny, i, j, ii, jj, nP, nQ, count, count2, countMax, nC
! paramètres pour archivages intermédiaires des résultats
integer nnn
! procédure hauteurs d'eau négatives
integer bufferStrip,neighb

! zone d'amenenée de débit amont: le débit amont sera amené
! sur toute la largeur et sur QinStrip pixels (en y) tout à
! l'amont du dem
integer QinStrip

! arguments pour la fonction WaterSpeed, pour la résolution
! de Darcy-W en turbulent
integer method
real paramMeth
real C_L

! température, pour calcul de la viscosité de l'eau et visco-
! sité cinématique [m2/s] (1e-6 à 20°C, 1.3e-6 à 10°C)
real t_degree, nu

! valeur pour le calcul du temps de propagation du front d'eau
! (tip lancement chrono, top arrêt chrono, et i j les coord des
! cellules de tip top)
```

```
integer tipCell_i,tipCell_j,topCell_i,topCell_j
real tip,top

! vitesse maximum admissible
real v_max

!chaines de caractères
character*100 titre
character FileName*13
character FileName1*13
character FileName2*9
character FileName3*9
character FileName4*9
character FileName5*9
character FileName6*8
character FileName7*8
character FileName8*12
character FileName9*12


   !****************************************************
!! DECLARATION CONSTANTES
real g, rho ! constantes: g la gravité 9.81m/s2;
! rho la masse volumique de l'eau [kg/m3]
! et C_L la constante pour le nominateur en
! situation laminaire
parameter(g=9.81, rho=1000.)
   !****************************************************
! ATTRIBUTION DES VALEURS
! chargement dem et introduction dans z
open (unit=1, file='dem.in', status='old')
read(1,*) titre
read(1,*) ny, nx

AdamsCount=0
SurfStorage=0.

if (nx.eq.1) then
print *, 'Connectivity computation (0/1) ? nb: if 1, &
&connect.in required';read *, ConnectOK
if (ConnectOK.eq.1) then
print *, 'Connectivity taken into account'
```

```
endif
if (ConnectOK.eq.0) then
print *, 'Connectivity NOT taken into account'
endif
endif

read(1,*) titre
read(1,*) dy, dx !taille maille (m)
read(1,*) titre
read(1,*) bufferStrip



! allocation des matrices liées à la taille du dem et
! du bufferStrip
allocate (dem(nx,ny))
allocate (z(nx+2*bufferStrip,ny+2*bufferStrip))
allocate (h_t(nx+2*bufferStrip,ny+2*bufferStrip))
allocate (rh_0(nx+2*bufferStrip,ny+2*bufferStrip))
allocate (rh_1(nx+2*bufferStrip,ny+2*bufferStrip))
allocate (rh_2(nx+2*bufferStrip,ny+2*bufferStrip))

allocate (h_tp1(nx+2*bufferStrip,ny+2*bufferStrip))
allocate (h_x(nx+2*bufferStrip-1,ny+2*bufferStrip))
allocate (h_y(nx+2*bufferStrip,ny+2*bufferStrip-1))
allocate (hmean(nx+2*bufferStrip,ny+2*bufferStrip))
allocate (u(nx+2*bufferStrip,ny+2*bufferStrip))
allocate (umean(nx+2*bufferStrip,ny+2*bufferStrip))
allocate (u_dc(nx+2*bufferStrip-1,ny+2*bufferStrip))
allocate (Qx_dcmean(nx+2*bufferStrip-1,ny+2*bufferStrip))
allocate (u_dc_last(nx+2*bufferStrip-1,ny+2*bufferStrip))
allocate (v(nx+2*bufferStrip,ny+2*bufferStrip))
allocate (vmean(nx+2*bufferStrip,ny+2*bufferStrip))
allocate (v_dc(nx+2*bufferStrip,ny+2*bufferStrip-1))
allocate (Qy_dcmean(nx+2*bufferStrip,ny+2*bufferStrip-1))
allocate (v_dc_last(nx+2*bufferStrip,ny+2*bufferStrip-1))

allocate (Q_dev(nx+2*bufferStrip,1))
allocate (Q_dev_0(nx+2*bufferStrip,1))
allocate (Q_dev_1(nx+2*bufferStrip,1))
allocate (Q_dev_2(nx+2*bufferStrip,1))
```

```
read(1,*) titre
read(1,*) QinStrip
read(1,*) titre

do i=1,ny
read(1,*) (dem(j,i),j=1,nx)
enddo
close (1)
! z, le dem entouré de 0
z=0.; !altitude de 0 entourant le dem
do i=bufferStrip+1,ny+bufferStrip
do j=bufferStrip+1,nx+bufferStrip
z(j,i)=dem(j-bufferStrip,i-bufferStrip)
enddo
enddo
! chargement des apports d'eau
open (unit=1, file='water.in', status='old')
read(1,*) titre
read(1,*) nP, nQ
allocate (Rain(2,nP))
allocate (Q_up(2,nQ))
read(1,*) titre
do i=1,nP
read(1,*) (Rain(j,i),j=1,2)
enddo
read(1,*) titre
do i=1,nQ
read(1,*) (Q_up(j,i),j=1,2)
enddo
close (1)

! chargement de la connectivité
if (ConnectOK.eq.1) then
open (unit=1, file='connect.in', status='old')
read(1,*) titre
read(1,*) nC
allocate (Connectivity(2,nC))
read(1,*) titre
do i=1,nC
read(1,*) (Connectivity(j,i),j=1,2)
enddo
endif
```

```
! chargement des données temporelles
open (unit=1, file='time.in', status='old')
read(1,*) titre
read(1,*) t, t_debut, t_fin
read(1,*) titre
read(1,*) dt_ini, dt_min, dt_max
read(1,*) titre
read(1,*) Cn
read(1,*) titre
read(1,*) countMax, t_print
if (t_fin>99.*t_print) then
write(*,*) 't_print trop petit! 99 archives maximum, &
&ou les données seront écrasée au fur et a mesure &
&(press enter)'
read(*,*)
endif
read(1,*) titre
read(1,*) C_L, method, paramMeth
read(1,*) titre
read(1,*) AdamsOK
read(1,*) titre
read(1,*) v_max
read(1,*) titre
read(1,*) t_degree
read(1,*) titre
read(1,*) tipCell_i,tipCell_j,topCell_i,topCell_j
close (1)
allocate (hydrogramG(6,int((t_fin-t_debut)/(dt_min*(countMax)))))

!Calcul de la viscosité par la formule de Sutherlands
nu=(2.414e-5*10.**(247.8/(273.15+t_degree-140.)))/rho

   !*************************************************
!INITIALISATION DES VALEURS (NULLE)

nnn=int(t/t_print)+1 ! vaut 1 s'il n'y a pas eu d'autre
 ! simulation préalable et que t = 0
write(*,*) 'nnn=',nnn

if (t.eq.t_debut) then
count2=0
```

```
hydrogramG=0. ! à modifier si reprise d'un ancien
! calcul en cours v_dc_last=v_dc_last
! dernière sauvegarde
h_t=0. ! à modifier si reprise d'un ancien calcul en
 ! cours h_t=hmean dernière sauvegarde
u_dc_last=0. ! à modifier si reprise d'un ancien calcul
 ! en cours u_dc_last=u_dc_last dernière sauvegarde
v_dc_last=0. ! à modifier si reprise d'un ancien calcul
 ! en cours v_dc_last=v_dc_last dernière sauvegarde
else ! reprise d'ancien calculs (il suffit que t actuel soit
 ! différent de t début. attention à ne pas modifier la
 ! fréquence des printing times)
count2=0
write(FileName1,'(A12)') 'hydrogram.  '
write(FileName2,'(A8)') 'hmean.  '
write(FileName6,'(A7)') 'u_dc.  '
write(FileName7,'(A7)') 'v_dc.  '
!! creation des noms de fichier à explorer
if (nnn-1<10) then
write(FileName1(11:11),'(A1)') '0'
write(FileName1(12:12),'(I1)') nnn-1
write(FileName2(7:7),'(A1)') '0'
write(FileName2(8:8),'(I1)') nnn-1
write(FileName6(6:6),'(A1)') '0'
write(FileName6(7:7),'(I1)') nnn-1
write(FileName7(6:6),'(A1)') '0'
write(FileName7(7:7),'(I1)') nnn-1
elseif (nnn-1>=10 .and. nnn<100) then
write(FileName1(11:12),'(I2)') nnn-1
write(FileName2(7:8),'(I2)') nnn-1
write(FileName6(6:7),'(I2)') nnn-1
write(FileName7(6:7),'(I2)') nnn-1
else
write(*,*) '99 archives maximum, (press enter), erreur'
read(*,*)
endif

open (unit=1, file=FileName1, status='old')
count2=0
i=1
do
read(1,*,end=110) (hydrogramG(j,i),j=1,6) ! quand on
```

```
! arrive à la fin du fichier on saute au label 110
count2=count2+1
i=i+1
enddo
110 close (1)
write(*,*) 'count2 (press enter)=',count2
read(*,*)

t=hydrogramG(1,count2) ! on récupère le temps précis
 ! du dernier enregistrement
write(*,*) 'time (press enter)=',t
read(*,*)

h_t=0.
open (unit=1, file=FileName2, status='old')
do i=bufferStrip+1,ny+bufferStrip
do j=bufferStrip+1,nx+bufferStrip
read(1,*) h_t(j,i) ! reprise des anciennes valeurs
enddo
enddo
close (1)

u_dc_last=0.
open (unit=1, file=FileName6, status='old')
do i=bufferStrip+1,ny+bufferStrip
do j=bufferStrip+1,nx+bufferStrip-1
read(1,*) u_dc_last(j,i) ! reprise des anciennes valeurs
enddo
enddo
close (1)

v_dc_last=0.
open (unit=1, file=FileName7, status='old')
do i=bufferStrip+1,ny+bufferStrip
do j=bufferStrip+1,nx+bufferStrip
read(1,*) v_dc_last(j,i) ! reprise des anciennes valeurs
enddo
enddo
close (1)


endif
```

```
h_tp1=0.
h_x=0.
h_y=0.
hmean=0.
u=0.
umean=0.
u_dc=0.
v=0.
vmean=0.
v_dc=0.
Q_dev=0.
Q_dev_0=0.
Q_dev_1=0.
Q_dev_2=0.




Infi=0. ! infiltration [m/s]

   !***************************************************
!INITIALISATION DES DONNES POUR L'ITERATION
dt=dt_ini !pas de temps dans l'iteration [s]
count=0 !compteur de boucle
BILAN=0.
DEFAUT=0.
Q_dev_cum=0. ![m3]
Q_R_I_cum=0. ![m3]
Q_up_cum=0. ![m3]
Rmean=0.
!! nnn a été défini dans la rubrique précédente

tip=0. ![s]
tip=0. ![s]

   !***************************************************
! BOUCLE TEMPORELLE
   !***************************************************
do while (t<=t_fin)
t=t+dt
count=count+1
   !***************************************************
```

```
!pluie, débit et infiltration correspondants
R=0.
do i=1,nP
if (Rain(1,i)<=t ) then
R=Rain(2,i) !dernière pluie en date [m/s]
endif
end do
Q=0.
do i=1,nQ
if (Q_up(1,i)<=t) then
Q=Q_up(2,i) !dernier débit en date apporté à l'amont [m3/s]...
endif
end do
Q=Q/(nx*dx*QinStrip*dy) !...et transformé en lamme [m/s]


   !***************************************************
! grille des altitudes du fond et des hauteurs d'eau
! interpolée en x décentré
! write(*,*) 'grille des altitudes'
do i=bufferStrip+1,ny+bufferStrip
do j=bufferStrip+1,nx+bufferStrip-1
h_x(j,i)=(h_t(j,i)+h_t(j+1,i))/2. !interpolation linéaire
enddo
enddo
do i=bufferStrip+1,ny+bufferStrip
do j=bufferStrip+1,nx+bufferStrip
h_y(j,i)=(h_t(j,i)+h_t(j,i+1))/2. !interpolation linéaire
enddo
enddo

   !***************************************************
!calcul des vitesses [m/s] en x
!write(*,*) 'calcul des vitesses'
do i=bufferStrip+1,ny+bufferStrip
do j=bufferStrip+1,nx+bufferStrip-1
u_dc(j,i)=WATERSPEED(h_t(j,i),h_t(j+1,i),z(j,i), &
z(j+1,i),dx,u_dc_last(j,i),C_L,method,paramMeth,nu,v_max);
enddo
enddo
!write(*,*) 'ok u_dc'
!read(*,*)
```

```
do i=bufferStrip+1,ny+bufferStrip-1
do j=bufferStrip+1,nx+bufferStrip
v_dc(j,i)=WATERSPEED(h_t(j,i),h_t(j,i+1),z(j,i),z(j,i+1), &
dy,v_dc_last(j,i),C_L,method,paramMeth,nu,v_max) !idem
enddo
enddo
i=ny+bufferStrip !aval: z identique et hauteur d'eau nulle
do j=bufferStrip+1,nx+bufferStrip
v_dc(j,i)=WATERSPEED(h_t(j,i),0.,z(j,i),z(j,i),dy,v_dc_last(j,i), &
C_L,method,paramMeth,nu,v_max) !idem
enddo

   !*************************************************
!ajustemet des hauteur (taylor 1er degré)
!write(*,*) 'ajustemet des hauteur'
if (ConnectOK.eq.1) then ! on tient compte de la
! connectivite pour pondéré le terme puit-source
!connectivité correspondante
Conn=0
do i=1,nC
if (Connectivity(1,i)<=SurfStorage) then
Conn=Connectivity(2,i) !dernière connectivité en date [-]
endif
end do
! incrémentation du stockage superficiel
SurfStorage=SurfStorage+(R-Infi)*(1-Conn)*dt*dx*dy*nx*ny

do i=bufferStrip+1,ny+bufferStrip
do j=bufferStrip+1,nx+bufferStrip
if (i>=(bufferStrip+1) .and. i<=(bufferStrip+QinStrip)) then
h_tp1(j,i)=h_t(j,i)+dt*((R+Q-Infi)*Conn-(u_dc(j,i)*h_x(j,i)-&
u_dc(j-1,i)*h_x(j-1,i))/dx-(v_dc(j,i)*h_y(j,i)-v_dc(j,i-1)* &
h_y(j,i-1))/dy);
else
h_tp1(j,i)=h_t(j,i)+dt*((R-Infi)*Conn-(u_dc(j,i)*h_x(j,i)-&
u_dc(j-1,i)*h_x(j-1,i))/dx-(v_dc(j,i)*h_y(j,i)-v_dc(j,i-1)* &
h_y(j,i-1))/dy);

endif
enddo
enddo
! calcul flux aval
```

```
i=ny+bufferStrip
do j=bufferStrip+1,nx+bufferStrip
Q_dev(j,1)=v_dc(j,i)*h_y(j,i)*dx
enddo

else if (AdamsOK.eq.1) then ! procedure Adams-Bashfort
AdamsCount=AdamsCount+1
do i=bufferStrip+1,ny+bufferStrip
do j=bufferStrip+1,nx+bufferStrip
if (i>=(bufferStrip+1) .and. i<=(bufferStrip+QinStrip)) then
if (AdamsCount.eq.1) then ! Euler
rh_0(j,i)=((R+Q-Infi)-(u_dc(j,i)*h_x(j,i)-u_dc(j-1,i)* &
h_x(j-1,i))/dx-(v_dc(j,i)*h_y(j,i)-v_dc(j,i-1)*h_y(j,i-1))/dy);
h_tp1(j,i)=h_t(j,i)+dt*rh_0(j,i);
rh_1(j,i)=rh_0(j,i);
else if (AdamsCount.eq.2) then ! AB2
rh_0(j,i)=((R+Q-Infi)-(u_dc(j,i)*h_x(j,i)-u_dc(j-1,i)* &
h_x(j-1,i))/dx-(v_dc(j,i)*h_y(j,i)-v_dc(j,i-1)*h_y(j,i-1))/dy);
h_tp1(j,i)=h_t(j,i)+dt*((3./2.)*rh_0(j,i)-(1./2.)*rh_1(j,i));
rh_1(j,i)=rh_0(j,i);
rh_2(j,i)=rh_1(j,i);
else ! AB3
rh_0(j,i)=((R+Q-Infi)-(u_dc(j,i)*h_x(j,i)-u_dc(j-1,i)* &
h_x(j-1,i))/dx-(v_dc(j,i)*h_y(j,i)-v_dc(j,i-1)*h_y(j,i-1))/dy);
h_tp1(j,i)=h_t(j,i)+dt*((23./12.)*rh_0(j,i)-(16./12.)*&
rh_1(j,i)+(5./12.)*rh_2(j,i));
rh_1(j,i)=rh_0(j,i);
rh_2(j,i)=rh_1(j,i);
endif

else
if (AdamsCount.eq.1) then ! Euler
rh_0(j,i)=((R-Infi)-(u_dc(j,i)*h_x(j,i)-u_dc(j-1,i)* &
h_x(j-1,i))/dx-(v_dc(j,i)*h_y(j,i)-v_dc(j,i-1)*h_y(j,i-1))/dy);
h_tp1(j,i)=h_t(j,i)+dt*rh_0(j,i);
rh_1(j,i)=rh_0(j,i);
else if (AdamsCount.eq.2) then ! AB2
rh_0(j,i)=((R-Infi)-(u_dc(j,i)*h_x(j,i)-u_dc(j-1,i)* &
h_x(j-1,i))/dx-(v_dc(j,i)*h_y(j,i)-v_dc(j,i-1)*h_y(j,i-1))/dy);
h_tp1(j,i)=h_t(j,i)+dt*((3./2.)*rh_0(j,i)-(1./2.)*rh_1(j,i));
rh_1(j,i)=rh_0(j,i);
rh_2(j,i)=rh_1(j,i);
```

```
else ! AB3
rh_0(j,i)=((R-Infi)-(u_dc(j,i)*h_x(j,i)-u_dc(j-1,i)* &
h_x(j-1,i))/dx-(v_dc(j,i)*h_y(j,i)-v_dc(j,i-1)*h_y(j,i-1))/dy);
h_tp1(j,i)=h_t(j,i)+dt*((23./12.)*rh_0(j,i)-(16./12.)* &
rh_1(j,i)+(5./12.)*rh_2(j,i));
rh_1(j,i)=rh_0(j,i);
rh_2(j,i)=rh_1(j,i);

endif

endif
enddo
enddo
! calcul flux aval
i=ny+bufferStrip
if (AdamsCount.eq.1) then ! Euler
do j=bufferStrip+1,nx+bufferStrip
Q_dev_0(j,1)=v_dc(j,i)*h_y(j,i)*dx
Q_dev(j,1)=Q_dev_0(j,1)
Q_dev_1(j,1)=Q_dev_0(j,1)
enddo
else if (AdamsCount.eq.2) then ! AB2
do j=bufferStrip+1,nx+bufferStrip
Q_dev_0(j,1)=v_dc(j,i)*h_y(j,i)*dx
Q_dev(j,1)=(3./2.)*Q_dev_0(j,1)-(1./2.)*Q_dev_1(j,1)
Q_dev_1(j,1)=Q_dev_0(j,1)
Q_dev_2(j,1)=Q_dev_1(j,1)
enddo
else ! AB3
do j=bufferStrip+1,nx+bufferStrip
Q_dev_0(j,1)=v_dc(j,i)*h_y(j,i)*dx
Q_dev(j,1)=(23./12.)*Q_dev_0(j,1)-(16./12.)*Q_dev_1(j,1)+ &
(5./12.)*Q_dev_2(j,1)
Q_dev_1(j,1)=Q_dev_0(j,1)
Q_dev_2(j,1)=Q_dev_1(j,1)
enddo
endif


else ! procedure classique
do i=bufferStrip+1,ny+bufferStrip
do j=bufferStrip+1,nx+bufferStrip
```

```
if (i>=(bufferStrip+1) .and. i<=(bufferStrip+QinStrip)) then
h_tp1(j,i)=h_t(j,i)+dt*((R+Q-Infi)-(u_dc(j,i)*h_x(j,i)- u_dc(j-1,i)* &
h_x(j-1,i))/dx-(v_dc(j,i)*h_y(j,i)-v_dc(j,i-1)*h_y(j,i-1))/dy);
else
h_tp1(j,i)=h_t(j,i)+dt*((R-Infi)-(u_dc(j,i)*h_x(j,i)-u_dc(j-1,i)* &
h_x(j-1,i))/dx-(v_dc(j,i)*h_y(j,i)-v_dc(j,i-1)*h_y(j,i-1))/dy);

endif
enddo
enddo
! calcul flux aval
i=ny+bufferStrip
do j=bufferStrip+1,nx+bufferStrip
Q_dev(j,1)=v_dc(j,i)*h_y(j,i)*dx
enddo
endif

!*****************************************************
   !**************************************************
!comblement des hauteurs négatives
!write(*,*) 'comblement des hauteur'
do i=bufferStrip+1,ny+bufferStrip
do j=bufferStrip+1,nx+bufferStrip
if (h_tp1(j,i)<0) then
h_neg=abs(h_tp1(j,i))
h_tp1(j,i)=0.
h_sum=h_tp1(j,i-1)+h_tp1(j,i+1)+h_tp1(j-1,i)+h_tp1(j+1,i)
! cellules cardinales
if (h_sum>=h_neg) then
h_tp1(j,i-1)=h_tp1(j,i-1)-h_neg*h_tp1(j,i-1)/max(h_sum,1e-20)
h_tp1(j,i+1)=h_tp1(j,i+1)-h_neg*h_tp1(j,i+1)/max(h_sum,1e-20)
h_tp1(j-1,i)=h_tp1(j-1,i)-h_neg*h_tp1(j-1,i)/max(h_sum,1e-20)
h_tp1(j+1,i)=h_tp1(j+1,i)-h_neg*h_tp1(j+1,i)/max(h_sum,1e-20)
else  ! h_sum<hneg, il faut puiser plus largement que les cellules
! cardinales
neighb=0
do while (h_sum<h_neg .and. neighb<bufferStrip)
neighb=neighb+1
h_sum=sum(h_tp1(j-neighb:j+neighb,i-neighb:i+neighb))
enddo
if (h_sum<h_neg) then !si on ne trouve pas suffisemment d'eau
! dans le voisinage, on met tout à 0 et on archive le défaut
```

```
! de hauteur
DEFAUT=DEFAUT+(h_neg-h_sum)
do ii=-bufferStrip,bufferStrip
do jj=-bufferStrip,bufferStrip
h_tp1(j+jj,i+ii)=0.
enddo
enddo
else
do ii=-neighb,neighb
do jj=-neighb,neighb
h_tp1(j+jj,i+ii)=h_tp1(j+jj,i+ii)-h_neg* &
h_tp1(j+jj,i+ii)/max(h_sum,1e-20)
enddo
enddo
endif
endif
endif
enddo
enddo

   !**************************************************
! traitement résultat
!write(*,*) 'traitement resultat'
tmean=tmean+t
dtmean=dtmean+dt
Q_devT_mean=Q_devT_mean+sum(Q_dev)
RT_mean=RT_mean+R*nx*dx*ny*dy
RT_QT_mean=RT_QT_mean+R*nx*dx*ny*dy+Q*nx*dx*QinStrip*dy
Rmean=Rmean+R
Q_dev_cum=Q_dev_cum+sum(Q_dev)*dt
Q_R_I_cum=Q_R_I_cum+(R-Infi)*nx*dx*ny*dy*dt
Q_up_cum=Q_up_cum+Q*nx*dx*QinStrip*dy*dt
!BILAN=BILAN+(sum((h_tp1-h_t)*dx*dy)+(R-Infi)*(1-Conn)* &
dt*dx*dy*nx*ny-((R-Infi)*dx*dy*nx*ny*dt+Q*nx*dx*QinStrip* &
dy*dt-(sum(Q_dev*dt))))
! quantité en trop (+) ou en défaut(-), infiltration pas
! prise en compte!!!
BILAN=BILAN+sum((h_tp1-h_t)*dx*dy)-(R-Infi)*dt*dx*dy*nx*ny- &
Q*nx*dx*QinStrip*dy*dt+sum(Q_dev*dt) !
   !**************************************************
! calcul des vitesse centrée par Roe's average
!write(*,*) 'Roes average'
```

```
do i=bufferStrip+1,ny+bufferStrip
do j=bufferStrip+1,nx+bufferStrip
u(j,i)=(h_x(j-1,i)**0.5*u_dc(j-1,i)+(h_x(j,i))**0.5* &
u_dc(j,i))/max(1e-20,h_x(j-1,i)**0.5+(h_x(j,i))**0.5)
enddo
enddo
!write(*,*) 'ok vitesse u centree'
!read(*,*)
do i=bufferStrip+1,ny+bufferStrip
do j=bufferStrip+1,nx+bufferStrip
v(j,i)=(h_y(j,i-1)**0.5*v_dc(j,i-1)+(h_y(j,i))**0.5* &
v_dc(j,i))/max(1e-20,h_y(j,i-1)**0.5+(h_y(j,i))**0.5)
enddo
enddo
!write(*,*) 'ok vitesse v centree'
!read(*,*)
   !**************************************************
! condition de stabibilité CFL
!write(*,*) 'CFL'
dt=dt_max
!write(*,*) 'CFL debut'
!read(*,*)
do i=bufferStrip+1,ny+bufferStrip
do j=bufferStrip+1,nx+bufferStrip
if (nx.eq.1) then
dt=min(dt,Cn/(abs(v(j,i))/dy + (g*h_tp1(j,i)/(dy*dy))**0.5))
!CFL 1D
else
dt=min(dt,Cn/(abs(u(j,i))/dx + abs(v(j,i))/dy + &
(g*h_tp1(j,i)/(dx*dx)+g*h_tp1(j,i)/(dy*dy))**0.5)) !CFL 2D
endif

enddo
enddo
if (dt<dt_min) then
dt=dt_min
endif
!write(*,*) 'ok CFL'
!read(*,*)
   !**************************************************
! préparation boucle suivante
u_dc_last=u_dc
```

```
v_dc_last=v_dc
Qx_dcmean=Qx_dcmean+u_dc*h_x
Qy_dcmean=Qy_dcmean+v_dc*h_y
umean=umean+u
vmean=vmean+v
hmean=hmean+h_tp1
h_t=h_tp1
!write(*,*) 'ok boucle suivante'
!read(*,*)
   !************************************************
! moyennisation
if (count==countMax) then
count2=count2+1

hmean=hmean/real(countMax)
umean=umean/real(countMax)
vmean=vmean/real(countMax)
Qx_dcmean=Qx_dcmean/real(countMax)
Qy_dcmean=Qy_dcmean/real(countMax)
tmean=tmean/real(countMax)
dtmean=dtmean/real(countMax)
Q_devT_mean=Q_devT_mean/real(countMax)
RT_mean=RT_mean/real(countMax)
RT_QT_mean=RT_QT_mean/real(countMax)
Rmean=Rmean/real(countMax)

hydrogramG(1,count2)= tmean
hydrogramG(2,count2)= dtmean
hydrogramG(3,count2)= Q_devT_mean
hydrogramG(4,count2)= RT_mean
hydrogramG(5,count2)= RT_QT_mean
hydrogramG(6,count2)= 100.*BILAN/(Q_R_I_cum+Q_up_cum)
! à verifier s'il est correct dans le cas d'une
! reprise de calcul

write(*,*) tmean,'[s]:',Q_devT_mean,'[m3/s], bilan [%]', &
100.*BILAN/(Q_R_I_cum+Q_up_cum)

if (tmean>=nnn*t_print) then
write(FileName1,'(A12)') 'hydrogram.  '
write(FileName2,'(A8)') 'hmean.  '
write(FileName3,'(A8)') 'vmean.  '
```

```
write(FileName4,'(A8)') 'umean.  '
write(FileName5,'(A8)') 'h_tp1.  '
write(FileName6,'(A7)') 'u_dc.  '
write(FileName7,'(A7)') 'v_dc.  '
write(FileName8,'(A11)') 'Qx_dcmean.  '
write(FileName9,'(A11)') 'Qy_dcmean.  '

if (nnn<10) then
write(FileName1(11:11),'(A1)') '0'
write(FileName1(12:12),'(I1)') nnn
write(FileName2(7:7),'(A1)') '0'
write(FileName2(8:8),'(I1)') nnn
write(FileName3(7:7),'(A1)') '0'
write(FileName3(8:8),'(I1)') nnn
write(FileName4(7:7),'(A1)') '0'
write(FileName4(8:8),'(I1)') nnn
write(FileName5(7:7),'(A1)') '0'
write(FileName5(8:8),'(I1)') nnn
write(FileName6(6:6),'(A1)') '0'
write(FileName6(7:7),'(I1)') nnn
write(FileName7(6:6),'(A1)') '0'
write(FileName7(7:7),'(I1)') nnn
write(FileName8(10:10),'(A1)') '0'
write(FileName8(11:11),'(I1)') nnn
write(FileName9(10:10),'(A1)') '0'
write(FileName9(11:11),'(I1)') nnn

elseif (nnn>=10 .and. nnn<100) then
write(FileName1(11:12),'(I2)') nnn
write(FileName2(7:8),'(I2)') nnn
write(FileName3(7:8),'(I2)') nnn
write(FileName4(7:8),'(I2)') nnn
write(FileName5(7:8),'(I2)') nnn
write(FileName6(6:7),'(I2)') nnn
write(FileName7(6:7),'(I2)') nnn
write(FileName8(10:11),'(I2)') nnn
write(FileName9(10:11),'(I2)') nnn

else
write(*,*) '99 archives maximum, (press enter), retour à 1'
read(*,*)
nnn=0
```

```
endif
write(*,*) 'saved values at time ', t,' (s)'
write(*,*) '------------------------------'
write(*,*) FileName1, FileName2, FileName3, FileName4, &
FileName5, FileName6, FileName7, FileName8, FileName9

nnn=nnn+1
open (unit=1, file=FileName1, status='replace')
write(1,60) hydrogramG(:,1:count2)
close (1)

open (unit=1, file=FileName2, status='replace')
write(1,10) hmean(bufferStrip+1:nx+bufferStrip, &
bufferStrip+1:ny+bufferStrip)
close (1)

open (unit=1, file=FileName3, status='replace')
write(1,10) vmean(bufferStrip+1:nx+bufferStrip, &
bufferStrip+1:ny+bufferStrip)
close (1)

open (unit=1, file=FileName4, status='replace')
write(1,10) umean(bufferStrip+1:nx+bufferStrip, &
bufferStrip+1:ny+bufferStrip)
close (1)

open (unit=1, file=FileName5, status='replace')
write(1,10) h_tp1(bufferStrip+1:nx+bufferStrip, &
bufferStrip+1:ny+bufferStrip)
close (1)

open (unit=1, file=FileName6, status='replace')
write(1,10) u_dc(bufferStrip+1:nx+bufferStrip-1, &
bufferStrip+1:ny+bufferStrip)
close (1)

open (unit=1, file=FileName7, status='replace')
write(1,10) v_dc(bufferStrip+1:nx+bufferStrip, &
bufferStrip+1:ny+bufferStrip)
close (1)

open (unit=1, file=FileName8, status='replace')
```

```
write(1,10) Qx_dcmean(bufferStrip+1:nx+bufferStrip-1, &
bufferStrip+1:ny+bufferStrip)
close (1)

open (unit=1, file=FileName9, status='replace')
write(1,10) Qy_dcmean(bufferStrip+1:nx+bufferStrip, &
bufferStrip+1:ny+bufferStrip)
close (1)
endif
hmean=0.
umean=0.
vmean=0.
Qx_dcmean=0.
Qy_dcmean=0.
count=0
tmean=0.
dtmean=0.
Q_devT_mean=0.
RT_mean=0.
RT_QT_mean=0.

Rmean=0.

endif

enddo ! fin de la boucle temporelle

   !****************************************************
FileName='hydrogram.out'
open (unit=1, file=FileName, status='replace')
write(1,60) hydrogramG(:,1:count2)
close (1)


write(*,*) 'tip [s]',tip,'top [s]',top
write(*,*) 'top-tip [s]',top-tip

FileName='tiptop.out'
open (unit=1, file=FileName, status='replace')
write(1,30) tip,top,top-tip
close (1)
write(*,*) 'END'
```

```
!read(*,*)

!********************!

!********************!
10 format(1e14.6)
20 format(2e12.3)
30 format(3e12.3)
40 format(4e12.3)
50 format(5e12.3)
60 format(6e14.6)
end !program DIRECT_FLOW
```

D.2 Function WATERSPEED

```
!  WATERSPEED.f90
!
!  FUNCTIONS:
! WATERSPEED      - Entry point of console application.
!



!*******************************************************
!
!  Function: WATERSPEED
!
! M. Antoine (04/05/07)
! Return runoff speed, considering equilibrium of forces
! (Darcy-Weisbach) with assumption no variation of movement
! quantity u=sqrt(8g/la h Sf), la (or lamda) = CL/Re for
! laminar and is found by the modified Coolebrook-White
! equation (Henderson 1966) for turbulent flow
!
! u=WATERSPEED(h_i,h_ip1,z_i,z_ip1,dx,utm1,C_L,method,paramMeth)
!
! where:
! u is the velocity [m/s], negative value means water flows
! from i+1 to i
! _i is the value at cell i
! _ip1 is the value at cell i+1
! h is the water level above the ground [m]
! z is the ground altitude [m]
! utm1 is the velocity à t-1 [m/s], in order to evaluate
! a-priori the regime of flux
! C_L is a constante for computation of the friction factor
! in the laminar domain (Horton: C_L=96); to be optimised
! method: for computation of the friction factor in the turbulent
! domain:
! if method = 1, lambda is founded from modified
!   Colebrook; if method = 2, lambda is constant and fixed
!  by the user
! paramMeth: if method = 1, paramMethod = ks which is the size
!   of grain
! particles [m] that provoke friction;
!  if method = 2, paramMethod = the fixed lambda in
```

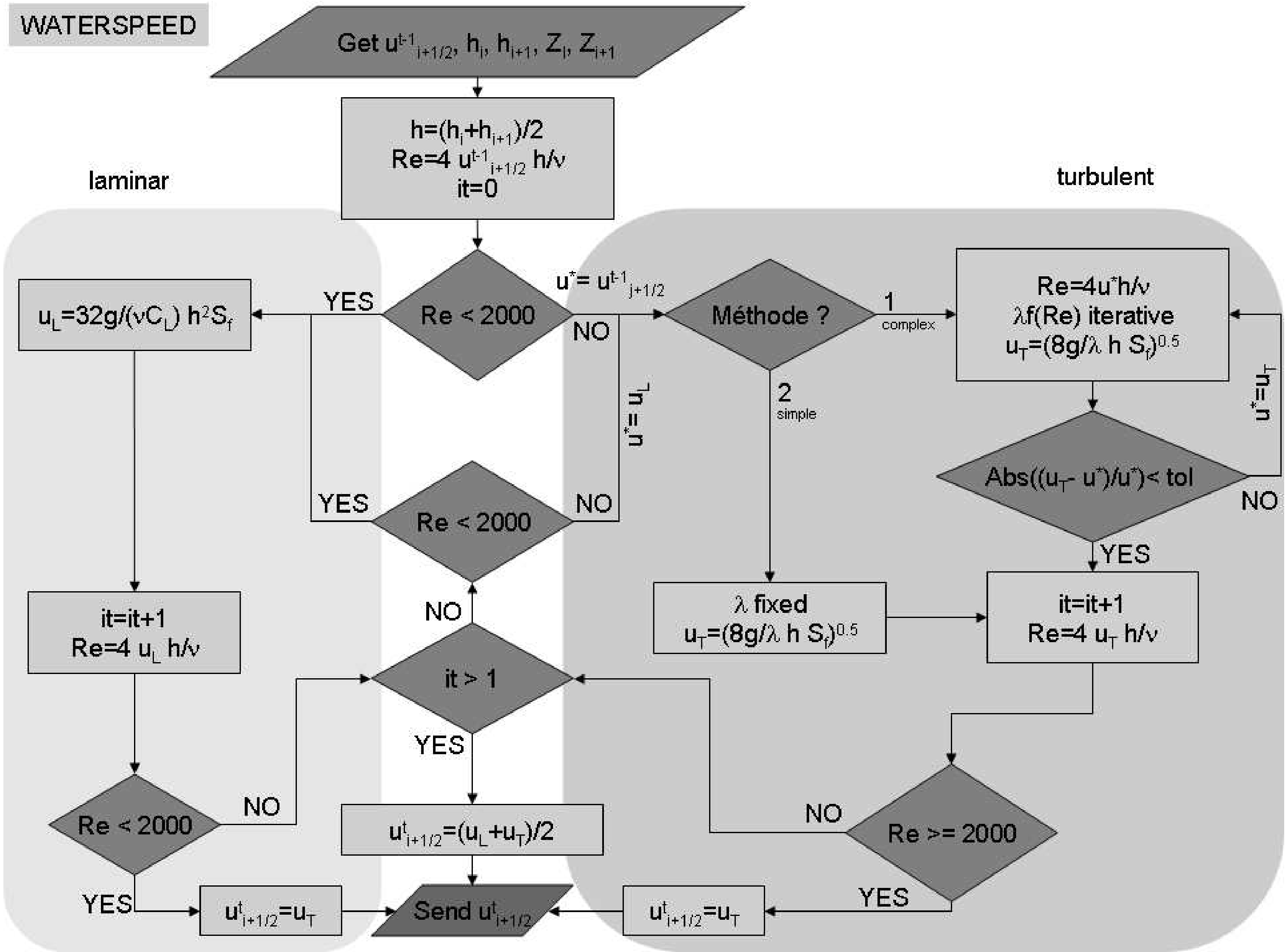

Figure D.3: WATERSPEED functioning scheme.

```
!  turbulent domain.
!
!*******************************************************
real function WATERSPEED(h_i,h_ip1,z_i,z_ip1,dx,utm1, &
C_L,method,paramMeth,nu,v_max)

implicit none

! Variables
real u, h_i, h_ip1, z_i, z_ip1, dx, utm1, C_L, ks
! paramètres formels
real Sf, h, u_ini, la, la_ini, Re, u_L, u_T, eps
real tol, tol2, err, err2 !paramètres boucles while

real paramMeth
real nu ! nu, la viscosité cinématique [m2/s]
! (1e-6 à 20°C, 1.3e-6 à 10°C)
real v_max ! vitesse maximale admise; la mettre très élevée
 ! si on ne souhaite pas la restreindre en pratique
integer method, itMeth1, itHender


! Constantes
real g ! constantes: g la gravité 9.81m/s2
parameter(g=9.81)

!Initialisation
tol=0.1 ! erreur relative admissible pour calcul de la
! vitesse turbulent
tol2=0.1 ! erreur relative admissible pour calcul de
 ! lamda par Henderson

if (method.eq.2) then
    la=paramMeth
elseif (method.eq.1) then
ks=paramMeth
else
write(*,*) 'method must have value 1 or 2'
read(*,*)

endif
```

```
! Body of WATERSPEED

Sf=((h_i+z_i)-(h_ip1+z_ip1))/dx !pente de la surface d'eau

!Calcul préalable du Reynolds
h=(h_i+h_ip1)/2.
Re = abs(4.*utm1*h/nu)

if (Re.lt.2000.) then !à priori laminaire
u_L=32.*g*(h**2.)*Sf/(nu*C_L)
Re=abs(4.*u_L*h/nu)
if (Re.lt.2000.) then !à priori laminaire confirmé
u=u_L
else !la solution laminaire envoie vers le turbulent
if (method.eq.1) then !résolution Colebrook-White
u_ini=u_L
err=1.e20
itMeth1=0
do while (err.gt.tol) ! tant qu'on a pas convergé (
! à tol près)
itMeth1=itMeth1+1
if (itMeth1.gt.10) then ! si converge pas au bout de 10 it
tol=tol*2. ! alors on augmente le seuil de tolerance
!write(*,*) 'tol=',tol
itMeth1=0
endif
Re=abs(4.*u_ini*h/nu)
err2=1.e20
la_ini=0.05 !a priori lamda
eps=ks/(4.*h) !relative roughness
itHender=0
do while (err2.gt.tol2) ! tant qu'on a pas convergé
! (à tol2 près)
itHender=itHender+1
if (itHender.gt.10) then ! si converge pas au bout
tol2=2.*tol2 ! de 10 it alors on augmente le seuil
 ! de tolerance
!write(*,*) 'tol2=',tol2
itHender=0
endif
la=((-2.*log10(eps/3. + 2.5/(Re*la_ini**0.5)))**(-1.))**2.
err2=abs((la-la_ini)/la_ini)
```

```
la_ini=la
enddo
u_T=(h*Sf)/abs(h*Sf)*(8.*g*abs(h*Sf)/la)**0.5
err=abs((u_T-u_ini)/u_ini)
u_ini=u_T
enddo
elseif (method.eq.2) then
u_T=(h*Sf)/abs(h*Sf)*(8.*g*abs(h*Sf)/la)**0.5
endif
Re=abs(4.*u_T*h/nu)
if (Re.lt.2000) then ! mais la solution turbulente renvoie
 ! vers le laminaire
u=(u_L+u_T)/2. !moyenne des solutions laminaire et turbulente
else !turbulent finalement confirmé
u=u_T
endif
endif
else !à priori turbulent
if (method.eq.1) then
u_ini=utm1
err=1.e20
itMeth1=0
do while (err.gt.tol)
itMeth1=itMeth1+1
if (itMeth1.gt.10) then
tol=tol*2.
!write(*,*) 'tol=',tol
itMeth1=0
endif
Re=abs(4.*u_ini*h/nu)
!Henderson66
err2=1.e20
la_ini=0.05 !a priori lamda
eps=ks/(4.*h) !relative roughness
itHender=0
do while (err2.gt.tol2)
itHender=itHender+1
if (itHender.gt.10) then
tol2=2.*tol2
!write(*,*) 'tol2=',tol2
itHender=0
endif
```

```
la=((-2.*log10(eps/3. + 2.5/(Re*la_ini**0.5)))**(-1.))**2.
err2=abs((la-la_ini)/la_ini)
la_ini=la
enddo
u_T=(h*Sf)/abs(h*Sf)*(8.*g*abs(h*Sf)/la)**0.5
err=abs((u_T-u_ini)/u_ini)
u_ini=u_T
enddo
elseif (method.eq.2) then
    u_T=(h*Sf)/abs(h*Sf)*(8.*g*abs(h*Sf)/la)**0.5
endif
Re=abs(4.*u_T*h/nu)
if (Re.gt.2000) then !à priori turbulent confirmé
u=u_T
else !la solution turbulent envoie vers le laminaire
u_L=32.*g*(h**2.)*Sf/(nu*C_L)
Re=abs(4.*u_L*h/nu)
if (Re.gt.2000) then  ! mais la solution laminaire renvoie
! vers le turbulent
u=(u_L+u_T)/2. !moyenne des solutions laminaire et turbulente
else !laminaire finalement confirmé
u=u_L
endif
    endif
endif

! la vitesse est contrainte à v_max, pour réduire les temps
! de calculs et éviter les oscillations
if (u.gt.v_max) then
WATERSPEED=v_max
else
WATERSPEED=u
endif


return

end
```

D.3 Filling Algorithm

```
program COND_WALKER
!*******************************************************
! DECLARATION VARIABLES
implicit none
!coordonnées topographiqes
real, allocatable, dimension (:,:) :: dem,h,q
integer nl,nc
real dx,dy
real Qdev
real, allocatable, dimension (:,:) :: Rain
integer nP
real R
!real, allocatable, dimension (:,:) :: KK,LL
real marcheurV, marcheurV_ini
integer i,j,ilower,jlower,ii,jj,k,l
real Qin, QinC, QdevC
real hydrogram(6,100000) ! à améliorer en le dimensionnant
 ! dynamiquement
real resultat(3)
integer count
character*100 titre
real WATERSPEED

real t,dt

common /dataReal/Qdev,dx,dy,marcheurV,dt
common /dataInteger/nl,nc,ilower, jlower

!*******************************************************
! chargement MNT et entourage pour conditions limites
open (unit=1, file='dem.in', status='old')
read(1,*) titre
read(1,*) nl, nc
read(1,*) titre
read(1,*) dy, dx !taille maille (m)
read(1,*) titre
read(1,*) titre ! correpsondant au buffer strip, non
  ! utilisé dans ce model
read(1,*) titre
read(1,*) titre ! correpsondant au QinStripstrip, non
```

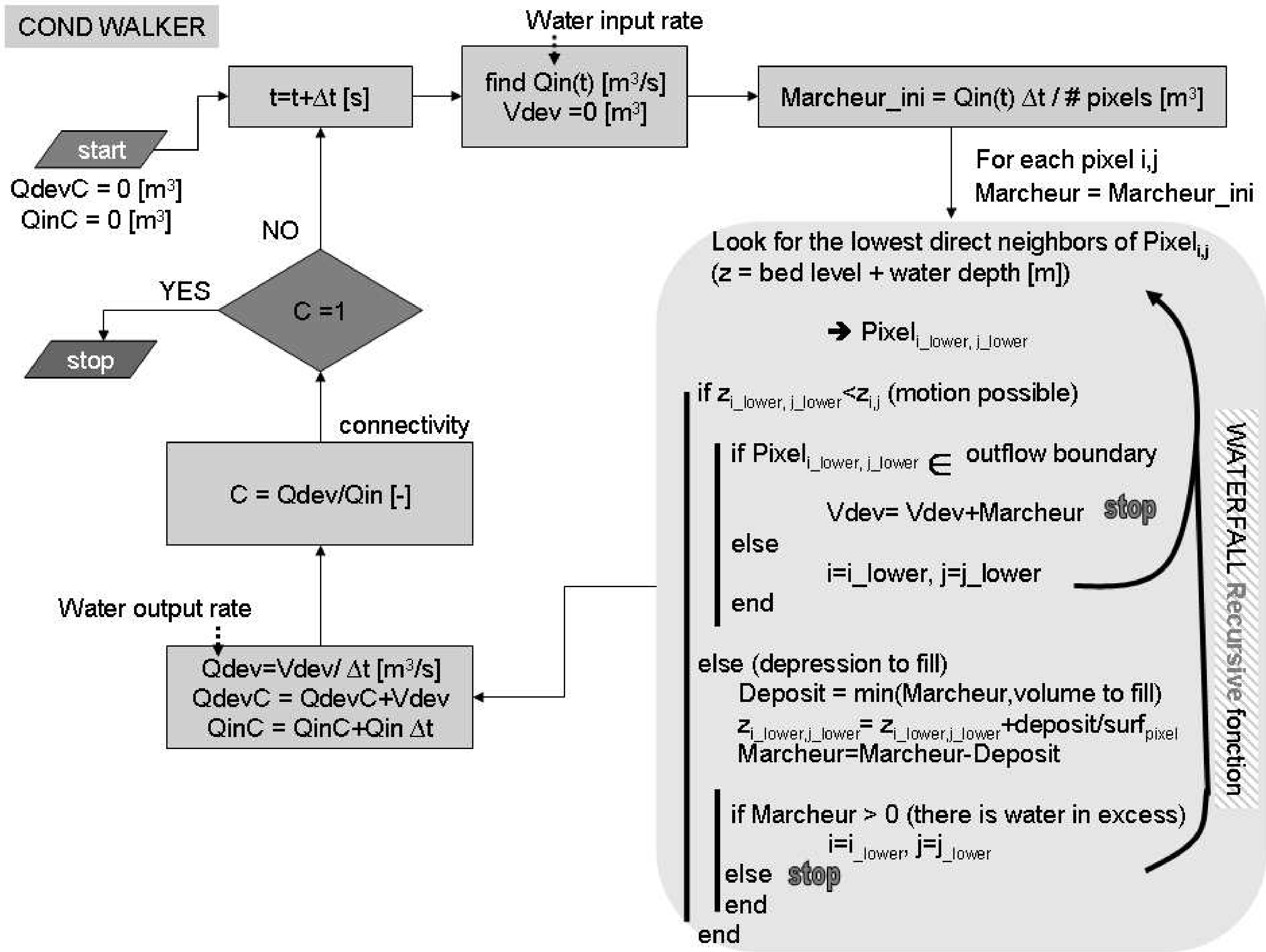

Figure D.4: COND WALKER functioning scheme.

```
! utilisé dans ce model actuellement, à
! adapter si l'on souhaite que l'eau soit
! amenée en amont seulement

! allocation des matrices liées à la taille du dem
allocate (dem(nc+2,nl+2))
allocate (h(nc+2,nl+2))
allocate (q(nc+2,nl+2))
!allocate (KK(nc+2,nl+2))
!allocate (LL(nc+2,nl+2))

dem=1000000. ! valeur élevée partout
 ! ==> no flux sur les bords
h=0.

read(1,*) titre
do i=2,nl+1
read(1,*) (dem(j,i),j=2,nc+1)
enddo
dem(:,nl+2)=dem(:,nl+1)! -1000000. ! valeur égale à
! la derniere ligne pour permettre à l'eau de la
! dernière cellule de retourner en arrière ! valeurs
! très basse à la base ==> tout s'évacue
close (1)
!*****************************************************
! chargement pluie
!open (unit=1, file='Q.in', status='old')
!read(1,*) titre
!read(1,*) Rain
!close (1)

open (unit=1, file='water.in', status='old')
read(1,*) titre
read(1,*) nP
allocate (Rain(2,nP))
read(1,*) titre
do i=1,nP
read(1,*) (Rain(j,i),j=1,2)
enddo
close (1)
```

```
!****************************************************
dt=1.
Qin=1000000
!Qin=Rain*nl*dy*nc*dx ![m3/s]
!marcheurV_ini=Qin*dt/(nl*nc) !volume marcheur [m3]

Qdev=0.
QinC=0.
QdevC=0.
t=0

count=0

!****************************************************
!BOUCLE
do while ((Qdev/dt)<Qin*0.99) ! 0.999 pour éviter problèmes
! d'arrondis
count=count+1
t=t+dt
Qdev=0
R=0

do i=1,nP
if (Rain(1,i)<=t ) then
R=Rain(2,i) !dernière pluie en date [m/s]
endif
end do
Qin=R*nl*dy*nc*dx ![m3/s]
marcheurV_ini=Qin*dt/(nl*nc) !volume marcheur [m3]
q=0.
do k=2,nl+1 ! a modifier si Qinstrip
do l=2,nc+1
ilower=k
jlower=l
marcheurV=marcheurV_ini
call WATERFALL2(dem,h,q,nc+2)
!KK(k,l)=ilower
!LL(k,l)=jlower
enddo
enddo
QinC=QinC+Qin*dt
QdevC=QdevC+Qdev
```

```
hydrogram(1,count)=t
hydrogram(2,count)=Qin
hydrogram(3,count)= Qdev/dt
hydrogram(4,count)= QinC
hydrogram(5,count)=QdevC
hydrogram(6,count)=(Qdev/dt)/Qin
write(*,*) 'time [s]: ',t,'| QinC [m3]: ',QinC, &
'| C [-]: ',(Qdev/dt)/Qin
enddo
open (unit=1, file='hydrogram.out', status='replace')
write(1,60) hydrogram(:,1:count)
close (1)

open (unit=1, file='h.out', status='replace')
write(1,10) h(2:nc+1,2:nl+1)
close (1)

open (unit=1, file='q.out', status='replace')
write(1,10) q(2:nc+1,2:nl+1)
close (1)

open (unit=1, file='dem.out', status='replace')
write(1,10) dem(2:nc+1,2:nl+1)
close (1)


write(*,*) 'END'
!read(*,*)

10 format(1e14.6)
60 format(6e11.3)
end ! program COND_WALKER

!*****************************************************

SUBROUTINE WATERFALL2(dem,h,q,a)
implicit none

common /dataReal/Qdev,dx,dy,marcheurV,dt
common /dataInteger/nl,nc,ilower, jlower

integer ilower,jlower,nl,nc
```

```
integer a
real dem(a,*)
real h(a,*)
real q(a,*)

real dx,dy
real dt
real Qdev
real marcheurV
real epsilon
real z_h, z_h_lower
integer i,j,ii,jj
real depot

100 continue
i=ilower
j=jlower

epsilon=0.0001 ! évite d'avoir des zones complètements
 ! planes (1% de pente puisque dx =0.01)

! trouver le voisin immédiat le plus bas
z_h_lower=100000000.
do ii=i-1,i+1
do jj=j-1,j+1
if (ii.ne.i.or.jj.ne.j ) then !tous sauf lui-meme
!write(*,*) 'i,j: ',i,',',j,' ii,jj: ',ii,',',jj
z_h=dem(jj,ii)+h(jj,ii)
if (z_h<z_h_lower) then
z_h_lower=z_h
ilower=ii
jlower=jj
endif
endif
enddo
enddo
z_h=dem(j,i)+h(j,i)

if (z_h_lower<z_h) then  ! si mouvement possible
if (ilower==nl+2) then ! bord aval, le marcheur est sommé
 ! pour calculer le flux de sortie
```

```
Qdev=Qdev+marcheurV ![m3]
q(j,i)=q(j,i)+marcheurV/dt ![m3/s]
marcheurV=0
else
!write(*,*) i,j,z_h,ilower,jlower,z_h_lower
q(j,i)=q(j,i)+marcheurV/dt ![m3/s]
go to 100 ! on continue le déplacement vers l'aval
endif
else ! si comblement d'une dépression nécessaire
depot=min(marcheurV/(dx*dy), &
(z_h_lower-(h(j,i)+dem(j,i))+epsilon)) ![m]
h(j,i)=h(j,i)+depot ! [m]
marcheurV=marcheurV-depot*dx*dy ! [m3]
if (marcheurV>0) then ! il y a encore de l'eau qui
! peut être transporté
if (ilower==nl+2) then ! bord aval, le marcheur est sommé
 ! pour calculer le flux de sortie
Qdev=Qdev+marcheurV ! [m3]
q(j,i)=q(j,i)+marcheurV/dt ![m3/s]
marcheurV=0
else
q(j,i)=q(j,i)+marcheurV/dt ![m3/s]
go to 100 ! on continue le déplacement vers l'aval
endif
endif
endif

end ! WATERFALL
```

Bibliography

Abedini, M. J., Dickinson, W. T., and Rudra, R. P. 2006. On depressional storages: The effect of DEM spatial resolution. Journal of Hydrology, 318(1-4):138–150.

Alberts, E., Nearing, M., Weltz, M., Risse, L., Pierson, F., Zhang, X., Laflen, J., and Simanton, J. 1995. Soil component. In: Flanagan, D.C., Nearing, M.A. (Eds.), USDA - Water Erosion Prediction Project: Hillslope Profile Model Documentation (Chapter 7). Nserl report no. 2. Tech. rep.,. Technical report, USDA-ARS National Soil Erosion Research Laboratory.

Ali, G. and Roy, A. 2009. Revisiting Hydrologic Sampling Strategies for an Accurate Assessment of Hydrologic Connectivity in Humid Temperate Systems. Geography Compass, 3/1:350 – 374.

Allard, D. and HERESIM-Group. 1993. *Geostatistic Troia '92*, volume 1, chapter On the connectivity of two random set models: the trucated Gaussian and the Boolean, pages 467–478. Norwell, MA: Kluwer Acad.

Ambroise, B. 2004. Variable 'active' versus 'contributing' areas or periods: a necessary distinction. Hydrological Processes, 18(6):1149–1155.

Banavar, J. R., Colaiori, F., Flammini, A., Maritan, A., and Rinaldo, A. 2000. Topology of the fittest transportation network. Physical Review Letters, 84(20):4745–4748.

Bellin, N., van Wesemael, B., Meerkerk, A., Vanacker, V., and Barbera, G. G. 2009. Abandonment of soil and water conservation structures in Mediterranean ecosystems A case study from south east Spain. Catena, 76(2):114–121.

Beven, K. 2001. *Rainfall-runoff modelling (The Primer), Chap.5*. Wiley.

Bhallamudi, S. M. and Chaudhry, M. H. 1992. Computation Of Flows In Open-Channel Transitions. Journal of Hydraulic Research, 30(1):77–93.

Bogaert, P. 2005. *Probabilités pour Scientifiques et Ingénieurs*, chapter Nombres aléatoires, page 228. De Boeck Univ.

Bracken, L. J. and Croke, J. 2007. The concept of hydrological connectivity and its contribution to understanding runoff-dominated geomorphic systems. Hydrological Processes, 21(13):1749–1763.

Bronstert, A. and Bardossy, A. 1999. The role of spatial variability of soil moisture for modelling surface runoff generation at the small catchment scale. Hydrology and Earth System Sciences, 3(4):505–516.

Cammeraat, L. H. 2002. A review of two strongly contrasting geomorphological systems within the context of scale. Earth Surface Processes and Landforms, 27(11):1201–1222.

Cappelaere, B., Touma, J., and Peugeot, C. 2000. A recursive algorithm for connectivity analysis in a grid; application to 2D hydrodynamic modeling in heterogeneous soils. Computers & Geosciences, 26(2):121–135.

Carluer, N. and De Marsily, G. 2004. Assessment and modelling of the influence of man-made networks on the hydrology of a small watershed: implications for fast flow components, water quality and landscape management. Journal of Hydrology, 285(1-4):76–95.

Carvajal, F., Aguilar, M. A., Aguera, F., Aguilar, F. J., and Giraldez, J. V. 2006. Maximum depression storage and surface drainage network in uneven agricultural landforms. Biosystems Engineering, 95(2):281–293.

Cerdan, O., Le Bissonnais, Y., Govers, G., Lecomte, V., van Oost, K., Couturier, A., King, C., and Dubreuil, N. 2004. Scale effect on runoff from experimental plots to catchments in agricultural areas in Normandy. Journal of Hydrology, 299(1-2):4–14.

Chahinian, N., Moussa, R., Andrieux, P., and Voltz, M. 2006. Accounting for temporal variation in soil hydrological properties when simulating surface runoff on tilled plots. Journal Of Hydrology, 326(1-4):135–152.

Chanson, H. 2006. *RiverFlow 2006: Analytical solutions of laminar and turbulent dam break wave*, pages 465–474. Taylor & Francis Group.

Chetkiewicz, C. L. B., Clair, C. C. S., and Boyce, M. S. 2006. Corridors for conservation: Integrating pattern and process. Annual Review of Ecology Evolution and Systematics, 37:317–342.

Chow, V. T., Maidment, D. R., and Mays, L. W. 1988. *Applied Hydrology*. McGraw-Hill Publishing Co.

Colebrook, C. February 1939. Turbulent flow in pipes, with particular reference to the transition region between smooth and rough pipe laws. Journal of the Institution of Civil Engineers.

Colebrook, C. F. and White, C. M. 1937. Experiments with Fluid Friction in Roughened Pipes. Proceedings of the Royal Society of London. Series A, Mathematical and Physical Sciences, 161 (906):367–381.

Colizza, V., Banavar, J. R., Maritan, A., and Rinaldo, A. 2004. Network structures from selection principles. Physical Review Letters, 92(19):198701.

Courant, R., Friedrichs, K., and Lewy, H. 1928. Uber die partiellen Differenzengleichungen der mathematischen Physik. Mathematische Annalen, 100 (1):32–74.

Croke, J., Mockler, S., Fogarty, P., and Takken, I. 2005. Sediment concentration changes in runoff pathways from a forest road network and the resultant spatial pattern of catchment connectivity. Geomorphology, 68(3-4):257–268.

Darboux, F. and Huang, C. 2003. An instantaneous-profile laser scanner to measure soil surface microtopography. Soil Science Society of America Journal, 67(1):92–99.

Darboux, F. and Huang, C. H. 2005. Does soil surface roughness increase or decrease water and particle transfers? Soil Science Society of America Journal, 69(3):748–756.

Darboux, F., Davy, P., Gascuel-Odoux, C., and Huang, C. 2002. Evolution of soil surface roughness and flowpath connectivity in overland flow experiments. Catena, 46(2-3):125–139.

Darboux, F., Davy, P., and Gascuel-Odoux, C. 2002b. Effect of depression storage capacity on overland-flow generation for rough horizontal surfaces: Water transfer distance and scaling. Earth Surface Processes and Landforms, 27(2):177–191.

de Roo, A., Jetten, V., Wesseling, C., and Ritsema, C. 1998. *Modeling soil erosion by water, NATO ASI Series I. LISEM: a physically-based hydrologic and soil erosion catchment model.*, chapter vol. 55. (Chapter 32), pages 430–440.

de Saint-Venant, A. 1871. Théorie du mouvement non-permanent des eaux, avec application aux crues des rivieres et à l'introduction des marées dans leur lit. C. R. Math. Acad. Sci. Paris, pages 73:147–154.

Delestre, O. 2010. *Simulation du ruissellement d'eau de pluie sur des surfaces agricoles, these de doctorat*. Ph.D. thesis, Université d'Orléans.

Deutsch, C. V. 1998. Fortran programs for calculating connectivity of three-dimensional numerical models and for ranking multiple realizations. Computers & Geosciences, 24(1):69–76.

Dunkerley, D. 2001. Estimating the mean speed of laminar overland flow using dye injection-uncertainty on rough surfaces. Earth Surface Processes and Landforms, 26:363–374.

Dunkerley, D. L. 2003. Determining friction coefficients for interrill flows: the significance of flow filaments and backwater effects. Earth Surface Processes and Landforms, 28:475–491.

Elbasit, M. A. M. A., Anyoji, H., Yasuda, H., and Yamamoto, S. 2009. Potential of low cost close-range photogrammetry system in soil microtopography quantification. Hydrological Processes, 23(10):1408–1417.

Esteves, M., Faucher, X., Galle, S., and Vauclin, M. 2000. Overland flow and infiltration modelling for small plots during unsteady rain: numerical results versus observed values. Journal of Hydrology, 228(3-4):265–282.

FAO, ISRIC, and ISSS. 1998. *World Reference Base for Soil Resources, World Soil Resources Report 84.*. FAO, Rome.

Favis-Mortlock, D. 1998. A self-organizing dynamic systems approach to the simulation of rill initiation and development on hillslopes. Computers & Geosciences, 24(4):353–372.

Flanagan, D. and Nearing, M. 1995. USDA-Water Erosion Prediction Project: hillslope profile and watershed model documentation. NSERL Report 10. Technical report, USDA-ARS National Soil Erosion Research Laboratory, West Lafayette, Indiana 47907.

Foster, G. R., Huggins, L. F., and Meyer, L. D. 1984. A Laboratory Study Of Rill Hydraulics .1. Velocity Relationships. Transactions of the ASAE, 27(3):790–796.

Fox, D. M., Le Bissonnais, Y., and Bruand, A. 1998. The effect of ponding depth on infiltration in a crusted surface depression. Catena, 32(2):87–100.

Fryirs, K. A., Brierley, G. J., Preston, N. J., and Kasai, M. 2007. Buffers, barriers and blankets: The (dis)connectivity of catchment-scale sediment cascades. Catena, 70(1):49–67.

Garcia-Sanchez, L. 1997. *Modelisation de la dynamique ruissellement-infiltration en fonction des etats de surface*. Ph.D. thesis, Universite Montpellier II.

Gayle, G. A. and Skaggs, R. W. 1978. Surface Storage On Bedded Cultivated Lands. Transactions of the ASAE, 21(1):101–&.

Gilley, J. E. and Finkner, S. C. 1991. Hydraulic Roughness Coefficients As Affected By Random Roughness. Transactions of the ASAE, 34(3):897–903.

Gomez, J. A. and Nearing, M. A. 2005. Runoff and sediment losses from rough and smooth soil surfaces in a laboratory experiment. Catena, 59(3):253–266.

Grayson, R. B., Western, A. W., Chiew, F. H. S., and Bloschl, G. 1997. Preferred states in spatial soil moisture patterns: Local and nonlocal controls. Water Resources Research, 33(12):2897–2908.

Grayson, R. B., Bloschl, G., Western, A. W., and McMahon, T. A. 2002. Advances in the use of observed spatial patterns of catchment hydrological response. Advances in Water Resources, 25(8-12):1313–1334.

Guillobez, S. and Arnaud, M. 1998. Regionalized soil roughness indices. Soil & Tillage Research, 45(3-4):419–432.

Guntner, A., Seibert, J., and Uhlenbrook, S. 2004. Modeling spatial patterns of saturated areas: An evaluation of different terrain indices. Water Resources Research, 40(5):W05114.

Gustafson, E. J. 1998. Quantifying landscape spatial pattern: What is the state of the art? Ecosystems, 1(2):143–156.

Guzha, A. C. 2004. Effects of tillage on soil microrelief, surface depression storage and soil water storage. Soil & Tillage Research, 76(2):105–114.

Heathwaite, A. L., Quinn, P. F., and Hewett, C. J. M. 2005. Modelling and managing critical source areas of diffuse pollution from agricultural land using flow connectivity simulation. Journal of Hydrology, 304(1-4):446–461.

Helming, K., Romkens, M. J. M., and Prasad, S. N. 1998. Surface roughness related processes of runoff and soil loss: A flume study. Soil Science Society of America Journal, 62(1):243–250.

Henderson, F. M. 1966. *Open Channel Flow (Macmillan Series in Civil Engineering)*. Prentice Hall.

Heng, B. C. P., Sander, G. C., and Scott, C. F. 2009. Modeling overland flow and soil erosion on nonuniform hillslopes: a finite volume scheme. Water Resources Research, 45(5):W05423.

Hirsch, L. M. and Schuette, J. F. 1999. Graph theory applications to continuity and ranking in geologic models. Computers & Geosciences, 25(2):127–139.

Hopp, L. and McDonnell, J. J. 2009. Connectivity at the hillslope scale: Identifying interactions between storm size, bedrock permeability, slope angle and soil depth. Journal of Hydrology, 376(3-4):378–391.

Hunt, A. G. 2005. Continuum percolation theory for saturation dependence of air permeability. Vadose Zone Journal, 4(1):134–138.

Imeson, A. C. and Prinsen, H. A. M. 2004. Vegetation patterns as biological indicators for identifying runoff and sediment source and sink areas for semi-arid landscapes in Spain. Agriculture Ecosystems & Environment, 104(2):333–342.

Jencso, K. G., McGlynn, B. L., Gooseff, M. N., Wondzell, S. M., Bencala, K. E., and Marshall, L. A. 2009. Hydrologic connectivity between landscapes and streams: transferring reach- and plot-scale understanding to the catchment scale. Water Resources Research, 45(4):W04428.

Jester, W. and Klik, A. 2005. Soil surface roughness measurement - methods, applicability, and surface representation. Catena, 64(2-3):174–192.

Journel, A. G. and Deutsch, C. V. 1993. Entropy And Spatial Disorder. Mathematical Geology, 25(3):329–355.

Kamphorst, E. C. 2000a. *Mesures et méthodes d'estimation de la capacité de stockage d'eau dans le micro-relief créé par les opérations de travail du sol*. Ph.D. thesis, Institut National Agronomique Paris-Grignon.

Kamphorst, E. C. and Duval, Y. 2001. Validation of a numerical method to quantify depression storage by direct measurements on moulded surfaces. Catena, 43(1):1–14.

Kamphorst, E. C., Jetten, V., Guerif, J., Pitkanen, J., Iversen, B. V., Douglas, J. T., and Paz, A. 2000. Predicting depressional storage from soil surface roughness. Soil Science Society of America Journal, 64(5):1749–1758.

Kamphorst, E. C., Chadoeuf, J., Jetten, V., and Guerif, J. 2005. Generating 3D soil surfaces from 2D height measurements to determine depression storage. Catena, 62(2-3):189–205.

Kazezyilmaz-Alhan, C. M. and Medina, M. A. 2007. Kinematic and diffusion waves: Analytical and numerical solutions to overland and channel flow. Journal Of Hydraulic Engineering-Asce, 133(2):217–228.

Knudby, C. and Carrera, J. 2005. On the relationship between indicators of geostatistical, flow and transport connectivity. Advances in Water Resources, 28(4):405–421.

Knudby, C. and Carrera, J. 2006. On the use of apparent hydraulic diffusivity as an indicator of connectivity. Journal of Hydrology, 329(3-4):377–389.

Krishnan, S. and Journel, A. G. 2003. Spatial connectivity: From variograms to multiple-point measures. Mathematical Geology, 35(8):915–925.

Laloy, E. and Bielders, C. L. 2008. Plot scale continuous modelling of runoff in a maize cropping system with dynamic soil, surface properties. Journal of Hydrology, 349(3-4):455–469.

Lane, S. N., Reaney, S. M., and Heathwaite, A. L. 2009. Representation of landscape hydrological connectivity using a topographically driven surface flow index. Water Resources Research, 45(8):W08423.

Langford, K. J. and Turner, A. K. 1972. Effects of rain and depression storage on overland flow. Trans. Inst. Eng. Aust. CE, 14:137–141.

Langhans, C., Govers, G., Diels, J., Leys, A., Clymans, W., and Van den Putte, J., A. andValckx. 2010. Experimental rainfall-runoff data: the concept of infiltration capacity needs re-thinking. Journal of Hydrology (under review).

Lawrence, D. S. L. 1997. Macroscale surface roughness and frictional resistance in overland flow. Earth Surface Processes and Landforms, 22(4):365–382.

Lawrence, D. S. L. 2000. Hydraulic resistance in overland flow during partial and marginal surface inundation: Experimental observations and modeling. Water Resources Research, 36(8):2381–2393.

Lehmann, P., Hinz, C., McGrath, G., Tromp-van Meerveld, H. J., and McDonnell, J. J. 2007. Rainfall threshold for hillslope outflow: an emergent property of flow pathway connectivity. Hydrology and Earth System Sciences, 11(2):1047–1063.

Lexartza-Artza, I. and Wainwright, J. 2009. Hydrological connectivity: Linking concepts with practical implications. Catena, 79(2):146–152.

Linsley, R. K., Kohler, M. A., and L., P. J. 1949. *Applied Hydrology*. New York,McGraw-Hill.

Martin, Y., Valeo, C., and Tait, M. 2008. Centimetre-scale digital representations of terrain and impacts on depression storage and runoff. Catena, 75(2):223–233.

Mathias, S. A., Butler, A. P., McIntyre, N., and Wheater, H. S. 2005. The significance of flow in the matrix of the Chalk unsaturated zone. Journal of Hydrology, 310(1-4):62–77.

Mayor, A. G., Bautista, S., Small, E. E., Dixon, M., and Bellot, J. 2008. Measurement of the connectivity of runoff source areas as determined by vegetation pattern and topography: a tool for assessing potential water and soil losses in drylands. Water Resources Research, 44(10):W10423.

Meerkerk, A. L., van Wesemael, B., and Bellin, N. 2009. Application of connectivity theory to model the impact of terrace failure on runoff in semi-arid catchments. Hydrological Processes, 23(19):2792–2803.

Michaelides, K. and Chappell, A. 2009. Connectivity as a concept for characterising hydrological behaviour. Hydrological Processes, 23(3):517–522.

Moore, I. D. and Larson, C. L. 1979. Estimating Micro-Relief Surface Storage From Point Data. Transactions of the ASAE, 22(5):1073–1077.

Moreno, R. G., Alvarez, M. C. D., Alonso, A. T., Barrington, S., and Requejo, A. S. 2008. Tillage and soil type effects on soil surface roughness at semiarid climatic conditions. Soil & Tillage Research, 98(1):35–44.

Morgan, R. P. C., Quinton, J. N., and Rickson, R. J. 1994. Modeling Methodology For Soil-Erosion Assessment And Soil Conservation Design - The Eurosem Approach. Outlook on Agriculture, 23(1):5–9.

Mueller, E. N., Wainwright, J., and Parsons, A. J. 2007. Impact of connectivity on the modeling of overland flow within semiarid shrubland environments. Water Resources Research, 43(9):W09412.

Mwendera, E. J. and Feyen, J. 1992. Estimation Of Depression-Storage And Manning Resistance Coefficient From Random Roughness Measurements. Geoderma, 52(3-4):235–250.

Nash, J. and Sutcliffe, J. 1970. River flow forecasting through conceptual models part I - A discussion of principles. Journal of Hydrology, 10/3:282–290.

Neuweiler, I. and Cirpka, O. A. 2005. Homogenization of Richards equation in permeability fields with different connectivities. Water Resources Research, 41(2):W02009.

Nikuradse, J. 1933. Stromungsgesetze in rauhen Rohren. Forschung auf dem Gebiete des Ingenieurwesens. NACA Technical Memorandum 1292.

Ocampo, C. J., Sivapalan, M., and Oldham, C. 2006. Hydrological connectivity of upland-riparian zones in agricultural catchments: Implications for runoff generation and nitrate transport. Journal of Hydrology, 331(3-4):643–658.

Pardo-Iguzquiza, E. and Dowd, P. A. 2003. CONNEC3D: a computer program for connectivity analysis of 3D random set models. Computers & Geosciences, 29(6):775–785.

Paz-Ferreiro, J., Bertol, I., and Vazquez, E. V. 2008. Quantification of tillage, plant cover, and cumulative rainfall effects on soil surface microrelief by statistical, geostatistical and fractal indices. Nonlinear Processes in Geophysics, 15(4):575–590.

Picouet, C., Hingray, B., and Musy, A. 2009. *Hydrologie - Une science pour l'ingénieur (Volume 2)*. Geodif.

Planchon, O. and Darboux, F. 2002. A fast, simple and versatile algorithm to fill the depressions of digital elevation models. Catena, 46(2-3):159–176.

Puigdefabregas, J., Sole, A., Gutierrez, L., del Barrio, G., and Boer, M. 1999. Scales and processes of water and sediment redistribution in drylands: results from the Rambla Honda field site in Southeast Spain. Earth-Science Reviews, 48(1-2):39–70.

Razafison, U., Cordier, S., Delestre, O., Darboux, F., Lucas, C., and James, F. not communicated. A shallow water model for the numerical simulation of overland flow on surfaces with ridges and furrows. 93A30, 81T80, 58J45, 35L65.

Reaney, S. M., Bracken, L. J., and Kirkby, M. J. 2007. Use of the Connectivity of Runoff Model (CRUM) to investigate the influence of storm characteristics on runoff generation and connectivity in semi-arid areas. Hydrological Processes, 21(7):894–906.

Rinaldo, A., Banavar, J. R., Colizza, V., and Maritan, A. 2004. On network form and function. Physica A-Statistical Mechanics And Its Applications, 340(4):749–755.

Roche, N., Daian, J. F., and Lawrence, D. S. L. 2007. Hydraulic modeling of runoff over a rough surface under partial inundation. Water Resources Research, 43(8):W08410.

Rodriguez-Iturbe, I., Rinaldo, A., Rigon, R., Bras, R. L., Ijjaszvasquez, E., and Marani, A. 1992. Fractal Structures As Least Energy Patterns - The Case Of River Networks. Geophysical Research Letters, 19(9):889–892.

Samouelian, A., Vogel, H. J., and Ippisch, O. 2007. Upscaling hydraulic conductivity based on the topology of the sub-scale structure. Advances in Water Resources, 30(5):1179–1189.

Scheibe, T. 1993. *Characterization of the spatial structuring of natural porous media and its impacts on subsurface flow and transport*. Ph.D. thesis, Stanford University.

Singh, V. P. 1995. Computer models of watershed hydrology. Computer models of watershed hydrology., pages xiv + 1130 pp.

Singh, V. P. and Frevert, D. 2002. Mathematical models of small watershed hydrology and applications. Mathematical models of small watershed hydrology and applications, pages xxi + 950 pp.

Smart, G. M., Duncan, M. J., and Walsh, J. M. 2002. Relatively rough flow resistance equations. Journal of Hydraulic Engineering-Asce, 128(6):568–578.

Smith, M. W., Cox, N. J., and Bracken, L. J. 2007. Applying flow restistance equations to overland flows. Progress in Physical Geography, 31:363–387.

Stammers, W. N. and Ayers, H. D. 1957. The effect of slope and microtopography on depression storage and surface detention. General Assembly of Toronto, 3:89–93.

Stieglitz, M., Shaman, J., McNamara, J., Engel, V., Shanley, J., and Kling, G. W. 2003. An approach to understanding hydrologic connectivity on the hillslope and the implications for nutrient transport. Global Biogeochemical Cycles, 17(4).

Takken, I. and Govers, G. 2000. Hydraulics of interrill overland flow on rough, bare soil surfaces. Earth Surface Processes and Landforms, 25:1387–1402.

Takken, I., Govers, G., Steegen, A., Nachtergaele, J., and Guerif, J. 2001a. The prediction of runoff flow directions on tilled fields. Journal of Hydrology, 248(1-4):1–13.

Takken, I., Jetten, V., Govers, G., Nachtergaele, J., and Steegen, A. 2001b. The effect of tillage-induced roughness on runoff and erosion patterns. Geomorphology, 37(1-2):1–14.

Tatard, L., Planchon, O., Wainwright, J., Nord, G., Favis-Mortlock, D., Silvera, N., Ribolzi, O., Esteves, M., and Huang, C. H. 2008. Measurement and modelling of high-resolution flow-velocity data under simulated rainfall on a low-slope sandy soil. Journal of Hydrology, 348:1–12.

Taylor, P., Fahrig, L., and With, K. A. 2006. *Connectivity Conservation*, chapter Landscape connectivity: back to the basics, pages 29–44. Cambridge University Press.

Taylor, P. D., Fahrig, L., Henein, K., and Merriam, G. 1993. Connectivity Is A Vital Element Of Landscape Structure. Oikos, 68(3):571–573.

Tischendorf, L. and Fahring, L. 2000. On the usage and measurement of landscape connectivity. Oikos, 90(1):7–19.

Tyndale-Biscoe, J. P., Moore, G. A., and Western, A. W. 1998. A system for collecting spatially variable terrain data. Computers and Electronics in Agriculture, 19(2):113–128.

Verstraeten, G., Van Oost, K., Van Rompaey, A., Poesen, J., and Govers, G. 2001. Integraal land- en waterbeheer in landelijke gebieden met het oog op het beperken van bodemverlies en modderoverlast (proefproject gemeente Gingelom). Technical report, Laboratorium voor Experimentele Geomorfologie, Afdeling Fysische en Regionale Geografie, Universiteit KULeuven, Leuven, Belgium.

Verstraeten, G., Poesen, J., Demaree, G., and Salles, C. 2006. Long-term (105 years) variability in rain erosivity as derived from 10-min rainfall depth data for Ukkel (Brussels, Belgium): implications for assessing soil erosion rates. Journal of Geophysical Research-Part D-Atmospheres, pages D22109–1–11.

Vidal Vazquez, E., Vivas Miranda, J. G., and Paz Gonzalez, A. 2005. Characterizing anisotropy and heterogeneity of soil surface microtopography using fractal models. Ecological Modelling, 182(3-4):337–353.

Vincent, S., Caltagirone, J. P., and Bonneton, P. 2001. Numerical modelling of bore propagation and run-up on sloping beaches using a MacCormack TVD scheme. Journal of Hydraulic Research, 39(1):41–49.

Vogel, H. . J. 2002. Topological characterization of porous media. Morphology of Condensed Matter. Physics and Geometry of Spatially Complex Systems. 2nd International Workshop 'Statistical Physics and Spatial Statistics', pages 75–92—xviii+439.

Vogel, H. J. 2000. A numerical experiment on pore size, pore connectivity, water retention, permeability, and solute transport using network models. European Journal of Soil Science, 51(1):99–105.

Vogel, H. J. and Roth, K. 2001. Quantitative morphology and network representation of soil pore structure. Advances in Water Resources, 24(3-4):233–242.

Western, A. W., Bloschl, G., and Grayson, R. B. 1998. How well do indicator variograms capture the spatial connectivity of soil moisture? Hydrological Processes, 12(12):1851–1868.

Western, A. W., Bloschl, G., and Grayson, R. B. 2001. Toward capturing hydrologically significant connectivity in spatial patterns. Water Resources Research, 37(1):83–97.

Woolhiser, D., Smith, R., and Goodrich, D. 1990. KINEROS, a kinematic runoff and erosion model: documentation and user manual. Technical report, USDA, Agricultural Research Service.

Xu, C., Dowd, P. A., Mardia, K. V., and Fowell, R. J. 2006. A connectivity index for discrete fracture networks. Mathematical Geology, 38(5):611–634.

Zech, Y., Sorel, M., and Vansnick, M. 1983. Mathematical modelling of floods in rivers flooding and uncovering of flood plains. In *Hydraulic Aspects of Floods & Flood Control*.

Zinn, B. and Harvey, C. F. 2003. When good statistical models of aquifer heterogeneity go bad: A comparison of flow, dispersion, and mass transfer in connected and multivariate Gaussian hydraulic conductivity fields. Water Resources Research, 39(3):1051.

Titres récents de la collection

2001

Département des sciences du milieu et de l'aménagement du territoire

- N°1. Auquiere, Eric, SAR temporal series interpretation and backscattering modeling for maize growth monitoring.

Département de biologie appliquée et des productions agricoles

- Debier, Cathy, A study of the dynamics of vitamin A, vitamin E and PCBs in seals during lactation.

2002

Département des sciences du milieu et de l'aménagement du territoire

- N°7. Kruyts, Nathalie, Influence de la nature des constituants du sol sur la mobilisation rhizosphérique du radiocésium dans quelques sols forestiers.
- N°8. Mounir, Fouad, Conception d'un système d'information géographique pour l'aménagement et la gestion forestière au Maroc. Intégration des critères et indicateurs du développement durable: Application à la Forêt de la Maâmora.
- N°10. Tilmant, Amaury, Sustainable management of reservoir resources using flexible stochastic dynamic programming.
- N°11. du Bus de Warnaffe, Gaëtan, Impact des systèmes sylvicoles sur la biodiversité: une approche comparative en Ardenne.
- N°13. Kolai, Lounas, Etude d'un écosystème forestier: phytosociologie, phytodiversité, productivité et hydrologie au Bois de Lauzelle.
- N°18. Jourez, Benoit, Etude de l'effet d'unstimulus gravitationnel induit artificiellement sur la formation du bois de tension et du bois opposé dans de jeunes pousses de peuplier (Populus auramericana cv 'Ghoy').

- N°21. Hang, Peou, Les données pédologiques enrichissent la modélisation de la relation pluie-débit.
- N°23. de Wasseige, Carlos, Spatio-temporal characterisation of the sub-equatorial forest canopy based on multiscale approach from field and space observations.

Département de biologie appliquée et des productions agricoles

- Graindorge, Céline, Modélisation régionalisée bio-économique du secteur agricole pour l'analyse des politiques durables.
- Toyi, Isidore, Politique de libéralisation et efficience des marchés de céréales locales au Burkina Faso.
- N°3. Henao-Toro, Martha-Cécilia, Dynamique d'éléments fertilisants dans les sols dérivés de cendres volcaniques de la zone caféière centrale de Colombie, sous culture de bananier plantain.
- N°12. Nusura, Hassan, Les stratégies de développement et les politiques de sécurité alimentaire en Afrique sub-saharienne : le poids des incohérences.
- N°15. Sqalli Adoui, Driss, Evaluation des effets du Programme d'Ajustement Structurel Agricole sur la petite agriculture irriguée au Maroc.
- N°19. Kouam, Emile, L'intégration régionale du Cameroun par la promotion des échanges transfrontaliers des produits agricoles vivriers avec les pays voisins: rôle des marchés frontalier.
- N°20. Nchare, Amadou, Effets de la libéralisation économique et de la dévaluation du franc CFA sur l'offre du café arabica et des cultures concurrentes au Cameroun.

Département de chimie appliquée et des bio-industries

- Dambly, Stéphanie, The two main plant plasma membrane H(+)-ATPase isoforms differ in their regulatory properties.
- N°4. Coulibaly, Lacina, Bioconversion de macromolécules dans un réacteur simulant un écoulement piston en régime transitoire : cas de la bioremédiation d'eaux usées synthétiques par Aspergillus nige.
- N°6. Godard, Eric, Hydrogénation de l'anhydride maléique en présence de catalyseurs métalliques supportés sur charbon actif.
- N°14. Lermusieau, Guillaume, Influence de la variété de houblon sur les propriétés organoleptiques de la bière.
- N°16. Owsianik, Grzegorz, Identification of transcriptional and post-translational pathways linking protein degradation and multiple drug resistance in yeast.
- N°17. Grec, Sébastien, Caractérisation du promoteur de transcription de NpABC1, un gène codant pour un transporteur ABC de Nicotiana plumbaginifolia induit en présence d'un diterpène.
- N°22. Fetter, Karolina, Functional studies of plasma membrane aquaporins from Zea mays.
- N°24. De Cupere, Vinciane, Supramolecular organization of adsorbed collagen layers and nanoscale structure of polymer surfaces.

Faculté des sciences, département de biologie

- N°5. Levie, Amandine, Development of a biological control method of wheat aphids, by using Aphidiinae parasitoids (Hymenoptera : Braconidae).

Christian de Duve Institute of Cellular Pathology, Laboratoire de Chimie Physiologique

- N°9. Ghislain, Delpierre, Fructosamine 3-kinase, an enzyme involved in protein deglycation.

2003

Département des sciences du milieu et de l'aménagement du territoire

- N°25. Goor, François, Processes and dynamics of radio cesium cycling in Chernobyl-contaminated pine forests : a multi-scale approach.
- N°28. D'Or, Dimitri, Spatial prediction of soil properties: the Bayesian Maximum Entropy approach.
- N°29. Vincke, Caroline, Approche écophysiologique des flux d'eau au sein d'une chênaie pédonculée (Q. robur L.) dépérissante sur sol à régime hydrique alternatif.
- N°37. Lambot, Sébastien, Hydrogeophysical characterization of soil using ground penetrating radar.
- N°39. Hupet, François, Estimation of evapotranspiration fluxes at the field-scale: parameter estimation, variability and uncertainties.

Département de biologie appliquée et des productions agricoles

- N°26. Oum Eloma, Janvier, Analyse économique comparée de la gestion forestière publique des différentes stratégies de production ligneuse au Cameroun.
- N°31. Tilquin, Pierre, Methodological aspects of the mapping of disease resistance loci in livestock.
- N°35. Nsengimana, Jérémie, Contribution to the analysis of linkage disequilibrium in livestock : effects of selection and inbreeding.
- N°38. Tangni, Emmanuel, Occurrence of mycotoxins in beer, exposure assessment for consumers and development of biological detoxification options for the control of ochratoxin A during brewing.

Département de chimie appliquée et des bio-industries

- Di Croce, Pascal, Phillips catalysts for ethylene polymerization : surface organization, active sites and performances.
- N°27. Gijs, Laurence, Controlling the minor sulfur compounds in beer.

- N°30. Cellier, Caroline, Catalytic removal of nitrogen- and sulfur-containing volatile organic compoundsDestruction.
- N°32. Ramazzotti, Anna, Mitochondrial functional interactions between the yeast frataxin Yfh1p and Isu1p, a member of the iron-sulphur cluster assembly machinery in Saccharomyces cerevisiae.
- N°34. Stukkens, Yvan, Expression and roles of NpABC1 : a Nicotiana plumbaginifolia ABC transporter involved in the plant-pathogen response.
- N°36. Popescu Florea, Mihaela, Relationship between structure and activity of vanadium aluminium oxynitrides in propane ammoxidation.
- N°40. Wiame, Hugues, Characterisation and catalytic properties of mixed vanadium and aluminium oxynitride catalysts: "AlVON".

Faculté des Sciences, département de biologie

- N°33. Ducarme, Xavier, Convergences et divergences microadaptatives chez les acariens endogés et cavernicoles.

2004

Département de biologie appliquée et des productions agricoles

- N°43. Yankam Njonou, Rabelais, Analyse économique de la réponse du marché du blé différencié aux instruments de l'organisation commune des marchés du secteur des céréales : Le cas de la France.
- N°47. Collard, François, Characterization of frutctosamine 3-kinase related protein.
- N°49. Ruibal Mendieta, Nike Luisa, Lipids and minerals in spelt (Triticum aestivum ssp. spelta) and common wheat (T. aestivum ssp. vulgare): Chemical and nutritional distinction between both cereals.

Département de chimie appliquée et des bio-industries

- N°41. Kanczewska, Justyna, Regulation of the plant plasma membrane H+-ATPase by phosphorylation and 14-3-3 proteins.
- N°42. Liégeois, Catherine, Pour un meilleur contrôle du statut pro-oxydant/ antioxydant des matières premières de la bière. Etude de la contribution des différentes étapes de fabrication du moût aux teneurs en trans-2-nonénal des bières vieillies.
- N°44. Counet, Christine, Détermination des structures chimiques des polyphénols du chocolat et étude de leurs principales propriétés fonctionnelles.
- N°46. Lefebvre, Benoît, Plant H+-ATPase targeting to the plasma membrane is not by default and requires cytosolic structural determinants.
- N°50. Dries Jan, Development and comparison of different multifunctional permeable reactive barrier (MPRB) concepts for the treatment of groundwater contaminated by pollutant mixtures.

- N°51. Cranenbrouck, La culture monoxénique, un outil privilégié pour la systématique des champignons mycorhiziens à arbuscules et l'étude de leurs relations symbiotiques avec la plante hôte.
- N°52. Callewaert Maïté, Surface modification by stimuli-responsive polymers : from model systems to stainless steel cleanability.

Département des sciences du milieu et de l'aménagement du territoire

- N°45. Javaux, Mathieu, Solute transport in a heterogeneous unsaturated subsoil: experiments and modeling.
- N°48. Fontenelle, Jean-Philippe, Dynamiques agraires, irrigation et institutions dans le delta du Fleuve rouge (Viêt-nam).

2005

Département de biologie appliquée et des productions agricoles

- N°53. Nkunzimana, Tharcisse, Une filière agro-industrielle en mutation. Cas de la filière théicole au Burundi.
- N°55. Meunier, Alexandre, Detection of rhizomania in Belgium: Diversity and characterization of Beet necrotic yellow vein virus RNAs-2 and -3.
- N°56. Grissa, Kaouthar, Étude de la dynamique des populations et du contrôle des acariens ravageurs dans les vergers de pommiers tunisiens.
- N°62. Rubayiza, Aloys, Authentication and quality control of coffee by fluorescence and Raman spectroscopy.
- N°68. Odjo, Sunday Pierre, Modélisation en équilibre général non séparable et analyse de réformes agricoles et commerciales au Bénin.
- N°69. Célestin, Dario Styve, Stabilisation du secteur caféier en Haïti par la promotion de la concurrence et la mise en œuvre d'un plan d'assurance pour la gestion des risques agricoles.

Département de chimie appliquée et des bio-industries

- N° 57. Vermeulen, Catherine, Synthèse et caractérisation organoleptique de thiols polyfonctionnels Recherche de leur présence dans la bière.
- N°58. Van Wilder, Valérie, Phosphorylation des aquaporines de la membrane plasmique de maïs.
- N°64. Bertinchamps, Fabrice, Total oxidation of chlorinated VOCs on supported oxide catalysts.
- N°65. Demoulin, Olivier, Dynamic aspects of the surface of a palladium on alumina catalyst used in combustion of methane.
- N°67. Trincal, Mathieu, Grx5p, a mitochondrial glutaredoxin required for mitochondrial DNA maintenance.
- N°70. Dury, Frédéric, Coupling of the deoxygenation of benzoic acid with the oxidation of propylene as a new tool to elucidate the architecture of Mo-based oxide catalysts.

Département des sciences du milieu et de l'aménagement du territoire

- N°54. Romanowicz, Agnieszka Aleksandra, The impacts of environmental change on water resources: A case study in the Dyle catchment (Belgium) in support of the implementation of the Water Framework Directive.
- N°59. Delfosse, Thomas, Acid Neutralisation and Sulphur Retention in S-Impacted Andosols
- N°60. Titeux, Hugues, Transfert de carbone organique dissous et de métaux dans des sols forestiers acides: influence du fonctionnement de la litière et des réserves minérales du sol.
- N°61. Blaes, Xavier, Crop monitoring by advanced SAR remote sensing techniques : modelling and experimental analysis.
- N°63. Farcy, Christine, L'aménagement forestier à la croisée des chemins. Éléments de réponse au défi posé par les nouvelles attentes d'une société en mutation.
- N°66. Jonard, Mathieu, Dynamique des litières foliaires en peuplements purs et mélangés de chêne et de hêtre : Retombées foliaires et premières étapes de la décomposition.

2006

Département de biologie appliquée et des productions agricoles

- N°71. Muratori, Frédéric, Reconnaissance des facteurs cuticulaires de l'hôte et conséquences sur l'exploitation des colonies par le parasitoïde de pucerons, Aphidius rhopalosiphi (Hymenoptera: Aphidiinae).
- N°72. Condori Ali, Paulino Bruno, Analyse comparative et modélisation de la croissance et du développement de tubercules andins dans les Andes en Bolivie.
- N°75. Doucet, Diane, Development of a model and similarities with a benyvirus.
- N°76. Nkwembe Unsital, Guy-Bernard, La problématique de la pauvreté des ménages agricoles ruraux et urbains dans la périphérie de la ville de Kinshasa. Essai d'analyse du phénomène et de ses implications sur la sécurité alimentaire.
- N°78. Ndayiragjie, Alexis, Relations entre métabolisme des polyamines et la résistance au stress salin chez le riz (Oryza sativa L.).
- N°80. Secheli Ringot, Diana, Risk analysis of ochratoxin A and developpement of a decontamination procedure based on the biosorption of ochratoxin A onto yeast industry derivatives.
- N°82. Abboudi, Tarik, The indispensable amino acid requirements for maintenance in Atlantic salmon fry.
- N°83. Martins da Silva, Evaldo, Polyphenols from the Amazonian plant Inga edulis: process optimization for the production of purified extracts with high antioxidant capacity.
- N°84. Fadlaoui, Aziz, Modélisation bioéconomique de la conservation des ressources génétiques animales.

- N°85. Kambale Valimunzigha, Charles, Étude du comportement physiologique et agronomique de la tomate (Solanum lycopersicum L.) en réponse à un stress hydrique précoce.
- N°86. Lepoint, Pascale, Speciation within the African Coffee Wilt Pathogen.
- N°88. Mushagalusa Nachigera, Gustave, Competitive relationships in potato/maize intercropping: involvement of root system architecture
- N°89. Nyamangyoku Ishibwela, Obedi, Ferrous iron toxicity: Mechanisms of resistance and impact on nutrient elements at the vegetative stage in cultivated rices (Oryza sativa L., Oryza glaberrima Steud and interspecific hybrids)

Département de chimie appliquée et des bio-industries

- N°73. Pety de Thozée, Cédric, Implication of the ER quality control in the degradation of the yeast plasma membrane Pdr5 L183P ABC transporter.
- N°79. Gurdak, Elzbieta, Supramolecular organization of collagen layers adsorbed on polymers.
- N°87. Janssens, Xavier, Monitoring and predicting elusive species colonisation - Application to the otter in the Cévennes National Park (France).

Département des sciences du milieu et de l'aménagement du territoire

- N°74. Kayitakire, François, Forest stand characterisation using very high resolutions satellite remote sensing
- N°77. Van der Velde, Marijn, Agricultural and climatic impacts on the groundwater resources of a small island: measuring and modelling water and solute transport in soil and groundwater on Tongatapu.
- N°81. Degen, Thomas, Dynamique initiale de la végétation herbacée et de la régénération ligneuse dans le cas de trouées, au sein d'une hêtraie (Luzulo-Fagetum).

2007

Département de biologie appliquée et des productions agricoles

- N°97, De Dorlodot, Sophie, Root system architecture : a genetic analysis in rice.
- N°99, Daoui, Khalid, Recherche de stratégies d'amélioration de l'efficience d'utilisation du phosphore chez la fève (Vicia faba L.) dans les conditions d'agriculture pluviale au Maroc.
- N°101, Vanloqueren, Gaëtan, Penser et gérer l'innovation en agriculture à l'heure du génie génétique. Contribution d'une approche systémique d'innovations scientifiques dans deux filières agroalimentaires wallonnes pour l'évaluation, la gestion et les politiques d'innovation.
- N°109, Pairon, Marie, Ecology and population genetics of an invasive forest tree species: Prunus serotina Ehrh.

- N°111, Manyonga, Madika, Modelling the competition for light in maize (Zea mays L.)/bean (Phaseolus vulgaris L.) intercropping with three-dimensional approach.
- N°115, Silva de Souza, Jesus Nazareno, Etude des propriétés antioxydantes in vitro d'extraits de feuilles de Byrsonima crassifolia et Inga edulis et caractérisation partielle des composés phénoliques.
- N°116, Colinet, Hervé, Une approche écologique et biochimique de la résistance au froid chez un parasitoïde de puceron Aphidius colemani (Hymenoptera: Aphidiinae).

Département de chimie appliquée et des bio-industries

- N°90. Eyers, Laurent, Characterization of bacterial populations of 2,4,6-trinitrotoluene (TNT) contaminated soils and isolation of a Pseudomonas aeruginosa strain with TNT denitration activities.
- N°91. Dupré de Boulois, Hervé, Role of arbuscular mycorrhizal fungi on the accumulation of radiocaesium by plants.
- N°92. Crouzet, Jérôme, Expression pattern, ectopic expression and gene silencing of two Nicotiana Pleiotropic Drug Resistance transporters.
- N°93, Drugmand, Jean-Christophe, Characterization of Insect Cell Lines Is Required for Appropriate Industrial Processes.
- N°94, De La Providencia, Ivan Enrique, Contribution of Anastomosis and Hyphal Healing Mechanism to the Extraradical Mycelium Architecture of Arbuscular Mycorrhizal Fungi.
- N°95, Sebari, Karima, Optimisation de la gestion conjointe des ressources en eau de surface et des ressources en eau souterraines dans une région semi aride - la Vallée du Drâa.
- N°100, Vandermeeren, Caroline, Quaternary Structure and Regulation of the Nicotiana plumbaginifolia Plasma Membrane Proton Pump ATPase.
- N°102, Morales Belpaire Isabel, Fate of the active form of proteins in selected environmental matrices. Investigation with green fluorescent protein, ?-glucosidase, and amyloid fibrils in wastewater sludges, biofilms and soils.
- N°103, Trombik Tomasz, Characterization of two Pleiotropic Drug Resistance transporters from Nicotiana plumbaginifolia.
- N°104, Callemien, Delphine, Use of new methodologies to study phenolic compounds through beer storage.
- N°106, Van der Auwera, Géraldine, pAW63: A molecular wanderer in the Bacillus cereus gene pool.
- N°107, Mateos Pedrero, Cecilia, Synthesis and characterization of Rh supported on Ti-modified oxides: catalytic activity in the partial oxidation of methane.
- N°108, Voets, Liesbeth, Role of arbuscular mycorrhizal networks on plant interconnection and carbon transfer.
- N°110, Jerkovic, Vesna, Découverte du resvératrol dans les houblons. Impact de la variété, de l'année de récolte et du conditionnement en vue de la préparation d'extraits polyphénoliques enrichis en stilbènes.

- N°112, Dekeyser, Caroline, Elaboration and evaluation of nanostructured surfaces for the control of cell behavior.
- N°113, Nonckreman, Cristèle, Design of materials with nanostructured surface to improve hemocompatibility.
- N°114, Caillou, Samuel, Protein Adsorption: from Interfacial Interactions to Enzyme Activity.
- N°96, Lefèvre, Isabelle, Investigation of three Mediterranean plant species suspected to accumulate and tolerate high cadmium and zinc levels: morphological, physiological and biochemical characterization under controlled conditions.
- N°98, Desclée, Baudouin, Automated object-based change detection for forest monitoring by satellite remote sensing: applications in temperate and tropical regions.
- N°105, André, Frédéric, Influence of the heterogeneity of canopy structure on the spatio-temporal variability of atmospheric deposition within a mixed oak-beech stand

2008

Département de biologie appliquée et des productions agricoles

- N°120, Chirinos Gallardo, Rosana Sonia, Polyphenols from the Andean mashua (Tropaeolum tuberosum) tuber: Evaluation of genotypes, extraction, chemical characterization and antioxidant properties.
- N°126, Romier, Béatrice, Modulation of intestinal inflammation by polyphenols.
- N°130, Vaïanopoulos, Céline, Widespread occurrence of soil-borne mosaic viruses in Belgium. Preferential associations of Polymyxa graminis and mosaic viruses on cereals.
- N°131, Tran, Thi Nang Thu, Nutritional value of sesame oil cake and lysine utilization efficiency in plant protein-based diets for rainbow trout.
- N°134, Ngirente, Edouard, Les marchés agricoles intérieurs et les mutations agro- économiques en milieu rural rwandais. Application à la filière pomme de terre.
- N°139, Gilbert, Valérie, Genetic and pathogenic diversity of Pseudomonas syringae isolates associated with diseases on Belgian fruit trees.
- N°141, Delpierre, Matthieu, A Non-cooperative Approach to Rural Development Issues.
- N°142, André, Christelle, Evaluation of Andean potato cultivars as a source of dietary antioxidants.
- N°145, Bodin, Noëlie, Nutritional and interspecies effects on the estimation of threonine and lysine requirements in salmonid fry with a highlight on methodological impacts.
- N°147, Pissard, Audrey, Structure and genetic diversity of two Andean tuber crops, oca (Oxalis tuberosa Mol.) and mashua (Tropaeolum tuberosum R.&P.): influence of the mode of conservation and of the agronomic and biological characteristics

Département de chimie appliquée et des bio-industries

- N°117, Zelazny, Enric, Regulation of maize aquaporin trafficking to the plasma membrane.
- N°122, Bobik, Krzysztof, The two major tobacco plasma membrane H+-ATPases, PMA2 and PMA4 are differentially phosphorylated on their penultimate threonine.
- N°123, Cabana, Hubert, Elimination des perturbateurs endocriniens nonylphénol, bisphénol A et triclosan à l'aide de laccase de Coriolopsis polyzona. C
- N°133, Delannoy, Mélanie, Identification of peptidases in the Nicotiana tabacum leaf intercellular fluid.
- N°132, De Palmenaer, Daniel, Genomic portrayal of IS4 family -Modular insertion sequences, mobile insertion cassettes and overall family snapshot.
- N°135, Manente, Myriam, Rta1, a yeast plasma membrane protein which confers resistance to fungicides.
- N°129, Srasra, Mondher, Preparation and characterization of new basic catalyst by nitridation of Y zeolites.
- N°137, Hachez, Charles, The expression pattern and activity of Zea mays plasma membrane aquaporins highlight their central role in the control of the cell membrane water permeability.
- N°146, Soria, Miguel Angel, Etude des paramètres gouvernant les performances catalytiques d'AlPO, AlGaPO et GaPO purs et en présence de vanadium dans l'ammoxydation du propane

Département des sciences du milieu et de l'aménagement du territoire

- N°118, Van Cauwenbergh, Nora, Expert and local knowledge in decision support for natural resource management.
- N°119, Henriet, Céline, Silicon in banana (Musa spp.): a soil-plant system approach.C
- N°121, Tidjani, Adamou Didier, Erosion éolienne dans le Damagaram Est (Sud-Est du Niger) : Paramétrisation, quantification et moyens de lutte.
- N°124, Akponikpe, Pierre Bienvenu Irénikatché, Millet response to water and soil fertility management in the Sahelian Niger: experiments and modeling Erosion éolienne dans le Damagaram Est (Sud-Est du Niger) : Paramétrisation, quantification et moyens de lutte.
- N°125, Vancutsem, Christelle, Revisiting satellite time series compositing for earth observation applications.
- N°127, Opfergelt, Sophie, Silicon cycle in the soil-plant system: biogeochemical tracing using Si isotopes.
- N°128, de Araujo Marinho Filho, Eduardo Celsio, Economics of Hunger: Several Methods, Levels and Scales.
- N°136, Saqalli, Mehdi, Populations, Farming systems & Social transitions in Sahelian Niger: An Agent-based modeling approach.
- N°138, Lucau-Danila, Cozmin Catalin, LAI retrieval from SAR remote sensing for crop monitoring at regional scale.

- N°140, Iboukassene, Soraya, Dynamique de la végétation des forêts à Quercus suber anthropisées du Nord-Est de l'Algérie (Parc National d'El-Kala).
- N°143, Fasbender, Dominique, Bayesian data fusion in environmental sciences: Theory and applications.
- N°144, Hoang Thi Thai, Hoa, Soil characteristics, cropping patterns, and use of organic resources in the coastal sandy area of Thua Thien Hue province, Central Vietnam

2009

Département de biologie appliquée et des productions agricoles

- N°149, de Lespinay, Alexis, Study of seed priming mechanisms of three plant species used in revegetation of industrial sites
- N°153, Harahagazwe, Dieudonné, Heat tolerance assessment of the potato crop: evaluation of CIP clones in the lowlands of Burundi.

Département de chimie appliquée et des bio-industries

- N°148, Pokrzywa, Wojcieh, Targeting of the yeast Sna3p and Sna4p to the endosomal pathway depends on their interaction with ubiquitin ligase Rsp5p.
- N°150, Hoton, Florence, Insights into the Ecology and Genetic Diversity of Cereulide-producing Bacillus cereus strains.
- N°151, Fornelos Martins, Nadine, GIL01 and relatives, a new generation of tectiviruses infecting the Bacillus cereus group.

Département des sciences du milieu et de l'aménagement du territoire

- N°152, Marghadi, Saïd, Intégration des méthodes d'aide à la décision dans l'aménagement multifonctionnel des forêts au Maroc.
- N°160, Mattern, Samuel, Mapping and source identification of groundwater pollution by nitrate. Theory and application to the Brusselian sand groundwater body.

2010

Institut des Sciences de la Vie

- N°163, Cochonneau Daphné, Characterization of yeast polymerase gamma mutations associated with human disorders.
- N°165, Lebrun, Anne-Sophie, Towards functional and structural characterization of maize ZmSIP proteins belonging to a divergent aquaporin subfamily.

Earth and Life Institute

- N°161, Mehrvar Mohsen, Harahagazwe, Dieudonné, Diversity of soil-borne sugar beet viruses in Iran.
- N°162, Radoux, Julien, Updating land cover maps by GIS driven analysis of very high resolution satellite images.
- N°164, Obsomer, Valérie, Multi-scale Environmental Analysis and Prediction for Insects Vector of Disease. Application to Malaria Vector of Southeast Asia.
- N°166, Kalonda Mbulu, Gabriel, Analyse de la transmission des prix internationaux des produits agricoles sur les marchés des pays ACP.
- N°167, Fiamohe Rose, Facteur determinant les échanges de produits vivriers au Bénin : Rôle des institutions de marché.
- N°169, Eric Laloy, Measuring and modelling the impact of intercrop management on plot-scale runoff and erosion in a continuous maize cropping system.
- N°173, Mamadou Sall, Transfert de nitrate à travers la zone non saturée du sol vers la nappe phréatique de la zone de Niayes (Sénégal): caractérisation et modélisation.
- N°175, Michaël Antoine, Overland flow connectivity : theory and application at the interrill scale.

Pour plus d'informations, visitez http://edoc.bib.ucl.ac.be/

Publications and Conferences

Publications in international peer-reviewed journals or books

- Antoine, M., Javaux, M., Bielders, C., **What indicators can capture runoff-relevant connectivity properties of the micro-topography at the plot scale ?**, Advances in Water Resources, 2009, 32, p. 1297-1310.

- Antoine, M., Chalon, C., Darboux, F., Javaux M., Bielder, C., **Estimating changes in effective values of surface detention, depression storage and friction factor at the interrill scale, using a cheap and fast method to mold the soil surface micro-topography**, CATENA, accepted article.

- Antoine, M., Javaux, M., Bielders, C., **Integrating subgrid connectivity properties of the micro-topography in distributed runoff models, at the interrill scale**, Journal of Hydrology, submitted article.

- Antoine, M., Javaux, M., Bielders, C., **Connectivity evolution of micro-topography: measurement for a bare loamy plot and reproduction in a numerical field generator**, Advances in Water Resources, article to be submitted.

- Van Nieuwenhuyse, B., Antoine, M., Wyseure, G., Govers, G., **Pattern-process relationships in surface hydrology: hydrological connectivity expressed in landscape metrics**, Hydrological Processes, submitted article.

- Lambot, S., Antoine, M., Vanclooster, M., Slob E.C., **Effect of soil roughness on the inversion of off-ground monostatic GPR signal for non-invasive quantification of soil properties**, Water Resources Research, 2006, 42, W03403.

- Lambot S., Antoine M., Van den Bosch, I., Slob, E.C., Vanclooster, M., **Sequential electromagnetic and hydrodynamic inversion of GPR signal**

to reconstruct the distibution of the vadose zone hydraulic properties, Vadose Zone Journal, 2004, 3, p. 1072-1081.

Conferences

- Antoine, M., Javaux, M., Bielders, C., **Surface detention and depression storage evolution as a function of rainfall erosivity**, 3d PhD Student Day of the Graduate School ENVITAM, FUNDP, Namur, 12 January 2010.
- Antoine M., Javaux M., Bielders C, **Runoff triggering at the plot scale: from indices of structural and functional connectivity to the hydrograph prediction**, AGU Fall Meeting, San Francisco, USA, 14-18 December 2009.
- Bielders C., Antoine M., Javaux M., **Seasonal evolution of surface detention and retention properties with rain erosivity, at the interill scale**, AGU Fall Meeting, San Francisco, USA, 14-18 December 2009.
- Antoine M., Chalon C., Darboux F., Javaux M., Bielders C., **Square meter scale new moulding method to study the temporal evolution of the soil surface micro-topography and its impact on the runoff dynamics**, EGU General Assembly, Vienna, Austria, 20-24 April 2009.
- Antoine M., Bielders C., Javaux M., **Comparative study of connectivity indicators in surface hydrology**, EGU General Assembly 2008, Vienna, Austria, 14-18 April 2008.
- Antoine M., Javaux M., Bielders C., **DIRECTFLOW, a small scale hydraulic model for complex topography**, PhD Day Envitam, University of Liège, Belgium, 29 January 2008.
- Antoine M., Bielders C., Javaux M., Vanclooster M., **Application of the connectivity concept on soil surface micro-topography, and impact on runoff dynamics: numerical experiment**, EGU General Assembly, Vienna, Austria, 16-19 April 2007.
- Lambot S., Antoine M., Slob E.C., Vanclooster M., **Estimation on the effective vadose zone hydraulic properties, based on electromagnetics and hydrodynamic invesions of GPR signals**, EGU General Assembly, Vienna, Austria, 25-29 April 2005.
- Lambot S., Van den Bosch I., Antoine M., Gregoire M., Vanclooster M., Slob E.C., **Modeling of GPR Signal and Inversion for Identifying the Subsurface Dielectric Properties**, 30th International conference on Ground Penetrating Radar, Delft University of Technology, The Netherlands, 21-24 June 2004.

Summary

To predict the hydrological response of a hillslope to a rainfall event, the spatial configuration of soil roughness needs to be taken into account. Quantitative expressions of hydrological connectivity based on topography may improve the prediction of overland flow propagation, especially if the connectivity concept is applied at the subgrid scale of current hillslope models, which corresponds to the interrill scale.

Our first objective was to measure the effect of micro-topography on overland flow. Some of the water is stored in depressions (depression storage) and some is temporarily stored in the flowing water layer (surface detention). To measure those storages, we used a new molding technique that reproduced realistic but waterproof soil surfaces, which were subjected to artificial runoff. The evolution of both storages following rainfall was related to the cumulative rainfall erosivity value.

Our second objective was to find runoff-relevant connectivity properties of micro-topography. Based on numerical runoff experiments, we found that, among a number of existing structural connectivity indices and a proposed new functional connectivity index (namely the Relative Surface Connection function), the RSC function was the most robust and directly linkable to the runoff dynamics.

Our last objective was to introduce the connectivity properties captured by the RSC function at the subgrid (interrill) scale in distributed hydrological models. A corrective procedure was proposed to combine both surface detention and depression storage dynamics. It allows mimicking the hydraulic behavior of small plots where the effect of the micro-topography is characterized by few (1 or 2) effective parameters implementable in hillslope models.

Born in Brussels on the 8th of April 1981, Michaël Antoine holds a Masters degree in bio-engineering (2004) from the Université catholique de Louvain. He was then teaching assistant in hydrology and devoted half of its professional time to research.